Tampere University

ATENA REZAEI

Forward and Inverse Modeling via Finite Elements in EEG/MEG Source Localization

Application to Event Related Responses

Tampere University Dissertations 506

Tampere University Dissertations 506

ATENA REZAEI

Forward and Inverse Modeling via Finite Elements in EEG/MEG Source Localization

Application to Event Related Responses

ACADEMIC DISSERTATION
To be presented, with the permission of
the Faculty of Engineering and Natural Sciences
of Tampere University,
for public discussion in the auditorium S2
of the Sähkötalo, Korkeakoulunkatu 3, Tampere,
on 17 December 2021, at 12 o'clock.

ACADEMIC DISSERTATION
Tampere University, Faculty of Engineering and Natural Sciences
Finland

Responsible supervisor and Custos	Associate Professor (tenure track) Sampsa Pursiainen Tampere University Finland	
Supervisor	Professor Carsten H. Wolters University of Münster Germany	
Pre-examiners	Professor Francesca Pitolli Università di Roma “La Sapienza” Italy	Professor Alberto Sorrentino Universita degli studi di Genova Italy
Opponent	Associate Professor Stephanie Lohrengel Université de Reims Champagne-Ardenne France	

The originality of this thesis has been checked using the Turnitin OriginalityCheck service.

Cover design: Roihu Inc.

ISBN 978-952-03-2179-6 (print)
ISBN 978-952-03-2180-2 (pdf)
ISSN 2489-9860 (print)
ISSN 2490-0028 (pdf)
http://urn.fi/URN:ISBN:978-952-03-2180-2

PunaMusta Oy – Yliopistopaino
Joensuu 2021

Dedicated to my parents for all their devotion and efforts to teach us how to fly!

ACKNOWLEDGEMENTS

This thesis serves as a documentation of the final part of my doctoral studies. It was conducted at the Inverse Problems research group, Faculty of Information Technology and Communication Sciences (ITC), Unit of Computing Sciences at Tampere University between 2017–2021. The research projects in this thesis were supported by Academy of Finland Center of Excellence in Inverse Modeling and Imaging 2018-2025 (CoE 336792), DAAD project (334465), Vilho, Yrjö and Kalle Väisälä Foundation, Alfred Kordelini Foundation, and ERA PerMed project PerEpi (344712). The research in this thesis was carried out in collaboration with the institute of Biomagnetism and Biosignalanalysis (IBB), University of Münster, Germany.

The completion of this thesis would not have been possible without the contribution of several individuals. First and foremost, I would like to express my sincere gratitude to my supervisor, Associate Professor Sampsa Pursiainen for his continuous support of my PhD studies and related research, for his patience and invaluable advice during my studies. I am grateful for every single learning I gained from his immense knowledge and plentiful experience. My deep gratitude is also extended to my cosupervisor, Professor Carsten H. Wolters from Institute for Biomagentism and Biosignal Analysis (IBB), University of Münster, Germany, for sharing his priceless experience and taking care of ethical regulations for sharing experimental datasets from IBB. For his insightful comments and support, which incented me to widen my research from various perspectives. I would like to thank doctoral researcher Marios Antonakakis and postdoctoral researcher Mariacarla Piastra from IBB and Donders Institute for Brain, Cognition and Behaviour for their support in preparing and preprocessing somatosensory evoked datasets.

I owe my thank you to Professor Jukka Peltola, Neurologist, and Herkko Matilla, Medical Physicist from Tampere University Hospital for sharing their extensive knowledge and experience on deep brain stimulation (DBS) and measured data, providing relevant training and seminars. I would have never forgotten the unique experience

I gained by participating in DBS surgery visit that organized by medical physicist Herkko Matilla. It once more reminded me how much brain is a peculiar and mysterious organ and how less I know about its functionality. My appreciation goes to postdoctoral researcher Narayan Puthanmadam Subramaniyam from faculty of Medicine and Health Technology, Tampere University, for his biomedical knowledge and instructions on analyzing and processing of evoked datasets. I would like to thank Associate Professor Tiina Parviainen, a director of the Center for Interdisciplinary Brain Research (CIBR) and PhD Simo Monto for sharing their knowledge on MEG and organizing MEG driving license course and hands-on training at MEG lab at the University of Jyväskylä. I thank inverse problem research team and my former and recent office-mates for bringing such a friendly ambiance for working.

My deepest thank you belongs to Taina and Markku Matis and Isoäiti for their all-time care and support here in Finland. My heartfelt thanks go to my dear friends who accompanied me during this journey in sweet and bitter moments.

I owe a thank you to Finland, the land of unparalleled nature and peace, for the opportunity it gave me to make my dreams come true through any hardship. The life experience that made me stronger and courageous enough to move forward after each falling down. I have enjoyed every moment ride of this roller coaster! Thank you Finland for teaching me how to carry my Sisu spirit in every circumstance. Kiitos!

Last but not least, my deepest love and thank you belong to my parents, Shahla and Rafat, the pillars of my life, for their everlasting love and support. For always standing by my side no matter when and where. For sure passing this journey without them was impossible. Miles away but hearts are close. And my brother, Ebrahim, without you life was so serious!

I would like to end this chapter of my life by a verse of a poem from Hafez, a Persian poet who said: " I wish I could show you, when you are lonely or in darkness,
the astonishing light of your own being! "

Tampere, 1 October 2021
Atena Rezaei

ABSTRACT

This thesis aims at advancing the development of forward and inverse modeling techniques to solve the electromagnetic inverse problems arising in electro and magnetoencephalography (EEG and MEG) of the human brain. A finite element method (FEM)-based and divergence conforming H(div) forward modeling approach is applied to obtain the electric and magnetic field of the neural activity in a thin, heavily folded and multicompartment head model. This accurate H(div) approach enables inversion techniques to localize the primary current distribution of the brain robustly. Furthermore, this thesis introduces the Zeffiro Interface (ZI) code package which provides a platform for integrating forward and inverse solvers for a realistic head model. ZI uses graphics processing unit (GPU) acceleration and can, therefore, flexibly utilize finite element (FE) models with a high 1 mm accuracy. Herein, ZI is applied in method development and experimental studies.

In this thesis, a source localization approach is built upon conditionally Gaussian hierarchical Bayesian modeling (HBM), the iterative alternating sequential (IAS) reconstruction technique, a variable resolution of the source space, and random sampling. These different aspects are combined in the randomized multiresolution scanning (RAMUS) method, which is introduced as a strategy to marginalize the effect of discretization and optimization errors and thereby, minimize the depth-bias of the reconstructed activity. A prior-over-measurement signal-to-noise ratio (PM-SNR) is introduced as a way to choose hyperprior parameters for a given mesh resolution and noise level. The proposed methods are investigated using simulated and experimental somatosensory evoked potentials and fields (SEPs and SEFs). RAMUS was found to be a promising technique to distinguish the subcortical activity of the brain, which might occur simultaneously with cortical components. The non-invasive detection of subcortical activity is a scientifically important and timely topic which can have remarkable implications for the treatment of Alzheimer's or Parkinson's disease and, in particular, for localizing refractory epilepsy.

CONTENTS

List of Figures

ABBREVIATIONS

ANT-DBS	Anterior Nuclei of Thalamus Deep Brain Stimulation
AP	Action Potential
ASSRs	Auditory Steady-State Responses
BEM	Boundary Element Method
CEM	Complete Electrode Model
CM	Conditional Mean
CSF	Cerebrospinal Fluid
DBS	Deep Brain Stimulation
DoF	Degrees of Freedom
e.g.	for example, from Latin *exempli gratia*
ECD	Equivalent Current Dipole
EEG	Electroencephalography
EIT	Electrical Impedance Tomography
EPc	Erb's Point
ERR	Evoked Related Responses
et al.	and others, from Latin *et alii*
EW	Edge Wise
FE	Finite Element
FEM	Finite Element Method
FI	Face Intersecting
GPU	Graphics Processing Unit

HBM	Hierarchical Bayesian Modeling
i.e.	that is, from Latin *id est*
IAS	Iterative Alternating Sequential
ICA	Independent Component Analysis
IDR	Interdecile Range
IQR	Interquartile Range
LF	Lead Field
LP	Linear Programming
MAG	Magnitude Measure
MAP	Maximum *a posteriori*
MCE	Minimum Current Estimate
MCMC	Markov chain Monte Carlo
MEG	Magnetoencephalography
MNE	Minimum Norm Estimate
MPO	Mean Position Orientation
MRI	Magnetic Resonance Imaging
ms	Millisecond
mV	Millivolt
PBO	Position Based Optimization
PI	Partial Integration
PM-SNR	Prior-over-Measurement Signal-to-Noise Ratio
RAMUS	Randomized Multiresolution Scanning
RDM	Relative Difference Measure
ROI	Region of Interest
SEEG	Stereo-EEG
SEF	Somatosensory Evoked Field
SEP	Somatosensory Evoked Potential

SI	Système International
SNR	Signal-to-Noise Ratio
SOA	Stimulus Onset Asynchrony
SQUID	Superconducting Quantum Interference Device
STD	Standard Deviation
SV	St. Venant
tACS	Transcranial Alternating Current Stimulation
tDCS	Transcranial Direct Current Stimulation
tES	Transcranial Electrical Stimulation
tPCS	Transcranial Pulse Current Stimulation
tRNS	Transcranial Random Noise Stimulation
VPL	Ventral Posterolateral
ZI	Zeffiro Interface

LIST OF SYMBOLS

G	Gamma Hyperprior
IG	Inverse Gamma Hyperprior
L	Lead Field Matrix
R	Restriction Matrix
S_{ε}^{+}	Detectable Source Space
S_{ε}^{-}	Undetectable Source Space
T	Transfer Matrix
Ω	Bounded Head Domain
$\vec{J}^{p}$	Primary Current Density
$\vec{J}_{h}^{p}$	Discretized Primary Current Distribution
$\vec{J}^{t}$	Total Current
$\vec{\omega}$	Divergence Conforming Basis Function
$\vec{n}$	Normal Vector
$\vec{q}$	Dipolar Moment
$\vec{r}$	Dipolar Position
β	Shape Parameter
λ	Regularization Parameter
ω	Weighting Coefficient
ψ	Nodal Basis Function
σ	Conductivity Tensor
θ	Hyperparameter

θ_0	Scale Parameter
f	Load Vector
m	Monopolar Load
$p(\theta)$	Hyperprior
$p(x \mid \theta)$	Conditional Prior
$p(x \mid y)$	Posterior Probability Density
$p(x)$	Prior
$p(y \mid x)$	Likelihood
u	Electric Potential
u_h	Discretized Electric Potential
v	Test Function
x	Unknown Source
y	Measurement Vector
$H^1(\Omega)$	Sobolev Space
H(div)	Current Preserving (divergence conforming) Source Modeling

ORIGINAL PUBLICATIONS

Publication I T. Miinalainen, A. Rezaei, D. Us, A. Nüßing, C. Engwer, C. H. Wolters and S. Pursiainen. A realistic, accurate and fast source modeling approach for the EEG forward problem. *Journal of NeuroImage* 184 (2019), 56–67. DOI: 10.1016/j.neuroimage.2018.08.054.

Publication II Q. He, A. Rezaei and S. Pursiainen. Zeffiro user interface for electromagnetic brain imaging: A GPU accelerated fem tool for forward and inverse computations in Matlab. *Journal of Neuroinformatics* 18 (2019), 1–14. DOI: 10.1007/s12021-019-09436-9.

Publication III A. Rezaei, A. Koulouri and S. Pursiainen. Randomized multiresolution scanning in focal and fast E/MEG sensing of brain activity with a variable depth. *Journal of Brain Topography* 33.2 (2020), 161–175. DOI: 10.1007/s10548-020-00755-8.

Publication IV A. Rezaei, M. Antonakakis, M. Piastra, C. H. Wolters and S. Pursiainen. Parametrizing the Conditionally Gaussian Prior Model for Source Localization with Reference to the P20/N20 Component of Median Nerve SEP/SEF. *Journal of Brain Sciences* 10.12 (2020), 934. DOI: 10.3390/brainsci10120934.

Publication V A. Rezaei, J. Lahtinen, F. Neugebauer, M. Antonakakis, M. Piastra, A. Koulouri, C. H. Wolters and S. Pursiainen. Reconstructing Subcortical and Cortical Somatosensory Activity via the RAMUS Inverse Source Analysis Technique using Median Nerve SEP Data. (2021). Submitted to NeuroImage Journal, 21.

Author's contribution

Publication I	The author assisted in the inverse modeling analysis and discussion together with S.Pursiainen and served as a corresponding author to prepare and edit the manuscript for submission.
Publication II	The author implemented the FreeSurfer to Zeffiro Interface (ZI) pipeline for segmentation, performed the analysis for Brainstorm's EEG and epilepsy dataset and served as a corresponding author. The author prepared and wrote the manuscript together with S.Pursiainen and Q.He.
Publication III	The author had contribution in running the numerical results for deep and superficial source localization. The author participated in analyzing the statistical results and writing the article together with S.Pursiainen and A.Koulouri and served as a corresponding author.
Publication IV	The author performed the analysis for SEP/SEF measurements and investigated the appropriate parameters for inverse modeling. The author analyzed the results together with S.Pursiainen and served as a corresponding author. The author wrote and edited the manuscript together with the other co-authors.
Publication V	The author had major contribution in the investigation of different components analysis, running the results and writing the article. The author served as a corresponding author and edited the manuscript together with S.Pursiainen and the other co-authors.

1 INTRODUCTION

This thesis work serves as a stepping stone towards using complex forward and inverse modeling processes to solve electromagnetic inverse problems associated with fully realistic human head models and experimental measurements, while providing short computing time and appropriate usability of these techniques. The research works of this dissertation, in particular, shed light on the deeper understanding and contribution of mathematical numerical techniques concerning electro and magnetoencephalography (EEG and MEG), where advanced forward and inverse techniques need to be combined to enable the appropriate localization of the primary current distribution of the neural activity.

On the one hand, forward methods are needed to simulate the electromagnetic field originating from strongly folded thin cortical layers or subcortical nuclei, taking into account the complex effects caused by different tissue types within the human head. On the other hand, careful modeling is needed since a misplaced current source can lead to large deviations of the simulated field, even if the head model and its numerical discretization would otherwise be accurate. Following this, inverse techniques utilizing the simulated field information effectively are necessary, since the field includes highly suppressed components, e.g., the ones corresponding to the deep activity of the brain. Preserving these suppressed components in the solution, while at the same time localizing the well-visible ones accurately at their originating locations poses a challenge which is not solvable without special techniques. The findings obtained in this thesis offer useful insights for the neuroscience community for future studies.

1.1 Aim and scope of this thesis

This thesis aims to: **(I)** Advance the implementation of forward and inverse techniques for electromagnetic brain imaging applications, e.g., electroencephalography

(EEG) and magnetoencephalography (MEG). To this end, a finite element method (FEM) based forward modeling [35] and approach for multicompartment and complex head model has been developed to simulate precisely the generators of EEG and MEG signals, i.e., primary current density of apical dendrites of the pyramidal cell within the thin layers of the brain. Correspondingly, the inverse modeling techniques coupled with forward modeling were investigated to localize the primary current density of neurons robustly. To approach these topics, **(II)** we introduced Zeffiro Interface (ZI) [59] as an openly available platform implemented in MATLAB (MathWorks Inc., USA). It is equipped with forward and inverse solvers to reconstruct the neural activity in EEG and MEG from heavily folded brain tissues with a high resolution (1 mm) realistic head model. Furthermore, the application of ZI is not solely restricted to EEG and MEG, e.g., the interface can map the conductivity distribution for electrical impedance tomography (EIT) [123] for region of interest (ROI), for cases such as hemorrhage in stroke [32] and incorporating an inverse solver. Additionally, as a future potential, the transcranial electrical stimulation (tES) [91] solver and current pattern optimization of deep brain stimulation (DBS) [131] can be merged to the current version of the interface. The former technique is a non-invasive brain stimulation to modulate the neural activity and the latter one is known as an invasive technique by implanting electrodes deep inside the brain. ZI is utilized with graphics processing unit (GPU) to minimize the computational and time cost and, thereby, to advance finite element mesh generation, forward and inverse computations, source interpolation, and 3D visualization of the final reconstruction.

The research conducted in this thesis investigates the implementation of advanced forward and inverse modeling techniques to resolve research questions arising from the need to place and localize the distribution of dipolar sources in a complex brain structure. Correspondingly, the neural activity can originate from a thin and highly folded cortical layer or deeper structures which are lying far from the sensor positions if non-invasive measurement is applied. The research carried out in this dissertation introduced, among other things, the divergence conforming dipolar source modeling [79] to estimate the electric potential field or magnetic field of a neural source. Furthermore, source localization was examined through hierarchical Bayesian modeling (HBM) [26, 65], which utilizes a hyperprior, i.e., gamma (G) and inverse gamma (IG) to localize the active sources at different depths of the brain.

(III) Herein, we present prior-over-measurement signal-to-noise (PM-SNR) model to propose the appropriate values for scale parameter, θ_0 in the context of the SNR for close-to-optimal shape parameter $\beta = 3$.

To learn about the advantages of combining advanced forward and inverse techniques, we analyze the simultaneous detection of the cortical and subcortical activity of the brain. In recent years, the interest of the neuroscience community has given rise to non-invasive attempts to detect the far-field activity of subcortical domain for the treatment of the brain disorders such as Alzheimer's and Parkinson's diseases or refractory epilepsy. Distinguishing the far-field activity poses a challenge due to the far distance from the sensors attached to scalp. Therefore, several studies have investigated non-invasive source localization for the subcortical domain via various techniques recently [9, 67, 95, 105, 109]. **(IV)** In this thesis, randomized multiresolution scanning (RAMUS) [101] technique which incorporates sparse source model and coarse to fine resolution level [67] is applied as an inverse approach in the framework of HBM to detect both cortical and weakly distinguishable far-field activity corresponds to the subcortical domain simultaneously [67, 101]. Moreover, this thesis concentrates on the aforementioned numerical forward and inverse approaches on experimental measurements, in particular, somatosensory evoked potential (SEP) and somatosensory evoked field (SEF) of median nerve stimulation. The research work sheds light on the connectivity analysis of the cortical and subcortical (far-field) activity at different and consecutive latencies 14–30 ms, which the source localization results are in agreement with previous studies. Our findings reveal that utilizing RAMUS technique as a sparse source model [67] plays a significant role in detecting the deep-lying sources for the early component, e.g., P14/N14 [82] and superficial activity for P20/N20 component at Brodmann area 3b [2, 23]. The methods implemented and employed in this dissertation aim to be applied in a wider scope as future research work such as multiple subjects and children's brain studies, utilizing different evoked response measurements and combined E/MEG imaging modalities and to be compared with other inversion techniques, e.g., beamformer.

1.2 Thesis structure

This thesis is divided into 5 chapters in total. **Chapter 1** concentrates on the research goal and the outline of this dissertation. **Chapter 2** begins by laying out the theoret-

ical background and knowledge of the research work that carried out in this thesis. **Chapter 3** demonstrates the methodology in this thesis including mathematical concepts, techniques and head models which are utilized in this dissertation to obtain the results and analysis. **Chapter 4** describes the key results and novel scientific knowledge which obtained during the completion of this thesis and discuss the significant findings of our research works that can be advantageous for the community. **Chapter 5** summarizes and concludes the studies investigated in this thesis and highlights the work that can be continued as a future research potential. Furthermore, Appendix is attached to this thesis draft which includes the correlated knowledge to the chapters described above.

2 PHYSICAL AND NEUROPHYSIOLOGICAL MODELING ASPECTS

Our brain is a complex organ which is composed of several regions where each area is responsible for a particular function. The brain contains about 10^{10} [50] neurons which are responsible for brain activity. The neurons can be excited and make the membrane potential from the resting state to the threshold potential where the action potential (AP) occurs. The AP is induced as a result of differences in the concentration gradient of ions between the inside and outside of the cell membrane. When a neuron is at resting state, the potential inside the cell is approximately 70 mV more negative than outside. When the AP fires off, positive ions enter the cell causing the membrane potential to reach the positive peak and to reach the depolarization state. After that, the cell is again returning to negative membrane potential where repolarization state occurs to make the balance between the ion concentration inside and outside of the cell membrane [50, 55].

A neuron mainly consists of a soma or nucleus body, dendrites, and axon [14]. When the neuron is excited, it fires off the signal which transfers along the axon until it reaches the target tissue. This process is called the postsynaptic potential which is visualized in Figure 2.2 (a), and can be mathematically modelled as a current dipole [26, 50]. Since the neural activity of a single neuron is small, its electromagnetic field can be measured only as a net effect of a bundle of neurons. The electrical activity of neurons can be recorded by electroencephalography (EEG) electrodes on the scalp and the net magnetic field of the brain can be measured by magnetoencephalography (MEG). The EEG and MEG modalities record the brain activity non-invasively. The postsynaptic potential of the apical dendrites of pyramidal cells are orthogonally-oriented to the surface of the cortex and constitutes the main generators of both EEG and MEG signals [50]. The brain activity can be measured as a result of different evoked responses for different stimuli, e.g., visual, auditory or somatosensory

stimulus [55]. EEG and MEG measurements provide the opportunity to process and analyze the neural signal, and thereby, it broadens our knowledge on the functionality of the brain.

2.1 Electroencephalography (EEG)

EEG as a method to investigate brain activity was born in 1924 when the first measurement of the electric activity of the human brain was conducted by German psychiatrist Hans Berger. Today, EEG is a neuroimaging technique which is extensively used to measure the spontaneous activity on the scalp non-invasively. The term *spontaneous activity* describes the ongoing activity in living individuals [73]. The largest EEG amplitude are about 100 μV on the scalp and about 1-2 mV on the surface of the brain with the bandwidth of 1 Hz to 50 Hz. Practically, EEG can be utilized up to 256 electrodes. The electrodes can be either attached to the skin directly or located on an elastic cap and cover the whole scalp [12]. Currently, EEG is widely used in not only clinical applications such as epilepsy, sleep disorders, Alzheimer's disease, head injury, etc, but also cognitive and psychology applications, e.g., depression [84].

2.2 Magnetoencephalography (MEG)

MEG is a non-invasive imaging technique to measure the magnetic fields generated by neural currents in the brain. A classical MEG sensor includes superconducting quantum interference device (SQUID), which is a sensitive detector of the magnetic flux. The first SQUID was introduced in the late 1960s by James Zimmerman and the first SQUID based measurement of human brain activity was conducted by David Cohen [12]. The weak neuromagnetic signals are about 10fT–1pT [52] and need to be measured by sensitive enough SQUIDs. To this end, pick-up coil or flux transformer, which associates with SQUID, is employed to collect the magnetic fields and induce the current into the coil [52, 55]. Magnetometer and gradiometer (axial or planar) constitute two different pick-up coil types. Magnetometer is more sensitive to noise and consists of a single loop which picks up the magnetic flux, while the gradiometer includes more than one loop sensing the differential changes of the magnetic field either in the axial or planar direction. Gradiometers are more

sensitive to detect near-field than far-field signals and that is, they neglect the distant signals.

MEG achieves a better spatial accuracy compared to EEG with respect to the source localization since the magnetic field is mainly generated by the currents in the intracranial space, whereas EEG can be affected by inhomogenities with different conductivity values in the head [52]. MEG is more sensitive to detect the tangential and superficial sources, while EEG performs better for radial activity but in principle can detect all primary current components including the deeper ones [57].

2.3 Cortical and subcortical structures

From the anatomical perspective, human brain can be divided into superficial area and deep structures. The superficial layer is called cerebral cortex which is depicted in Figure 2.1(a) and consists of new cortex and old cortex. The new cortex or neocortex contains six layers of gray matter over a layer of white matter. The neocortex is specifically in mammals and plays a crucial role in functions such as language, memory, attention and other functions [15]. On the other hand, old cortex or limbic cortex includes three or four layers of gray matter on top of a layer of white matter. Limbic cortex is known to be more primitive than neocortex. Moreover, the limbic cortex is involved in emotional change states and neocortex functions. Other structures beneath the cerebral cortex are considered as subcortical compartments which are shown in Figure 2.1 (b) and (c). The subcortical structures, e.g., caudate, putamen, pallidum, thalamus, lateral ventricles, hippocampus, amygdala, brainstem, etc, can be segmented based on the atlas which includes information about the location of each label from MRI image [39]. Figure 2.1 shows the subcortical structures which are segmented by FreeSurfer software suite[1] and visualized in Zeffiro Interface[2].

2.4 Evoked related responses (ERR)

Sensory stimuli, e.g., auditory, visual, or somatosensory, can produce both *evoked* and *induced* activities, of which evoked responses are time and phase-locked to the stimulus, while the induced activity is not [57]. The evoked signals can be detected

[1] `https://surfer.nmr.mgh.harvard.edu/`

[2] `https://github.com/sampsapursiainen/zeffiro_interface`

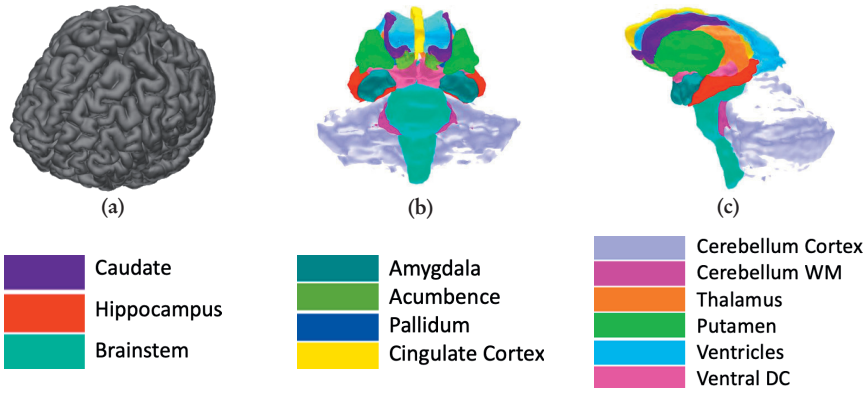

Figure 2.1 Visualization of human brain obtained via Zeffiro Interface (ZI). **(a)** illustrates the superficial area of brain known as cortex. **(b)** and **(c)** show the deep structures of brain from coronal and sagittal view, respectively. Each subcortical structure is illustrated by a specific color.

by repetitive measurements and averaging responses over the measured sample. Signal averaging leads to the improvement of the signal-to-noise ratio (SNR) [73] for the weak evoked responses, which are otherwise not distinguishable. Furthermore, finding the optimal interstimulus interval (ISI) for suitable SNR of given measurement can be beneficial for clinical applications due to the fact that evoked signals are getting weaker within shorter ISI [57]. Additionally, pre-stimulus baseline of 100 to 250 ms is considered as an efficient interval for distinguishing the evoked responses [55]. Evoked responses can be scalp-positive (P) and scalp-negative (N) potentials, e.g., P20 and N20, where the polarities represent the active electrode [55]. The evoked responses can be recorded by both EEG and MEG modalities where the output measurement depends on the stimulus parameters such as repetition rates, subject's vigilance, height, age and some other factors [57].

2.4.1 Somatosensory evoked responses

Primary somatosensory cortex (SI) is located at the posterior wall of the central sulcus, particularly at cytoarchitectonic area 3b [2, 24, 55] and can be activated by tactile stimuli from the skin. The peripheral nerves, e.g., the median nerve at wrist can be stimulated by electrical pulses which induce action potential volley along the bundle of fibers to the somatosensory cortex and make the thumb twitching as a result of evoked responses [2, 24, 43, 53, 54, 55, 62, 63, 66, 118]. The evoked responses can

be detected as a generator of P20/N20 component at the posterior wall of the central sulcus, Brodmann area 3b at 20 ms. Somatosensory evoked potential (SEP) and somatosensory evoked field (SEF) can be obtained by EEG and MEG recording of somatosensory evoked responses, respectively. Figure 2.2 (b) shows the tangential and radial orientation of sources on the surface of the cortex.

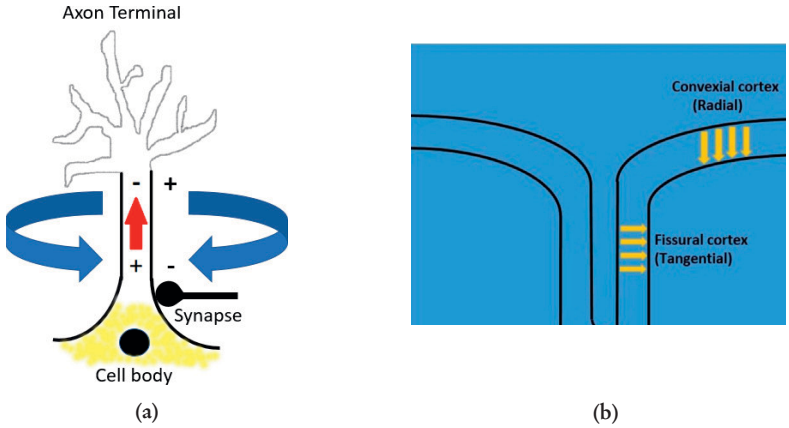

Figure 2.2 Illustration of the postsynaptic potential of apical dendrites of the pyramidal cell which can be modelled by current dipole (red) in **(a)** and orientation of radial and tangential sources to the convexial and fissural cortex in **(b)**.

2.5 Deep brain stimulation (DBS)

Deep brain stimulation (DBS) is offered as a treatment for patients with neurological disorders such as Parkinson's disease, tremor, or epilepsy [92]. The implementation follows by implanting the electrodes in the subthalamic region where the electrodes are located at the anterior nucleus of the thalamus (ANT) to apply high frequency pulses to reduce the seizures frequency, namely, in case of epilepsy patients. However, neurophysiological effects can vary from subject to subject. Clinically, therapeutic stimulation is utilized with high-frequency pulses to desynchronize the same thalamocortical networks which are responsible for synchronization in epilepsy to reduce the severity of the seizure. After that, the generated cortical responses can be recorded by EEG [131].

2.6 Transcranial electrical stimulation (tES)

Transcranial electrical stimulation (tES) is a non-invasive stimulation technique which modifies the membrane potential of neurons and modulates the excitability of neurons via short pulses [91]. tES plays a crucial role for the treatment of diseases such as Alzheimer's disease [19], Parkinson's disease [40], refractory focal epilepsy [5], stroke [36] and depression [81]. There are four main domains of the low-intensity tES including: transcranial direct current stimulation (tDCS), transcranial pulse current stimulation (tPCS), transcranial alternating current stimulation (tACS) and transcranial random noise stimulation (tRNS) [91]. All the four methods associate with spontaneous and non-spontaneous (including cognitive tasks) neuronal activity which make the changes in neural networks [64].

Principally, tES is utilized with two electrodes which are saline-soaked sponges where low-intensity constant current (0.5–2 mA) is applied to the head. Consequently, the current enters the brain via anode (+) and passes through the cortical and subcortical structures and leaves through the cathode (-). This non-invasive stimulation approach can change the neuronal excitability and these alterations can last for about 30–120 minutes after the end of the stimulation [64]. Moreover, further investigations can be carried out via combined tES and EEG measurement to track the brain activity with respect to the changes of neuronal excitability. To this end, comprehensive electrode model, i.e., complete electrode model (CEM) [97] can be applied for both tES and EEG to provide sufficient information of the skin-electrode interface. Furthermore, tES can be considered as a potential investigation to incorporate with evoked related responses, e.g., SEP [74].

2.7 Network analysis of cortical and subcortical structures for different components

Recently, several investigations have been carried out to analyze the thalamocortical network for better understanding of subcortical activity [67, 95, 109]. Subcortical structures play significant role in brain functioning and neural activity from subcortical structures can be recorded non-invasively [67]. However, the deep activity is weaker than generated cortical signals, therefore, it is challenging to detect the far-

field activity by distant electrodes on the scalp. Herein, we utilized somatosensory evoked potential (SEP) measurements of median nerve stimulation at the wrist to track the afferent volley pathway through the thalamocortical fibers. Thalamocortical activity is reflected in several peaks at different latencies, e.g., 14–30 ms where the thalamus and brainstem are involved as main subcortical structures in sensory processing [67]. Detecting the subcortical activity [3, 9, 67, 105] is vital for the neuroscience community for a deeper understanding of brain disorders such as, stroke, refractory focal epilepsy[10, 11], Alzheimer's [68] and Parkinson's [18] disease and its implications are crucial with respect to many other brain processes including language, action, motor or emotion. To this end, EEG recordings can provide sufficient information for the analysis of the subcortical activity. As part of this dissertation, a comprehensive analysis of the earlier and late SEP components occurring as a response to median nerve stimulation is conducted. These components include P14/N14, P16/N16, P18/N18, P20/N20, P22/N22, and P30/N30 and are described in detail below.

2.7.1 P14/N14

The positive component at 14 ms, i.e., P14 corresponds to a far-field potential and it can be recorded between the ipsilateral centroparietal electrode (CPi) and non-cephalic reference which is typically located at the contralateral Erb's point (EPc)[41]. The P14 far-field peak originates in the brainstem region, particularly, in the medial lemniscus pathway which is known as a bundle of fibers [23, 75, 82]. The turning point between P14 and N14 is located at the medulla-pontine junction. Furthermore, some studies [90, 121] reveal that the P14 peak can originate from above the cuneate nucleus and travel to the ventral posterolateral (VPL) part of the thalamus [75].

2.7.2 P16/N16

The far-field activity for the early P16/N16 component is located either at the subthalamic region or it constitutes a thalamocortical radiation [22, 120]. The originator of P16 component corresponds to ventral thalamus [22]. The negative N16 peak has been associated with the cuneate nucleus [61]. A study by Tsuji et al. [120] showed

that N16 reflects the subcortical activity onto the fronto-central areas of the cortex. Figure 2.3 depicts a quadrupolar visualization of P16/N16 along the pathway of afferent volley where it becomes visible as downward source (red) at cuneate nucleus and simultaneously as an upward component at ventral part of the thalamus [22].

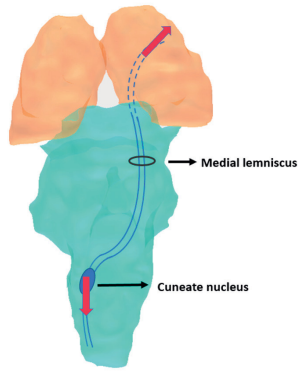

Figure 2.3 Quadrupolar (in red) visualization of the P16/N16 component in the pathway of afferent volley from cuneate nucleus to thalamus through medial lemniscus.

2.7.3 P18/N18

The distribution of far-field activity has been found to be relatively widespread and bilateral at 18 ms poststimulus. Multiple generators for N18 peak were detected at brainstem in [75, 82] and from upper midbrain to the thalamus in [76, 85, 90]. Moreover, study by Urasaki et al. [121] suggested that N18 peak can be visible between the upper pons and midbrain while excluding the thalamus as an active area. A study by Noel et al. [82] demonstrated that the N18 peak is originating from lower medulla nuclei and the study by Sonoo et al. [113] concluded N18 peak to be derived from the dorsal column to the cuneate nucleus by the primary afferent depolarization.

2.7.4 P20/N20

The P20/N20 component is known to have the maximum peak at 20 ms as a poststimulus response of human somatosensory cortex (SI) at the posterior wall of the central sulcus at Brodmann area 3b with tangentially oriented generator [2, 6, 23, 24, 43]. From the scalp recordings, it is evident that the cortical activity at 20 ms is

contralateral to the stimulated median nerve [2] and simultaneous far-field activity has been found to be visible at thalamus [48, 50]. Figure 2.4 highlights the area of occurrence of P20/N20 component in the hand-knob of Broadmann area 3b [57].

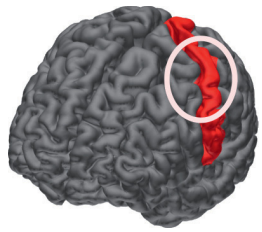

Figure 2.4 The postcentral area is depicted by the red colour. It includes omega-shaped hand-knob highlighted by the circle. P20/N20 component occurs in the posterior wall of the central sulcus in the hand-knob [57] (Broadmann area 3b).

2.7.5 P22/N22

The P22/N22 component occurs a few millisecond after the P20/N20 peak [87]. The maximum peak of P22/N22 is detectable at the crown of either the first precentral (Brodmann area 4) or postcentral (Brodmann area 1) gyrus corresponding to a radially oriented source [2, 24, 43]. Hence, P22/N22 is principally radial in contrast to tangential P20/N20. In addition, ventral posterolateral (VPL) thalamus has been found to be active simultaneously [58].

2.7.6 P30/N30

The post-stimulus peak for P30/N30 component builds a network between cortical areas, i.e., pre-motor areas, primary motor cortex and subcortical structures such as the basal ganglia and thalamus. The P30/N30 component has been determined as a marker for sensorimotor processing [90]. It links the motor, pre-motor and pre-frontal cortex area [29, 30, 90]. Moreover, a study by Cebolla et al. [29] suggested that the P30/N30 component also involves somatosensory activity which is located at Brodmann area 3b [2, 24] of the primary somatosensory cortex. N30 generator, in particular, corresponds to the pre-central (BA4 and BA6) and the pre-frontal (BA9) cortex [29]. However, deep structures, namely, basal ganglia and ventrolateral thalamus have been observed to be active when N30 is at its maximum peak [29, 90, 94,

108].

3 RESEARCH METHODOLOGY

This section concentrates on the methodology applied on the research work in this thesis. The mathematical modeling employed in this thesis includes accurate forward and advanced inverse methods which are combined in Zeffiro Interface (ZI), a platform for reconstructing the primary current distribution in brain imaging applications using realistic and complex human head model. Moreover, a model based on signal-to-noise ratio (SNR) is introduced to improve the performance of hierarchical Bayesian modeling (HBM) inverse techniques by selecting the optimal hyperparameters of gamma or inverse gamma hyperprior. In the framework of HBM, an approach based on multiresolution and sparse source space is implemented to detect simultaneous cortical and subcortical activity.

3.1 Mathematical modeling

The apical dendrites of pyramidal cells can be modelled as a dipolar point-like source, i.e., an equivalent current dipole (ECD) representing a generator of the brain activity in EEG and MEG. The amplitude of the ECD is estimated to be 10 nAm [52] to 100 nAm [56]. In the cortical area, the ECD orientation is known to be normal to the surface of the strongly-folded cortex which was shown by Creutsfeldt et al. [33]. Figure 2.2 (b) shows direction of ECD with respect to the surface of the cortex. In subcortical areas the orientation can be either constrained or unconstrained since the neuronal tissue structures vary in different subcortical nuclei [8].

The mathematical techniques implemented in this thesis covered the aspects of the advanced forward [50, 79] and inverse modeling [25, 26, 42, 71, 83, 107, 112, 114, 126] to localize the primary current density as an originator of the EEG and MEG signal from heavily folded tissues of the brain. In general, forward modeling aims to estimate the measurement of the signal given the neuronal activity and inverse modeling seeks to find the accurate location of the primary current distribution [80].

Figure 3.1 illustrates the concept of the forward and inverse modeling in the case of EEG.

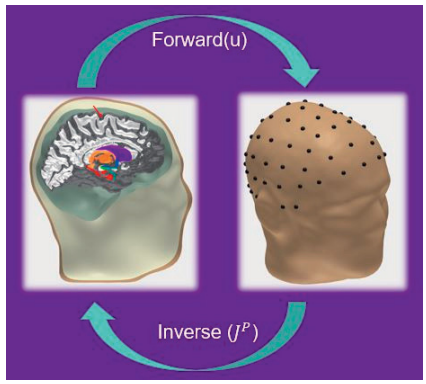

Figure 3.1 Illustration of forward and inverse modeling in brain application. The forward approach finds the electric potential (u) for a given EEG sensor set attached to the scalp given the primary current density (J^p) whereas the inverse approach aims to localize J^p given u.

As a forward approach we use the divergence conforming H(div) source model and its implementation via the finite element method (FEM). The inverse techniques applied in this thesis include hierarchical Bayesian model (HBM) and randomized multiresolution scanning (RAMUS) technique. The latter one of these is implemented to fulfil the goal of detecting simultaneous cortical and subcortical activity. It is known that the deep-lying far-field sources generate weak signals [9, 45] due to the far distance from the sensors attached to the scalp and thereby, it is challenging to reconstruct the activity from deeper structures.

3.1.1 Finite element method (FEM)

In order to localize the focal brain activity, accurate forward solution is required. In addition to the FEM [20, 35], there are multiple different numerical methods such as boundary element method (BEM) [52] and finite difference method (FDM) [50] which allow finding a solution with a realistic head geometry. BEM does not include the volumetric structures of the head geometry, e.g., skull compacta and spongiosa [124] and merely includes the elements at the boundaries. Again, FDM is a volumetric technique but is not fully adaptive with respect to the strongly folded internal tissue boundaries. FEM allows both advanced boundary and volume modeling [98, 124], including anisotropic structures such as the white matter, as each element can

be locally associated with its own conductivity tensor. On the contrary, utilizing FEM as a forward approach requires high computing power [35] and is, therefore, generally considered to be computationally costly. Furthermore, to obtain an accurate forward solution, advanced features such as a complex realistic head model, tissue boundaries and tissue conductivity including anisotropic conductivity of the white matter [99, 127] should be taken into account to approximate the data for a given source position and orientation precisely.

3.1.2 H(div) source modeling

In this thesis, forward modeling refers to the simulation of the scalp potential or magnetic field of the neuronal activity at a finite set of sensor locations [21, 80]. To achieve this goal we utilize the FEM [20] by first generating finite element (FE) mesh for complex [55] and multicompartment head model based on MRI image and then finding a solution of a linear system. Herein, H(div) source modeling [1, 79] is applied to model a finitely supported dipolar source, since mathematical dipole sources are not directly applicable with FEM. The H(div) approach deals with hierarchic basis functions of arbitrary order to give a conforming approximation of FE basis functions on unstructured mesh. In the H(div) model, linear and quadratic basis functions are used. The smooth properties of H(div) allow to have continuous finite element functions in subspace, notably, at the boundaries. Divergence conforming H(div) source modeling presents the accurate source configuration compared to the reference techniques such as partial integration (PI) [125, 130] and St. Venant (SV) [25, 119] method, i.e., monopolar source placement techniques to approximate a dipole. Detailed information of the mathematical model and the implementation of H(div) source modeling applied in study I (section 4.1) of this thesis, can be found in section 2 of the study by [79].

The current preserving H(div) source space modeling [79, 98] is employed to estimate the primary current density of the brain activity, where dipolar sources belong to Hilbert space H(div), which includes current distributions with a square integrable divergence. The model is computationally efficient compared to other classical source modeling approaches such as, PI and SV and can be well-localized in thin cortical area, e.g., in children. Divergence conforming H(div) source modeling can be applied using either linear or quadratic basis functions with face intersecting

(FI) and edgewise (EW) orientations, respectively, and the interpolation of the dipolar sources can be implemented via two different methods, namely, position based optimization (PBO) [13] and the mean position/orientation (MPO) method [98]. The investigations of dipolar H(div) approach in recent studies [79, 98] showed that its accuracy outperforms the classical source modeling, e.g., PI and SV [129] which can be associated with monopolar source configurations instead of dipoles. In this work, the eventual forward model is a lead field (LF) matrix that can be generated given the sensor configuration and a FE mesh, which here is considered to be tetrahedral [98].

Herein, the forward model is presented for EEG, whereas MEG forward model can be obtained similarly. The EEG implementation follows by applying the Kirchoff's current preservation law to the total current density $\vec{J}^t = \vec{J}^p - \sigma \nabla u$, where $\vec{J}^p$ and σ denote the primary current density and conductivity tensor, respectively, and u denotes the electric potential field on the surface $\partial\Omega$ of head model Ω. Forward model is based on the quasi-static approximation of Maxwell's equations, where electric potential is obtained from Poisson equation with respect to the Neumann boundary condition. The head model is electrically isolated [50, 106], i.e., no current can flow out of the head, therefore, the current density at the surface of the head is equal to zero due to the conservation law, i.e.,

$$\nabla \cdot \vec{J}^t = 0, \quad \nabla \cdot \vec{J}^p = \nabla \cdot (\sigma \nabla u) \quad \text{in} \quad \Omega \quad \text{with} \quad (\sigma \nabla u) \cdot \vec{n} = 0 \quad \text{on} \quad \partial\Omega \tag{3.1}$$

in which, $(\sigma \nabla u) \cdot \vec{n} = 0$ refers to the boundary condition on $\partial\Omega$ where $\vec{n}$ denotes the normal vector pointing outward. By multiplying both sides of the equation 3.1 with test function v and taking the partial integral over the Ω, the weak form is obtained as [20, 79],

$$\int_\Omega \nabla v \cdot (\sigma \nabla u) dV = -\int_\Omega v(\nabla \cdot \vec{J}^p) dV \quad \text{for all} \quad v \in H^1(\Omega) \tag{3.2}$$

where the left side presents the operator part and the right side is source part. Herein, $-\nabla \cdot (\sigma \nabla u)$ is volume current density and $H^1(\Omega)$ denotes the Sobolev space which includes the functions that have square integrable first-order partial derivatives belonging to $L_2(\Omega)$. The divergence of the primary current density needs to be square integrable, i.e., $\vec{J}^p \in H(\text{div}) = \{\vec{w} | \nabla \cdot \vec{w} \in L^2(\Omega)\}$ so that the right-hand side defines a source with finite energy [79, 98].

We assume that the potential u belongs to a subspace $S \in H^1(\Omega)$ which is considered as spanned by the FE basis functions. The potential distribution of the finite sum is $u_h = \sum_{i=1}^{N} z_i \psi_i$ where u_h represents the discrete form of the electric potential, in which $\psi_1, \psi_2, \ldots, \psi_N \in H^1(\Omega)$ are piecewise linear nodal basis (hat) functions. Furthermore, the primary current distribution modelled by H(div) technique can be represented as $\vec{J}_h^P = \sum_{j=1}^{K} x_j \vec{w}_j$ where $\vec{w}_1, \vec{w}_2, \ldots, \vec{w}_K \in H(\mathrm{div})$ are the divergence conforming basis functions [98]. Assuming that the ground potential level has been fixed, the relation between u_h and $\vec{J}_h^P$ with coordinate vectors $\mathbf{z} = (z_1, z_2, \ldots, z_N)$ and $\mathbf{x} = (x_1, x_2, \ldots, x_K)$ can be determined in a solvable linear system:

$$\mathbf{Az} = \mathbf{Gx} \tag{3.3}$$

where $\mathbf{A} \in \mathbb{R}^{(N \times N)}$ and $\mathbf{G} \in \mathbb{R}^{(N \times K)}$ with

$$A_{i,j} = \int_\Omega \nabla \psi_j \cdot (\sigma \nabla \psi_i) dV \quad \text{and} \quad G_{i,j} = \int_\Omega \psi_i (\nabla \cdot \vec{w}_j) dV. \tag{3.4}$$

The equation 3.4 is obtained by substituting the discretized electric potential and primary current density, u_h and $\vec{J}_h^P$, respectively into the equation 3.2.

The measurement vector $\mathbf{y}$ can be presented via $\mathbf{y} = \mathbf{RA}^{-1}\mathbf{Gx} = \mathbf{Tf}$, where $\mathbf{f} = \mathbf{Gx}$ is a load vector which represents the activity in the brain and $\mathbf{T} = \mathbf{RA}^{-1}$ is a so-called transfer matrix [37, 44].

Additionally, the matrix $\mathbf{R}$ presents a restriction operator for picking the skin potentials at the electrode locations on head surface $\partial\Omega$ [98]. The matrix $\mathbf{R}$ defines the ground potential (zero potential) level which is here obtained as the mean of the measurements $\mathbf{y}$. The elements of matrix $\mathbf{R}$ are defined as follows: if the ℓ–th electrode on the boundary $\partial\Omega$ is located at the i_ℓ-th node, then $R_{\ell,i_\ell} = 1 - 1/L$, and if $\ell \neq j$, then $R_{\ell,i_j} = -1/L$. Finally, $R_{\ell,j} = 0$, if the j-th node is not associated with any electrode [98]. Particularly, the primary current density is modelled based on the linear and quadratic basis functions of $H(\mathrm{div})$ [1]. The dipolar moment $\vec{q}_{\vec{w}}$ of the basis function $\vec{w}$ is defined as $\vec{q}_{\vec{w}} = \int_\Omega \vec{w}\, dV$. In a tetrahedral FE mesh, the moment and position of a dipole can be obtained for the given two mesh nodes P_i and P_j in the following straightforward fashion (detailed information can be found

in the Appendix of the study [98]):

$$\vec{q}_{\vec{w}} = \frac{\vec{r}_{P_j} - \vec{r}_{P_i}}{||\vec{r}_{P_j} - \vec{r}_{P_i}||} \tag{3.5}$$

and

$$\vec{r}_{\vec{w}} = \frac{1}{2}(\vec{r}_{P_i} + \vec{r}_{P_j}) \tag{3.6}$$

in which $\vec{r}_{P_i}$ and $\vec{r}_{P_j}$ are the position vectors of mesh nodes P_i and P_j and equation 3.6 states that the position of the source dipole is the midpoint of the positions at i and j nodes [98].The right-hand side matrix **G** of equation 3.3 can be formed as follows:

$$G_{\psi,\vec{w}} = \int_{\Omega} \psi(\nabla \cdot \vec{w}) dV = \frac{s_{\{\psi,P_j\}} - s_{\{\psi,P_i\}}}{||\vec{r}_{P_j} - \vec{r}_{P_i}||} \tag{3.7}$$

for a given pair ψ, $\vec{w}$ of the basis functions with $s_{\{\psi,P\}} = 1$, i.e., the non-zero entry at ith and jth node, if ψ corresponds to node P and $s_{\{\psi,P\}} = 0$, otherwise. Detailed mathematical information can be found in studies by [13, 98].

With linear $H(\mathrm{div})$ basis functions (extensive mathematical description can be found in Appendix B of study [98]), the source dipole is defined by nodes P_i and P_j which are located on the opposite sides of a shared face in a neighbouring tetrahedron pair, and is called face intersecting (FI) orientation. For the quadratic basis, P_i and P_j are attached by an edge, i.e., an edgewise (EW) orientation. Hence, various source configurations can be made by considering different combinations of these dipoles. Correspondingly, two different interpolation approaches, namely, PBO and MPO methods were applied in order to interpolate the source dipole with given position $\vec{r}$ and dipole moment $\vec{p}$ via a sum of dipolar FI and EW sources, i.e., $\vec{p} \approx \sum_{\ell=1}^{L} c_\ell \vec{q}_{\vec{w}_\ell}$ (subsection 3.1.2.2) and $\vec{r} \approx \sum_{\ell=1}^{L} c_\ell \vec{r}_{\vec{w}_\ell}$ (subsection 3.1.2.1), respectively. In overall, PBO tends to weight $\vec{p}$ more than $\vec{r}$ while in MPO both dipole position and moment are determined to be in the equal order. However, MPO involves a higher number of degrees of freedom which is why its performance is limited in restricted configurations which might be necessary in thin cortical geometries, e.g., in children [79].

3.1.2.1 Position based optimization (PBO)

Position based optimization (PBO) [13] seeks for the coefficient vector $\mathbf{c} = (c_1, c_2, \ldots, c_L)$ for the solution of the linear system,

$$\min_{c} \sum_{\ell=1}^{L} {c_\ell}^2 {\omega_\ell}^2 \quad \text{for} \quad \mathbf{Qc} = \mathbf{p} \tag{3.8}$$

in which ω_ℓ indicates a weighting coefficient $\omega_\ell = ||\vec{r}_{\vec{\omega}_\ell} - \vec{r}||_2$. Moreover, the matrix $\mathbf{Q}$ defines the source dipole moments as $\mathbf{Q} = (\tilde{\mathbf{q}}_{\tilde{\mathbf{w}}_1}, \tilde{\mathbf{q}}_{\tilde{\mathbf{w}}_2}, \ldots, \tilde{\mathbf{q}}_{\tilde{\mathbf{w}}_L})$, where the constraint $\mathbf{Qc} = \mathbf{p}$ is to ensure that the orientation of the interpolated dipole matches the actual one. PBO finds the minimizer of $\sum_{\ell=1}^{L} {c_\ell}^2 {\omega_\ell}^2$, where L denotes the number of source dipoles based on the source configuration. The method of Lagrangian multipliers applied to 3.8 implies the following uniquely solvable linear system,

$$\begin{bmatrix} \mathbf{D} & \mathbf{Q}^{\mathrm{T}} \\ \mathbf{Q} & 0 \end{bmatrix} \begin{bmatrix} \mathbf{c} \\ \mathbf{d} \end{bmatrix} = \begin{bmatrix} 0 \\ \mathbf{P} \end{bmatrix} \tag{3.9}$$

with a diagonal matrix $\mathbf{D} = \text{diag}\,(\omega_1^2, \ldots, \omega_L^2)$ and auxiliary multiplier vector $\mathbf{d} = (\lambda_1, \lambda_2, \lambda_3)$ including the Lagrangian multiplies. Total number of the interpolation conditions $(L+3)$ is equivalent to the number of the rows in the matrix 3.9.

3.1.2.2 Mean position/orientation (MPO)

The mean position/orientation (MPO) method aims to look for $\mathbf{c} = (c_1, c_2, \ldots, c_L)$ to satisfy the following conditions:

$$\begin{aligned} \vec{p} &\approx \sum_{\ell=1}^{L} c_\ell \vec{q}_{\vec{w}_\ell} \\ 0 &= \frac{1}{\alpha} \sum_{\ell=1}^{L} c_\ell \vec{q}_{\vec{w}_\ell} [(\vec{r}_{\vec{w}_\ell} - \vec{r}).\vec{e}_j] \quad \text{for} \quad j = 1, 2, 3. \end{aligned} \tag{3.10}$$

The former of these equations refers to the orientation constraint and the latter one denotes the average position of the dipolar moments of given source dipole with

respect to each Cartesian direction $\vec{e}_j$ for $j = 1,2,3$; α denotes a distance parameter based on a uniform mesh reference distance which is at least double the length of the longest edge in the FE mesh. Least square solution, i.e., ℓ^2- norm of the equation 3.10 is determined through the equation:

$$\mathbf{c} = \mathbf{M}^{\dagger}\mathbf{b} \quad \text{with} \quad \mathbf{M} = \begin{bmatrix} Q \\ QP_1 \\ QP_2 \\ QP_3 \end{bmatrix} \quad \text{and} \quad \mathbf{b} = \begin{bmatrix} P \\ 0 \\ 0 \\ 0 \end{bmatrix}. \tag{3.11}$$

Here, to regularize the outcome, the approximate solution is obtained using the Moore–Penrose pseudoinverse $\mathbf{M}^{\dagger}$ of $\mathbf{M}$ [46] and

$$\mathbf{P}_j = \frac{1}{\alpha}\mathrm{diag}((\vec{r}_{\vec{w}_1} - \vec{r}).\vec{e}_j, (\vec{r}_{\vec{w}_2} - \vec{r}).\vec{e}_j, \ldots, (\vec{r}_{\vec{w}_L} - \vec{r}).\vec{e}_j) \tag{3.12}$$

for $j = 1,2,3$ and equation 3.11 represents the total number of (local) sources within the interpolation.

3.1.3 Classical source modeling

3.1.3.1 St. Venant (SV)

St. Venant's (SV) principle is based on estimating a dipolar source with monopolar sources and lever arms [104, 119]. SV models a dipole by placing monopolar sources on all neighbouring FE nodes attached to the one whose distance is the closest to the actual source position [25, 78, 98]. That is, a dipole moment $\vec{p}$ at position $\vec{r}$ is estimated via monopolar loads $m_0, m_1, \ldots, m_L$ which are located at the FE mesh nodes $\vec{r}_0, \vec{r}_1, \ldots, \vec{r}_L$, in which, $\vec{r}_1, \ldots, \vec{r}_L$ share an edge with the node $\vec{r}_0$ closest to $\vec{r}$.

The following moment conditions are set:

$$\begin{aligned} 0 &= \sum_{i=0}^{L} m_i \\ \frac{1}{\alpha}\vec{p} &= \sum_{i=0}^{k} \frac{m_i}{\alpha}(\vec{r}_i - \vec{r}) \\ 0 &= \sum_{i=0}^{L} \frac{m_i}{\alpha^2}[(\vec{r}_i - \vec{r}).\vec{e}_j]^2 \quad \text{for} \quad j = 1,2,3. \end{aligned} \tag{3.13}$$

The conditions in 3.13 are assumed that the resulting total effect of the monopoles can approximate the dipole. Herein, α denotes the reference distance which is at least double the length of the longest edge in FE. The conditions above refer to the conservation of the charge, the approximation of the dipole moment, and suppression (balancing out) of the higher order moments, respectively. Furthermore, in order to compute the load vector, i.e., $\mathbf{m} = (\mathbf{m_1}, \ldots, \mathbf{m_L})$, a regularized least-squares approach is applied in the following fashion: $\mathbf{m} = (\mathbf{P^T P} + \lambda \mathbf{D})^{-1}\mathbf{P^T b}$, where

$$\mathbf{P} = \begin{bmatrix} \mathbf{P_1} \\ \mathbf{P_2} \\ \mathbf{P_3} \end{bmatrix} \quad \text{with} \quad \mathbf{P_j} = \begin{bmatrix} 1 \ldots 1 \\ \alpha^{-1}(\vec{r}_1 - \vec{r}) \cdot \vec{e}_j \ldots \alpha^{-1}(\vec{r}_L - \vec{r}) \cdot \vec{e}_j \\ \alpha^{-2}[(\vec{r}_1 - \vec{r}) \cdot \vec{e}_j]^2 \ldots \alpha^{-2}[(\vec{r}_L - \vec{r}) \cdot \vec{e}_j]^2 \end{bmatrix}. \tag{3.14}$$

Here, matrix $\mathbf{D} = \text{diag}(||\vec{r}_1 - \vec{r}||^2, ||\vec{r}_2 - \vec{r}||^2, \ldots ||\vec{r}_L - \vec{r}||^2)$ is a regularization matrix which is multiplied by a regularization parameter λ and

$$\mathbf{b} = \begin{bmatrix} \mathbf{b_1} \\ \mathbf{b_2} \\ \mathbf{b_3} \end{bmatrix} \quad \text{with} \quad \mathbf{b_j} = \begin{bmatrix} 0 \\ \alpha^{-1}\vec{P}_j \\ 0 \end{bmatrix}. \tag{3.15}$$

3.1.3.2 Partial integration (PI)

Partial integration (PI) method [125, 130] determines a dipole source in single FE mesh element by placing monopolar weights on the nodes of that element. Thus, the local source configuration applied in estimating the dipole is very well-localized or focal. For a given dipole moment $\vec{p}$ located at the point $\vec{r}$, the weights are obtained

as follows:

$$f_i = -\int_\Omega (\nabla \cdot \vec{J}^p)\psi_i dV = \int_\Omega \vec{J}^p \cdot \nabla\psi_i dV - \int_{\partial\Omega} \partial_n \vec{J}^p \cdot \psi_i dS$$
$$= \int_\Omega \vec{J}^p \cdot \nabla\psi_i dV = \begin{cases} \vec{p} \cdot \nabla\psi_i \mid_{\vec{r}}, & \text{if} \quad \vec{r} \quad \text{in support of} \quad \psi_i, \\ 0, & \text{otherwise,} \end{cases} \tag{3.16}$$

where $\vec{J}^p = \vec{p}\vec{\delta}\vec{r}$ denotes the primary current density of the form with $\delta_{\vec{r}}$ a Dirac's delta distribution [130]. Correspondingly, the right-hand side of the vector $\mathbf{f}$ can be derived from equation 3.16. There are 4 different conditions of PI including non-zero entries of the vector $\mathbf{f}$. The major difference of SV and PI is the interpolation strategy. Due to lower number of degrees of freedom present in the interpolation, PI finds more focal source compared to SV [98].

3.1.4 Error measurement implementation

The relative difference (RDM) and magnitude (MAG) measure can be employed to evaluate the forward modeling errors [98] and accuracy of the source localization between H(div) source modeling and classical SV [25, 119] and PI methods [125, 130]. To this end, RDM and MAG are defined as follows [98]:

$$\mathrm{RDM}(\mathbf{y}_{\mathrm{ana}}, \mathbf{y}_{\mathrm{num}}) = 50 \left\| \frac{\mathbf{y}_{\mathrm{ana}}}{||\mathbf{y}_{\mathrm{ana}}||_2} - \frac{\mathbf{y}_{\mathrm{num}}}{||\mathbf{y}_{\mathrm{num}}||_2} \right\|_2 \tag{3.17}$$

$$\mathrm{MAG}(\mathbf{y}_{\mathrm{ana}}, \mathbf{y}_{\mathrm{num}}) = 100(\frac{\left\|\mathbf{y}_{\mathrm{num}}\right\|_2}{||\mathbf{y}_{\mathrm{ana}}||_2} - 1). \tag{3.18}$$

Here $\mathbf{y}_{ana}$ and $\mathbf{y}_{num}$ denote the analytical and numerical solution, respectively.

The distinction between these two approaches is that RDM presents the topographical modeling error with respect to the location and orientation while MAG denotes the changes in potential amplitude or variations in the source strength. The error measurement implementation is analyzed as box plots (Figure 4.2), which present the lower (25%), middle (50%) and upper (75%) quartiles within the target distribution. The interquartile range (IQR) is shown as a vertical rectangle between 25% and 75% range and a horizontal line inside the box shows the median, i.e., the 50%

quartile. The whiskers present the range extending beyond IQR.

3.1.5 Inverse modeling

Inverse modeling aims at finding a solution for the inverse problem. In terms of Bayesian statistics [65], the solution can be characterized as a *posterior* probability distribution for the unknown, taking into account all the measurement data and *a priori* information available. Within this interpretation, the accuracy of the solution is determined by the uncertainty of the posterior model.

3.1.5.1 Prior information and regularization

The inverse problem is rather generally underdetermined, i.e., the number of sensors is less than the sources in the lead field and, thereby, there are infinite number of current distributions fitting to the measurements. Hence, a unique solution cannot be found without using additional prior information or regularization. In many connections these two concepts can be interpreted to coincide.

Prior information or regularization is often the governing factor characterizing the structure of the candidate solution. For example, it can motivate different approaches to parametrize the inverse problem: (1) distributional and (2) dipolar or multipolar, i.e., the assumption that the primary current density is composed of a few dipolar or multipolar sources. In the case of (2), the solution is always focal (well-localized), whereas in (1) the degree of focality can vary.

3.1.5.2 Hierarchical Bayesian model (HBM)

Principally, the observation model for both EEG and MEG can be expressed as a linear equation of the form:

$$\mathbf{y} = \mathbf{L}\mathbf{x} + \mathbf{n}, \tag{3.19}$$

$\mathbf{x}$ is the *unknown* time-dependent source field, where each entry describes a source set to a given source position and one of the three Cartesian orientations. The vector $\mathbf{y}$ includes the measurements, $\mathbf{L}$ denotes the lead field (gain) matrix in which a given column and row corresponds to the lead field of the corresponding EEG/MEG sensor and source, respectively. The term lead field refers to a field which is generated by

the sensor itself, when it acts as a unit source [73]. The noise vector $\mathbf{n}$ contains the measurement uncertainties which are here assumed to consist of zero-mean white Gaussian noise.

The E/MEG inverse problem of reconstructing the primary current density is ill-posed, i.e., it does not have a unique solution [106]. Therefore, we aim to use all available *a priori* information to obtain an accurate and robust solution [65] for inverse problem. The *a priori* or prior information can concern [21, 107], e.g., the anatomical head model, active regions, and the focality of the sources to restrict the number of source configurations applied in reconstructing the brain activity. Furthermore, regularization technique in a deterministic framework [27] is required to incorporate prior information and, thereby to suppress the measurement noise and modeling errors to achieve a unique solution. Herein, we focused on hierarchical Bayesian model (HBM) [65], which follows from the classical Bayes formula that corresponds to the posterior distribution aiming to approximate the *unknown* primary current density $\mathbf{x}$ as follows:

$$p(\mathbf{x} \mid \mathbf{y}) = \frac{p(\mathbf{x})\, p(\mathbf{y} \mid \mathbf{x})}{p(\mathbf{y})} \propto p(\mathbf{x})\, p(\mathbf{y} \mid \mathbf{x}). \tag{3.20}$$

Here $p(\mathbf{x})$ and $p(\mathbf{x} \mid \mathbf{y})$ denote the prior and posterior probability density of $\mathbf{x}$, respectively, and $p(\mathbf{y} \mid \mathbf{x})$ is the likelihood following from the zero-mean Gaussian noise according to $p(\mathbf{y} \mid \mathbf{x}) \propto \exp(-(2\sigma^2)^{-1}||\mathbf{LX}-\mathbf{Y}||^2)$ with σ denoting the standard deviation of the noise. In HBM, the prior is assumed to depend on a hyperparameter. Here this dependency is represented via the joint density $p(\mathbf{x}, \theta) \propto p(\theta)\, p(\mathbf{x} \mid \theta)$, where θ is a hyperparameter, $p(\theta)$ the corresponding hyperprior, i.e., the prior of θ, and $p(\mathbf{x} \mid \theta)$ is a conditional prior. Consequently, the posterior is a joint distribution of the form:

$$p(\mathbf{x}, \theta \mid \mathbf{y}) = \frac{p(\mathbf{x}, \theta)\, p(\mathbf{y} \mid \mathbf{x})}{p(\mathbf{y})} \propto p(\mathbf{x}, \theta)\, p(\mathbf{y} \mid \mathbf{x}) \tag{3.21}$$

or, alternatively, $p(\mathbf{x}, \theta \mid \mathbf{y}) \propto p(\theta)\, p(\mathbf{x} \mid \theta)\, p(\mathbf{y} \mid \mathbf{x})$. In this work, the conditional prior $p(\mathbf{x} \mid \theta)$ is assumed to be Gaussian, and the hyperprior is either the gamma (G) or inverse gamma (IG) distribution. These hyperpriors incorporate within two parameters β and θ_0, which are known as the *shape* and *scale parameter*, respectively. It is interpreted that β and θ_0 steer the sensitivity of the prior to find outliers (sources) in the brain and the general tendency to reconstruct fluctuations due to noise or

brain activity, respectively. The shape parameter can be associated with the tail part of the hyperprior while the scale parameter corresponds to its expectation as described in Figure 3.2. Detailed mathematical information about the behaviour and optimization of shape and scale parameter can be found in section 3.1.6 of this thesis.

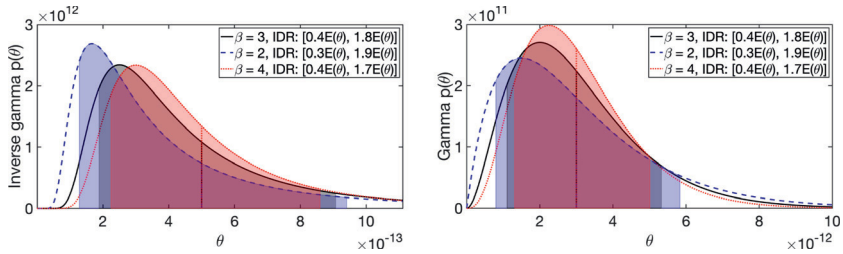

Figure 3.2 The visualization of the shape and scale parameter's behaviour with respect to the hyperprior: inverse gamma (IG) on the *left* and gamma (G) on the *right*. The longer tail corresponds to a smaller shape parameter and enhanced outliers or sensitivity to find a source. The interdecile range (IDR), i.e., the interval between 10 and 90%, is illustrated with respect to the expectation $E(\theta)$ which can be associated with a typical source magnitude resulting from noise deviations. The solid black line depicts the hyperprior density for $\beta = 3$, the dashed blue line and red line for $\beta = 2$ and $\beta = 4$, respectively.

3.1.5.3 Iterative alternating sequential maximum *a posteriori* (IAS MAP) algorithm

The task of reconstructing the unknown ($\mathbf{x}$ in equation 3.19) primary current density given the posterior distribution is challenging, since the dimensionality of the source space is likely to be large. This work concentrates on finding a *maximum a posteriori* estimate (MAP) which maximizes the posterior probability density [1, 65, 126], i.e., $p(\mathbf{x} \mid \mathbf{y})$ of the unknown $\mathbf{x} \in \mathbb{R}^n$, $\mathbf{x}_{MAP} = \arg\max p(\mathbf{x} \mid \mathbf{y})$. Iterative alternating sequential (IAS) algorithm constitutes an advantageous minimization approach to estimate the MAP of a posterior density corresponding to HBM. IAS algorithm is an efficient, simple and fast algorithm [26], and therefore, suitable with the large source spaces of EEG and MEG. IAS algorithm for MAP estimate $(x_{MAP}, \theta_{MAP}) = \arg\max\{p(x, \theta \mid y)\}$ can be described as below: (Extensive mathematical information can be found in study [26].)

1. Set $j = 0$ and $\theta^{(0)} = (\theta_0, \theta_0, \ldots, \theta_0)$.
2. Update x by choosing $x^{(j)} = \arg\max\{p(x \mid y, \theta^{(j-1)})\}$;

3. Update θ by choosing $\theta^{(j)} = \arg\max\{p(\theta \mid y, x^{(j)})\}$;

   - If hyperprior is set to G, then;
     $\theta_i = \frac{1}{2}\theta_0(\eta + \sqrt{\eta^2 + 2{x_i}^{(j)^2}/\theta_0})$
     $\eta = \beta - 3/2$, $i = 1, 2, ..., n$
   - Otherwise, if hyperprior is set to IG, then;
     ${\theta_i}^{(j+1)} = (\theta_0 + \frac{{x_i}^{(j)^2}}{2})/k$
     for $k = \beta + 3/2$, $i = 1, 2, ..., n$.

4. Set $j = j + 1$ and continue from step 2 until it converges.

And IAS algorithm with respect to the lead field can be interpreted as:

1. Set $j = 0$ and $\theta^{(0)} = (\theta_0, \theta_0, \ldots, \theta_0)$.
2. Set $\mathbf{L}^{(j)} = \mathbf{L}\mathbf{D}_{\theta^{(j)}}^{1/2}$ with

$$\mathbf{D}_{\theta^{(j)}}^{1/2} = \mathrm{diag}(\sqrt{|\theta_1^{(j)}|}, \sqrt{|\theta_2^{(j)}|}, \ldots, \sqrt{|\theta_n^{(j)}|}). \tag{3.22}$$

3. Find

$$\mathbf{x}^{(j+1)} = \mathbf{D}_{\theta^{(j)}}^{1/2}{\mathbf{L}^{(j)}}^T(\mathbf{L}^{(j)}{\mathbf{L}^{(j)}}^T + \sigma^2\mathbf{I})^{-1}\mathbf{y}, \tag{3.23}$$

   where σ is the standard deviation of the likelihood.

4. Update x by choosing $x^{(j)} = \arg\max\{p(x \mid y, \theta^{(j-1)})\}$;
5. Update θ by choosing $\theta^{(j)} = \arg\max\{p(\theta \mid y, x^{(j)})\}$;

   - If hyperprior is set to G, then;
     $\theta_i = \frac{1}{2}\theta_0(\eta + \sqrt{\eta^2 + 2{x_i}^{(j)^2}/\theta_0})$
     $\eta = \beta - 3/2$, $i = 1, 2, ..., n$
   - Otherwise, if hyperprior is set to IG, then;
     ${\theta_i}^{(j+1)} = (\theta_0 + \frac{{x_i}^{(j)^2}}{2})/k$
     for $k = \beta + 3/2$, $i = 1, 2, ..., n$.

6. Set $j = j + 1$ and continue from step 2 until it converges.

3.1.5.4 Markov chain Monte Carlo (MCMC) sampling technique

Markov chain Monte Carlo (MCMC) is, principally, a sampling technique for generating sampling sequences in large dimensional spaces to approximate a given probability density [17]. MCMC generates a sequence of independent and identically distributed set of samples, i.e., $x^{(1)}, x^{(2)}, ..., x^{(t)}$ for a given probability density, i.e., $p(\mathbf{x})$, $x \in R^n$. In Markov chain, the next state is a random variable depending on the previous one, i.e., it can be defined as:

$$p(x^{(i)} \mid x^{(i-1)}, ..., x^{(1)}) = \boldsymbol{T}(x^{(i)} \mid x^{(i-1)}), \tag{3.24}$$

where $\boldsymbol{T}$ denotes a transition probability function describing the conditional probability of the subsequent states [4, 17], i.e., the probability distribution of the chain. In this thesis and in the context of HBM, we use MCMC to estimate the conditional mean (CM) of the posterior, i.e., $x_{CM} = E(\mathbf{x}, \theta \mid \mathbf{y}) = \int (\mathbf{x}, \theta) p_{\text{post}}(\mathbf{x}, \theta \mid \mathbf{y}) \, \mathrm{d}\mathbf{x} \, \mathrm{d}\theta$. MCMC algorithm [26, 27] provides a robust way to estimate CM but can be computationally expensive, when the source space is large, unless the active part of the brain is constrained into a smaller set, e.g., into a region of interest (ROI) which can be selected, e.g., via the *a priori* information available on the active brain areas.

3.1.5.5 Minimum norm estimate (MNE) and Minimum current estimate (MCE)

In the Bayesian framework, *l^p-norm* prior can be utilized for source reconstruction with a variable value of $0 < p < \infty$. Minimum norm estimate (MNE) [51] and Minimum current estimate (MCE) [122] correspond to ℓ^2 and ℓ^1 norm prior or regularization, respectively. With the former interpretation, MNE can be considered as the maximum *a posteriori* probability estimate obtained with Gaussian *a priori* current distribution, whereas MCE associates with an exponential *a priori* distribution. Both MNE and MCE can be interpreted as special cases of HBM [26], however, MCE provides more focal source localization compared to MNE [115].

MNE Minimum norm estimate (MNE) minimizes the least-squares solution of $\mathbf{Lx} = \mathbf{y}$ with the minimal ℓ^2-norm to obtain a minimally biased regular candidate solution for the inverse problem. The regularization corresponds to minimizing the norm of the solution, which prevents any deviations following from possible

noise effects. MNE also follows as a limit, i.e., $\lim_{\delta \to 0} \mathbf{x}^{\ddagger}$ of the classical Tikhonov (ℓ^2-norm) regularization $\mathbf{x}^{\ddagger} = \arg\min_{\mathbf{x}} ||\mathbf{L}\mathbf{x} - \mathbf{y}||_2^2 + \delta^2 ||\mathbf{x}||_2^2$. Thereby, MNE can be approximated via a Tikhonov regularization, that is, by finding the balance between the fitting of measured data (minimizing the residual) and minimizing the noise in the data [60]. The Tikhonov regularized solution can be presented as:

$$\mathbf{x}^{\ddagger} = (\mathbf{L}^T\mathbf{L} + \delta^2\mathbf{I})^{-1}\mathbf{L}^T\mathbf{y} = \mathbf{L}^T(\mathbf{L}\mathbf{L}^T + \delta^2\mathbf{I})^{-1}\mathbf{y}, \tag{3.25}$$

corresponds to the first iterate of the IAS method (subsection 3.1.5.3) [26]. Detailed mathematical description of the minimum norm estimate can be found in section 2.2 of study [52].

MCE Minimum current estimate (MCE), i.e., ℓ^1 regularized reconstruction minimizes the sum of the absolute currents, which leads to a more focal estimate for the primary current distribution compared to ℓ^2 norm regularization or MNE [115, 122]. Namely, when used in regularization, ℓ^1 norm can be shown to favor sparse distributions with few non-zero entries. The MCE estimate can be shown to follow from the IAS MAP iteration (subsection 3.1.5.3), when $\beta = 1.5$ and the hyperprior is G [26].

Depth-bias When the depth of the source is unknown, both MNE and MCE have bias towards the superficial sources [26, 69], therefore, leading to the ambiguity of localizing the far-field sources. To suppress this bias, e.g., depth-weighting approaches [69] or sparse source distributions [67, 101] can be utilized for more robust localization of deeper sources.

3.1.5.6 Randomized multiresolution scanning (RAMUS)

Randomized multiresolution scanning (RAMUS) technique constitutes a multiresolution concept. Multiresolution setting often refers to an energy-preserving and orthogonal or biorthogonal wavelet decomposition, i.e., a set of complementary components with different resolutions and a total energy that matches the signal, which can be obtained in a regular grid, see for example studies by [47, 72]. Since the source position grid inside the complex brain structure is generally not regular, instead of wavelets, our approach applies random projections [16, 28, 88] each with a

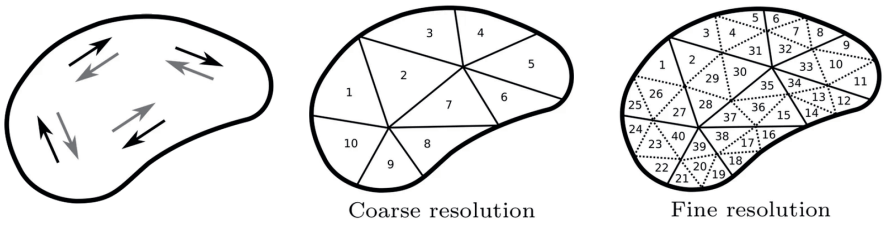

Figure 3.3 Coarse-to-fine resolution process. *Left:* An illustration of the coarse source configuration which belongs to S_ε^+, i.e., detectable source space (black) and undetectable sources belonging to S_ε^- (grey). The source subsets constituting the coarse resolution can be divided into smallest subsets to obtain a finer resolution. RAMUS utilizes a sparsity factor in this subdivision process, i.e., the ratio of source counts between two subsequent levels is kept constant.

given resolution and due to the absence of orthogonality, the energy is preserved approximately via averaging the outcome coming from this averaging. Our approach aims to reconstruct the activity at different source depths, finding focal and accurate source localization, while at the same time avoiding bias at different source depths [101]. At each resolution level, RAMUS finds an IAS MAP (subsection 3.1.5.3) for multiple randomized source spaces using the IG hyperprior which is known to be favourable to detect the deep activity [26]. The final reconstruction is found as the average of these estimates. Detailed mathematical description and algorithms of the RAMUS technique can be found in Appendix A of this thesis.

RAMUS technique follows the principles of *coarse-to-fine optimization* (Figure 3.3 and 3.4) [96] and *randomized scanning* (randomized multiresolution decompositions and projections) [16, 28, 31, 70, 88, 101]. The former concept is based on decomposing the source space as $S = S_\varepsilon^+ \oplus S_\varepsilon^-$ into the subsets of detectable S_ε^+ and undetectable S_ε^- fluctuations [70, 96, 101]. The subsets S_ε^+ and S_ε^- can be defined as $S_\varepsilon^+ = \{0\} \cup \{\mathbf{x} : ||\mathbf{Lx}|| \geq \varepsilon\}$ and $S_\varepsilon^- = \{\mathbf{x} : ||\mathbf{Lx}|| < \varepsilon\}$, where ε follows from the total error level which can be interpreted as the net effect of both measurement and modeling errors. The subset S_ε^+ presents detectable source space, whereas S_ε^- represents the set of undetectable source distributions [96] and can be interpreted as the numerical or practical null-space of $\mathbf{L}$.

The set S_ε^+ can be approximated by a sparse source space, since in a sparse set the effect of each source can be distinguished. This can be also understood from the viewpoint of linear algebra, since when the number of sources (columns in $\mathbf{L}$) is smaller than the number of data entries (rows), the null space of $\mathbf{L}$ can be a trivial

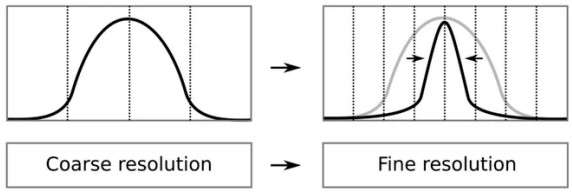

Figure 3.4 An illustration of the progress from a coarse to fine resolution. The source estimate obtained at the coarse level is utilized as an initial guess for the finer one which leads to focal estimation.

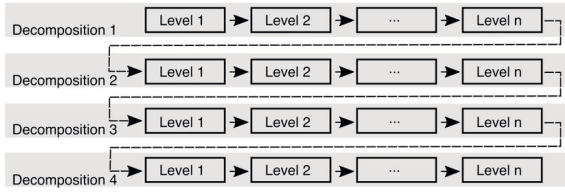

Figure 3.5 A schematic visualization of a randomized set of multiresolution decompositions $1,\ldots,D$ for levels $1,\ldots,L$. Each decomposition associates with multiple resolution levels. In RAMUS, the final estimate is obtained by averaging over multiple resolution levels and decompositions. The reconstruction obtained for one decomposition is used as an initial guess for the next one. This strategy can be interpreted as a surrogate to reduce the discretization and optimization errors in the final reconstruction.

set, i.e., it only contains the origin. Therefore, a coarse source space plays a significant role in localizing deep-lying brain activity [67]. However, when the number of sources exceeds the number of entries in the measured data, $\mathbf{L}$ has a non-trivial null-space belonging to S_{ε}^{-} and the inverse problem set by $\mathbf{L}$ is underdetermined.

In the coarse-to-fine refinement process, the resolution of each subset of the source space S is gradually increased to that of the original source space. The ratio of the source counts between two subsequent source spaces is determined by the constant sparsity factor $s > 1$ (Figure 3.3). The finer resolution levels are vital in reconstructing focal cortical activity: increasing the resolution aims to the gradual refinement of the details found [72]. This process is enhanced by utilizing the source estimate obtained at one level as the initial guess at the next one (Figure 3.5). Consequently, the presence of higher resolution levels is essential for obtaining a more focal reconstruction. Eventually, a final approximation will be obtained by averaging the estimates obtained over different resolution levels (Figure 3.5). The aim of randomized scanning is to reduce the discretization and optimization errors by presenting and averaging over a large number of randomized source spaces [101].

3.1.6 Prior-over-measurement signal-to-noise ratio (PM-SNR) model

The prior-over-measurement signal-to-noise ratio (PM-SNR) [100] refers to the relative weight of the prior with respect to the measurement noise and is a crucial concept in adopting a suitable parametrization for hyperpriors. PM-SNR plays a significant role in obtaining a focal and accurate source localization. The PM-SNR model proposed in [100] is significant in selecting the shape β and scale θ_0 parameters determining the hyperprior, i.e., G or IG. It associates with the expectation of G and IG, given by: $E_G = \beta\theta_0$ and $E_{IG} = \frac{\theta_0}{\beta-1}$, respectively. The behaviour of G and IG with respect to the opted parameters is illustrated in Figure 3.2, with an expected noise-induced fluctuation in the reconstruction based on the assumption that a peak due to brain activity in a given spatio-temporal point is a relatively rare event compared to a peak due to noise. In this context, noise can include errors from different sources, e.g., measurement, forward modeling, and source localization.

To allow selecting θ_0, the concept of the total scale $\theta^{(\text{tot})}$ has been formulated in [100]. The total scale is interpreted to be a *a priori* set constant describing the relative strength of the prior, while the source-wise scale θ_0 can change. Given the standard deviation (STD) σ of the measurement noise, the amplitude A of the measured signal, the number of the sources N in forward modeling, the relationship between the total and source-wise scale can be expressed as follows:

$$\theta_0 = \frac{\theta_0^{(\text{tot})}\sigma^2 A^2}{N} \quad \text{or} \quad \theta_0^{(\text{tot})} = \frac{\theta_0 N}{\sigma^2 A^2}. \tag{3.26}$$

It is further interpreted that the square-root $\sqrt{\theta_0^{(\text{tot})}}$ describes the ratio between the integrated STD of a Gaussian (or a conditionally Gaussian) prior and the STD of the measurement noise. PM-SNR is defined as a measure of this ratio:

$$\text{PM-SNR} = \text{dB}(\sqrt{\theta_0^{(\text{tot})}}) = \text{dB}(\sqrt{N}) + \text{dB}(\delta) + \text{dB}(A) - \text{dB}(\delta^{(\text{ref})}) \tag{3.27}$$

$$\text{with} \quad \delta = \frac{\sqrt{\theta_0}}{\sigma A}, \quad \delta^{(\text{ref})} = \frac{|\vec{J}^p|}{A}, \tag{3.28}$$

and $\text{dB}(x) = 20\log_{10} x$. Here $\delta^{(\text{ref})}$ is a reference level which is obtained as a ratio between *a priori* estimated norm of the primary current density $|\vec{J}^p|$ and the signal

amplitude A. At the reference level, when PM-SNR is 0 dB, $\sqrt{\theta_0}$ matches the *a priori* noise-induced fluctuation of the candidate solution normalized by $A\sqrt{N}$, that is,

$$\sqrt{\theta_0} = \frac{\sigma|\vec{J}^p|}{A\sqrt{N}}. \tag{3.29}$$

Assuming that a 10 nAm source is to be reconstructed based on measurement data with 10 microvolt amplitude and 3 % relative noise standard deviation using a source space with 1.5E+04 sources, i.e., $A =$ 10E-06 V, $\sigma = 0.03$, $|\vec{J}^p| =$ 1E-08, and $N =$ 15000 [45, 52, 128], i.e., implies roughly $\theta_0 =$ 6E-14 with PM-SNR 0 dB. In 3.27, δ denotes the source-wise relative weight of a Gaussian prior and correlates to the Tikhonov regularization parameter of MNE [12, 26, 65]. In the Brainstorm software tutorial [1], the default value for this ratio is set to be $dB(\delta)=$ 9 dB in the case of the MNE reconstruction. Referring to the current example parameter choices, Brainstorm's default prior strength for MNE would coincide with a PM-SNR of 9 dB. In [100], a 20 dB PM-SNR has been found advantageous with the IAS method.

PM-SNR can be interpreted to be method-specific since, in addition to the given noise with respect to the measurement, also latent noise can be taken into account. The relative (total) noise standard deviation is assumed to be of the form $\sigma = s\overline{\sigma}$, where $\overline{\sigma}$ yields the standard deviation of the nominal noise, not including the latent effects, and $s \geq 1$ interprets those, e.g., the forward modeling errors of the quasi-static approximation, head compartment's conductivity differences and segmentation errors, etc. [6]. It follows that the PM-SNR is of the form :

$$\text{PM-SNR} = \overline{\text{PM-SNR}} + \text{dB}(s), \tag{3.30}$$

where dB(s) refers to the total contribution of the latent noise effects. Therefore, the actual PM-SNR will be greater than the nominal value $\overline{\text{PM-SNR}}$ for models including latent noise, i.e., when $s > 1$. Hence, the greater the latent noise, the greater weight of the prior will be necessary. When $\overline{\text{PM-SNR}}$ is set to 0 dB, PM-SNR is given by dB(s) and the explicit formula for the scaling parameter is $\sqrt{\theta_0} = s\sigma|\vec{J}^p|/(A\sqrt{N})$, where σ corresponds to the known noise level and s to the *a priori* assumption of the latent noise strength.

The probability for the occurrence of the actual activity is considered to be pre-

[1] `https://neuroimage.usc.edu/brainstorm/Tutorials/SourceEstimation`

dicted by the tail (decay rate) of the hyperprior. The central factor enabling the appropriate function of the hyperprior is that its relative decay rate with respect to the amplitude of the reconstructed peak is slower than that of the likelihood with respect to the observed data amplitude. Due to this difference, the peaks of the actual activity will be distinguishable. The distance between the expectation and a given level of the tail follows from β; the smaller β, the greater the variability in the amplitude of the reconstruction. Hence, β can be associated with the uncertainty allowed by the reconstructed peak, which could follow, e.g., from different source depths altering the amplitude of the measurement. This work considers an experimental reference value $\beta = 3$ which can be interpreted as a balance point in which this distance is approximately the same for both IG and G prior and, therefore, both hyperpriors can be expected to provide a roughly similar outcome [100]. The deeper analysis of the dynamical effects related to selecting β are omitted in this work, while the concentration is on selecting θ_0. Further information of the PM-SNR model with respect to the hyperprior and their behaviour is described in section 2 and Appendix of [100] which is part of this thesis.

3.2 Zeffiro Interface (ZI)

The advanced forward and inverse techniques introduced and employed in this thesis are combined as a code package Zeffiro Interface (ZI) [59] which is a platform to integrate advanced finite element (FE)-based forward and inverse modeling for electromagnetic brain applications in MATLAB (The Mathworks Inc.) environment and is openly available in Github[2]. FEM-based forward approach, namely, H(div) source model and inverse modeling such as hierarchical Bayesian model (HBM) can be utilized in ZI for brain source localization. A high-resolution (1 mm) head model is employed in ZI in order to obtain a high accuracy with respect to the complex brain structure and its heavily folded tissues and thin layers, including, in particular, the grey matter and the skull. The methods of ZI can be accelerated with a graphics processing unit (GPU) in the mesh generation, lead field computation (forward simulation), interpolation, and inversion stages, Figure 3.6. The basic functions of ZI, Figures 3.7 and 3.8, can be operated via its segmentation tool, mesh tool, inverse tool, parcellation tool and plugins, which can be developed by the users and added

[2] https://github.com/sampsapursiainen/zeffiro_interface

into ZI by placing them into its plugin folder, providing a flexible approach for software development via the Matlab platform. Using a workstation, desktop or laptop equipped with a high-end GPU, the full process of forward and inverse modeling, beginning from a surface segmentation of the volumetric domain, can be run within approximately one hour at 1 mm FE mesh resolution. The time needed for 1 mm FE mesh generation, EEG lead field matrix evaluation and source space interpolation took roughly 21, 39 and 3.5 minutes, respectively, in a Lenovo P910 workstation equipped with NVIDIA Quadro P6000 GPU[3]. In the segmentation tool, ASCII files exported from FreeSurfer Software Suite can be imported to ZI separately or as individual ASCII files, to establish the surface segmentation.

The FE mesh is a uniform tetrahedral mesh based on the surface segmentation. It can be created for multicompartment head model via ZI after importing the surface segmentation and setting the mesh parameters in the mesh tool. The mesh is generated from its inner compartment to the outer layer. Each source distribution is obtained by picking a randomly (uniformly) permuted set of tetrahedron centers in the brain compartment. Since the mesh structure is uniform, this process leads to an evenly distributed set of source points. After generating the FE mesh, a lead field is calculated and its source space is interpolated to integrate it with the FE mesh. Next, a reconstruction of the brain activity can be obtained using one of the inverse tools of the HBM-based tools, which were implemented over the completion of this thesis. The HBM inverse tools allow selecting the hyperprior parameters, i.e., shape and scale parameters of the G and IG hypermodel, via the PM-SNR model (section 3.1.6). The orientation of sources can be constrained or unconstrained. In the former case, the sources are assumed to be oriented along with the local surface normal to the compartment and, in the latter case, it can be freely oriented as a vector field consisting of three Cartesian components.

3.2.1 FreeSurfer to Zeffiro Interface pipeline

This section describes the process of extracting segmented files from FreeSurfer and importing them to Zeffiro Interface. The FreeSurfer to Zeffiro Interface pipeline is written as a part of this work and is illustrated in Figure 3.9. It includes the following steps:

[3] https://en.wikipedia.org/wiki/List_of_Nvidia_graphics_processing_units

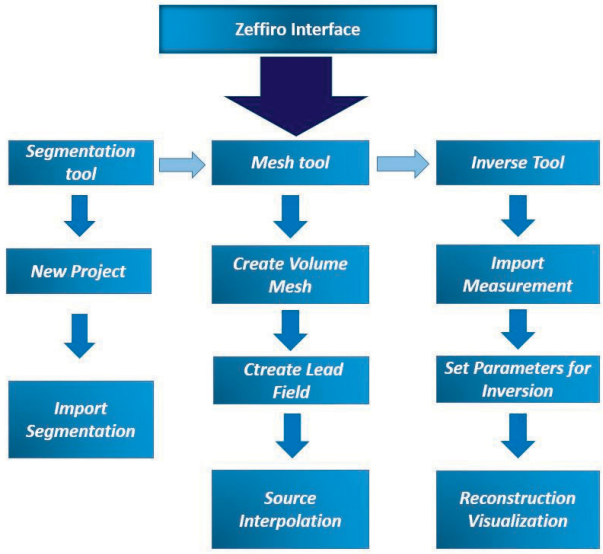

Figure 3.6 A diagram of Zeffiro Interface (ZI) presenting the main tools for mesh generation and source localization.

1. Perform recon-all command in FreeSurfer on T1-weighted MRI data in the format of the single DICOM (file.dcm) file or NIFTI (file.nii) file including the subcortical structures. To do this, the subject identification string, input directory of MRI data and output directory for saving the reconstructed files are required.
2. Strip the skull and other outer non-brain tissues.
3. Convert the extracted files for surface and subcortical structures to ASCII (file.asc) files.
4. Processing the .annot file to obtain parcellation labels based on the Aseg atlas of MRI data. Parcellation can be Desikan-Killiany or Destrieux atlases with 36 and 76 labels, respectively.
5. Merge the label files as a single file for left and right hemisphere.
6. Eventually, all the extracted segmentation and ASCII files are imported to ZI to implement the inversion, analyzing and 3D visualization.

Example files for exporting a segmentation from FreeSurfer and importing it to ZI can be found in ZI's repository and have been included as Appendix B and C, respectively. The import file allows for configuring a complete exported segmentation and

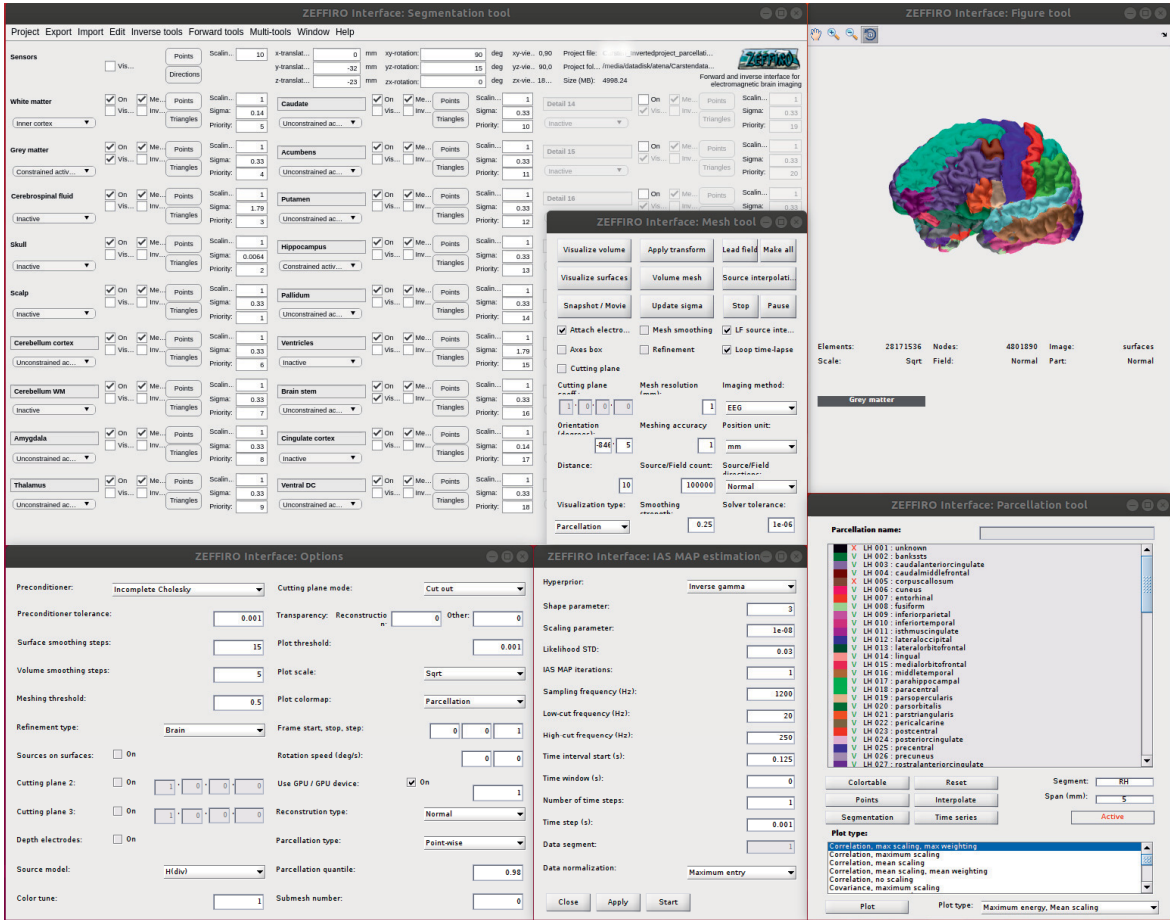

Figure 3.7 Zeffiro Interface (ZI) illustrated with a set of tools opened.

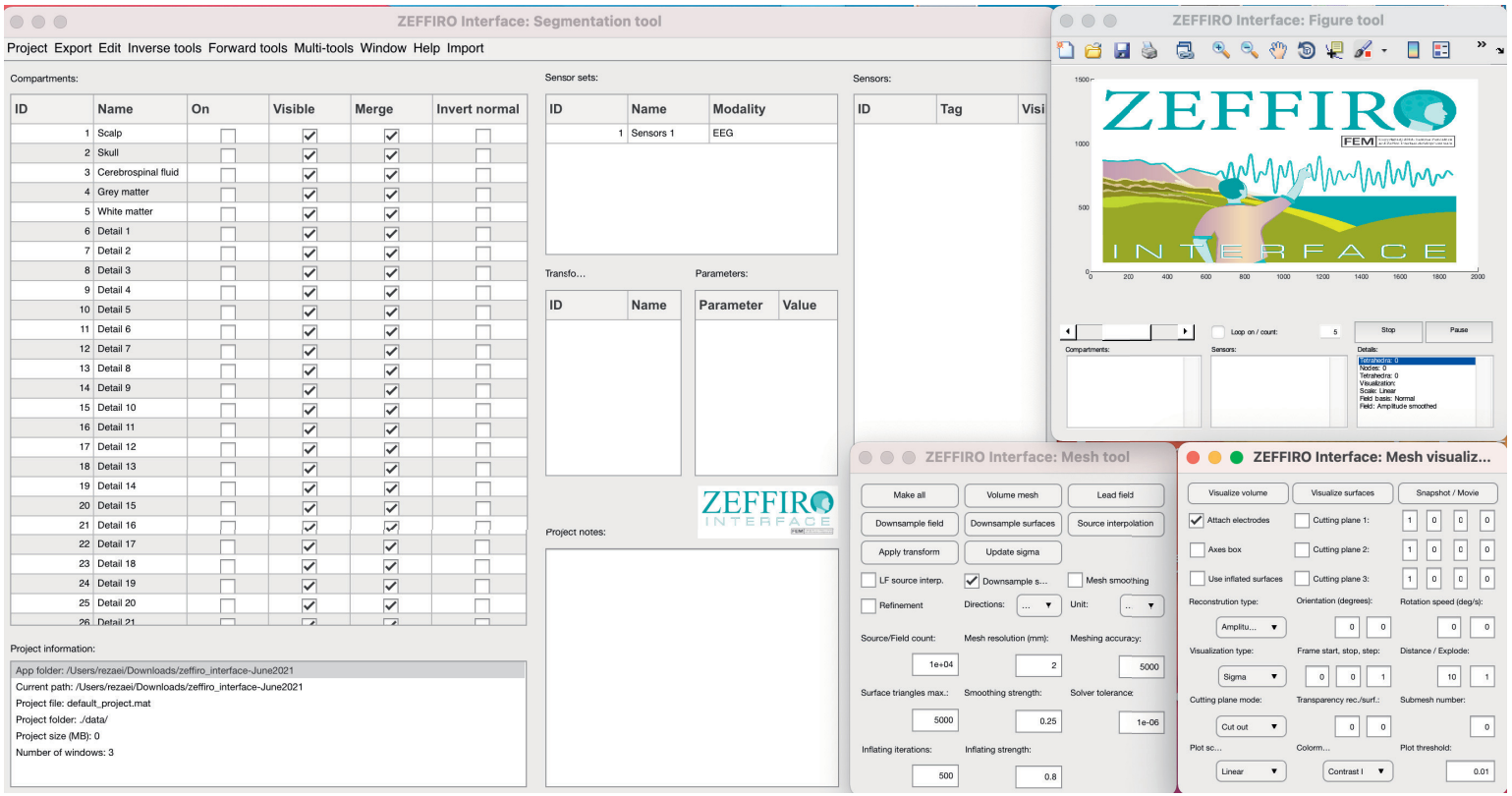

Figure 3.8 Visualization of the latest version (June2021) of the ZI.

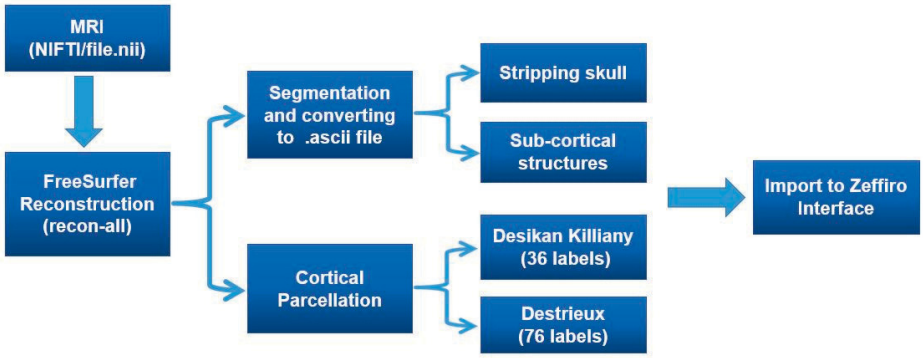

Figure 3.9 A diagram of FreeSurfer to Zeffiro Interface for importing the ascii files.

defining the activity mode and conductivity of each compartment.

3.3 Head models and measurement data

This section sheds light on the data acquisition, preprocessing, and the head models, e.g., spherical and real human head models, which have been used in this thesis to obtain the results for studies I-V.

3.3.1 Spherical and real head model

3.3.1.1 Study I

In this study (section 4.1), a four-layered Stok model [116] including brain (0.33 S/m), CSF (1.79 S/m), skull (0.0042 S/m), and scalp (0.33 S/m) was used to show the performance of the implemented source H(div) model and its adapted version with 2 mm thickness of the gray matter. The particular concentration was on the effects that follow, when the source is approaching the surface of the gray matter, which is inevident, since the grey matter layer is in the lower end of the normal 2–4 mm thickness interval in adults.

A real and multilayered human head model was utilized to investigate the localization of the brain activity in the context of H(div) source model. This head model consists of skin (0.43 S/m), skull compacta (0.0064 S/m), skull spongiosa

(0.028 S/M), cerebrospinal fluid (CSF) (1.79 S/m), gray matter (0.33 S/m), white matter (0.14 S/m), and eyes (0.505 S/m). The conductivity value for each compartment follows the studies [34, 97], in which, the latter one of these studies used the same model. In the source localization tests, the goal was to show the performance of H(div) forward model in the cortex, in particular, with ℓ^1 and ℓ^2 -norm regularized estimates.

3.3.1.2 Study II

In this study (section 4.2), we used a realistic head model and dataset of Brainstorm's *EEG and Epilepsy* tutorial[4] with the consent of Prof. Andreas Schulze-Bonhage, Epilepsy Center, University Hospital Freiburg, Germany. The head model with EEG measurement from an epilepsy patient was applied to detect the epilepsy spikes in the left fronto-central region of the head. Additionally, the applicability of ZI to localize a simulated hemorrhage via electrical impedance tomography (EIT), was shown using a five-layered population head model (PHM) [5] including white matter (0.14 S/m), gray matter (0.33 S/m), CSF (1.79 S/M), skull (0.0064 S/m), and scalp (0.43 S/m). In this experiment, the IAS inversion technique was utilized to solve a linear inverse problem of the form 3.19 with respect to linearized EIT equations as shown in study II (section 4.2).

3.3.1.3 Study III

In study III (section 4.3), a three-layered and spherical Ary model including grey matter (0.33 S/m), skull (0.0042 S/m) and scalp (0.33 S/m) [7] was employed for numerical analysis to investigate the performance of the RAMUS method in reconstructing brain activity for different depths, e.g., for superficial and deep layers. Additionally, a population head model (PHM) was used to demonstrate that RAMUS has the potential to reconstruct the simultaneous superficial and deep activity for the P20/N20 component of SEP and thalamic region.

[4] https://neuroimage.usc.edu/brainstorm/Tutorials/Epilepsy

[5] https://itis.swiss/virtual-population/regional-human-models/phm-repository/

3.3.1.4 Study IV and V

Three realistic and human head models based on MRI measurements were obtained and used for the experimental analysis of studies IV and V (section 4.4 and 4.5). Each head model includes six layers of brain, white matter, gray matter, CSF, skull and scalp and subcortical structures which are segmented from Aseg atlas of FreeSurfer software suite[6]. The extracted subcortical structures included the amygdala, putamen, thalamus, brainstem, caudate, accumbens, hippocampus, pallidum, cerebellum, ventricles, and ventral DC. Of these subcortical structures, thalamus and brainstem were included in the set of active compartments for the SEP/SEF analysis due to their contribution in sensory processing [67]. The conductivity value of the outer layers followed by the study of [34], whereas that of the subcortical structures matches with the cereberal cortex, i.e., 0.33 S/m, based on [111]. Of the three head models, one is openly available at Zenodo repository [7]. The head models in study IV were applied to investigate the reconstructed evoked responses for SEP/SEF measurement with respect to the hyperprior parameters chosen by PM-SNR model. The motivation in study V was to analyze the implementation of RAMUS technique on a realistic head model to reconstruct the simultaneous cortical and subcortical activity for SEP dataset at different latencies.

3.3.2 Subjects and ethical clearance

In study II, Brainstorm's EEG and epilepsy tutorial dataset[8] was utilized under the the consent of Prof. A. Schulze-Bonhage from Epilepsy Centre, University Hospital Freiburg, Germany. The data was obtained from a patient who suffered from focal epilepsy with focal sensory, dyscognitive, and secondarily generalized seizures since the age of eight years. The data was measured by non-invasive telemetry recording during night at the Epilepsy Center Freiburg, Germany. The EEG data was employed to reconstruct the left fronto-central polyspikes by HBM inversion tests in ZI[9].

The SEP/SEF measurements in studies IV and V were obtained for three right-

[6] https://surfer.nmr.mgh.harvard.edu/
[7] https://doi.org/10.5281/zenodo.3888381
[8] https://neuroimage.usc.edu/brainstorm/Tutorials/Epilepsy
[9] https://github.com/sampsapursiainen/zeffiro_interface

handed healthy adult male subjects (**I**), (**II**) and (**III**), 49, 32 and 27 years old, respectively. The subjects had no history of psychiatric or neurological disorders and had given written informed consent before the experiment. The institution's ethical review board (Ethik Kommission der Ärztekammer Westfalen-Lippe und der WWU) approved all experimental procedures on 02.02.2018 (Ref. No. 2014-156-f-S). The Neurophysiological data and head model (for one subject) are available at the Zenodo portal. The SEP/SEF measurements were utilized to detect the generator of P20/N20 component of evoked responses at Brodmann area 3b and simultaneous far-field activity at subcortical region, respectively.

3.4 MRI acquisition for experimental analysis in study IV and V

For each subject, MRI dataset was obtained by a 3T MAGNETOM prisma -scanner (release D13, Siemens Medical Solutions, Erlangen, Germany). For the measurement, a 3D T1-weighted (T1w) fast gradient echo pulse sequence with water selective excitation was utilized to prevent fat shift (TR/TE/ FW = 2300/3.51 ms/8°, inversion pre-pulse with TI= 1.1 s, cubic voxels of 1 mm edge length) was measured and a 3D T2-weighted (T2w) was acquired as a turbo spin echo pulse sequence (TR/TE/FA = 3200/408 ms/90°, cubic voxels, 1 mm edge length). Gadolinium markers were used at the same nasion, left and right distal outer ear canal positions for landmark-based registration of combined EEG and MEG were obtained during the T1w-MRI measurement. All the measurements were carried out in a supine position to minimize head movements and avoid cerebrospinal fluid (CSF) effects because of a brain shift when EEG/MEG and MRI are combined [102].

3.5 EEG and MEG measurements for experimental analysis in study IV and V

The SEP and SEF measurements were obtained from three right-handed adult subjects to detect the simultaneous originators of the P20/N20 component at Brodmann area 3b and simultaneous far-field activity with different source localization

approaches were implemented in studies IV and V. The SEP and SEF data were measured at the same time in a magnetically shielded room. The measurement utilized 80 AgCL sintered EEG ring electrodes (EASYCAP GmbH, Herrsching, Germany, 74 channel EEG with additional 6 channels EOG to detect eye movements). For MEG measurement, a system with 275 axial gradiometers and 29 reference sensors (OMEGA2005, VSM MedTech Ltd., Canada) was utilized. Moreover, cardiac activity was measured by electrocardiography (ECG) electrode.

The MEG reference coils were employed to compute the first-order synthetic gradiometers to minimize the interference of magnetic fields derived from far locations. A Polhemus device (FASTRAK, Polhemus Incorporated, Colchester, Vermont, U.S.A.) was utilized to digitize the electrode positions of the EEG cap prior to the measurements. Furthermore, the head position inside the MEG was checked via three head localization coils which are on the nasion, left and right distal outer ear canal, i.e., preauricular points.

In order to record the evoked responses of the primary somatosensory cortex (SI), the peripheral nerve of the right wrist for each subject was stimulated. To this end, monophasic square-wave electrical pulses with a duration of 0.5 ms were applied to the median nerve. The measurements were obtained with a sampling frequency rate of 1200 Hz and low-pass filtered with 300 Hz as the cut-off frequency. The duration of each experiment was 9 minutes during which 1200 trials were obtained. The stimulus onset asynchrony (SOA) varied randomly between 350 and 450 ms in order to prevent habituation and obtain clear pre-stimulus intervals for signal-to-noise ratio (SNR) determination.

Data preprocessing In the preprocessing stage, the raw combined EEG and MEG measurement was band-pass filtered between 20–250 Hz as suggested in [24]. A notch filter was applied to remove the interference caused by 50 Hz power line frequency and its harmonics and by 60 Hz of the used monitor. After that, the preprocessed recordings were divided into evenly large segments of 300 ms (100 ms pre and 200 ms post stimulus onset). After removing the bad channels visually by FieldTrip toolbox [10], non-cerebral activity was reduced according to a threshold-based procedure in FieldTrip, followed by the visual inspection of the bad trials candidate in each modality. Eventually, the SEP and SEF evoked responses were averaged over

[10] https://www.fieldtriptoolbox.org/

the remaining trials per single subject.

3.5.1 Finite element (FE) mesh and lead field matrices

In study I, a FE mesh for Stok model was generated via Gmsh software [11], whereas ZI was used in generating the other meshes, mainly utilizing less than 1 mm mesh resolution to take the complex three-dimensional structure of the human head appropriately into account as proposed in [103]. The FE mesh of the realistic head model (section 3.3.1) was generated using 0.85 mm resolution, resulting into 37.9 M and 6.45 M elements and nodes, respectively. In study II, the EIT inversion tests were performed using 1 mm mesh resolution, and in III, the mesh resolutions 0.85 and 1 mm were utilized with PHM and Ary model, respectively. In IV, the results obtained with 1 and 2 mm FE mesh resolution were compared. These meshes contained 3.8 M vs. 0.47 M nodes and 22 M vs. 2.7 M tetrahedra, respectively. In V, each FE mesh was generated with 1 mm mesh resolution. In each of I–V studies, the LF matrices utilized in source localization were obtained for a set of sources in Cartesian orientation, i.e., along x-, y- and z-directions.

[11] https://gmsh.info/

4 RESULTS AND DISCUSSIONS

This dissertation focused on the following four major domains and goals:

1. Advancing a volumetric modeling and FEM-based forward techniques for source modeling within complex and multicompartment human head model.
2. Combining accurate forward and inverse solvers as a brain interface package for source localization of neural activity in brain imaging applications.
3. Introducing a model based on noise level for selecting appropriate range of hyperparameters and better performance of the inverse techniques in the framework of the hierarchical Bayesian modeling (HBM).
4. Investigating the advanced inverse technique based on the multiresolution concept and sparse source space to detect weakly distinguishable deep activity utilizing somatosensory evoked potential (SEP) measurement and realistic human head model.

In the following sections, the results and findings for individual studies are described.

4.1 Outline of Study I

Motivation & **Goal**

This study sheds light on accurate forward modeling for non-invasive EEG brain imaging, particularly for thin cortices where the source configurations need to be focal. FEM and tetrahedral finite element mesh are utilized in forward source modeling in brain to model the complex head geometry. However, FEM incorporates outliers, particularly at the boundary of domain where the electrical conductivity value jumps to other compartments, e.g., from gray matter to CSF and causes forward modeling errors. Therefore, the proposed source modeling approach in the current study aims to avoid forward modeling errors in the restricted domain where few sources are interpolated.

Approach

This study investigated advanced FEM-based forward modeling for EEG source localization, and showed that the divergence conforming H(div) approach performs well when being utilized with complex and realistic geometries with a thin grey matter layer, e.g., 2.3 mm thick human cortex [38, 49, 77] and potentially also with thinner cortices, e.g., in children brain and pathological applications. Herein, numerical experiments within the spherical model are conducted to evaluate the performance of H(div) approach with classical PI and SV source modeling techniques.

4.1.1 Overall results

The findings show that the H(div) model is computationally fast. The adaptable source stencil introduced in this study allows varying the number of elements applied in interpolating the mesh-based H(div) elements into a Cartesian orientation. A stencil consisting of one to five elements was found to be advantageous for different cortical thicknesses; the adaptable stencil is centered around a given tetrahedron and includes only those adjacent tetrahedra that belong to the grey matter, thereby, allowing the center element being placed right next to the surface of the grey matter layer.

The results for the multilayered spherical model show that a higher accuracy and computational performance was obtained for the proposed model compared to other classical techniques, i.e., St.Venant (SV) and partial integration (PI). On one hand, we found also that our model accuracy increases as the number of elements applied in the stencil grows, and, on the other hand, the number of source elements should be restricted for thin cortices as it might overlap with other compartments at the boundary of grey matter such as CSF where leads to the discontinuity of the electrical conductivity and reduce the focality of the model. Additionally, the performance of the H(div) method in source localization was found to potentially reduce the spotty artifacts due to interpolation errors as compared to SV and PI by evaluating l^2 and l^1 regularized estimates for the primary current distribution using a realistic head model and a simulated source.

4.1.2 Results in detail

The implementation of the divergence conforming (current preserving) source model covers two cases: (i) *non-adaptive* H(div) and (ii) *adaptive* H(div). The former refers to the higher accuracy for thicker cortices with the basic five-element configuration, i.e., the five-element stencil, and the latter is adaptive from one to five elements in the stencil and is more favourable in thin cortices.

The results were evaluated via relative difference measure (RDM) and magnitude difference (MAG) for 200 dipoles with random positions and orientations of 1.5 mm depth sources and superficial sources of 0.1 mm for 98% and 99% eccentricity, respectively. The accuracy of the H(div) model improved along with the number of mesh nodes estimating a single source. Figure 4.1 demonstrates the configuration of nodes centered around a single center tetrahedron.

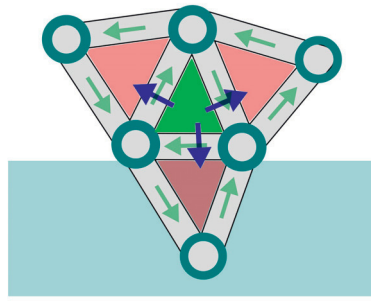

Figure 4.1 The illustration of the five element H(div) source stencil in the boundary of grey matter. The dark arrows refer to FI and light green ones show the EW sources, respectively.

The smallest median for RDM at 98 and 99 % eccentricity was obtained for a five-element patch. The results in Figure 4.2 show that as the number of elements grow, the spread or IQR of RDM decreases, i.e., the accuracy increases. When the number of elements included in the stencil was increased from 2 to 5 the median differences between different methods improved 0.28 and 0.26% for eccentricity of 98 and 99.9%, respectively.

The results demonstrate that the single-element H(div) gave identical results as those obtained with PI. At 98% eccentricity, the median RDM obtained for SV approach was close to the value obtained for the five-element H(div) source configuration. Nevertheless, for the 99% eccentricity, the H(div) model gave the superior re-

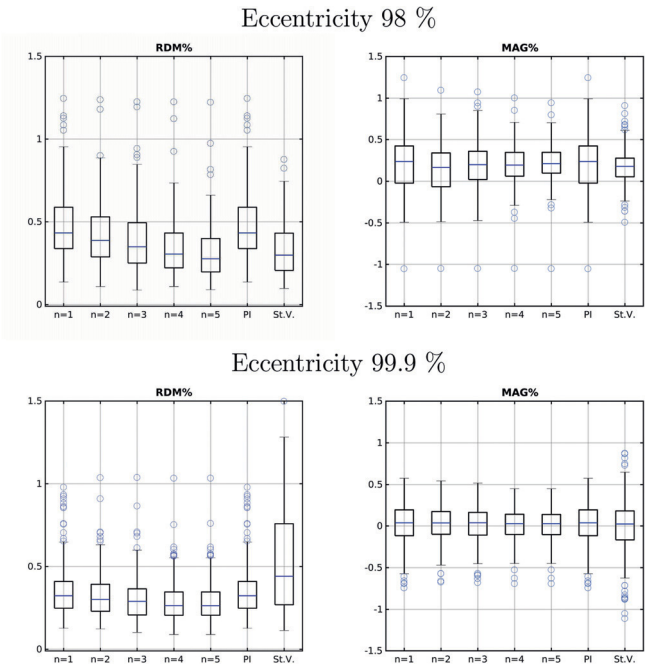

Figure 4.2 The boxplots visualization of RDM and MAG errors for H(div) source modeling with n elements and PI and St.V (SV) approaches. The boxplots are drawn for 200 randomly distributed dipolar sources for 98 and 99% eccentricity, respectively.

sult. Moreover, the boxplots for MAG with respect to 98% eccentricity showed that SV performs well compared to five-element H(div) model, while the performance of SV is weaker for 99% eccentricity compared to H(div) model.

The l^2 and l^1 regularized source localization estimates obtained with a simulated source demonstrated how the adaptive and non-adaptive approach performs within a realistic head model. In the case of the l^2 regularized estimate, the reconstruction with the non-adaptive technique was found to be more focal than the adaptive one. The reconstruction by l^1 estimate revealed fairly similar results. However, the reconstructions for H(div) approach were found to be smoother and less distributed compared to SV and PI. In particular, they were less spotty or corrupted by artifacts.

4.1.3 Summary

The RDM differences were found to be more significant compared to MAG. Thus, in the case of RDM, the modeling accuracy increased along with the number of ele-

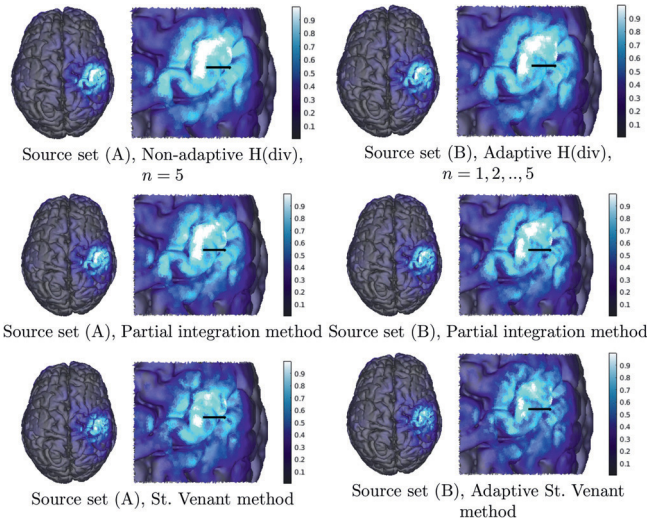

Figure 4.3 An illustration of the l^2 regularized estimates obtained in study I, showing a comparison between the outcome obtained with the H(div), SV and PI source models in *non-adaptive* and *adaptive* cases. The synthetic source is visualized in black.

ments included in the stencil. Moreover, the results obtained with the single-element stencil, emerged to be similar to the PI, suggesting that H(div) and PI approach might yield identical results in that case. A remarkable difference to SV was observed for 99% eccentricity. Based on the results presented in this study, *non-adaptive* H(div) source model is more robust compared to *adaptive* case and preferable to be applied for normal cortical thickness [38, 49, 77], albeit the *adaptive* case can be considered for thinner cortices, namely, in children or infant studies and pathological applications.

Limitations and weaknesses

The findings of this study have to be seen in light of some limitations. The first limitation concerns with the performance of H(div) model with anisotropic head model since the electrical conductivity of the white matter affects the source position and orientation and correspondingly influences the accuracy of H(div) source modeling. The second limitation is the implementation of H(div), which is currently available as C++ code package via *dunero* software [1] library of DUNE. The implementation can be extended to a pipeline between DUNE and other platforms such as MATLAB or Python [2].

[1] `http://duneuro.org/`
[2] `https://www.python.org/`

Outlook

As a future study, divergence conforming H(div) source modeling can be applied on a realistic and multicompartment human head model utilizing real EEG measurements. To assess the performance of the present source modeling, other physiological criteria such as thin cortices, especially in children and anisotropic head model can be investigated. Furthermore, the H(div) source modeling implementation can be integrated with other commonly used toolboxes such as FieldTrip or Brainstorm.

4.2 Outline of study II

Motivation & Goal

This study aims to introduce a platform, where advanced and complex forward and inverse techniques are combined for source localization of brain imaging applications. Zeffiro Interface (ZI) is applicable to realistic and multicompartment head models.

Approach

The ZI is an openly available MATLAB-based code package [3] which utilizes graphics processing unit (GPU) acceleration, i.e., parallelization, to minimize the computation time needed in the FE mesh and lead field generation as well as in interpolation and source localization processes. As part of the ZI package (Appendix B and C), FreeSurfer to ZI segmentation pipeline, which is described in section 3.2.1 is developed to enable importing the brain segmentation to ZI.

4.2.1 Overall results

In order to validate the functionality of ZI, inversion tests were conducted using Brainstorm's EEG and epilepsy dataset (with a consent of Prof. Andreas Schulze-Bonhage, Feiburg, Germany) and simulated EIT datasets concerning the localization of a hemorrhage. A high resolution (1 mm) mesh was generated and employed for reconstructing the activity. Our findings revealed that the reconstructed activity for the epilepsy dataset is in agreement with the results of Brainstorm software and ZI is applicable to multilayered and realistic head models. The EIT experiment

[3] `https://www.mathworks.com/matlabcentral/fileexchange/68285-zeffiro-forward-and-inverse-interface-for-brain-imaging`

successfully localized the hemorrhage.

4.2.2 Results in detail

Figure 4.4 demonstrates the reconstruction of the brain activity with IG hyperprior for Brainstorm's EEG and epilepsy tutorial dataset. The surface visualization confirms the similarity of the reconstructed activity shown in the tutorial. IG hyperprior found more focal and accurate activity compared to G. In addition to the surface visualization, volume cut visualization was obtained to illustrate the depth of the reconstructed activity, Figure 4.4. Our analysis showed that a realistic and multicompartment human head model can be utilized in ZI and a similar result with Brainstorm could be obtained in the case of the tutorial dataset. With GPU acceleration, the computing time required by the different stages of forward modeling and localizing the brain activity was found to be around one hour.

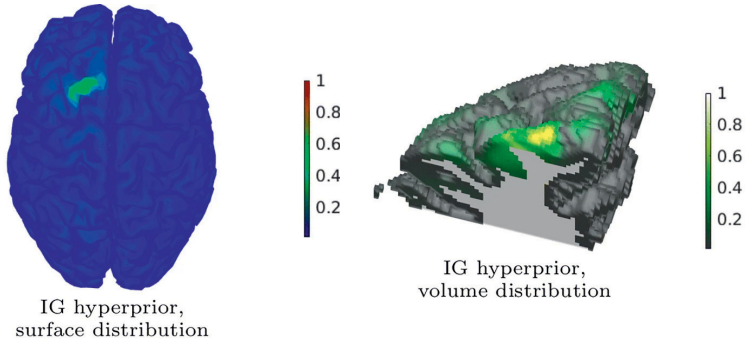

Figure 4.4 Surface and volume visualization of reconstructed brain activity by IG hypermodels. *Left:* the surface reconstruction of brain activity on grey matter. *Right:* illustration of cutted volumetric reconstruction for IG hyperpriors. The color bars show the amplitude strength with normalization to one.

In addition to the EEG analysis, EIT inversion test was conducted to localize a synthetic hemorrhage to show ZI's potential adaptability to EIT. Averaging reconstruction for randomized source spaces sharing a single resolution was observed to improve the result compared to the case of a single source space, which is demonstrated in Figure 4.5. This result was expected as averaging over multiple resolutions that can be interpreted to marginalize the discretization error compared to the non-averaged case. It also suggests that the RAMUS method might be used not only for EEG/MEG but also for other electromagnetic inverse imaging applications such as

EIT.

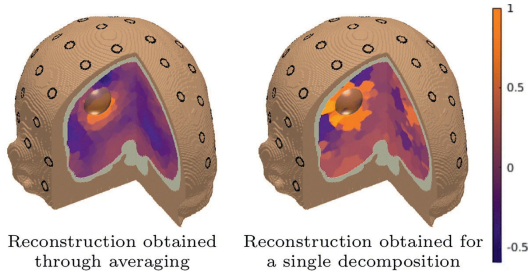

Figure 4.5 Visualization of an EIT reconstruction obtained for a synthetic conductivity distribuion including a hemorrhage. A population head model with 72 CEM electrodes were employed in the inversion test. A 30 mm diameter sphere as ROI is determined for hemorrhage. *Left:* An average reconstruction obtained using the IAS MAP multiresolution inverse tool and multiple discretizations of the piecewise constant approximation for the conductivity. *Right:* A widespread reconstruction for non-averaged case which has been obtained using a single decomposition. The color bars shows the amplitude strength with normalization to one.

4.2.3 Summary

The core finding of this study was that advanced multicompartment head models can be generated and processed using the H(div) forward and HBM source localization approaches of this study together with GPU acceleration, and that sufficiently short computing times can be achieved with respect to the potential clinical applications of the present methodology. The inversion results suggest that the pipeline is valid and performs appropriately with respect to both accuracy and computational efficiency. The multicompartment processing is enabled by the FE approach applied in ZI. It allows a flexible usage and combination of the forward and inverse techniques as well as the adaptation and adjustment of the conductivity values and activity of different parts of the brain not only in the case of EEG and MEG but also in other applications such as in EIT, potentially in a combined fashion, where two or more inverse imaging modalities are used simultaneously. In particular, for this work, the introduction of the ZI was a crucial step, which enabled using the forward approach introduced in study I in the development of source localization methods which constituted the latter part, i.e., studies III–V.

Limitations and Weaknesses

This study, however, is subjected to some limitations. Firstly, the current version

of ZI can generate mesh for the isotropic head model, while mesh generation routine can also be developed for anisotropic model including the white matter electrical conductivity. Secondly, ZI is limited to FreeSurfer atlases, i.e., Desikan-killiany and Destrieux, however, further anatomical atlases can be imported to ZI to improve connectivity analysis.

Outlook

As a future study, further investigations would be required to validate ZI for various experimental measurements and clinical applications. As a potential topic, the mesh generation routine in ZI can be extended to create anisotropic model from diffusion tensor imaging (DTI) data. Furthermore, the inversion techniques coupled to ZI can be improved for more robust source localization, particularly for the subcortical domain. Developing sampling-based posterior exploration techniques, e.g., the Gibbs sampler for HBM inverse solver can be also taken as a future work for source localization in ZI.

4.3 Outline of study III

Motivation & Goal

This research work aims to propose an advanced inverse modeling technique, i.e., the randomized multiresolution scanning (RAMUS) method. RAMUS is based on (i) multiresolution concept for localizing active sources within different layers of the brain and to minimize the depth bias for final reconstruction, and (ii) randomizing the source space to marginalize the discretization and optimization errors and, thereby, to enhance the reconstruction quality obtained at each resolution level. RAMUS associates with sparse source space which plays a significant role in distinguishing weak subcortical activity.

Approach

RAMUS utilizes the IAS MAP estimation technique to detect the cortical and weakly distinguishable subcortical activity for a given resolution and source space. Herein, numerical experiments for the spherical model are conducted to evaluate the performance of RAMUS for superficial and deep source localization.

4.3.1 Overall results

We found RAMUS as an efficient and robust source localization technique, as it corrects the inaccuracies of depth bias, otherwise present in the MAP estimates, via the multiresolution technique, especially, for localizing deep-lying sources far away from the sensors' locations. The numerical results obtained with a spherical model show that a sparse source space and a coarse-to-fine progression over multiple resolution levels play a significant role in the challenging task of detecting the deep activity.

The findings reveal that, when RAMUS is equipped with the IG hyperprior, it can distinguish both superficial and deep activity, whereas, with G hyperprior it tends to be biased towards superficial activity. Furthermore, classical minimum norm estimate (MNE) technique was compared with RAMUS. The results demonstrate that MNE has a greater tendency towards superficial sources and, therefore, it did not distinguish appropriately the deep activity. The sparsity factor, i.e., the ratio of the source counts between two subsequent levels, was observed to be one of the key factors affecting the performance of RAMUS. Of the two values of the sparsity factor, 8 and 5, the former one was found to be favorable in finding the deep activity. Additionally, we applied RAMUS method to a realistic head model, e.g., population head model (PHM) using two synthetic sources with respect to superficial and thalamic activity. RAMUS was found to reconstruct both superficial and simultaneous deep activity for the realistic and multilayered head model.

4.3.2 Results in detail

Figure 4.6 shows the numerical analyses for spherical Ary model, where the reconstructed sources (purple) are depicted with respect to the actual/synthetic sources (red) for the superficial and deep layers. As can be observed from the results, RAMUS technique with IG hyperprior could detect the activity for both superficial and deep sources. The findings pointed out that utilizing G hyperprior is not beneficial for localizing deep-lying sources, while the active superficial sources can be detected and the position and orientation of the reconstructed sources are in line with the actual ones, particularly, in the superficial case. Additionally, we implemented MNE approach to compare the results with the performance of RAMUS technique. MNE did not detect the deep activity and the reconstructed source was relatively deviated

from the actual one, Figure 4.6.

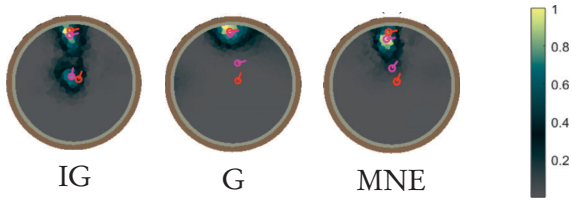

Figure 4.6 Visualization of numerical experiments on spherical model. Each visualization corresponds to two sources, i.e., the actual one (red) and center of mass of the reconstruction (purple) within ROI for superficial and deep area. *Left:* A reconstruction obtained with IG hyperprior. *Center:* A reconstruction obtained with G hyperprior. *Right:* A reconstruction obtained with MNE as the source localization approach.

The accuracy of RAMUS reconstructions for the cases in Figure 4.6 is shown in Figure 4.7 via histograms with respect to the position (mm), orientation (deg), amplitude, and the relative maximum of the current density corresponding to the global maximum which refers to a measure for the detectability of the source within the ROI. In the case of IG hyperprior reconstruction, the accuracy for superficial sources is a median of 8 mm for positioning accuracy, angle difference of 4.5° and logarithmic (basis log10) relative amplitude error -0.25, i.e., the amplitude of the reconstructed source is 56% of the actual source. For deep source reconstruction, the positioning, orientation, and amplitude accuracy found to be 15 mm, 12°, -0.65 (22% amplitude), respectively. Additionally, about 50% of the global reconstruction in median is obtained for deep source. The histogram results for G hyperprior and MNE approach are in line with reconstruction's results, in which both cases were successful to distinguish only the superficial sources.

4.3.3 Summary

This study formulated and analyzed the RAMUS method and showed its capability to localize both superficial and deep activity simultaneously. Our findings suggest that the multiresolution approach is necessary following from the enhanced detectability of deep sources at lower resolution levels. Namely, the deep activity component was found only when a sufficiently sparse source space, with dimension comparable to the number of data entries, i.e., in a case where the lead field matrix has a trivial or low-dimensional null-space, was present in the reconstruction process.

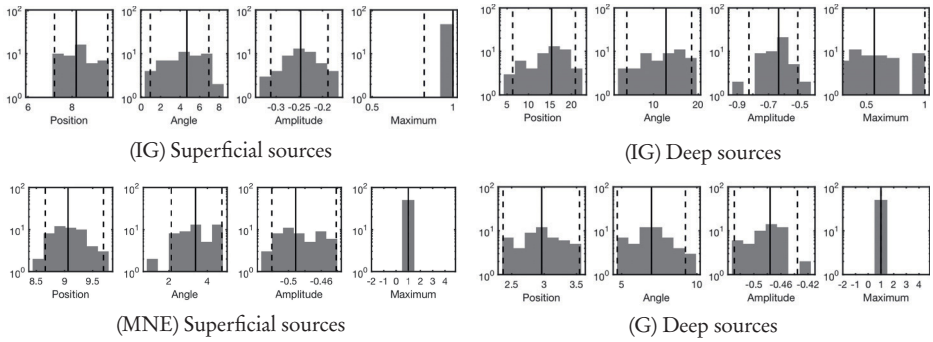

Figure 4.7 Histogram illustrations of numerical analysis depicted in Figure 4.6 for cases of IG and G hyperpriors and MNE approach. The histograms show the accuracy of RAMUS reconstructions with respect to the source position (mm), angle (°), amplitude, and relative maximum of the source within the ROI with respect to the global maximum for both superficial and deep sources.

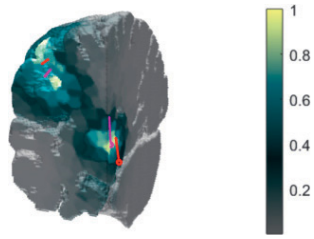

Figure 4.8 The illustration of reconstructed primary current distribution on population head model (PHM). A realistic and multicompartment head model is employed for numerical modeling of superficial source, namely, somatosensory P20/N20 and deep source for thalamic activity.

Figure 4.8 shows that RAMUS was found to be applicable to a realistic and multilayered head model, i.e., PHM, where superficial activity for P20/N20 component and simultaneous deep activity were found to be visible.

Limitations & Weaknesses

The results of this study were obtained with a certain range of scale and shape parameter values to reconstruct focal activity, however, the deep activity was not distinguished properly for the values outside the suggested range of parameters. Furthermore, the numerical analysis with the realistic head model, PHM, is only concerned with simultaneous superficial and deep activity for simulated P14/N14 and P20/N20 sources.

Outlook

As a future work, RAMUS can be applied to real datasets, namely, the somatosen-

sory evoked potential (SEP) of median nerve stimulation to reconstruct the P20/N20 component at Brodmann area 3b and simultaneous deep activity at the thalamus corresponding P14/N14 component. A comparison of RAMUS with other inverse modeling techniques would be of paramount importance, particularly for deep brain source localization. Additionally, deeper investigation of the hyperprior decomposition parameters and finding further approaches for updating the initial guess for the IAS MAP estimation technique would be vital to obtain the focal reconstruction.

4.4 Outline of study IV

Motivation & Goal

This study introduced prior-over-measurement signal-to-noise ratio (PM-SNR) model (section 3.1.6) to improve the performance of the HBM for source localization via finding the appropriate prior weight with respect to the noise level.

Approach

PM-SNR is determined by the G or IG hyperprior; given the shape parameter β, it can be associated with the value of the scale parameter θ_0. In this study, we concentrated on selecting θ_0 with the shape parameter fixed to $\beta = 3$, which was shown to constitute an approximative balance point, where G and IG hyperprior perform similarly. PM-SNR was defined as the square-root of the total scale, i.e., θ_0 multiplied by the number of source positions in the model. PM-SNR was interpreted as a measure of latent error sources, e.g., modeling errors and algorithm inaccuracy, the presence of which necessitates increasing the prior strength with respect to the observed error level.

4.4.1 Overall results

We utilized SEP and SEF measurements to investigate the applicability and accuracy of HBM when the scale parameter was selected based on the PM-SNR. In the experiments, our goal was to detect the cortical and subcortical originator of the P20/N20 component located in the Brodmann area 3b and ventral posterolateral (VPL) thalamus (Figure 4.10), respectively. Both synthetic and experimental EEG and MEG measurement data were used. The MAP and CM estimates were evaluated via the IAS MAP iteration and an MCMC sampler, respectively. Additionally, the classical

MNE and MCE approaches were used as alternative reconstruction techniques.

4.4.2 Results in detail

The findings revealed that both MAP and CM estimates with selected set of parameters can reconstruct the generator of P20/N20 component at the posterior bank of the central sulcus. Figure 4.9 illustrates the MAP estimation results in the case of SEP and SEF. The scale parameters applied in the experiments (from $\theta_0 = 1E-12$ to $\theta_0 = 1E-8$) followed roughly our PM-SNR model regarding, both synthetic and experimental data, the number of source positions N, the default level of Brainstorm software's MNE solver, and the estimated latent method-related and modeling errors.

An important finding was that the scale parameter predicted via PM-SNR was appropriate for both the dense and sparse model applied in reconstructing the cortical and subcortical originator of the P20/N20 component. The MCMC sampler allowed for a lower PM-SNR than the IAS MAP iteration, which was interpreted to be due to reduced latent errors in the reconstruction process, i.e., the sampling technique is more accurate than the gradient-based IAS technique. Especially, in the case of synthetic data, the sampling process was successfully performed with 0 dB PM-SNR, reflecting the comparably small latent errors of the synthetic data generation process. The results concerning the scale parameter value also generally matched appropriately with our previous experience and results [59, 101].

MNE and MCE estimates resulted in less intense source localization estimates compared to those obtained with HBM. In particular, the deep activity in the thalamus was weak with MCE. As MNE corresponds to the first step of the iteration and MCE to the estimate obtained with G prior and $\beta = 1.5$, they can be interpreted as special cases of HBM, and hence the results highlight the importance of performing complete IAS MAP process and the proposed balancing of the shape parameter. Namely, with the choice $\beta = 1.5$, the maximum of the conditional posterior for the hyperparameter $\theta_i^{(j+1)}$, found in the third step of the IAS algorithm (section 3.1.5.3) corresponds to zero, if $x_i^{(j)} = 0$, explaining the vanishing of the deep or weak activity in the case of MCE. When the proposed balancing between G and IG is applied, i.e., $\beta = 3$, the maximum is greater than zero, thus preventing the suppression of the weak components. To further confirm the validity of our PM-SNR model, we ana-

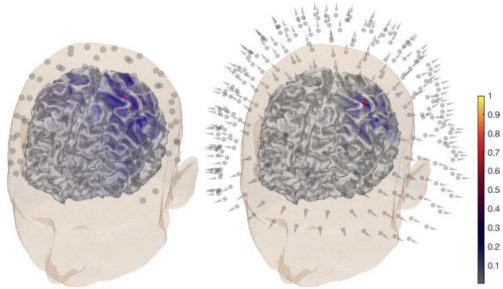

Figure 4.9 An illustration of MAP estimate for SEP and SEF dataset. *Left:* The reconstructed activity for P20/N20 component at posterior wall of the central sulcus with 72 EEG electrodes attached on the scalp. *Right:* A visualization of the P20/N20 activity for MEG and with 271 magnetometers.

lyzed the measurements for two more subjects to show the inter-subject variability of the analysis with respect to the proposed parameterization. The source localization outcome of this additional analysis was found to be appropriate but somewhat less well-localized, which was deemed to be rather due to aspects related to the head model generation and the measurement process than to the mathematical model *per se*. That is, the accuracy was not significantly improved by any parameter choice.

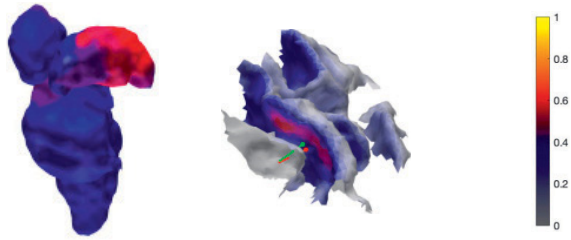

Figure 4.10 Visualization of MAP estimation results obtained with G hyperprior, EEG data and 1 mm FE mesh. The reconstruction was observed to detect the activity corresponding to the P20/N20 component in Brodmann area 3b, i.e., in the posterior wall of the central sulcus. The red pin refers to the reference point and green one shows the center of the reconstruction. The deep activity in the VPL thalamus is reconstructed by employing a sparse source space.

4.4.3 Summary

The activity for both superficial and deep areas corresponding to the P20/N20 component was reconstructed accordingly via HBM together with the parametrization approach and PM-SNR model proposed in this study. Based on the results, we could

motivate a robust and nearly resolution-independent approach for predicting the hyperprior of the IAS MAP iteration, and show that, with the parameters predicted by the PM-SNR model, this iteration can perform well in comparison to the classical MNE and MCE techniques in source localization. Our findings are significant regarding the potential future development of source localization techniques, where a single solver might be utilized at multiple resolution levels, which is the case, e.g., in the RAMUS technique.

Limitations & Weaknesses

The results of this study remain as a proof-of-concept, in which, an estimated range of parameters are potentially applicable for the SEP and SEF applications. Furthermore, the model for hyperprior parametrazation is only focused on CG-HBM as a reconstruction technique.

Outlook

As a future application, the proposed model for hyperprior parametrezation can be applied to more and different types of dataset, e.g., auditory evoked responses [86] or combined E/MEG. From the mathematical perspective, further developments toward source localization techniques for multiple resolution levels would also be essential.

4.5 Outline of study V

Motivation & Goal

In this study, we aim at investigating the performance of RAMUS to analyze the network of SEP components including simultaneous cortical and subcortical activity at different latencies between 14–30 ms for three adult subjects. Our goal was to confirm the numerical results of study III experimentally, to perform a more comprehensive analysis of finding the deep activity, and reconstructing a complete network of consecutive SEP components.

Approach

Herein, RAMUS (subsection 3.1.5.6) is applied to detect both cortical and subcortical activity [101] utilizing a realistic and multicompartment head model and experimental applications, i.e., median nerve stimulation.

4.5.1 Overall results

Akin to study IV, the head models included an accurate segmentation of the subcortical layers, obtained via FreeSurfer's Aseg atlas, in order to achieve the best possible forward modeling and source localization accuracy. Our analysis covered altogether three subjects.

The originators of the early SEP responses P14/N14, P16/N16, P18/ N18, P20/ N20, P22/N22, and P30/N30 which are investigated in this study, have been covered, e.g., in [22, 23, 24, 29, 75, 82, 87, 90, 121]. Of these responses, we especially concentrated on P14/N14 and P20/N20, i.e., the earliest components of subcortical and cortical activity, respectively, as similar cases were already analyzed numerically in study III, and as the literature availability for those is comparably wide.

The results demonstrate that the generator of the P14/N14 component stems mainly from the medial lemniscus of brainstem, where the afferent volley travels towards the thalamus. The cortical surface included a weak projection, which might be due to the preceding ongoing trials during the stimulation process. The reconstructed activity for P20/N20 component was found to be simultaneously concentrated at the Brodmann area 3b and VPL thalamus. The other reconstructed components were found to reflect the movement of the afferent volley upwards from the brainstem to the cortex.

The MNE and MNE-RAMUS were used as alternative reconstruction techniques. The MNE reconstruction is obtained as a single step of IAS and MNE-RAMUS refers to multiresolution implementation of RAMUS and using MNE instead of IAS as the optimization technique. MNE did not find the deep activity, whereas MNE-RAMUS could distinguish it appropriately for P14/N14. However, for P20/N20 component, the deep activity obtained with MNE-RAMUS is more distributed over the thalamic region compared to RAMUS.

4.5.2 Results in detail

The consecutive SEP components P14/N14, P16/N16, P18/N18, P20/N20, P22/ N22, and P30/N30 were analyzed for three different subjects in this study. The experimental data for subject (I) is openly available at the Zenodo portal [93]. Herein, the results for subject (I) are presented and highlight the P14/N14 and P20/N20

components as early responses for subcortical and cortical activity, respectively.

As can be seen in Figure 4.11, RAMUS found strong activity for deep structures, i.e., brainstem and thalamus for early P14/N14 component. In particular, deep activity mirrors afferent volley travelling along medial lemniscus to the thalamus. In addition to the deep activity, a weak projection was detected on cortical surface, notably, at parietal lobe for P14/N14. The cortical projection might occur due to the ongoing processing of the preceding trial even when trying to reduce phase-locking by means of the randomization of the inter-stimulus interval when the stimulation is still going on with later trials.

The generator of P20/N20 component was detected at Brodmann area 3b. Moreover, RAMUS distinguished simultaneous subcortical activity at contralateral VPL thalamus at 20 ms. The findings for MNE and MNE-RAMUS are demonstrated in Figure 4.11. As can be observed, MNE was not very favourable to reconstruct the deep activity for both P14/N14 and P20/N20 originators, while MNE-RAMUS could reconstruct the activity with respect to the P14/N14 and P20/N20 components at the subcortical region. The reconstructed subcortical activity by MNE-RAMUS was found to be distributed widely over thalamus and not very focal compared to RAMUS technique.

Figure 4.12 demonstrates the RAMUS reconstructions for sequential early components P16/N16, P18/N18 and late components, i.e., P22/N22 and P30/N30. At 16 ms, the activity is mainly concentrated at subcortical domain. The activity stems from lower medulla, i.e., cuneate nucleus and also it was detected at anterior and ventral thalamus. At 18 ms, the activity found to be relatively widespread at brainstem where stronger amplitude was distinguished at lower medulla, i.e., dorsal column to VPL thalamus. Correspondingly, for P18/N18 component, weak cortical projection was distinguished at occipital lobe, assumably, due to the measurement or stimulation uncertainties.

Following that, the cortical activity for P22/N22 is reconstructed at the crown of postcentral gyrus and simultaneous deep activity found to be at VPL thalamus. At 30 ms, cortical activity was reconstructed more distributed, particularly towards frontal lobe (BA4 and BA6). Simultaneously, subcortical activity was found to be more concentrated at left VPL thalamus. As a potential application for RAMUS performance, the activity was reconstructed for the simulated source at superiortemporal gyrus corresponding auditory evoked responses and following subcortical ac-

tivity at inferior colliculus, Figure 4.13.

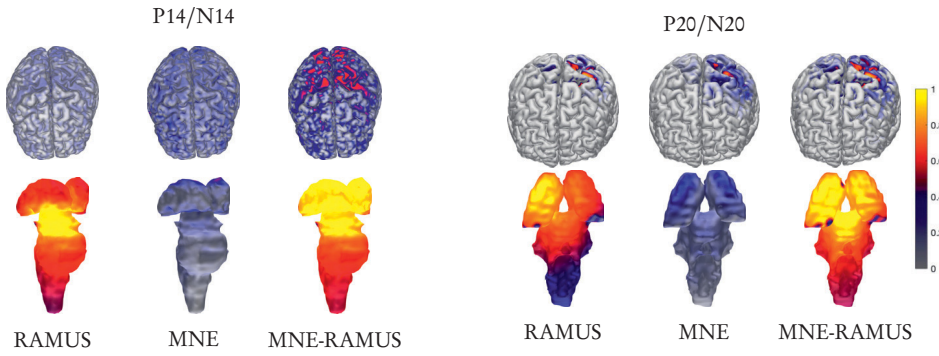

Figure 4.11 Illustration of reconstructed cortical and subcortical activity for P14/N14 and P20/N20 components. The results obtained via RAMUS, MNE, and MNE-RAMUS, the last one incorporates with MNE instead of the IAS as an optimization algorithm.

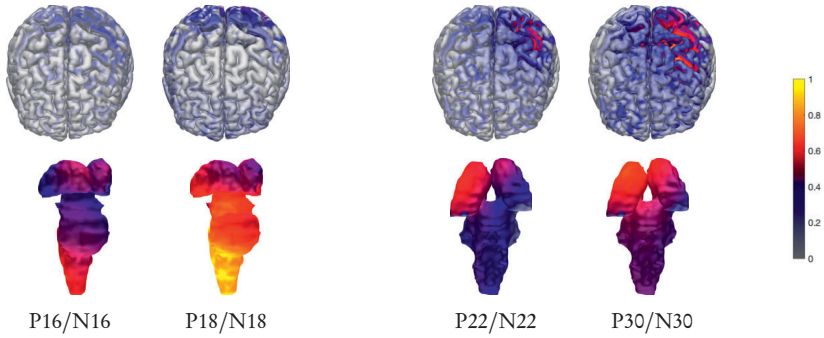

Figure 4.12 Visualization of reconstructed cortical and subcortical activity via RAMUS for earlier latencies of SEP measurement, i.e., 16 and 18 ms and late latencies which occur after 20 ms, i.e., 22 and 30 ms. The cortex is visualized from frontal view and subcortical domain is demonstrated from lateral and posterior view for early and late component, respectively. The color bar demonstrates the maximum amplitude normalized to 1 with respect to the reconstructed activity.

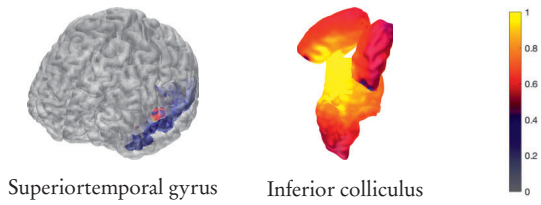

Figure 4.13 Visualization of simulated reconstructed activity for auditory steady-state responses (ASSR) via RAMUS at superior temporal gyrus and simultaneous activity at *inferior colliculus*.

4.5.3 Summary

The findings demonstrate that RAMUS [101] is a potential approach for reconstructing both cortical and weakly distinguishable activity in experimental studies utilizing realistic head models with subcortical structures. The results showed that the multiresolution and randomized decomposition properties of RAMUS play a significant role in detecting the activity at different depths, i.e., cortical and subcortical domain. In particular, RAMUS could detect the far-field activity at medial lemniscus at 14 ms and reconstruct the originator of evoked responses at 20 ms for both cortical and simultaneous subcortical activity. Results obtained with three subjects confirm the findings. Of these, the superior outcome was obtained in subject (I), while subjects (II) and (III) show some signs of lower reconstruction accuracy, for example, a significant cortical projection prior to 20 ms, which was deemed to be due to a somewhat lower pre-processing quality, measurement error, or remaining phase-locking to the preceding trial.

Limitations & Weaknesses

The results in this study show the performance of RAMUS for SEP application. Further analysis would be necessary to present the performance of RAMUS in a wider scope, i.e., utilizing different measurements. The focality and accuracy of the RAMUS is case-specific due to the complexity of brain and source configuration, and it also depends on the multiresolution decomposition or the optimization method used in RAMUS.

Outlook

Together these results also motivate the potential use of RAMUS for more datasets or in other modalities such as MEG or combined E/MEG or with other evoked measurements, e.g., auditory evoked field (AEF) analysis, ASSRs [86]. Another future direction would be investigating the role of cerebellum in median nerve stimulation [3, 117], especially, in analysis of somatosensory networks.

5 CONCLUSIONS

The studies conducted in this thesis focused on combining advanced forward and inverse solvers as a platform to reconstruct the primary current density of neural activity from the strongly folded tissues of the brain. The work sheds light on developing an accurate FEM-based H(div) forward model [79] for realistic and multicompartment human head model to estimate the electric and magnetic field of the brain activity. It shows how to interface a GPU-accelerated and multicompartment FEM forward solver with inverse algorithms, and how to effectively utilize such a combination in the inversion process via multiple resolution levels and the RAMUS method. The Zeffiro Interface (ZI) [59] was created during this study and enhances detecting cortical and subcortical activity [67, 105], particularly, via the combination of the multicompartment architecture of the solver and the multiresolution [72] approach introduced for source localization. This is scientifically important and timely, since the deep activity has recently been suggested to be distinguishable from non-invasive measurements [95, 109]. Furthermore, by establishing a pipeline between the FreeSurfer software suite and ZI, an advanced head segmentation can be imported to ZI. The segmentation includes an accurate cortical parcellation and atlas of the subcortical structures, and, thereby, enabled the experimental analysis of EEG and MEG data. An important enabling step towards this experimental analysis was provided by the concept of PM-SNR [100] which was found to provide a robust and nearly resolution-independent way for selecting the hyperprior for the conditionally Gaussian HBM.

The following outcomes were obtained in this work:

- The FEM-based approach was found to be advantageous for complex and multicompartment head models with variable cortical thickness, making it attractive for subjects belonging to any age group. Namely, the H(div) model allows using adaptive stencils, which are applicable to thin cortices, e.g., in children.
- The computational cost of the forward solver was tackled using GPU-acceleration,

which allows generating a FE mesh, running the forward simulation and interpolating it for a high 1 mm resolution [103] within an hour which makes the forward solver flexibly applicable in experimental analysis.

- ZI was equipped with a pipeline for importing a head segmentation which is created by the FreeSurfer software suite based on MRI data, including a cortical parcellation and subcortical atlas. The multicompartment architecture of ZI allows creating an arbitrary number of compartments which together with the segmentation provides grounds for accurate analysis, where the type of the activity within the volumetric FEM-based approach of ZI was found to enable the lead field creation for EIT, in which, the unknown is a scalar conductivity distribution inside the head. This shows that ZI is a potential platform for a wider variety of imaging modalities.
- The utilization of ZI with experimental data showed that it can be successfully used with realistic head models and studies including multiple subjects.
- Built upon ZI's FEM-based routines, the RAMUS (randomized multiresolution scanning) [101] source localization approach was found to localize both cortical and subcortical activity, which was shown both with numerically simulated and experimental measurement data. The analysis of RAMUS technique has provided deeper insights into source localization, in particular, to avoid depth bias via averaging the noise over multiple resolution levels and randomized decompositions.
- The PM-SNR model was found to be an important concept for selecting the G or IG hyperprior for the conditionally Gaussian HBM model and, in particular, the IAS MAP estimation routine and RAMUS. It was found to be nearly resolution-independent in the experiments and, thereby, multiresolution processes can be potentially assisted with the PM-SNR concept.

The results of this work motivate many numerical and experimental future research directions. The findings were found to be promising to consider RAMUS method for motivating further research on developing RAMUS as a source localization technique, for example, investigating the possibilities to improve the structure and implementation of the multiresolution decomposition, to use a similar approach with a variety of source localization methods as motivated by the improved outcome of RAMUS vs. IAS and MNE-RAMUS vs. MNE [52], or to compare the performance

of RAMUS with classical source localization methods such as, beamformer [110] or sLORETA [89], which are extensively utilized in deep source localization. An important future work would be to advance the experimental research on different evoked measurements, namely, auditory evoked responses, e.g., auditory steady-state responses (ASSRs)[86], and combined E/MEG modality. The potential of ZI to create and merge forward models or lead field matrices for different modalities might be investigated further.

REFERENCES

[1] M. Ainsworth and J. Coyle. Hierarchic finite element bases on unstructured tetrahedral meshes. *International journal for numerical methods in engineering* 58.14 (2003), 2103–2130.

[2] T. Allison, C. C. Wood, G. McCarthy and D. D. Spencer. Cortical somatosensory evoked potentials. II. Effects of excision of somatosensory or motor cortex in humans and monkeys. *Journal of neurophysiology* 66.1 (1991), 64–82.

[3] L. M. Andersen, K. Jerbi and S. S. Dalal. Can EEG and MEG detect signals from the human cerebellum?: *NeuroImage* (2020), 116817.

[4] C. Andrieu, N. De Freitas, A. Doucet and M. I. Jordan. An introduction to MCMC for machine learning. *Machine learning* 50.1 (2003), 5–43.

[5] M. Antonakakis, S. Rampp, C. Kellinghaus, C. H. Wolters and G. Moeddel. Individualized Targeting and Optimization of Multi-channel Transcranial Direct Current Stimulation in Drug-Resistant Epilepsy. *BIBE*. 2019, 871–876.

[6] M. Antonakakis, S. Schrader, A. Wollbrink, R. Oostenveld, S. Rampp, J. Haueisen and C. H. Wolters. The effect of stimulation type, head modeling, and combined EEG and MEG on the source reconstruction of the somatosensory P20/N20 component. *Human brain mapping* 40.17 (2019), 5011–5028.

[7] J. P. Ary, S. A. Klein and D. H. Fender. Location of sources of evoked scalp potentials: corrections for skull and scalp thicknesses. *IEEE Transactions on Biomedical Engineering* 6 (1981), 447–452.

[8] Y. Attal, B. Maess, A. Friederici and O. David. Head models and dynamic causal modeling of subcortical activity using magnetoencephalographic/electroencephalographic data. (2012).

[9] Y. Attal and D. Schwartz. Assessment of subcortical source localization using deep brain activity imaging model with minimum norm operators: a MEG study. *PLoS One* 8.3 (2013), e59856.

[10] Ü. Aydin, S. Rampp, A. Wollbrink, H. Kugel, J.-H. Cho, T. R. Knösche, C. Grova, J. Wellmer and C. Wolters. Zoomed MRI guided by combined EEG/MEG source analysis: a multimodal approach for optimizing presurgical epilepsy work-up and its application in a multi-focal epilepsy patient case study. *Brain topography* 30.4 (2017), 417–433.

[11] Ü. Aydin, J. Vorwerk, M. Dümpelmann, P. Küpper, H. Kugel, M. Heers, J. Wellmer, C. Kellinghaus, J. Haueisen, S. Rampp et al. Combined EEG/MEG can outperform single modality EEG or MEG source reconstruction in presurgical epilepsy diagnosis. *PloS one* 10.3 (2015), e0118753.

[12] S. Baillet, J. C. Mosher and R. M. Leahy. Electromagnetic brain mapping. *IEEE Signal processing magazine* 18.6 (2001), 14–30.

[13] M. Bauer, S. Pursiainen, J. Vorwerk, H. Köstler and C. H. Wolters. Comparison study for whitney (raviart–thomas)-type source models in finite-element-method-based eeg forward modeling. *IEEE Transactions on Biomedical Engineering* 62.11 (2015), 2648–2656.

[14] M. Bear, B. Connors and M. A. Paradiso. *Neuroscience: Exploring the brain*. Jones & Bartlett Learning, LLC, 2020.

[15] G. G. Berntson and J. T. Cacioppo. *Handbook of Neuroscience for the Behavioral Sciences, Volume 2*. Vol. 2. John Wiley & Sons, 2009.

[16] E. Bingham and H. Mannila. Random projection in dimensionality reduction: applications to image and text data. *Proceedings of the seventh ACM SIGKDD international conference on Knowledge discovery and data mining*. 2001, 245–250.

[17] C. M. Bishop. *Pattern recognition and machine learning*. springer, 2006.

[18] S. Bjerknes, I. M. Skogseid, T. J. Hauge, E. Dietrichs and M. Toft. Subthalamic deep brain stimulation improves sleep and excessive sweating in Parkinson's disease. *NPJ Parkinson's disease* 6.1 (2020), 1–7.

[19] P. S. Boggio, R. Ferrucci, F. Mameli, D. Martins, O. Martins, M. Vergari, L. Tadini, E. Scarpini, F. Fregni and A. Priori. Prolonged visual memory enhancement after direct current stimulation in Alzheimer's disease. *Brain stimulation* 5.3 (2012), 223–230.

[20] D. Braess. *Finite elements: Theory, fast solvers, and applications in solid mechanics*. Cambridge University Press, 2007.

[21] R. Brette and A. Destexhe. *Handbook of neural activity measurement*. Cambridge University Press, 2012.

[22] H. Buchner, T. Waberski, M. Fuchs, H.-A. Wischmann, R. Beckmann and A. Rienäcker. Origin of P16 median nerve SEP component identified by dipole source analysis—subthalamic or within the thalamo-cortical radiation?: *Experimental brain research* 104.3 (1995), 511–518.

[23] H. Buchner, L. Adams, A. Müller, I. Ludwig, A. Knepper, A. Thron, K. Niemann and M. Scherg. Somatotopy of human hand somatosensory cortex revealed by dipole source analysis of early somatosensory evoked potentials and 3D-NMR tomography. *Electroencephalography and Clinical Neurophysiology/Evoked Potentials Section* 96.2 (1995), 121–134.

[24] H. Buchner, M. Fuchs, H.-A. Wischmann, O. Dössel, I. Ludwig, A. Knepper and P. Berg. Source analysis of median nerve and finger stimulated somatosensory evoked potentials: multichannel simultaneous recording of electric and magnetic fields combined with 3D-MR tomography. *Brain topography* 6.4 (1994), 299–310.

[25] H. Buchner, G. Knoll, M. Fuchs, A. Rienäcker, R. Beckmann, M. Wagner, J. Silny and J. Pesch. Inverse localization of electric dipole current sources in finite element models of the human head. *Electroencephalography and clinical Neurophysiology* 102.4 (1997), 267–278.

[26] D. Calvetti, H. Hakula, S. Pursiainen and E. Somersalo. Conditionally Gaussian hypermodels for cerebral source localization. *SIAM Journal on Imaging Sciences* 2.3 (2009), 879–909.

[27] D. Calvetti, A. Pascarella, F. Pitolli, E. Somersalo and B. Vantaggi. Brain activity mapping from meg data via a hierarchical bayesian algorithm with automatic depth weighting. *Brain topography* 32.3 (2019), 363–393.

[28] C. Campi, A. Pascarella and F. Pitolli. Less Is Enough: Assessment of the Random Sampling Method for the Analysis of Magnetoencephalography (MEG) Data. *Mathematical and Computational Applications* 24.4 (2019), 98.

[29] A.-M. Cebolla, E. Palmero-Soler, B. Dan and G. Chéron. Frontal phasic and oscillatory generators of the N30 somatosensory evoked potential. *NeuroImage* 54.2 (2011), 1297–1306.

[30] G. Chéron, T. Piette, A. Thiriaux, J. Jacquy and E. Godaux. Somatosensory evoked potentials at rest and during movement in Parkinson's disease: evidence for a specific apomorphine effect on the frontal N30 wave. *Electroencephalography and Clinical Neurophysiology/Evoked Potentials Section* 92.6 (1994), 491–501.

[31] J.-A. Chevalier, A. Gramfort, J. Salmon and B. Thirion. Statistical control for spatio-temporal MEG/EEG source imaging with desparsified multi-task Lasso. *arXiv preprint arXiv:2009.14310* (2020).

[32] M. Clay and T. C. Ferree. Weighted regularization in electrical impedance tomography with applications to acute cerebral stroke. *IEEE Transactions on Medical Imaging* 21.6 (2002), 629–637.

[33] O. D. Creutzfeldt, G. H. Fromm and H. Kapp. Influence of transcortical dc currents on cortical neuronal activity. *Experimental neurology* 5.6 (1962), 436–452.

[34] M. Dannhauer, B. Lanfer, C. H. Wolters and T. R. Knösche. Modeling of the human skull in EEG source analysis. *Human brain mapping* 32.9 (2011), 1383–1399.

[35] J. De Munck, C. H. Wolters and M. Clerc. EEG and MEG: forward modeling. *Handbook of neural activity measurement* 19 (2012), 192–248.

[36] J. P. Dmochowski, A. Datta, Y. Huang, J. D. Richardson, M. Bikson, J. Fridriksson and L. C. Parra. Targeted transcranial direct current stimulation for rehabilitation after stroke. *Neuroimage* 75 (2013), 12–19.

[37] F. Drechsler, C. H. Wolters, T. Dierkes, H. Si and L. Grasedyck. A full subtraction approach for finite element method based source analysis using constrained Delaunay tetrahedralisation. *NeuroImage* 46.4 (2009), 1055–1065.

[38] B. Fischl and A. M. Dale. Measuring the thickness of the human cerebral cortex from magnetic resonance images. *Proceedings of the National Academy of Sciences* 97.20 (2000), 11050–11055.

[39] B. Fischl, D. H. Salat, E. Busa, M. Albert, M. Dieterich, C. Haselgrove, A. Van Der Kouwe, R. Killiany, D. Kennedy, S. Klaveness et al. Whole brain segmentation: automated labeling of neuroanatomical structures in the human brain. *Neuron* 33.3 (2002), 341–355.

[40] F. Fregni, P. S. Boggio, M. C. Santos, M. Lima, A. L. Vieira, S. P. Rigonatti, M. T. A. Silva, E. R. Barbosa, M. A. Nitsche and A. Pascual-Leone. Noninvasive cortical stimulation with transcranial direct current stimulation in Parkinson's disease. *Movement disorders* 21.10 (2006), 1693–1702.

[41] S. J. Fried and A. D. Legatt. The utility of a forehead-to-inion derivation in recording the subcortical far-field potential (P14) during median nerve somatosensory-evoked potential testing. *Clinical EEG and neuroscience* 43.2 (2012), 121–126.

[42] K. Friston, L. Harrison, J. Daunizeau, S. Kiebel, C. Phillips, N. Trujillo-Barreto, R. Henson, G. Flandin and J. Mattout. Multiple sparse priors for the M/EEG inverse problem. *NeuroImage* 39.3 (2008), 1104–1120.

[43] M. Fuchs, M. Wagner, H.-A. Wischmann, T. Köhler, A. Theißen, R. Drenckhahn and H. Buchner. Improving source reconstructions by combining bioelectric and biomagnetic data. *Electroencephalography and clinical neurophysiology* 107.2 (1998), 93–111.

[44] N. G. Gençer and C. E. Acar. Sensitivity of EEG and MEG measurements to tissue conductivity. *Physics in Medicine & Biology* 49.5 (2004), 701.

[45] D. M. Goldenholz, S. P. Ahlfors, M. S. Hämäläinen, D. Sharon, M. Ishitobi, L. M. Vaina and S. M. Stufflebeam. Mapping the signal-to-noise-ratios of cortical sources in magnetoencephalography and electroencephalography. *Human brain mapping* 30.4 (2009), 1077–1086.

[46] G. Golub. C, Van Loan, Matrix Computations, John Hopkins U. *P., Baltimore* (1989).

[47] L. Gori and F. Pitolli. A class of totally positive refinable functions. *Rendiconti di Matematica, Serie VII* 20 (2000), 305–322.

[48] T. Götz, R. Huonker, O. W. Witte and J. Haueisen. Thalamocortical impulse propagation and information transfer in EEG and MEG. *Journal Of Clinical Neurophysiology* 31.3 (2014), 253–260.

[49] J. C. Griffis, W. K. Burge and K. M. Visscher. Age-Dependent Cortical Thinning of Peripheral Visual Field Representations in Primary Visual Cortex. *Frontiers in aging neuroscience* 8 (2016), 248.

[50] H. Hallez, B. Vanrumste, R. Grech, J. Muscat, W. De Clercq, A. Vergult, Y. D'Asseler, K. P. Camilleri, S. G. Fabri, S. Van Huffel et al. Review on solving the forward problem in EEG source analysis. *Journal of neuroengineering and rehabilitation* 4.1 (2007), 46.

[51] M. S. Hämäläinen and R. J. Ilmoniemi. Interpreting magnetic fields of the brain: minimum norm estimates. *Medical & biological engineering & computing* 32.1 (1994), 35–42.

[52] M. Hämäläinen, R. Hari, R. J. Ilmoniemi, J. Knuutila and O. V. Lounasmaa. Magnetoencephalography—theory, instrumentation, and applications to noninvasive studies of the working human brain. *Reviews of modern Physics* 65.2 (1993), 413.

[53] R. Hari, J. Karhu, M. Hämäläinen, J. Knuutila, O. Salonen, M. Sams and V. Vilkman. Functional organization of the human first and second somatosensory cortices: a neuromagnetic study. *European Journal of Neuroscience* 5.6 (1993), 724–734.

[54] R. Hari and N. Forss. Magnetoencephalography in the study of human somatosensory cortical processing. *Philosophical Transactions of the Royal Society of London. Series B: Biological Sciences* 354.1387 (1999), 1145–1154.

[55] R. Hari and A. Puce. *MEG-EEG Primer*. Oxford University Press, 2017.

[56] R. Hari and R. Salmelin. Magnetoencephalography: From SQUIDs to neuroscience: Neuroimage 20th anniversary special edition. *Neuroimage* 61.2 (2012), 386–396.

[57] R. Hari, S. Baillet, G. Barnes, R. Burgess, N. Forss, J. Gross, M. Hämäläinen, O. Jensen, R. Kakigi, F. Mauguière et al. IFCN-endorsed practical guidelines for clinical magnetoencephalography (MEG). *Clinical Neurophysiology* 129.8 (2018), 1720–1747.

[58] J. Haueisen, L. Leistritz, T. Süsse, G. Curio and H. Witte. Identifying mutual information transfer in the brain with differential-algebraic modeling: Evidence for fast oscillatory coupling between cortical somatosensory areas 3b and 1. *Neuroimage* 37.1 (2007), 130–136.

[59] Q. He, A. Rezaei and S. Pursiainen. Zeffiro user interface for electromagnetic brain imaging: a GPU accelerated FEM tool for forward and inverse computations in Matlab. *Neuroinformatics* (2019), 1–14.

[60] A.-S. Hincapié, J. Kujala, J. Mattout, S. Daligault, C. Delpuech, D. Mery, D. Cosmelli and K. Jerbi. MEG connectivity and power detections with minimum norm estimates require different regularization parameters. *Computational intelligence and neuroscience* 2016 (2016).

[61] C.-L. Hsieh, F. Shima, S. Tobimatsu, S.-J. Sun and M. Kato. The interaction of the somatosensory evoked potentials to simultaneous finger stimuli in the human central nervous system. A study using direct recordings. *Electroencephalography and Clinical Neurophysiology/Evoked Potentials Section* 96.2 (1995), 135–142.

[62] M.-X. Huang, T. Song, D. J. Hagler Jr, I. Podgorny, V. Jousmaki, L. Cui, K. Gaa, D. L. Harrington, A. M. Dale, R. R. Lee et al. A novel integrated MEG and EEG analysis method for dipolar sources. *Neuroimage* 37.3 (2007), 731–748.

[63] P. Jung, U. Baumgärtner, T. Bauermann, W. Magerl, J. Gawehn, P. Stoeter and R.-D. Treede. Asymmetry in the human primary somatosensory cortex and handedness. *Neuroimage* 19.3 (2003), 913–923.

[64] R. C. Kadosh. *The stimulated brain: cognitive enhancement using non-invasive brain stimulation*. Elsevier, 2014.

[65] J. Kaipio and E. Somersalo. *Statistical and computational inverse problems*. Vol. 160. Springer Science & Business Media, 2006.

[66] R. Kakigi. Somatosensory evoked magnetic fields following median nerve stimulation. *Neuroscience research* 20.2 (1994), 165–174.

[67] P. Krishnaswamy, G. Obregon-Henao, J. Ahveninen, S. Khan, B. Babadi, J. E. Iglesias, M. S. Hämäläinen and P. L. Purdon. Sparsity enables estimation of

both subcortical and cortical activity from MEG and EEG. *Proceedings of the National Academy of Sciences* 114.48 (2017), E10465–E10474.

[68] A. W. Laxton and A. M. Lozano. Deep brain stimulation for the treatment of Alzheimer disease and dementias. *World neurosurgery* 80.3-4 (2013), S28–e1.

[69] F.-H. Lin, T. Witzel, S. P. Ahlfors, S. M. Stufflebeam, J. W. Belliveau and M. S. Hämäläinen. Assessing and improving the spatial accuracy in MEG source localization by depth-weighted minimum-norm estimates. *Neuroimage* 31.1 (2006), 160–171.

[70] J. Liu, B. Guenier and C. Benard. A sensitivity decomposition for the regularized solution of inverse heat conduction problems by wavelets. *Inverse Problems* 11.6 (1995), 1177.

[71] F. Lucka, S. Pursiainen, M. Burger and C. H. Wolters. Hierarchical Bayesian inference for the EEG inverse problem using realistic FE head models: depth localization and source separation for focal primary currents. *NeuroImage* 61.4 (2012), 1364–1382.

[72] S. G. Mallat. A theory for multiresolution signal decomposition: the wavelet representation. *IEEE transactions on pattern analysis and machine intelligence* 11.7 (1989), 674–693.

[73] J. Malmivuo, R. Plonsey et al. *Bioelectromagnetism: principles and applications of bioelectric and biomagnetic fields*. Oxford University Press, USA, 1995.

[74] K. Matsunaga, M. A. Nitsche, S. Tsuji and J. C. Rothwell. Effect of transcranial DC sensorimotor cortex stimulation on somatosensory evoked potentials in humans. *Clinical Neurophysiology* 115.2 (2004), 456–460.

[75] F. Mauguière, J. Desmedt and J. Courjon. Neural generators of N18 and P14 far-field somatosensory evoked potentials studied in patients with lesion of thalamus or thalamo-cortical radiations. *Electroencephalography and clinical neurophysiology* 56.4 (1983), 283–292.

[76] F. Mauguière and J. E. Desmedt. Bilateral somatosensory evoked potentials in four patients with long-standing surgical hemispherectomy. *Annals of Neurology: Official Journal of the American Neurological Association and the Child Neurology Society* 26.6 (1989), 724–731.

[77] S. M. McGinnis, M. Brickhouse, B. Pascual and B. C. Dickerson. Age-related changes in the thickness of cortical zones in humans. *Brain topography* 24.3 (2011), 279–291.

[78] T. Medani, D. Lautru, D. Schwartz, Z. Ren and G. Sou. FEM method for the EEG forward problem and improvement based on modification of the saint venant's method. *Progress In Electromagnetics Research* 153 (2015), 11–22.

[79] T. Miinalainen, A. Rezaei, D. Us, A. Nüßing, C. Engwer, C. H. Wolters and S. Pursiainen. A realistic, accurate and fast source modeling approach for the EEG forward problem. *NeuroImage* 184 (2019), 56–67.

[80] J. C. Mosher, S. Baillet and R. M. Leahy. EEG source localization and imaging using multiple signal classification approaches. *Journal of Clinical Neurophysiology* 16.3 (1999), 225–238.

[81] M. A. Nitsche, P. S. Boggio, F. Fregni and A. Pascual-Leone. Treatment of depression with transcranial direct current stimulation (tDCS): a review. *Experimental neurology* 219.1 (2009), 14–19.

[82] P. Noël, I. Ozaki and J. E. Desmedt. Origin of N18 and P14 far-fields of median nerve somatosensory evoked potentials studied in patients with a brainstem lesion. *Electroencephalography and clinical neurophysiology* 98.2 (1996), 167–170.

[83] A. Nummenmaa, T. Auranen, M. S. Hämäläinen, I. P. Jääskeläinen, J. Lampinen, M. Sams and A. Vehtari. Hierarchical Bayesian estimates of distributed MEG sources: theoretical aspects and comparison of variational and MCMC methods. *NeuroImage* 35.2 (2007), 669–685.

[84] P. L. Nunez, R. Srinivasan et al. *Electric fields of the brain: the neurophysics of EEG*. Oxford University Press, USA, 2006.

[85] M. R. Nuwer. Fundamentals of evoked potentials and common clinical applications today. *Electroencephalography and clinical neurophysiology* 106.2 (1998), 142–148.

[86] C. Pantev, L. E. Roberts, T. Elbert, B. Roβ and C. Wienbruch. Tonotopic organization of the sources of human auditory steady-state responses. *Hearing research* 101.1-2 (1996), 62–74.

[87] C. Papadelis, S. B. Eickhoff, K. Zilles and A. A. Ioannides. BA3b and BA1 activate in a serial fashion after median nerve stimulation: direct evidence from combining source analysis of evoked fields and cytoarchitectonic probabilistic maps. *Neuroimage* 54.1 (2011), 60–73.

[88] A. Pascarella and F. Pitolli. An inversion method based on random sampling for real-time MEG neuroimaging. *arXiv preprint arXiv:1610.01636* (2016).

[89] R. D. Pascual-Marqui et al. Standardized low-resolution brain electromagnetic tomography (sLORETA): technical details. *Methods Find Exp Clin Pharmacol* 24.Suppl D (2002), 5–12.

[90] S. R. Passmore, B. Murphy and T. D. Lee. The origin, and application of somatosensory evoked potentials as a neurophysiological technique to investigate neuroplasticity. *The Journal of the Canadian Chiropractic Association* 58.2 (2014), 170.

[91] W. Paulus. Transcranial electrical stimulation (tES–tDCS; tRNS, tACS) methods. *Neuropsychological rehabilitation* 21.5 (2011), 602–617.

[92] J. S. Perlmutter and J. W. Mink. Deep brain stimulation. *Annu. Rev. Neurosci.* 29 (2006), 229–257.

[93] M. C. Piastra, A. Nüßing, J. Vorwerk, H. Bornfleth, R. Oostenveld, C. Engwer and C. H. Wolters. The discontinuous Galerkin finite element method for solving the MEG and the combined MEG/EEG forward problem. *Frontiers in Neuroscience* 12 (2018), 30.

[94] M. Pierantozzi, P. Mazzone, A. Bassi, P. Rossini, A. Peppe, M. Altibrandi, A. Stefani, G. Bernardi and P. Stanzione. The effect of deep brain stimulation on the frontal N30 component of somatosensory evoked potentials in advanced Parkinson's disease patients. *Clinical neurophysiology* 110.10 (1999), 1700–1707.

[95] F. Pizzo, N. Roehri, S. M. Villalon, A. Trébuchon, S. Chen, S. Lagarde, R. Carron, M. Gavaret, B. Giusiano, A. McGonigal et al. Deep brain activities can be detected with magnetoencephalography. *Nature communications* 10.1 (2019), 1–13.

[96] S. Pursiainen. Coarse-to-fine reconstruction in linear inverse problems with application to limited-angle computerized tomography. *Journal of Inverse and Ill-posed Problems* 16.9 (2008), 873–886.

[97] S. Pursiainen, B. Agsten, S. Wagner and C. H. Wolters. Advanced boundary electrode modeling for tES and parallel tES/EEG. *IEEE Transactions on Neural Systems and Rehabilitation Engineering* 26.1 (2017), 37–44.

[98] S. Pursiainen, J. Vorwerk and C. H. Wolters. Electroencephalography (EEG) forward modeling via H (div) finite element sources with focal interpolation. *Physics in Medicine & Biology* 61.24 (2016), 8502.

[99] S. M. Rampersad, A. M. Janssen, F. Lucka, Ü. Aydin, B. Lanfer, S. Lew, C. H. Wolters, D. F. Stegeman and T. F. Oostendorp. Simulating transcranial direct current stimulation with a detailed anisotropic human head model. *IEEE Transactions on Neural Systems and Rehabilitation Engineering* 22.3 (2014), 441–452.

[100] A. Rezaei, M. Antonakakis, M. Piastra, C. H. Wolters and S. Pursiainen. Parametrizing the Conditionally Gaussian Prior Model for Source Localization with Reference to the P20/N20 Component of Median Nerve SEP/SEF. *Brain Sciences* 10.12 (2020), 934.

[101] A. Rezaei, A. Koulouri and S. Pursiainen. Randomized Multiresolution Scanning in Focal and Fast E/MEG Sensing of Brain Activity with a Variable Depth. *Brain Topography* 33.2 (2020), 161–175.

[102] J. K. Rice, C. Rorden, J. S. Little and L. C. Parra. Subject position affects EEG magnitudes. *NeuroImage* 64 (2013), 476–484.

[103] M. Rullmann, A. Anwander, M. Dannhauer, S. K. Warfield, F. H. Duffy and C. H. Wolters. EEG source analysis of epileptiform activity using a 1 mm anisotropic hexahedra finite element head model. *NeuroImage* 44.2 (2009), 399–410.

[104] M. de Saint-Venant. *Mémoire sur la torsion des prismes: avec des considérations sur leur flexion ainsi que sur l'équilibre intérieur des solides élastiques en général: et des formules pratiques pour le calcul de leur résistance à divers efforts s' exerçant simultanément*. Imprimerie nationale, 1856.

[105] J. G. Samuelsson, S. Khan, P. Sundaram, N. Peled and M. S. Hämäläinen. Cortical Signal Suppression (CSS) for detection of subcortical activity using MEG and EEG. *Brain topography* 32.2 (2019), 215–228.

[106] J. Sarvas. Basic mathematical and electromagnetic concepts of the biomagnetic inverse problem. *Physics in Medicine & Biology* 32.1 (1987), 11.

[107] M.-a. Sato, T. Yoshioka, S. Kajihara, K. Toyama, N. Goda, K. Doya and M. Kawato. Hierarchical Bayesian estimation for MEG inverse problem. *NeuroImage* 23.3 (2004), 806–826.

[108] G. R. Schell and P. L. Strick. The origin of thalamic inputs to the arcuate premotor and supplementary motor areas. *Journal of Neuroscience* 4.2 (1984), 539–560.

[109] M. Seeber, L.-M. Cantonas, M. Hoevels, T. Sesia, V. Visser-Vandewalle and C. M. Michel. Subcortical electrophysiological activity is detectable with high-density EEG source imaging. *Nature communications* 10.1 (2019), 1–7.

[110] K. Sekihara, S. S. Nagarajan, D. Poeppel, A. Marantz and Y. Miyashita. Reconstructing spatio-temporal activities of neural sources using an MEG vector beamformer technique. *IEEE Transactions on Biomedical Engineering* 48.7 (2001), 760–771.

[111] S. S. Shahid, M. Bikson, H. Salman, P. Wen and T. Ahfock. The value and cost of complexity in predictive modelling: role of tissue anisotropic conductivity and fibre tracts in neuromodulation. *Journal of neural engineering* 11.3 (2014), 036002.

[112] S. Sommariva and A. Sorrentino. Sequential Monte Carlo samplers for semi-linear inverse problems and application to magnetoencephalography. *Inverse Problems* 30.11 (2014), 114020.

[113] M. Sonoo, K. Genba, W. Zai, M. Iwata, T. Mannen and I. Kanazawa. Origin of the widespread N18 in median nerve SEP. *Electroencephalography and Clinical Neurophysiology/Evoked Potentials Section* 84.5 (1992), 418–425.

[114] A. Sorrentino, G. Luria and R. Aramini. Bayesian multi-dipole modelling of a single topography in MEG by adaptive sequential Monte Carlo samplers. *Inverse Problems* 30.4 (2014), 045010.

[115] L. Stenbacka, S. Vanni, K. Uutela and R. Hari. Comparison of minimum current estimate and dipole modeling in the analysis of simulated activity in the human visual cortices. *NeuroImage* 16.4 (2002), 936–943.

[116] C. J. Stok. The influence of model parameters on EEG/MEG single dipole source estimation. *IEEE Transactions on Biomedical Engineering* 4 (1987), 289–296.

[117] C. Tesche and J. Karhu. Somatosensory evoked magnetic fields arising from sources in the human cerebellum. *Brain research* 744.1 (1997), 23–31.

[118] P. J. Theuvenet, B. W. van Dijk, M. J. Peters, J. M. van Ree, F. L. L. da Silva and A. C. Chen. Whole-head MEG analysis of cortical spatial organization from unilateral stimulation of median nerve in both hands: No complete hemispheric homology. *Neuroimage* 28.2 (2005), 314–325.

[119] R. A. Toupin. Saint-Venant's principle. *Archive for Rational Mechanics and Analysis* 18.2 (1965), 83–96.

[120] S. Tsuji, H. Shibasaki, M. Kato, Y. Kuroiwa and F. Shima. Subcortical, thalamic and cortical somatosensory evoked potentials to median nerve stimulation. *Electroencephalography and Clinical Neurophysiology/Evoked Potentials Section* 59.6 (1984), 465–476.

[121] E. Urasaki, S.-i. Wada, C. Kadoya, A. Yokota, S. Matsuoka and F. Shima. Origin of scalp far-field N18 of SSEPs in response to median nerve stimulation. *Electroencephalography and Clinical Neurophysiology/Evoked Potentials Section* 77.1 (1990), 39–51.

[122] K. Uutela, M. Hämäläinen and E. Somersalo. Visualization of magnetoencephalographic data using minimum current estimates. *NeuroImage* 10.2 (1999), 173–180.

[123] M. Vauhkonen. Electrical impedance tomography and prior information. (1997).

[124] J. Vorwerk, J.-H. Cho, S. Rampp, H. Hamer, T. R. Knösche and C. H. Wolters. A guideline for head volume conductor modeling in EEG and MEG. *NeuroImage* 100 (2014), 590–607.

[125] D. Weinstein, L. Zhukov and C. Johnson. Lead-field bases for electroencephalography source imaging. *Annals of biomedical engineering* 28.9 (2000), 1059–1065.

[126] D. Wipf and S. Nagarajan. A unified Bayesian framework for MEG/EEG source imaging. *NeuroImage* 44.3 (2009), 947–966.

[127] C. H. Wolters, A. Anwander, X. Tricoche, D. Weinstein, M. A. Koch and R. S. Macleod. Influence of tissue conductivity anisotropy on EEG/MEG field and return current computation in a realistic head model: a simulation and visualization study using high-resolution finite element modeling. *NeuroImage* 30.3 (2006), 813–826.

[128] C. H. Wolters, S. Lew, R. S. MacLeod and M. Hämäläinen. Combined EEG/MEG source analysis using calibrated finite element head models. *Biomedizinische Technik/Biomedical Engineering. Rostock, Germany: Walter de Gruyter* 55.Suppl 1 (2010), 64–68.

[129] C. H. Wolters, H. Köstler, C. Möller, J. Härdtlein and A. Anwander. Numerical approaches for dipole modeling in finite element method based source analysis. *International Congress Series*. Vol. 1300. Elsevier. 2007, 189–192.

[130] Y. Yan, P. Nunez and R. Hart. Finite-element model of the human head: scalp potentials due to dipole sources. *Medical and Biological Engineering and Computing* 29.5 (1991), 475–481.

[131] D. Zumsteg, A. M. Lozano, H. G. Wieser and R. A. Wennberg. Cortical activation with deep brain stimulation of the anterior thalamus for epilepsy. *Clinical neurophysiology* 117.1 (2006), 192–207.

A RANDOMIZED MULTIRESOLUTION SCANNING (RAMUS) ALGORITHM

1. Select the optional number of the resolution levels L and sparsity factor (the ratio of the source count between the resolution levels) s. The number of the sources at the given resolution level will be $K_\ell = Ks^{(\ell-L)}$, where $\ell = 1,2,\ldots,L$ denotes the index of the resolution level. The larger value of the ℓ represents the finer resolution level.

2. For each resolution level $\ell = 1,2,\ldots,L$, a random uniformly distributed set of center points $\vec{p}_1, \vec{p}_2, \ldots, \vec{p}_{K_\ell}$ is created within the active brain compartment. Then, finding the source point subsets B_1, B_2, …, B_{K_ℓ} and applying the nearest neighbour for the point interpolation scheme with respect to the center points. That is, each subset B_j consists of those source positions of the total source space $\mathscr{S}$, whose nearest neighbor with respect to $\vec{p}_1, \vec{p}_2, \ldots, \vec{p}_{K_\ell}$ is $\vec{p}_j$. The average number of source positions associated with B_j which is approximately given by the sparsity factor s. The resolution of this subdivision grows along with the number of the center points . The unknown parameter is assumed to be constant in each subset, and the actual source count is assumed to stay unchanged regardless of the resolution.

3. The first two steps will be repeated to generate a desired number, D , of independent multiresolution decompositions $\mathfrak{S}_1$, $\mathfrak{S}_2$, …, $\mathfrak{S}_D$ each consisting of sequentially generated resolution levels from 1 to L.

4. Start the reconstruction process with the decomposition $\mathfrak{S}_1$ and a suitably chosen initial guess $\mathbf{x}^{(0)}$. (4) For decomposition $\mathfrak{S}_k$, find a reconstruction $\mathbf{x}^{(\ell)}$ with the IAS MAP technique with the initial guess $\mathbf{x}^{(\ell-1)}$ for the resolution levels $\ell = 1,2,\ldots,L$.

5. After going through all the decompositions, obtain the final estimate for the

decomposition (basis) k as the normalized mean

$$\overline{\mathbf{x}}^{(k)} = \sum_{\ell=1}^{L} \mathbf{x}^{(\ell)} / \sum_{\ell=1}^{L} s^{(L-\ell)}, \tag{A.1}$$

where the denominator is due to the need to balance out the effect of the multiplied source count following from the interpolation of a coarse level estimate to a denser resolution level.

6. If $k < D$, move to the next decomposition, i.e., update $k \rightarrow k+1$, and repeat the previous step with the initial guess $\overline{\mathbf{x}}^{(k-1)}$ for the resolution level $\ell = 1$.
7. Obtain the final reconstruction as the mean:

$$\overline{\overline{\mathbf{x}}}^{(k)} = \frac{1}{D} \sum_{k=1}^{D} \overline{\mathbf{x}}^{(k)}. \tag{A.2}$$

B SCRIPT OF SEGMENTING THE BRAIN COMPARTMENTS FROM FREESURFER

```
SUBJECT_DIR = "FreeSurfer input directory (freesurfer_subjects)"
SUBJECT = "subjectid"
OUT_DIR = "Output directory"

%Reconstructing the data out of T1-weighted data including subcortical

# -i <one slice in the anatomical dicom series> \
# -s  <subject id that you make up> \

recon-all -s filename -i file.nii  -all

%Convert any surface to ascii file:

mris_convert $SUBJECT_DIR/$SUBJECT/surf/lh.pial $OUT_DIR/lh.pial.asc
mris_convert $SUBJECT_DIR/$SUBJECT/surf/rh.pial $OUT_DIR/rh.pial.asc
mris_convert $SUBJECT_DIR/$SUBJECT/surf/rh.white $OUT_DIR/rh.wm.asc
mris_convert $SUBJECT_DIR/$SUBJECT/surf/lh.white $OUT_DIR/lh.wm.asc

%Extract subcortical structure

mri_mc $SUBJECT_DIR/$SUBJECT/mri/aseg.mgz 4 $OUT_DIR/lh_Lateral-Ventricle.asc
mri_mc $SUBJECT_DIR/$SUBJECT/mri/aseg.mgz 5 $OUT_DIR/lh_Inf-Lat-Vent.asc
mri_mc $SUBJECT_DIR/$SUBJECT/mri/aseg.mgz 7 $OUT_DIR/lh_CerebellumWM.asc
mri_mc $SUBJECT_DIR/$SUBJECT/mri/aseg.mgz 8 $OUT_DIR/lh_CerebellumCortex.asc
mri_mc $SUBJECT_DIR/$SUBJECT/mri/aseg.mgz 10 $OUT_DIR/lh.thalamus.asc
mri_mc $SUBJECT_DIR/$SUBJECT/mri/aseg.mgz 11 $OUT_DIR/lh.caudate.asc
mri_mc $SUBJECT_DIR/$SUBJECT/mri/aseg.mgz 12 $OUT_DIR/lh.putamen.asc
mri_mc $SUBJECT_DIR/$SUBJECT/mri/aseg.mgz 13 $OUT_DIR/lh.pallidum.asc
mri_mc $SUBJECT_DIR/$SUBJECT/mri/aseg.mgz 14 $OUT_DIR/3rd-Ventricle.asc
mri_mc $SUBJECT_DIR/$SUBJECT/mri/aseg.mgz 15 $OUT_DIR/4th-Ventricle.asc
mri_mc $SUBJECT_DIR/$SUBJECT/mri/aseg.mgz 16 $OUT_DIR/Brainstem.asc
mri_mc $SUBJECT_DIR/$SUBJECT/mri/aseg.mgz 17 $OUT_DIR/lh.Hippocampus.asc
mri_mc $SUBJECT_DIR/$SUBJECT/mri/aseg.mgz 18 $OUT_DIR/lh.Amygdala.asc
mri_mc $SUBJECT_DIR/$SUBJECT/mri/aseg.mgz 26 $OUT_DIR/lh.Accumbens.asc
mri_mc $SUBJECT_DIR/$SUBJECT/mri/aseg.mgz 28 $OUT_DIR/LVentral_DC.asc
mri_mc $SUBJECT_DIR/$SUBJECT/mri/aseg.mgz 30
```

```
$OUT_DIR/LVessel.asc
mri_mc $SUBJECT_DIR/$SUBJECT/mri/aseg.mgz 31 $OUT_DIR/LChoroid_plexus.asc
mri_mc $SUBJECT_DIR/$SUBJECT/mri/aseg.mgz 43 $OUT_DIR/rh_Lateral-Ventricle.asc
mri_mc $SUBJECT_DIR/$SUBJECT/mri/aseg.mgz 44 $OUT_DIR/rh_Inf-Lat-Vent.asc
mri_mc $SUBJECT_DIR/$SUBJECT/mri/aseg.mgz 46 $OUT_DIR/rh_CerebellumWM.asc
mri_mc $SUBJECT_DIR/$SUBJECT/mri/aseg.mgz 47 $OUT_DIR/rh_CerebellumCortex.asc
mri_mc $SUBJECT_DIR/$SUBJECT/mri/aseg.mgz 49 $OUT_DIR/rh.thalamus.asc
mri_mc $SUBJECT_DIR/$SUBJECT/mri/aseg.mgz 50 $OUT_DIR/rh.caudate.asc
mri_mc $SUBJECT_DIR/$SUBJECT/mri/aseg.mgz 51 $OUT_DIR/rh.putamen.asc
mri_mc $SUBJECT_DIR/$SUBJECT/mri/aseg.mgz 52 $OUT_DIR/rh.pallidum.asc
mri_mc $SUBJECT_DIR/$SUBJECT/mri/aseg.mgz 53 $OUT_DIR/rh.Hippocampus.asc
mri_mc $SUBJECT_DIR/$SUBJECT/mri/aseg.mgz 54 $OUT_DIR/rh.Amygdala.asc
mri_mc $SUBJECT_DIR/$SUBJECT/mri/aseg.mgz 58 $OUT_DIR/rh.Accumbens.asc
mri_mc $SUBJECT_DIR/$SUBJECT/mri/aseg.mgz 60 $OUT_DIR/RVentral_DC.asc
mri_mc $SUBJECT_DIR/$SUBJECT/mri/aseg.mgz 62
$OUT_DIR/RVessel.asc
mri_mc $SUBJECT_DIR/$SUBJECT/mri/aseg.mgz 63 $OUT_DIR/RChoroid_plexus.asc
mri_mc $SUBJECT_DIR/$SUBJECT/mri/aseg.mgz 251 $OUT_DIR/CC_posterior.asc
mri_mc $SUBJECT_DIR/$SUBJECT/mri/aseg.mgz 252 $OUT_DIR/CC_Mid_posterior.asc
mri_mc $SUBJECT_DIR/$SUBJECT/mri/aseg.mgz 253 $OUT_DIR/CC_Central.asc
mri_mc $SUBJECT_DIR/$SUBJECT/mri/aseg.mgz 254 $OUT_DIR/CC_Mid_Anterior.asc
mri_mc $SUBJECT_DIR/$SUBJECT/mri/aseg.mgz 255 $OUT_DIR/CC_Anterior.asc

%Visualizing the label numbers correspond to each structure:

#freeview -v $SUBJECT_DIR/$SUBJECT/mri/orig.mgz
 ↪   $SUBJECT_DIR/$SUBJECT/mri/aseg.mgz:colormap=lut:opacity=0.4

%Extracting the strip skull and other outer non-brain tissue

mri_watershed -useSRAS -surf  $SUBJECT_DIR/$SUBJECT/surf
 ↪   $SUBJECT_DIR/$SUBJECT/mri/orig_nu.mgz  $SUBJECT_DIR/$SUBJECT/trash/trash.mgz

mris_convert $SUBJECT_DIR/$SUBJECT/surf_outer_skin_surface $OUT_DIR/outer_skin.asc
mris_convert $SUBJECT_DIR/$SUBJECT/surf_outer_skull_surface $OUT_DIR/outer_skull.asc
mris_convert $SUBJECT_DIR/$SUBJECT/surf_inner_skull_surface $OUT_DIR/inner_skull.asc

%.annot files
#After Freesurfer processes a subject, in the subject's /label directory, there are
 ↪   .annot files containing the parcellation data for each hemishere.

#?h.aparc.annot files contain the desikan_killiany.gcs parcellation scheme
#(36 labels)
#?h.aparc.a2009s.annot files contain the destrieux.simple.2009-07-28.gcs
#scheme (76 labels)
#?h.aparc.DKTatlas.annot correspond to the DKTatas40.gcs scheme

%Cortical Parcellation
```

```
mri_annotation2label --subject $SUBJECT  --sd $SUBJECT_DIR --annotation aparc.a2009s
 ↪   --hemi lh --ctab aparc.annot.a2009s --outdir $OUT_DIR/lh.aparc_76
mri_annotation2label --subject $SUBJECT  --sd $SUBJECT_DIR --annotation aparc.a2009s
 ↪   --hemi rh --ctab aparc.annot.a2009s --outdir $OUT_DIR/rh.aparc_76
mri_annotation2label --subject $SUBJECT  --sd $SUBJECT_DIR --annotation aparc --hemi lh
 ↪   --ctab aparc.annot --outdir $OUT_DIR/lh.aparc_36
mri_annotation2label --subject $SUBJECT  --sd $SUBJECT_DIR --annotation aparc --hemi rh
 ↪   --ctab aparc.annot --outdir $OUT_DIR/rh.aparc_36

%The data in the .annot files can be read using the matlab script

matlab -nodisplay -nosplash -nodesktop -r "dir_name =
 ↪   '$SUBJECT_DIR/$SUBJECT/';[vertices,label,colortable]
=read_annotation([dir_name '/label/lh.aparc.a2009s.annot']);save color_table_lh_76.mat
 ↪   colortable label vertices; [vertices,label,colortable]=read_annotation([dir_name
 ↪   '/label/rh.aparc.a2009s.annot']); save color_table_rh_76.mat colortable label
 ↪   vertices; [vertices,label,colortable]=read_annotation([dir_name
 ↪   '/label/lh.aparc.annot']); save color_table_lh_36.mat colortable label vertices;
 ↪   [vertices,label,colortable]=read_annotation([dir_name '/label/rh.aparc.annot']);
 ↪   save color_table_rh_36.mat colortable label vertices;exit;";
#Create matlab version colortables.

%Merging labels

mri_mergelabels -d $OUT_DIR/lh.aparc_76/ -o $OUT_DIR/lh_labels_76.asc
mri_mergelabels -d $OUT_DIR/rh.aparc_76/ -o $OUT_DIR/rh_labels_76.asc
mri_mergelabels -d $OUT_DIR/lh.aparc_36/ -o $OUT_DIR/lh_labels_36.asc
mri_mergelabels -d $OUT_DIR/rh.aparc_36/ -o $OUT_DIR/rh_labels_36.asc
matlab -nodisplay -nosplash -nodesktop -r "dir_name = '$OUT_DIR/';a = dlmread([dir_name
 ↪   'lh_labels_76.asc'],' ',2,0);a = a(:,[1,3,5,7]);save -ascii lh_points_76.dat a; a
 ↪   = dlmread([dir_name 'rh_labels_76.asc'],' ',2,0);a = a(:,[1,3,5,7]); save -ascii
 ↪   rh_points_76.dat a; a = dlmread([dir_name 'lh_labels_36.asc'],' ',2,0);a =
 ↪   a(:,[1,3,5,7]);  save -ascii  lh_points_36.dat a; a = dlmread([dir_name
 ↪   'rh_labels_36.asc'],' ',2,0);a = a(:,[1,3,5,7]); save -ascii rh_points_36.dat
 ↪   a;quit";
```

C A FILE FOR IMPORTING THE SEGMENTED BRAIN COMPARTMENTS TO ZI

```
%%%%%%%%%%%%%%%%%%%%%%%%%%%% HEADER START %%%%%%%%%%%%%%%%%%%%%%%%%%%%
Do not change or remove this header. This file allows one to import a
surface segmentation consisting of a set of ASCII files to the Zeffiro
Interface (ZI), Copyright (c) Sampsa Pursiainen, 2018. For importing, this
file should be placed in the folder containing the files and opened via
ZI's import menu item 'Import segmentation from folder (ASCII)'. The files
can be either DAT files containing either points or triangles, or ASC
files exported from the FreeSurfer Software Suite, Copyright (c)
Freesufer, 2013.

In the former case, the folder must contain two files per each triangular
tissue surface mesh (filename_points.dat and filename_triangles.dat),
whereas in the latter case a single file is needed (filename.asc) per a
mesh. Each line in the list below corresponds to a single mesh. Each
compartment in the segmentation is described by one or more meshes which
will be automatically merged in the import process. The compartment
identifiers are the following:

sensor_points, sensor_directions, white_matter, grey_matter, csf, skull,
skin, detail_1, detail_2, ..., detail_22.

Of these, a mesh for each tissue compartment is specified by a single
comma-separated line of the following form:

filename, compartment name, scaling, sigma, priority, activity, name,
invert, extension


Here, the filename appears without any extensions; compartment_name is as
in the list above, scaling, sigma and priority parameters are as in ZI's
segmentation window with 0 corresponding to the default value; activity is
a number describing the activity of the compartment (0 = inactive, 1 =
constrained activity, 2 = unconstrained activity, or 3 = inner cortex [for
white_matter only]); name is the compartment name as it appears in ZI;
invert is for inverting an inward-pointing surface normal (0=not inverted,
1=inverted); and extension is either ASC (asc) or DAT (dat) for FreeSurfer
```

```
and other meshes, respectively.

In the special case of sensor_points and sensor_directions, it is only
possible to use the DAT format. Each one of these is imported via a single
file (filename.dat), and the line for importing is of the form

filename, compartment name, scaling, x-translation, y-translation,
z-translation, xy-rotation, yz-rotation, zx-rotation

The scaling, translating and rotation parameters are as they appear in
ZI's segmentation tool, and selecting 0 for them, means that the default
value will be used.

Any compartment-specific parameter can be imported only once. In case
there are multiple definitions in the list for a single compartment, only
the first one counts.


The segmentation list starts after the header and can be edited freely by
the user.
%%%%%%%%%%%%%%%%%%%%%%%%%%%%%% HEADER END %%%%%%%%%%%%%%%%%%%%%%%%%%%%%%
electrodes, sensor_points, 0, 0, 0, 0, 0, 0, 0 ,0,0,0
lh_CerebellumCortex, detail_1, 1, 0.33, 0, 2, Cerebellum cortex, 0, ASC,0,0,0
rh_CerebellumCortex, detail_1, 1, 0.33, 0, 2, Cerebellum cortex, 0, ASC,0,0,0
lh_CerebellumWM, detail_2, 1, 0.33, 0, 0, Cerebellum WM, 0, ASC,0,0,0
rh_CerebellumWM, detail_2, 1, 0.33, 0, 0, Cerebellum WM, 0, ASC,0,0,0
lh.Amygdala, detail_3, 1, 0.33, 0, 2, Amygdala, 0, ASC,0,0,0
rh.Amygdala, detail_3, 1, 0.33, 0, 2, Amygdala, 0, ASC,0,0,0
lh.thalamus, detail_4, 1, 0.33, 0, 2, Thalamus, 0, ASC,0,0,0
rh.thalamus, detail_4, 1, 0.33, 0, 2, Thalamus, 0, ASC,0,0,0
lh.caudate, detail_5, 1, 0.33, 0, 2, Caudate, 0, ASC,0,0,0
rh.caudate, detail_5, 1, 0.33, 0, 2, Caudate, 0, ASC,0,0,0
lh.Accumbens, detail_6, 1, 0.33, 0, 2, Acumbens, 0, ASC,0,0,0
rh.Accumbens, detail_6, 1, 0.33, 0, 2, Acumbens, 0, ASC,0,0,0
lh.putamen, detail_7, 1, 0.33, 0, 2, Putamen, 0, ASC,0,0,0
rh.putamen, detail_7, 1, 0.33, 0, 2, Putamen, 0, ASC,0,0,0
lh.Hippocampus, detail_8, 1, 0.33, 0, 1, Hippocampus, 0, ASC,0,0,0
rh.Hippocampus, detail_8, 1, 0.33, 0, 1, Hippocampus, 0, ASC,0,0,0
lh.pallidum, detail_9, 1, 0.33, 0, 2, Pallidum, 0, ASC,0,0,0
rh.pallidum, detail_9, 1, 0.33, 0, 2, Pallidum, 0, ASC,0,0,0
lh_Lateral-Ventricle, detail_10, 1, 1.79, 0, 0, Ventricles, 0, ASC,0,0,0
rh_Lateral-Ventricle, detail_10, 1, 1.79, 0, 0, Ventricles, 0, ASC,0,0,0
outer_skin, scalp, 1, 0.33, 0, 0, Scalp, 0, ASC,0,0,0
outer_skull, skull, 1, 0.0064, 0, 0, Skull, 0, ASC,0,0,0
inner_skull, csf, 1, 1.79, 0, 0, Cerebrospinal fluid, 0, ASC,0,0,0
Brainstem, detail_11, 1, 0.33, 0, 2, Brain stem, 0, ASC,0,0,0
CC_posterior, detail_12, 1, 0.14, 0, 0, Cingulate cortex, 0, ASC,0,0,0
CC_Mid_posterior, detail_12, 1, 0.14, 0, 0, Cingulate cortex, 0, ASC,0,0,0
CC_Central, detail_12, 1, 0.14, 0, 0, Cingulate cortex, 0, ASC,0,0,0
```

```
CC_Mid_Anterior, detail_12, 1, 0.14, 0, 0, Cingulate cortex, 0, ASC,0,0,0
CC_Anterior, detail_12, 1, 0.14, 0, 0, Cingulate cortex, 0, ASC,0,0,0
LVentral_DC, detail_13, 1, 0.33, 0, 2, Ventral DC, 0, ASC,0,0,0
RVentral_DC, detail_13, 1, 0.33, 0, 2, Ventral DC, 0, ASC,0,0,0
lh.wm, white_matter, 1, 0.14, 0, 3, White matter, 0, ASC,0,0,0
rh.wm, white_matter, 1, 0.14, 0, 3, White matter, 0, ASC,0,0,0
lh.pial, grey_matter, 1, 0.33, 0, 1, Grey matter, 0, ASC,0,0,0
rh.pial, grey_matter, 1, 0.33, 0, 1, Grey matter, 0, ASC,0,0,0
```

PUBLICATIONS

PUBLICATION I

A realistic, accurate and fast source modeling approach for the EEG forward problem

T. Miinalainen, A. Rezaei, D. Us, A. Nüßing, C. Engwer, C. H. Wolters and S. Pursiainen

Journal of NeuroImage 184, 56–67
DOI: 10.1016/j.neuroimage.2018.08.054

NeuroImage 184 (2019) 56–67

Contents lists available at ScienceDirect

NeuroImage

journal homepage: www.elsevier.com/locate/neuroimage

A realistic, accurate and fast source modeling approach for the EEG forward problem

Tuuli Miinalainen [a,c,d,e], Atena Rezaei [a,*], Defne Us [a,b], Andreas Nüßing [c,d], Christian Engwer [d], Carsten H. Wolters [c], Sampsa Pursiainen [a]

[a] Laboratory of Mathematics, Tampere University of Technology, P.O. Box 692, 33101, Tampere, Finland
[b] Laboratory of Signal Processing, Tampere University of Technology, Tampere, Finland, P.O. Box 553, 33101, Tampere, Finland
[c] Institute for Biomagnetism and Biosignalanalysis, University of Münster, Germany, Malmedyweg 15, D-48149, Münster, Germany
[d] Institute for Computational and Applied Mathematics, University of Münster, Germany, Einsteinstrasse 62, D-48149, Münster, Germany
[e] Department of Applied Physics, University of Eastern Finland, P.O.Box 1627, FI-70211 Kuopio, Finland

ARTICLE INFO

Keywords:
Electroencephalography (EEG)
Finite element method (FEM)
Divergence conforming vector fields
Focal sources
DUNE toolbox

ABSTRACT

The aim of this paper is to advance electroencephalography (EEG) source analysis using finite element method (FEM) head volume conductor models that go beyond the standard three compartment (skin, skull, brain) approach and take brain tissue inhomogeneity (gray and white matter and cerebrospinal fluid) into account. The new approach should enable accurate EEG forward modeling in the thin human cortical structures and, more specifically, in the especially thin cortices in children brain research or in pathological applications. The source model should thus be focal enough to be usable in the thin cortices, but should on the other side be more realistic than the current standard mathematical point dipole. Furthermore, it should be numerically accurate and computationally fast. We propose to achieve the best balance between these demands with a current preserving (divergence conforming) dipolar source model. We develop and investigate a varying number of current preserving source basis elements n ($n = 1, \ldots, n = 5$). For validation, we conducted numerical experiments within a multi-layered spherical domain, where an analytical solution exists. We show that the accuracy increases along with the number of basis elements, while focality decreases. The results suggest that the best balance between accuracy and focality in thin cortices is achieved with $n = 4$ (or in extreme cases even $n = 3$) basis functions, while in thicker cortices $n = 5$ is recommended to obtain the highest accuracy. We also compare the current preserving approach to two further FEM source modeling techniques, namely partial integration and St. Venant, and show that the best current preserving source model outperforms the competing methods with regard to overall balance. For all tested approaches, FEM transfer matrices enable high computational speed. We implemented the new EEG forward modeling approaches into the open source *duneuro* library for forward modeling in bioelectromagnetism to enable its broader use by the brain research community. This library is build upon the *DUNE* framework for parallel finite elements simulations and integrates with high-level toolboxes like *FieldTrip*. Additionally, an inversion test has been implemented using the realistic head model to demonstrate and compare the differences between the aforementioned source models.

1. Introduction

In electroencephalography (EEG) source analysis, brain activity is to be detected via voltage measurements on the scalp surface which leads to the so-called *EEG inverse problem* (Brette and Destexhe, 2012). The major advantages of the EEG include, for example, its high temporal resolution and noninvasive nature. That is, the measurements can be carried out fully outside of the head without a need to touch the brain itself or to apply high-intensity external electromagnetic fields present, for example, in functional magnetic resonance imaging (fMRI) (Brette and Destexhe, 2012). Because of these reasons, EEG source analysis is now one of the standard methods also in children, infant and even neonate brain research (see, e.g. (Hämäläinen et al., 2015; Roche-Labarbe et al., 2008)).

The EEG inverse problem is ill-posed, i.e., its solution is non-unique and sensitive to noise and modeling errors. Consequently, the reconstruction process necessitates clinical, physical and neurophysiological *a*

* Corresponding author.
E-mail address: atena.rezaei@tut.fi (A. Rezaei).

https://doi.org/10.1016/j.neuroimage.2018.08.054
Received 20 February 2018; Received in revised form 9 August 2018; Accepted 22 August 2018
Available online 28 August 2018

priori knowledge (Brette and Destexhe, 2012). It is also strongly relying on the accuracy of the solution to the *EEG forward problem*, where the electric potentials, generated by the impressed primary current sources in the brain, have to be simulated using a realistic head volume conductor model (Brette and Destexhe, 2012).

This paper aims at developing, implementing and validating a more accurate and realistic EEG forward approach. We want to strive for head volume conductor models that go beyond the standard three compartment (skin, skull, brain) approach and take brain tissue inhomogeneity, e.g., gray and white matter and cerebrospinal fluid (CSF), into account.

In order to solve the EEG forward problem in such realistic geometries, numerical approaches are needed and to guarantee the accuracy of modeling the neural currents, the source needs to be placed into the thin cortical layer which is on average only slightly more than 2 mm thick (Griffis et al., 2016; Fischl and Dale, 2000; McGinnis et al., 2011). That is, the focality of the source model is essential (Brette and Destexhe, 2012; Pursiainen et al., 2016). The boundary element method (BEM), which is currently the most extensively used numerical EEG forward modeling technique, hardly allows modeling of such tissue conductivity inhomogeneity. Although it is possible to include the distinction of tissue structures with BEM, this would lead to heavy computational complexity and significantly high memory demand (Brette and Destexhe, 2012; Vorwerk et al., 2012). A broader overview of EEG forward modeling techniques can be found, for example, in (Brette and Destexhe, 2012).

In this article, the forward problem is approached via the finite element method (FEM) (Braess, 2001). The FEM is known to provide an accurate modeling framework with advanced computational features for several applied fields of science and engineering. The FEM has also been proven to be a feasible method for the EEG forward problem (Marin et al., 1998; Haueisen et al., 2002; Ramon et al., 2006), where the finite element (FE) mesh can be generated based on a precise MRI based head geometry including its internal surfaces and complex 3D conductivity structures (Papageorgakis, 2017; Pursiainen et al., 2016). It has been shown that very fine 3D structures need to be modeled, e.g., the CSF and compact and spongious bone (Papageorgakis, 2017; Montes-Restrepo et al., 2014). The FEM allows modeling of such complex geometries and, consequently, it has a great potential regarding future EEG applications.

As the reference model for validation, we use a multi-layer sphere model and a classical mathematical point dipole determined by its location, orientation and magnitude, since analytical solutions have been derived for it (de Munck and Peters, 1993). However, it was also already shown that the point dipole source results in small, but systematic depth localization errors due to its over-focal nature when compared to a more realistic and slightly more extended source model (de Munck et al., 1988). The point dipole can also be modeled with its full focality in a FEM framework using the so-called *subtraction approach*, but it is known that this approach is computationally expensive and that numerical errors might get significant on the boundaries in thin cortices, where sources are very close to the next conductivity discontinuity (Bertrand et al., 1991; Awada et al., 1997; Marin et al., 1998; Schimpf et al., 2002; Drechsler et al., 2009). The computational costs of all direct approaches presented in this paper including the H(div) technique are very low compared to the computationally expensive full subtraction approach (Drechsler et al., 2009) and somewhat similar to each other, since it is considerably lower than what is needed for generating the transfer matrix.

In this paper, we will study current preserving H(div) source models, which are slightly less focal than the standard mathematical point dipole, but, as will be shown, well-localized enough to be embedded in the thin cortical structures (Griffis et al., 2016; Fischl and Dale, 2000; McGinnis et al., 2011) and the even thinner cortices as needed especially in children brain research (Li et al., 2014) and/or pathological situations (Seitz et al., 2014). The issues and sensitivity of the classical St. Venant (Buchner et al., 1997; Toupin, 1965) and partial integration (Yan et al., 1991; Weinstein et al., 2000) source models regarding these situations has recently been observed and studied in (Nüßing, 2018; Medani, 2016; Medani et al., 2015). The simplest case of the current preserving H(div) approach is the Whitney (Raviart-Thomas) source model (Bauer et al., 2015; Pursiainen, 2012) in which the linear Whitney functions constitute the sources. Recent studies (Pursiainen et al., 2016; Vorwerk et al., 2017; Tanzer et al., 2005) have shown that the generalized H(div) model results in a focal and highly exact solution for the EEG forward problem. It is also a fast technique compared to the full subtraction approach (Drechsler et al., 2009) as the source modeling process requires effectively the same computational cost as in the simple classical methods (Bauer et al., 2015). That is, the source field can be obtained in a fraction of the time which is required to evaluate the transfer matrix.

In this study, we implemented and validated an adaptable solver into *duneuro*[1] (Nüßing, 2018; Nüßing et al., 2016; Engwer et al., 2017; Vorwerk et al., 2017), an open source C++ library for solving forward problems in bioelectromagnetism applications belonging to the open source toolbox *DUNE*[2] (Blatt and Bastian, 2007; Blatt et al., 2016; Bastian et al., 2008a; b). *DUNE* is currently being developed for various different applications of partial differential equations. For its modular programming interface, it provides a suitable platform for EEG/MEG computations where the geometrical complexity of the biological tissue structures has to be taken into account in the modeling process. As a novel design, we explore how the number of the elements in the source configuration affects the modeling accuracy. Our interest is, in particular, in the areas close to the outer gray matter boundary, where the discontinuity in the electrical conductivity distribution easily causes forward errors. In order to prevent those, the element patch of the source configuration needs to be restricted to avoid an overlap with the cerebrospinal fluid (CSF) compartment.

In the numerical experiments, we find out how the H(div) model performs with respect to a varying number of current preserving source basis elements n ($n = 1, \ldots, n = 5$) in comparison to the St. Venant and partial integration method. We also give a computed example on how the adaptivity with respect to n potentially affects source localization inverse estimates in a realistic multi-compartment head model. The results suggest that the best H(div) source model outperforms the competing methods with regard to overall balance and that it is especially well-suited for situations in which the focality of the source model is essential such as on the boundaries. The best balance between accuracy and focality in thin cortices is achieved by *adaptive H(div)* $n = 4$ (or in extreme cases even $n = 3$) basis functions, while in thicker cortices $n = 5$ is recommended to obtain the highest accuracy by *non-adaptive H(div)*.

This paper is structured as follows: The materials and methods are described in Section 2 including the H(div) source model, its implementation into *duneuro*, and numerical evaluation process. After that, the results of the numerical experiments are presented in Section 3 and discussed in Section 4. Finally, the conclusions are summed up in Section 5.

2. Materials and methods

2.1. Forward model

The EEG forward problem is to solve the electric potential field u on the surface $\partial\Omega$ of the head model (domain) Ω with a given source current density $\vec{J}^P$ and a conductivity tensor distribution σ that is known to be point-wise symmetric and positive definite (Brette and Destexhe, 2012). Applying the quasi-static approximation.

The electric potential u can be modeled using the following Poisson type equation equipped with the zero Neumann boundary condition. That is, the normal current density on the surface equals zero, as the head is electrically isolated (Hallez et al., 2007; Brette and Destexhe, 2012):

[1] *duneuro*: http://www.duneuro.org.
[2] *DUNE*: https://www.dune-project.org.

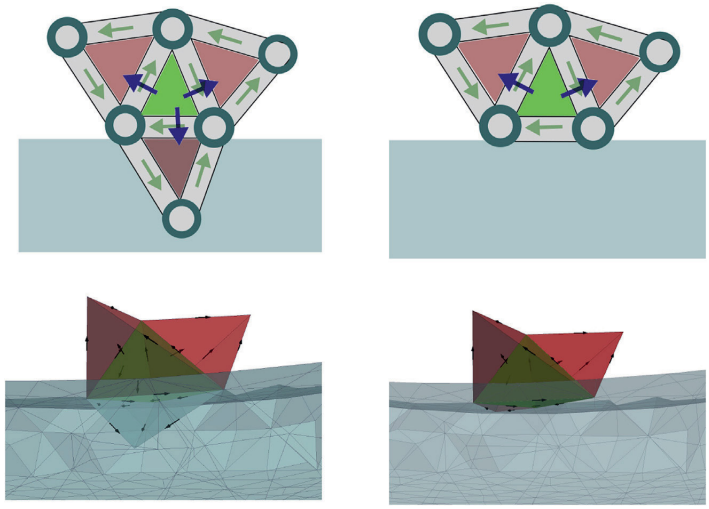

Fig. 1. The five-element source configuration near the gray matter boundary. The top row includes a two-dimensional schematic illustration of the dipolar FI (dark blue) and EW (light green) sources. The images on the left side present the scenario where the sources are not limited in the gray matter area. The restricted version is presented in the images on the right side, where elements not belonging to the gray matter are excluded to prevent the forward errors.

$$\nabla \cdot (\sigma \nabla u) = \nabla \cdot \vec{J}^{P} \quad \text{in} \quad \Omega \quad \text{with} \quad (\sigma \nabla u) \cdot \vec{n} = 0 \quad \text{on} \quad \partial\Omega \tag{1}$$

Multiplying both sides with a test function v, and taking the partial integral over Ω results in the weak form (Pursiainen et al., 2016)

$$\int_{\Omega} \nabla v \cdot (\sigma \nabla u) dV = -\int_{\Omega} v\left(\nabla \cdot \vec{J}^{P}\right) dV \quad \text{for all} \quad v \in H^1(\Omega) \tag{2}$$

which consists of two parts: the operator part on the left side and source part on the right side. Here, $H^1(\Omega)$ denotes the Sobolev space containing the functions that have square integrable first-order partial derivatives, i.e., that are in $L_2(\Omega)$. If the divergence of the primary current density is square integrable, i.e., if $\vec{J}^{P} \in H(\mathrm{div}) = \{\vec{w} | \nabla \cdot \vec{w} \in L^2(\Omega)\}$, the electric potential u determined by the weak form is unique up to choosing the ground level (Drechsler et al., 2009). Namely, $L^2(\Omega)$ means the primary current field is a finite energy.

The domain Ω is subdivided into a set of tetrahedral finite elements (FEs) (Braess, 2001). It is assumed that the potential u belongs to a subspace $S \in H^1(\Omega)$ that is spanned by the FE basis functions. The potential distribution is approximated as the finite sum $u_h = \sum_{i=1}^{N} z_i \psi_i$ in which $\psi_1, \psi_2, \ldots, \psi_N \in H^1(\Omega)$ are piecewise linear nodal basis functions. Similarly, the primary current distribution is modeled with the H(div) approach via $\vec{J}_h^{P} = \sum_{j=1}^{K} x_j \vec{w}_j$ where $\vec{w}_1, \vec{w}_2, \ldots, \vec{w}_K \in H(\mathrm{div})$ are the divergence conforming basis functions (Pursiainen et al., 2016). Associating u_h and $\vec{J}_h^{P}$ with coordinate vectors $\mathbf{z} = (z_1, z_2, \ldots, z_N)$ and $\mathbf{x} = (x_1, x_2, \ldots, x_K)$, the weak form turns to a solvable linear system $\mathbf{Az} = \mathbf{Gx}$ where $\mathbf{A} \in \mathbb{R}^{(N \times N)}$ and $\mathbf{G} \in \mathbb{R}^{(N \times K)}$ with

$$A_{i,j} = \int_{\Omega} \nabla \psi_j \cdot (\sigma \nabla \psi_i) dV \quad \text{and} \quad G_{i,j} = \int_{\Omega} \psi_i (\nabla \cdot \vec{w}_j) dV. \tag{3}$$

The measurement vector $\mathbf{y}$ for the electrode voltages can be formed as $\mathbf{y} = \mathbf{RA}^{-1}\mathbf{Gx} = \mathbf{Tf}$, in which $\mathbf{f} = \mathbf{Gx}$ is a load vector which represents the activity in the brain and $\mathbf{T} = \mathbf{RA}^{-1}$ is a so-called transfer matrix (Gencer and Acar, 2004; Drechsler et al., 2009). In addition, the matrix $\mathbf{R}$ is a restriction operator for picking the skin potentials at the electrode positions (Pursiainen et al., 2016). The matrix $\mathbf{R}$ denotes the zero potential level, here the mean of the measurements $\mathbf{y}$. The elements of matrix $\mathbf{R}$ are defined as follows: If the ℓ-th electrode on the boundary $\partial\Omega$ is positioned at the i_ℓ-th node, $R_{\ell,i_\ell} = 1 - 1/L$. Also, if $\ell \neq j$, $R_{\ell,i_j} = -1/L$. Finally, $R_{\ell,j} = 0$, if the j-th node is not associated with any electrode(Pursiainen et al., 2016).

2.2. Dipolar sources

In this study, the primary source currents are constructed using synthetic dipolar sources for the linear and quadratic basis functions of $H(\mathrm{div})$ (Ainsworth and Coyle, 2003). The dipolar moment $\vec{q}_{\vec{w}}$ of the basis function $\vec{w}$ is defined as $\vec{q}_{\vec{w}} = \int_{\Omega} \vec{w}\, dV$. In a tetrahedral FE mesh, the moment and position of a synthetic dipole can be expressed as follows:

$$\vec{q}_{\vec{w}} = \frac{\vec{r}_{P_j} - \vec{r}_{P_i}}{\left\| \vec{r}_{P_j} - \vec{r}_{P_i} \right\|} \quad \text{and} \quad \vec{r}_{\vec{w}} = \frac{1}{2}\left(\vec{r}_{P_i} + \vec{r}_{P_j}\right) \tag{4}$$

in which $\vec{r}_{P_i}$ and $\vec{r}_{P_j}$ are the position vectors of mesh nodes P_i and P_j (Pursiainen et al., 2016). The right-hand side matrix $\mathbf{G}$ can be formed as

$$G_{\psi,\vec{w}} = \int_{\Omega} \psi (\nabla \cdot \vec{w}) dV = \frac{s_{\{\psi,P_j\}} - s_{\{\psi,P_i\}}}{\left\| \vec{r}_{P_j} - \vec{r}_{P_i} \right\|} \tag{5}$$

for a given pair ψ, $\vec{w}$ of the basis functions with $s_{\{\psi,P\}} = 1$, if ψ corresponds to node P and $s_{\{\psi,P\}} = 0$, otherwise. For more detailed formulation, see e.g., (Pursiainen et al., 2016; Bauer et al., 2015).

For the linear $H(\mathrm{div})$ basis functions, the resulting source dipole is defined by nodes P_i and P_j that are located on the opposing sides of a shared face in an adjacent tetrahedron pair. This is referred to as the face intersecting (FI) orientation. For the quadratic basis, P_i and P_j are attached by an edge, leading to an edgewise (EW) orientation. As shown later on, various source configurations can be formed by taking different combinations of these dipoles.

For constructing the load vector $\mathbf{f} = \mathbf{Gx}$ for an arbitrary dipole position $\vec{r}$ and a moment $\vec{p}$, an interpolation technique needs to be applied. That is, to find coefficients $\mathbf{c} = (c_1, c_2, \ldots, c_M)$ such that

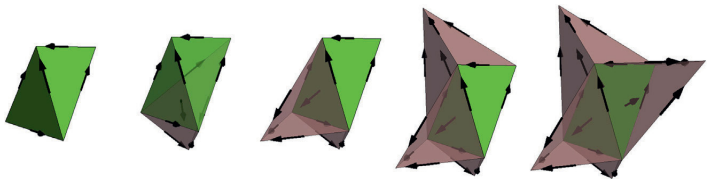

Fig. 2. From left to right, respectively: The element patch of the source configurations for $n = 1, 2, \ldots, 5$ elements with FI and EW dipoles. In each configuration, the center element is marked with green.

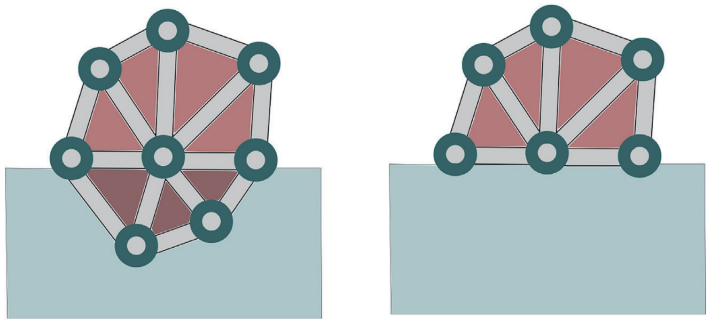

Fig. 3. A schematic illustration of the ball-like St. Venant source element patch. On the boundary of the gray matter approximately one half of the elements (darker red color in the image on the left side) are taken out of the final configuration (right) in its adapted version.

$$\vec{p} \approx \sum_{\ell=1}^{M} c_\ell \vec{q}_{\vec{w}_\ell} \quad \text{and} \quad \vec{r} \approx \sum_{\ell=1}^{M} c_\ell \vec{r}_{\vec{w}_\ell}. \tag{6}$$

In this study, we use the position based optimization (PBO) technique (Bauer et al., 2015) in which the preference is on $\vec{p}$ over $\vec{r}$. With PBO, the coefficients c_ℓ are found by solving the linear system $\min_{\mathbf{c}} \sum_{\ell=1}^{M} c_\ell^2 \omega_\ell^2$ subject to $\mathbf{Qc} = \mathbf{p}$. Here ω_ℓ is a weighting coefficient, defined as $\omega_\ell = \left\| \vec{r}_{\vec{\omega}_\ell} - \vec{r} \right\|_2$. Moreover, the matrix $\mathbf{Q}$ is determined by the synthetic source dipole moments as $\mathbf{Q} = (\tilde{\mathbf{q}}_{\vec{w}_1}, \tilde{\mathbf{q}}_{\vec{w}_2}, \ldots, \tilde{\mathbf{q}}_{\vec{w}_M})$. The minimizer of $\sum_{\ell=1}^{M} c_\ell^2 \omega_\ell^2$ is obtained by implementing the method of Langrangian multipliers, resulting in a uniquely solvable linear system. The number of source dipoles M depends on the source configuration, which is explained in more detail below.

We also test adaptability, i.e., how the number n of the elements in the patch affects the source modeling accuracy for $n = 1, 2, \ldots, 5$. In the simplest case $n = 1$, the sources correspond to the edges of a single tetrahedron (six EW dipoles). For $n = 2, \ldots, 5$, this configuration is extended by including the EW and FI dipoles from the neighboring elements, leading to a total of 10–22 synthetic dipoles (Fig. 2).

In the PBO interpolation scheme, a given dipole position and moment can be estimated with different combinations of the synthetic dipoles (Pursiainen et al., 2016). As a fundamental source configuration we use a set of 22 synthetic FI and EW dipoles corresponding to a five-element patch: a center tetrahedron together with its facial neighbors (Fig. 1). To avoid forward modeling errors due to discontinuities in the electrical conductivity distribution, those elements which do not belong to the gray matter are excluded from the configuration (Fig. 1). That is, in the vicinity of the boundary of the brain, fewer elements and sources are used in the interpolation.

In the partial integration method, the element patch consists of a single element which is assumed to contain the dipole source. The St. Venant approach is to place monopolar sources at the nodes of the element patch, so that their net effect corresponds to that of the given dipole. The ball-like patch is formed as the set of all the elements sharing the node that is closest to the dipole location. This strategy usually results in around 20 elements in an unstructured tetrahedral mesh. Fig. 3 shows that approximately one half of the elements are taken out of the final patch on the gray matter boundary.

2.3. Implementation in duneuro

As a platform of forward computations, we utilized the C++ based toolbox DUNE (Blatt and Bastian, 2007; Blatt et al., 2016; Bastian et al., 2008a; b). In fact, the implementation was created for the *duneuro* module (Nüßing et al., 2016; Engwer et al., 2017; Vorwerk et al., 2017), which is a DUNE based toolbox for bioelectromagnetic (EEG, MEG, tES) forward modeling. The divergence conforming H(div) source model was newly implemented whereas the scripts for the partial integration and St. Venant methods already existed in the toolbox.

As modular platforms, *DUNE/duneuro* are well-suited for implementing the H(div) source model together with the PBO interpolation approach. *DUNE* includes numerous lower level routines for handling the FE mesh and basis functions which can be effortlessly applied in the actual script. In the present case, the most central requirement for the programming environment is the ability to easily find the elements belonging to different tissue compartments and to identify the facial neighbors of a given center tetrahedron. In *DUNE*, these operations can be handled through the basic modules.

The algorithm for the EEG forward modeling numerical analysis with *duneuro* is presented in Fig. 4. The algorithm starts by creating a driver object which serves as the main interface to the *duneuro* module. This is done by defining the grid type, and the nodes, elements, and layer labels and conductivity values for each element. Next, the electrodes are passed to the driver object, and the algorithm can compute the transfer matrix. Then, the dipole set is delivered to the driver, and the source model is selected. After that, the toolbox can compute the potential values at the electrode locations. Furthermore, the analytical solution is calculated, and the statistics are then created for error measures. Finally, the error statistics are illustrated with MATLAB - boxplot[3] function.

[3] MATLAB, version 9.1 (R2016b), The MathWorks Inc., Natick, Massachusetts.

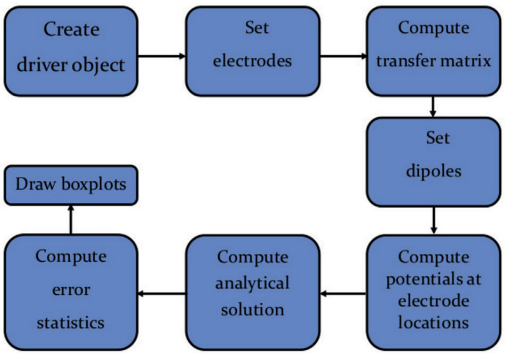

Fig. 4. The general algorithm for *duneuro* EEG forward problem implementation.

The FE mesh was chosen to be an unstructured and conforming tetrahedral mesh based on the *DUNE-ALUGrid* module (Alkämper et al., 2016). The weak form of the forward problem was discretized with the *DUNE-PDELab* module (Bastian et al., 2010).

The linear system was solved using an iterative preconditioned conjugate gradient method (PCG) equipped with an algebraic multigrid preconditioner (AMG) which uses a symmetric successive over relaxation (SSOR) as a smoother (Blatt, 2010). The stopping criteria for the PCG, i.e., the relative residual 2-norm, was set to 10^{-8}.

A source model function was implemented for H(div) sources that form the load vector $\mathbf{f}$ (right-hand side) of the forward problem. It proceeds as follows:

1. The position and moment of a given dipole are send to the source model.
2. *DUNE* detects the element in which the dipole is located and computes the EW source dipoles for that element.
3. The method loops through the neighboring elements with the help of the *intersections* function in *DUNE*, and computes the corresponding FI and EW source dipoles. This is done recursively until the required number of source elements is reached.
4. The generated source dipoles are delivered to the PBO interpolation method, and the resulting coefficients are used for computing the load vector $\mathbf{f}$, which represents the current field approximation in the global mesh.
5. Finally, the load vector $\mathbf{f}$ is passed to a solver that computes the corresponding potential distribution.

2.4. Numerical experiments

The spherical FE mesh applied in this study is presented in Fig. 5. It consists of 5.6 M elements and 0.9 M nodes and altogether six compartments: Brain layers 1–3 (white, dark gray, green), CSF (purple), Skull (blue), and Scalp (yellow). This mesh was designed based on the isotropic four-layered Stok model (Stok, 1987) (Brain, CSF, Skull, Scalp) specifically for evaluating how the source models perform in the 2 mm thick Brain 3 (gray matter) layer (green). The radii and conductivity values for all compartments can be found in Table 1. A similar 1:80 conductivity ratio between the skull and the brain has been recently used, e.g., in (Aydin et al., 2014).

The FE mesh was generated using the Gmsh software,[4] and it was refined towards the surface of the brain. The longest and shortest edge length in the mesh were 3.9 and 0.31 mm, respectively.

The accuracy of the FE solution was measured against the analytical solution, which can be obtained for a multi-layered sphere. Both the analytical and numerical solution were evaluated at 120 electrodes evenly distributed over the scalp layer. We generated two sample sets, each one consisting of 200 dipole sources with random orientations. The dipoles of the first set were located at 1.5 mm distance from the outer gray matter boundary, i.e., at the relative radius (eccentricity) of 98% with respect to the surface of the brain. The second set contained dipoles at 0.078 mm distance, that is, at an eccentricity of 99.9%. Due to the previous study about deeper lying sources by (Pursiainen et al., 2016), the interest was mostly on superficial areas of cortex in this study. That is the reason for considering 1.5 mm and 0.078 mm source dipoles in line with numerical approaches, i.e., RDM and MAG, which demonstrated that the less eccentric sources are, the lower is the numerical error, which leads to more focal sources regarding to the multi-layered sphere model.

2.5. Error measures

The analytical potential values were computed harnessing the method of De Munck and Peters (de Munck and Peters, 1993). The accuracy of the H(div) model was compared to that of the reference techniques, the St. Venant (Buchner et al., 1997; Toupin, 1965) and the partial integration method (Yan et al., 1991; Weinstein et al., 2000). The relative difference (RDM) and magnitude (MAG) measure (Pursiainen et al., 2016), defined below, were evaluated in percents.

$$\mathrm{RDM}(\mathbf{y}_{\mathrm{ana}}, \mathbf{y}_{\mathrm{num}}) = 50\left\| \frac{\mathbf{y}_{\mathrm{ana}}}{\|\mathbf{y}_{\mathrm{ana}}\|_2} - \frac{\mathbf{y}_{\mathrm{num}}}{\|\mathbf{y}_{\mathrm{num}}\|_2} \right\|_2 \tag{7}$$

$$\mathrm{MAG}(\mathbf{y}_{\mathrm{ana}}, \mathbf{y}_{\mathrm{num}}) = 100\left(\frac{\|\mathbf{y}_{\mathrm{num}}\|_2}{\|\mathbf{y}_{\mathrm{ana}}\|_2} - 1 \right). \tag{8}$$

The RDM reflects the topographical forward modeling error in terms of location and orientation. The MAG reveals the variations in potential amplitude or, in other words, alterations in the source strength.

The error measures are presented as box plots (Kirkman, 1996) which describe the lower (25%), middle (50%), and upper (75%) quartiles with a box graph. The thicker part shows the inter quartile range (IQR or spread) between 25% and 75% quartile. The median, i.e., the 50% quartile, is shown as a horizontal line in the IQR. The vertical lines, whiskers, show the maximum and minimum values of the dataset. Here the whiskers are limited with the 1.5IQR rule, i.e., their maximal extent is 1.5 times the length of the IQR, and the rest of the dataset is marked as outliers. Furthermore, the statistically significant mutual differences for RDM and MAG values were evaluated with the Mann Whitney *U* test (Mann and Whitney, 1947) with the confidence level of 95%.

2.6. Inversion test with a realistic geometry

In order to highlight the differences of the examined source models and the impact of the presented numerical forward errors, we performed an inverse investigation in a realistic head model. The motivation was that the adaptive H(div) FEM source model might help to interpret reconstructions by preventing deteriorated (e.g. spotty) inverse results which might occur as a result of minimum norm estimation (MNE) within a thin cortex. A head segmentation of a healthy 24 year old male subject obtained via T1-and T2-weighted magnetic resonance images (Pursiainen et al., 2012) was utilized to test the potential of the present H(div) approach in reconstructing the brain activity. The following seven different isotropic conductivity (S/m) compartments were distinguished: skin (0.43 S/m), the compact and spongious bone of the skull (0.0064 and 0.028 S/m, respectively), cerebrospinal fluid (1.79 S/m), gray matter (0.33 S/m), white matter (0.14 S/m), and eyes (0.505 S/m). Justification of conductivity values can be found, e.g., in (Dannhauer et al., 2011). The

[4] http://gmsh.info.

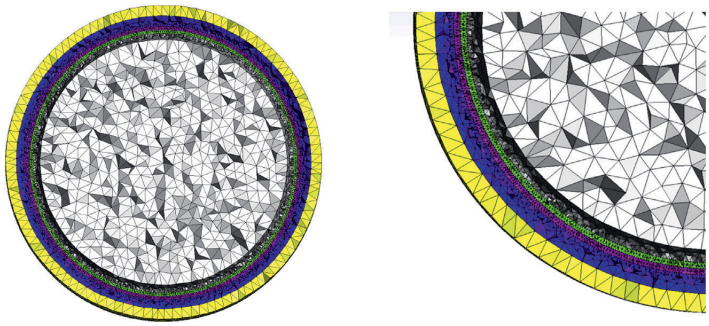

Fig. 5. A visualization of the spherical grid used for modeling.

Table 1
The sphere radii and conductivity values for all mesh compartments.

Compartment	Radius (mm)	Conductivity (S/m)
Scalp	92	0.33
Skull	86	0.0042
CSF	80	1.79
Brain 3 (Gray Matter)	78	0.33
Brain 2	76	0.33
Brain 1	72	0.33

segmentation was discretized by generating a regular tetrahedral grid with the element size 0.85 mm via the open source *Zeffiro* toolbox,[56] Matlab (The MathWorks, Inc.). The total number of elements and nodes in the resulting FE mesh was 37.9 M and 6.45 M, respectively.

The lead field matrix was computed for 0.5 M randomly chosen source positions with Cartesian orientations. Two different source sets (A) and (B) were used. In the first one of these, the sources were placed deep in the gray matter compartment. In the second one, the source positions extended also to the surface of the gray matter, i.e., part of the sources were associated with the surface tetrahedra. The following two current preserving source modeling strategies were tested: (i) non-adaptive H(div), i.e., the basic five-element configuration $n = 5$, and (ii) adaptive H(div) in which the configuration was adapted ($n = 1, 2, \ldots,$ 5) according to the local mesh geometry. Of (i) and (ii), the latter allows a more focal source placement, meaning that the source distribution extends closer to the surface of the gray matter compartment. For comparison, reconstructions for the sets (A) and (B) were also computed with the partial integration and St. Venant source modeling approach. The latter one of these was adapted as shown in Fig. 3 to enable source modeling in the vicinity of the boundary for the set (B).

The measurement data, i.e., the potential values $\mathbf{y}$, were simulated for a normally oriented source in Brodmann area 1 of the right somatosensory cortex (Fig. 6). Gaussian zero mean noise with 5% relative standard deviation with respect to the maximal data entry was added to the simulated measurements. The reconstruction was computed via one and two steps of the iterative alternating sequential (IAS) iteration (Calvetti et al., 2009; Lucka et al., 2012; Pursiainen, 2012) by setting the shape and scaling parameter to 1.5 and 1E-3, respectively. With the present choice of the shape parameter, the one- and two-step IAS estimate constitute an ℓ^2- and ℓ^1-regularized estimate, i.e., a minimum norm and minimum current estimate (MNE and MCE), respectively (Calvetti et al., 2009; Uutela et al., 1999).

[5] https://github.com/sampsapursiainen/zeffiro-interface/wiki.
[6] https://se.mathworks.com/matlabcentral/fileexchange/68285.

3. Results

The results of the numerical analysis have been included in Figs. 7, 8 and 9 as well as Tables 2 and 3.

It can be observed that, for the H(div) model, the forward simulation accuracy increases along with the number of elements in the source configuration. The smallest median RDM (0.28 and 0.26% for 98 and 99.9% eccentricity, respectively) is obtained with the five-element patch. Furthermore, the spread (IQR) of the RDM decreases as the source count grows. The results of the Mann-Whitney test suggest that, compared to the single-element source configuration, a (statistically) significant improvement in RDM can be obtained, when $n \geq 2$ and $n \geq 3$ for the eccentricity of 98 and 99.9%, respectively. For MAG, the spread decreases, when the number of the elements increases, but there is no such clear tendency for the median. The median differences were, however, found to be mainly insignificant based on the Mann-Whitney test.

In comparison between the H(div) approach and the St. Venant and partial integration method, the single-element H(div) was found to yield generally very similar results with the partial integration. At 98% eccentricity, the St. Venant method achieved a median RDM of 0.30% which is close to the value obtained with the five-element divergence conforming scheme. At 99.9% eccentricity, the difference was more obvious in favor of the H(div) model, as the median RDM for the St. Venant approach in that case was 0.44%. With respect to the MAG, the St. Venant was the superior method at 98% eccentricity, but not at 99.9%, where its performance was marginally weaker than that of the five-element H(div). According to the U test, the MAG differences at 99.9% eccentricity were statistically insignificant, and, therefore, those have been omitted in Table 2.

An obvious reason for the deteriorated performance of the St. Venant approach at the eccentricity of 99.9% can be found in Table 3, showing that the source element patch was significantly restricted in that case: the median for the number of elements in the patch was 20 and 10 for 98 and 99.9% eccentricity, respectively. For comparison, maximally one element was restricted out of the patch in the H(div) approach.

In the inversion test involving H(div) sources (Figs. 8 and 9), both the (i) non-adaptive ($n = 5$) and (ii) adaptive ($n = 1, 2, \ldots, 5$) technique enabled reconstructing the synthetic somatosensory source. The smoother reconstruction and superior focality was obtained with the source set (A) which is especially clear in the case of the ℓ^2-estimate. Namely, for (B), the set in which the ℓ^2-estimate essentially differs from zero extends up to 10 mm further away from the actual source position. Nevertheless, the ℓ^1-estimate converges towards the actual source position for both (A) and (B) resulting in a well-localized reconstruction. The results suggest that, of the tested source modeling techniques, the H(div) approach produces, generally, the smoothest distribution, which is more regular in the active area, than what is obtained with the partial integration and St. Venant method. In particular, the H(div)-based

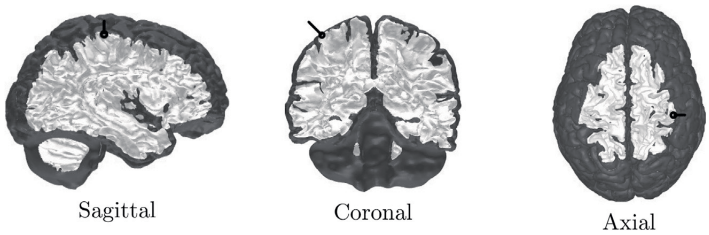

Fig. 6. Placement of a normally oriented source in Brodmann area 1 of the right somatosensory cortex in sagittal, coronal and axial projection (left, center and right, respectively). The actual source position and orientation is shown by the black circle and line segment, respectively.

Table 2
The results of the Mann-Whitney *U* test for restricted source models with *n* elements, for partial integration, and for St. Venant with 200 dipoles. The MAG results have been omitted for 99.9% eccentricity, since all the differences were insignificant in that case.

RDM at 98% eccentricity							
	n = 1	n = 2	n = 3	n = 4	n = 5	PI	St.V.
n = 1		*	*	*	*		*
n = 2	*		*	*	*	*	*
n = 3	*	*		*	*	*	*
n = 4	*	*	*		*	*	
n = 5	*	*	*	*		*	
PI		*	*	*	*		*
St.V.	*	*	*			*	
MAG at 98% eccentricity							
	n = 1	n = 2	n = 3	n = 4	n = 5	PI	St.V.
n = 1		*					*
n = 2	*				*	*	
n = 3							
n = 4							
n = 5		*					*
PI		*					*
St.V.	*				*	*	
RDM at 99.9% eccentricity							
	n = 1	n = 2	n = 3	n = 4	n = 5	PI	St.V.
n = 1			*	*	*		*
n = 2				*	*		*
n = 3	*					*	*
n = 4	*	*				*	*
n = 5	*	*				*	*
PI			*	*	*		*
St.V.	*	*	*	*	*	*	

Table 3
The number of the source elements (source element patch size) for each source model type in the numerical experiments.

At 98% eccentricity				
	min	max	median	mean
PI	1	1	1	1
St. V.	14	36	20	21.31
n = 1	1	1	1	1
n = 2	2	2	2	2
n = 3	3	3	3	3
n = 4	4	4	4	4
n = 5	5	5	5	5
At 99.9% eccentricity				
	min	max	median	mean
PI	1	1	1	1
St. V.	5	17	10	10.57
n = 1	1	1	1	1
n = 2	2	2	2	2
n = 3	3	3	3	3
n = 4	4	4	4	4
n = 5	4	5	4	4.12

reconstruction was the most intense and least spotty near the actual source position in the case (B), i.e., when the source distribution extended to the boundary. Overall, the results suggest that the H(div) approach is more regular and topographically stable compared to St. Venant and partial integration.

4. Discussion

This article presented, validated and evaluated an adaptable open source implementation of the current preserving (divergence conforming) H(div) model (Tanzer et al., 2005; Pursiainen et al., 2016; Bauer et al., 2015) for EEG forward computations (Brette and Destexhe, 2012) in unstructured tetrahedral grids. The H(div) approach is advantageous in modeling the primary current field generated by the neural activity, since it achieves the best balance between realism, focality, numerical accuracy and computational speed with regard to source placement in the thin and geometrically complex gray matter compartment, which is on average only slightly more than 2 mm thick (Griffis et al., 2016; Fischl and Dale, 2000; McGinnis et al., 2011). Especially, this is the case for exceptionally thin cortical compartments as can be found in children, infant and neonate brain research (Li et al., 2014; Hämäläinen et al., 2015; Roche-Labarbe et al., 2008) and/or in pathological situations (Seitz et al., 2014).

A function for the present source model was written for the C++ based *duneuro* library, which is integrated in *DUNE*. This function was evaluated numerically against the competing source models St. Venant (Buchner et al., 1997; Toupin, 1965; Medani et al., 2015; Medani, 2016) and partial integration (Yan et al., 1991; Weinstein et al., 2000), which are also implemented in *duneuro*. *duneuro* and *DUNE* were found to be suitable platforms for our research purpose, as they are openly accessible state-of-the-art modeling packages for bioelectromagnetic (EEG, MEG, tES) forward modeling (Nüßing, 2018; Nüßing et al., 2016; Engwer et al., 2017; Vorwerk et al., 2017), and, more generally, for solving partial differential equations (Blatt and Bastian, 2007; Blatt et al., 2016; Bastian et al., 2008a; b), respectively. Their modular structures allow easy operation of the lower level code and, thereby, enable the handling of the FE mesh and basic functions effortlessly such as, e.g., tracking the local mesh structure in the neighborhood of a given element, which was essential for this implementation. *duneuro* also offers mathematically advanced FE based EEG, MEG and tES forward modeling: In addition to the present classical continuous Galerkin (CG-FEM) approach, it also offers discontinuous Galerkin (DG-FEM) (Engwer et al., 2017), unfitted FEM approaches such as CUTFEM (Nüßing, 2018) and unfitted DG-FEM (Nüßing et al., 2016), and Mixed-FEM computations (Vorwerk et al., 2017). Especially, in the latter one of these, the primary source current is inherently assumed to be divergence conforming. Hence, a further optimization of the H(div) model can be considered.

Our code was evaluated numerically using a six-compartment spherical domain obtained by subdividing the brain compartment of the classical isotropic four-layered Stok model (Stok, 1987) into three

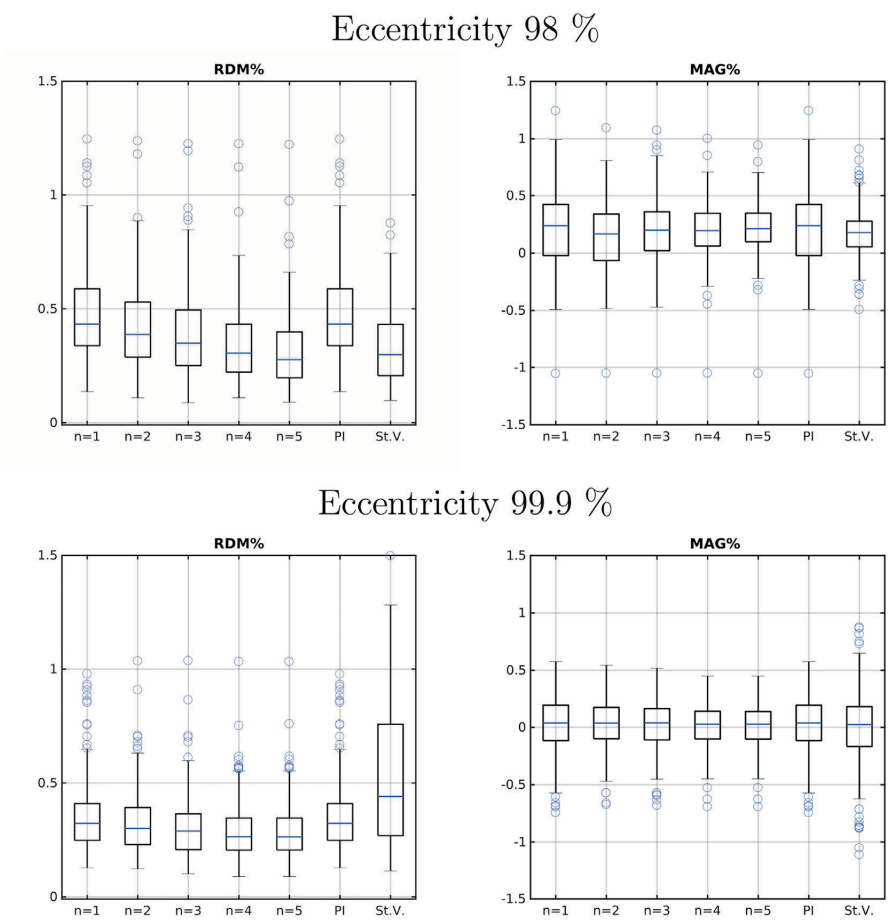

Fig. 7. The RDM and MAG errors for divergence conforming source models with n elements, for partial integration and for St. Venant tested with 200 dipoles at eccentricity 98% (top row) and 99.9% (bottom row).

parts. The outermost brain compartment modeled an only 2 mm thin gray matter layer. Akin to a realistic setting, all the elements in the patch of the source configuration belonged to this compartment. If necessary, a restricted patch was used. Our goal was to find out how the H(div) forward model performs in the vicinity of the gray matter boundary, where a restriction has to be made and the discontinuity of the electrical conductivity distribution between the brain and the CSF compartment can diminish the accuracy of the forward simulation. The relative difference and magnitude measures (RDM and MAG) were evaluated for two sets of 200 dipoles with random positions and orientations. One of these sets was located at the eccentricity of 98%, i.e., a source depth of 1.5 mm, which is typical in a realistic scenario. The other one concerned the eccentricity of 99.9%, i.e., an extraordinary shallow depth of about 0.1 mm, reflecting an exceptional situation in which the element patch of the source current needs to be placed very close to the surface of the gray matter. In realistic volume conductor modeling, these capabilities are vital as the cortex of healthy subjects is on average only slightly more than 2 mm thick (Griffis et al., 2016; Fischl and Dale, 2000; McGinnis et al., 2011) or even thinner such as in children, infant or neonate studies (Li et al., 2014; Hämäläinen et al., 2015; Roche-Labarbe et al., 2008), in pathological situations (Seitz et al., 2014) or in just segmentation related issues.

Of the present evaluated source models, the H(div) approach was found to be overall superior compared to the St. Venant and partial integration. With respect to RDM, the performance differences between the methods were significant based on the results of both boxplot analysis and the Mann-Whitney's significance test (U test). Nevertheless, the MAG differences were found to be mainly not crucial, suggesting that all three models yield essentially the same performance with respect to the magnitude.

Concentrating on the RDM, the modeling accuracy was observed to increase along with the number of elements in the source patch. The results obtained with a single-element ($n = 1$) patch were largely similar to those produced by the partial integration routine which is also based on a single element. It seems that a statistically significant improvement compared to the simplest $n = 1$ case can be obtained using a patch of three or more elements regardless of the eccentricity. The most significant difference to the St. Venant method was observed at 99.9% eccentricity which necessitated restricting the St. Venant's element patch into one half of its normal composition (a ball-like object cut into half) and, consequently, led to a considerably deteriorated RDM. Nevertheless, for H(div), only a minor single-element restriction was needed without a notable decrease in the performance. Thus, it seems that the patch formed around a given center element is advantageous with regard to source placement close to a boundary.

Skull conductivity is an important parameter in EEG source analysis.

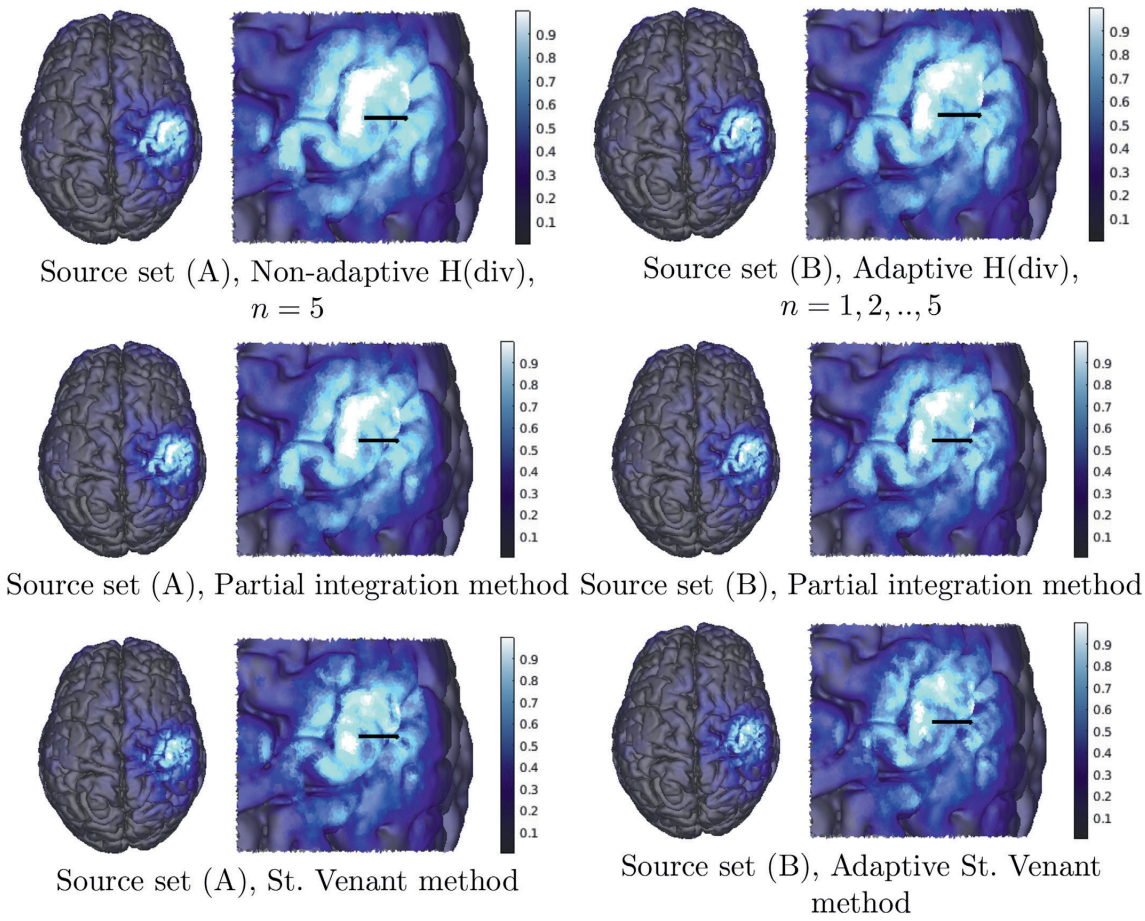

Fig. 8. The ℓ^2-regularized reconstructions (minimum norm estimates) of the primary current distribution for two source sets (A) and (B) in which the sources are positioned deep and everywhere in the gray matter compartment, respectively. The top row shows the results obtained with (i) the H(div) ($n = 5$) and (ii) the adaptive ($n = 1, 2, .., 5$) H(div) source model (left and right, respectively). The center row corresponds to the partial integration method, and the bottom row to the non-adaptive and adaptive version of the St. Venant method, respectively. Notice that as the partial integration method utilizes only a single element, it cannot be adapted akin to the H(div) and St. Venant model. The actual source position and orientation is shown by the left tip and the stem of the black line segment, respectively.

In the present multi-layered simulation study a conductivity of 0.0042 S/m for the skull layer and 0.33 S/m for the gray matter layer was chosen, i.e., a skull/brain conductivity ratio of about 1:80 was considered. This is the classical ratio (Homma et al., 1995), which is still used as a default in commercial software packages, see, e.g, (Fuchs et al., 1998). For higher skull/brain conductivity ratios as proposed by (Dannhauer et al., 2011), all presented numerical errors and, therefore, also the differences between the examined dipole modeling approaches decrease in both normal and tangential orientations. A better way for skull modeling might, however, be to distinguish the lower conducting skull compacta and higher conducting skull spongiosa compartments (Dannhauer et al., 2011; Montes-Restrepo et al., 2014) and to individually estimate their conductivity parameters. This has recently been done using a skull conductivity calibration procedure based on combined somatosensory evoked potential (SEP) and field (SEF) measurements, where estimated conductivity values were 0.0024 S/m and 0.0084 S/m in one (Aydin et al., 2014) and 0.0033 S/m and 0.0116 S/m in another epilepsy patient (Aydin et al., 2017) for the skull compacta and spongiosa compartments, respectively. This shows that individual differences in skull conductivity parameters have to be expected, which will significantly influence EEG based source analysis. In addition to the skull, also the white matter is important regarding the source modeling accuracy, especially, since the real white matter conductivity includes anisotropy (Wolters et al., 2006; Güllmar et al., 2010; Vorwerk et al., 2014). The actual effect of the anisotropy to the accuracy may be expected to depend strongly on source position and orientation, whereas the current model only reflects the average effect. Overall, we expect that the mutual performances between the investigated source models will be maintained for a wide range of conductivities, since the conductivity distribution is primarily a parameter for the system matrix, whereas the source model mainly reflects the accuracy of the right-hand-side vector of the forward problem.

Our validation results together with the inversion test suggest that our implementation can be beneficial for complex 3D meshes. It allows an extremely focal single-element source placement with the accuracy of the partial integration, which can be necessary at some locations in a realistic volume conductor. Additionally, if the local geometry allows using the full source configuration, then the accuracy of the St. Venant can be surpassed. Thus, a close to optimal accuracy can be achieved in each

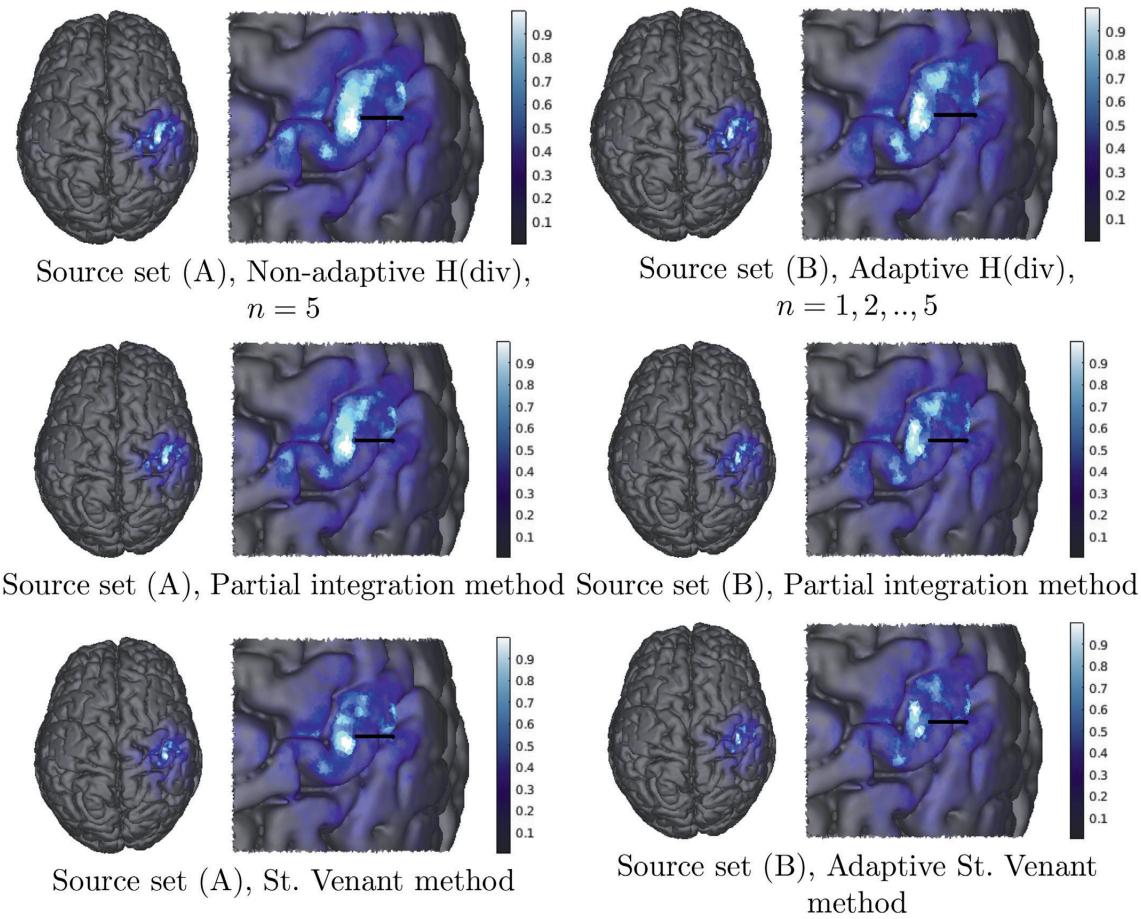

Fig. 9. The ℓ^1-regularized reconstructions (minimum current estimates) of the primary current distribution for two source sets (A) and (B).

situation without the need to choose between different source models. Based on the present numerical analysis, the non-adaptive H(div) source modeling approach (i) is more robust than the adaptive one (ii) and is, therefore, preferable for a normal cortex thickness, which is on average 2.3 mm (Griffis et al., 2016; McGinnis et al., 2011; Fischl and Dale, 2000). However, (ii) was found to be sufficient for special cases e.g. with extremely thin cortices.

In de Munck et al. (1988), it was presented that the mathematical point dipole, due to its over-focal nature, results in modest, but systematic errors for depth localization when compared to a more realistic and slightly more extended source model. Using the subtraction approach, the point dipole can also be modeled with its full focality in a FEM framework, but it is known that numerical errors might get significant in thin cortices where sources are very close to the next conductivity discontinuity and that it is currently still computationally expensive (Bertrand et al., 1991; Awada et al., 1997; Marin et al., 1998; Schimpf et al., 2002; Drechsler et al., 2009). In this paper, we showed that H(div)-type source models can be constructed in a way that is more realistic than the mathematical point dipole with regard to extent, but as accurate in multi-layer sphere model validations. In addition, the H(div) source models were found to be also focal enough to be induced in even thin cortices. As already mentioned, this feature is crucial in healthy subjects, but especially in children, infant and neonate EEG brain research or in pathological situations. In summary, the best H(div) source thus has the best balance between numerical accuracy, computational efficiency and modeling accuracy, i.e., focal enough to be usable in thin cortices, but less focal and thus more realistic than the mathematical point dipole.

An important future work will be to evaluate the present current preserving source model implementation in a group study with real EEG data and realistic FEM head models. To do so, the *duneuro* library will be coupled, for instance, with the *FieldTrip*[7] or *BrainStorm*[8] toolboxes, similar to the interface that has already been realized for the *duneuro*-predecessor *SimBio*[9] (Vorwerk et al., 2018). Likewise, both Python and Matlab bindings already exist for *duneuro*. Further analysis of the relationship between the presented source model and realistic physiological structures, e.g., thin cortices and anisotropy, will be necessary.

5. Conclusions

The purpose of this study was to improve EEG source analysis using finite element method (FEM) head volume conductor models that extend

[7] FieldTrip: http://www.fieldtriptoolbox.org.
[8] BrainStorm: http://neuroimage.usc.edu/brainstorm.
[9] SimBio: https://www.mrt.uni-jena.de/simbio.

the standard three compartment approach, and are able to take brain tissue inhomogeneity (gray and white matter and cerebrospinal fluid) into account. The focus was on determining the performance of the present current preserving H(div) source model which was implemented into the open source *duneuro* library for FEM forward modeling in bioelectromagnetism, and validated through numerical experiments for source configurations corresponding to $n = 1, \ldots, n = 5$ elements in the FEM mesh. The accuracy of the model was measured against an analytical solution in a multi-layer sphere model. The performance achieved was evaluated with two competing methods, partial integration and St. Venant. The results obtained within a spherical multi-layered domain suggest that our new approach provides a solid way to model the primary current distribution in the thin cortical compartment, and even in situations of exceptionally thin cortices. A superior performance was achieved in the vicinity of the outer gray matter boundary, in particular, as compared to the St. Venant reference method. The modeling precision was found to improve significantly as the size of the source modeling patch grew from one to three or more elements. No significant performance differences were observed between the four- and five-element patches when the sources were located close to the outer gray matter boundary. We also performed an inversion test suggesting that our development can be used to improve EEG forward modeling for realistic multi-compartment head models, and it might be of special importance in situations of thin cortices, e.g., in children and/or pathological applications.

Acknowledgements

TM was supported by SP's Tenure Track project funding, Tampere University of Technology, Finland. TM, DU, AR, and SP were supported by the Academy of Finland Key project (project 305055) and by the Academy of Finland Centre of Excellence in Inverse Problems Research (312341). AN, CE and CHW were partially supported by EU project ChildBrain (Marie Curie Innovative Training Networks, grant agreement 641652), by the Deutsche Forschungsgemeinschaft, project WO1425/7-1, by the DFG priority program SPP1665, project WO1425/5-2, and the DFG Cluster of Excellence 1003 (DFG EXC 1003 Cells in Motion). AR, CHW, and SP were supported by the Deutscher Akademischer Austauschdienst via funding from the Bundesministerium für Bildung und Forschung.

References

Ainsworth, M., Coyle, J., 2003. Hierarchic finite elements for unstructured tetrahedral meshes. Int. J. Numer. Meth. Eng. 58, 2103–2130.
Alkämper, M., Dedner, A., Klöfkorn, R., Nolte, M., 2016. The DUNE-ALUGrid module. Archive of Numerical Software 4 (1).
Awada, K.A., Jackson, D.R., Williams, J.T., Wilton, D.R., Baumann, S.B., Papanicolaou, A.C., 1997. Computational aspects of finite element modeling in EEG source localization. IEEE (Inst. Electr. Electron. Eng.) Trans. Biomed. Eng. 44 (8), 736–752.
Aydin, Ü., Rampp, S., Wollbrink, A., Kugel, H., Cho, J.-H., Knösche, T., Grova, C., Wellmer, J., Wolters, C., 2017. Zoomed MRI guided by combined EEG/MEG source analysis: a multimodal approach for optimizing presurgical epilepsy work-up and its application in a multi-focal epilepsy patient case study. Brain Topogrry 30 (4), 417–433.
Aydin, Ü., Vorwerk, J., Küpper, P., Heers, M., Kugel, H., Galka, A., Hamid, L., Wellmer, J., Kellinghaus, C., Rampp, S., et al., 2014. Combining EEG and MEG for the reconstruction of epileptic activity using a calibrated realistic volume conductor model. PLoS One 9 (3) e93154.
Bastian, P., Blatt, M., Dedner, A., Engwer, C., Klöfkorn, R., Kornhuber, R., Ohlberger, M., Sander, O., 2008a. A generic grid interface for parallel and adaptive scientific computing. Part I: abstract framework. Computing 82 (2–3), 103–119.
Bastian, P., Blatt, M., Dedner, A., Engwer, C., Klöfkorn, R., Kornhuber, R., Ohlberger, M., Sander, O., 2008b. A generic grid interface for parallel and adaptive scientific computing. Part II: implementation and tests in DUNE. Computing 82 (2–3), 121–138.
Bastian, P., Heimann, F., Marnach, S., 2010. Generic implementation of finite element methods in the distributed and unified numerics environment (DUNE). Kybernetika 46 (2), 294–315. URL. http://eudml.org/doc/197255.
Bauer, M., Pursiainen, S., Vorwerk, J., Köstler, H., Wolters, C.H., 2015. Comparison study for Whitney (Raviart-Thomas) type source models in finite element method based EEG forward modeling. IEEEEngineering(Inst. Electr. Electron. Eng.) Trans. Biomed. Eng. 62 (11), 2648–2656.
Bertrand, O., Thévenet, M., Perrin, F., 1991. 3D finite element method in brain electrical activity studies. In: Nenonen, J., Rajala, H., Katila, T. (Eds.), Biomagnetic Localization and 3D Modelling. Report of the Dep. of Tech.Physics. Helsinki University of Technology, pp. 154–171.
Blatt, M., 2010. A Parallel Algebraic Multigrid Method for Elliptic Problems with Highly Discontinuous Coefficients. Dissertation, Heidelberg University. URL. http://www.ub.uni-heidelberg.de/archiv/10856.
Blatt, M., Bastian, P., 2007. The Iterative Solver Template Library. Springer Berlin Heidelberg, pp. 666–675.
Blatt, M., Burchardt, A., Dedner, A., Engwer, C., Fahlke, J., Flemisch, B., Gersbacher, C., Gräser, C., Gruber, F., Grüninger, C., Kempf, D., Klöfkorn, R., Malkmus, T., Müthing, S., Nolte, M., Piatkowski, M., Sander, O., 2016. The distributed and unified numerics environment, version 2.4. Archive of Numerical Software 4 (100), 13–29.
Braess, D., 2001. Finite Elements. Cambridge University Press, Cambridge.
Brette, R., Destexhe, A., 2012. Handbook of Neural Activity Measurement. Cambridge University Press, New York.
Buchner, H., Knoll, G., Fuchs, M., Rienäcker, A., Beckmann, R., Wagner, M., Silny, J., Pesch, J., 1997. Inverse localization of electric dipole current sources in finite element models of the human head. Electroencephalogr. Clin. Neurophysiol. 102 (4), 267–278.
Calvetti, D., Hakula, H., Pursiainen, S., Somersalo, E., 2009. Conditionally Gaussian hypermodels for cerebral source localization. SIAM J. Imag. Sci. 2 (3), 879–909.
Dannhauer, M., Lanfer, B., Wolters, C.H., Knösche, T.R., 2011. Modeling of the human skull in EEG source analysis. Hum. Brain Mapp. 32, 1383–1399.
de Munck, J., Peters, M., 1993. A fast method to compute the potential in the multisphere model. IEEE Trans. Biomed. Eng. 40 (11), 1166–1174.
de Munck, J., van Dijk, B., Spekreijse, H., 1988. Mathematical dipoles are adequate to describe realistic generators of human brain activity 35 (11), 960–966.
Drechsler, F., Wolters, C., Dierkes, T., Si, H., Grasedyck, L., 2009. A full subtraction approach for finite element method based source analysis using constrained delaunay tetrahedralisation. Neuroimage 46 (4), 1055–1065.
Engwer, C., Vorwerk, J., Ludewig, J., Wolters, C.H., 2017. A discontinuous Galerkin method to solve the EEG forward problem using the subtraction approach. SIAM J. Sci. Comput. 39 (1). URL. http://epubs.siam.org/doi/abs/10.1137/15M1048392.
Fischl, B., Dale, A.M., 2000. Measuring the thickness of the human cerebral cortex from magnetic resonance images. Proc. Natl. Acad. Sci. Unit. States Am. 97 (20), 11050–11055.
Fuchs, M., Wagner, M., Wischmann, H.-A., Köhler, T., Theißen, A., Drenckhahn, R., Buchner, H., 1998. Improving source reconstructions by combining bioelectric and biomagnetic data. Clin. Neurophysiol. 107 (2), 93–111.
Gencer, N., Acar, C., 2004. Sensitivity of EEG and MEG measurements to tissue conductivity. Phys. Med. Biol.
Griffis, J.C., Burge, W.K., Visscher, K.M., 2016. Age-dependent cortical thinning of peripheral visual field representations in primary visual cortex. Front. Aging Neurosci. 8, 248.
Güllmar, D., Haueisen, J., Reichenbach, J., 2010. Influence of anisotropic electrical conductivity in white matter tissue on the EEG/MEG forward and inverse solution. A high-resolution whole head simulation study. NeuroImage 145–163. https://doi.org/10.1016/j.neuroimage.2010.02.014.
Hallez, H., Vanrumste, B., Grech, R., Muscat, J., De Clercq, W., Vergult, A., D'Asseler, Y., Camilleri, K.P., Fabri, S.G., Van Huffel, S., et al., 2007. Review on solving the forward problem in EEG source analysis. J. NeuroEng. Rehabil. 4 (1), 46.
Hämäläinen, J.A., Lohvansuu, K., Ervast, L., Leppänen, P.H., 2015. Event-related potentials to tones show differences between children with multiple risk factors for dyslexia and control children before the onset of formal reading instruction. Int. J. Psychophysiol. 95 (2), 101–112.
Haueisen, J., Tuch, D., Ramon, C., Schimpf, P., Wedeen, V., George, J., Belliveau, J., 2002. The influence of brain tissue anisotropy on human EEG and MEG. Neuroimage 15, 159–166.
Homma, S., Musha, T., Nakajima, Y., Okamoto, Y., Blom, S., Flink, R., Hagbarth, K.-E., 1995. Conductivity ratios of the scalp-skull-brain head model in estimating equivalent dipole sources in human brain. Neurosci. Res. 22 (1), 51–55.
Kirkman, T., 1996. Statistics to Use. URL. http://www.physics.csbsju.edu/stats/. (Accessed 2 August 2017).
Li, G., Nie, J., Wang, L., Shi, F., Gilmore, J.H., Lin, W., Shen, D., 2014. Measuring the dynamic longitudinal cortex development in infants by reconstruction of temporally consistent cortical surfaces. Neuroimage 90, 266–279.
Lucka, F., Pursiainen, S., Burger, M., Wolters, C.H., 2012. Hierarchical bayesian inference for the EEG inverse problem using realistic FE head models: depth localization and source separation for focal primary currents. Neuroimage 61 (4), 1364–1382.
Mann, H.B., Whitney, D.R., 1947. On a test of whether one of two random variables is stochastically larger than the other. Ann. Math. Stat. 18 (1), 50–60. URL. https://doi.org/10.1214/aoms/1177730491.
Marin, G., Guerin, C., Baillet, S., Garnero, L., Meunier, G., 1998. Influence of skull anisotropy for the forward and inverse problem in EEG: simulation studies using the FEM on realistic head models. Hum. Brain Mapp. 6, 250–269.
McGinnis, S.M., Brickhouse, M., Pascual, B., Dickerson, B.C., 2011. Age-related changes in the thickness of cortical zones in humans. Brain Topogr. 24 (3–4), 279.
Medani, T., 2016. Contribution a l'amelioration du modele de source dans la methode des elements finis pour la resolution du probleme direct en electroencephalographie. PhD thesis. Universite Pierre et Marie Curie - Paris, Paris, France. VI. NNT : 2016PA066166.
Medani, T., Lautru, D., Ren, Z., Schwartz, D., Sou, G., Apr, 2015. Modelling of brain sources using the modified saint Venant's method in FEM resolution of EEG forward

problem. In: Conference IEEE EMBS Conference on Neural Engineering 2015. 7th International IEEE EMBS Conference on Neural Engineering. Montpellier, France.
Montes-Restrepo, V., van Mierlo, P., Strobbe, G., Staelens, S., Vandenberghe, S., Hallez, H., 2014. Influence of skull modeling approaches on EEG source localization. Brain Topogr. 27, 95–111.
Nüßing, A., 2018. Fitted and Unitted Finite Element Methods for Solving the EEG Forward Problem. dissertation. Ph.D. thesis, Westfälische Wilhelms-Universität Münster, Germany.
Nüßing, A., Wolters, C., Brinck, H., Engwer, C., 2016. The unfitted discontinuous galerkin method for solving the EEG forward problem. IEEE Trans. Biomed. Eng. 63 (12), 2564–2575.
Papageorgakis, C., 2017. Patient Specific Conductivity Models: Characterization of the Skull Bones. Modeling and Simulation. Universite Cote d'Azur. URL. https://hal.inria.fr/tel-01662075.
Pursiainen, S., 2012. Raviart–thomas-type sources adapted to applied eeg and meg: implementation and results. Inverse Probl. 28 (6), 065013.
Pursiainen, S., Lucka, F., Wolters, C., 2012. Complete electrode model in EEG: relationship and differences to the point electrode model. Phys. Med. Biol. 57 (4), 999.
Pursiainen, S., Vorwerk, J., Wolters, C., 2016. Electroencephalography (EEG) forward modeling via H(div) finite element sources with focal interpolation. Phys. Med. Biol. 61 (24), 8502–8520.
Ramon, C., Schimpf, P., Haueisen, J., 2006. Influence of head models on EEG simulations and inverse source localizations. Biomed. Eng. Online 5 (10).
Roche-Labarbe, N., Aarabi, A., Kongolo, G., Gondry-Jouet, C., Dümpelmann, M., Grebe, R., Wallois, F., 2008. High-resolution electroencephalography and source localization in neonates. Hum. Brain Mapp. 29, 167–176.
Schimpf, P., Ramon, C., Haueisen, J., 2002. Dipole models for the EEG and MEG. IEEE Trans. Biomed. Eng. 49 (5), 409–418.
Seitz, J., Buehren, K., von Polier, G., Heussen, N., Herpertz-Dahlmann, B., Konrad, K., 2014. Morphological Changes in the Brain of Acutely Ill and Weight-recovered Patients with Anorexia Nervosa: a Meta-analysis and Qualitative Review, 42, pp. 7–18, 01.
Stok, C.J., 1987. The influence of model parameters on EEG/MEG single dipole source estimation. IEEE Trans. Biomed. Eng. 34, 289–296.
Tanzer, O., Järvenpää, S., Nenonen, J., Somersalo, E., 2005. Representation of bioelectric current sources using Whitney elements in the finite element method. Phys. Med. Biol. 50, 3023–3039.
Toupin, R., 1965. Saint-Venant's principle. Arch. Ration. Mech. Anal. 18 (2), 83–96.
Uutela, K., Hämäläinen, M., Somersalo, E., 1999. Visualization of magnetoencephalographic data using minimum current estimates. Neuroimage 10, 173–180.
Vorwerk, J., Cho, J.H., Rampp, S., Hamer, H., Knösche, T.R., Wolters, C.H., 2014. A guideline for head volume conductor modeling in EEG and MEG. Neuroimage 100, 590–607.
Vorwerk, J., Clerc, M., Burger, M., Wolters, C., 2012. Comparison of boundary element and finite element approaches to the EEG forward problem. Biomed. Eng./Biomed. Tech. 57 (SI-1 Track-O), 795–798. https://doi.org/10.1515/bmt-2012-4152.
Vorwerk, J., Engwer, C., Pursiainen, S., Wolters, C.H., 2017. A mixed finite element method to solve the EEG forward problem. IEEE Trans. Med. Imag. 36 (4), 930–941.
Vorwerk, J., Oostenveld, R., Piastra, M.C., Magyari, L., Wolters, C.H., 2018. The FieldTrip-Simbio pipeline for EEG forward solutions. Biomed. Eng. Online 17 (37).
Weinstein, D., Zhukov, L., Johnson, C., 2000. Lead-field bases for electroencephalography source imaging. Ann. Biomed. Eng. 28 (9), 1059–1065.
Wolters, C.H., Anwander, A., Tricoche, X., Weinstein, D., Koch, M.A., MacLeod, R.S., 2006. Influence of tissue conductivity anisotropy on EEG/MEG field and return current computation in a realistic head model: a simulation and visualization study using high-resolution finite element modeling. NeuroImage 30 (3), 813–826.
Yan, Y., Nunez, P.L., Hart, R.T., 1991. Finite-element model of the human head: scalp potentials due to dipole sources. Med. Biol. Eng. Comput. 29 (5), 475–481.

PUBLICATION II

Zeffiro User Interface for Electromagnetic Brain Imaging: A GPU Accelerated FEM Tool for Forward and Inverse Computations in Matlab

Q. He, A. Rezaei and S. Pursiainen

Journal of Neuroinformatics 18, 237–250

DOI: 10.1007/s12021-019-09436-9

Neuroinformatics (2020) 18:237–250
https://doi.org/10.1007/s12021-019-09436-9

SOFTWARE ORIGINAL ARTICLE

Zeffiro User Interface for Electromagnetic Brain Imaging: a GPU Accelerated FEM Tool for Forward and Inverse Computations in Matlab

Q. He[1] · **A. Rezaei**[2] · **S. Pursiainen**[2]

Published online: 9 October 2019

Abstract

This article introduces the *Zeffiro* interface (ZI) version 2.2 for brain imaging. ZI aims to provide a simple, accessible and multimodal open source platform for finite element method (FEM) based and graphics processing unit (GPU) accelerated forward and inverse computations in the Matlab environment. It allows one to (1) generate a given multi-compartment head model, (2) to evaluate a lead field matrix as well as (3) to invert and analyze a given set of measurements. GPU acceleration is applied in each of the processing stages (1)–(3). In its current configuration, ZI includes forward solvers for electro-/magnetoencephalography (EEG) and linearized electrical impedance tomography (EIT) as well as a set of inverse solvers based on the hierarchical Bayesian model (HBM). We report the results of EEG and EIT inversion tests performed with real and synthetic data, respectively, and demonstrate numerically how the inversion parameters affect the EEG inversion outcome in HBM. The GPU acceleration was found to be essential in the generation of the FE mesh and the LF matrix in order to achieve a reasonable computing time. The code package can be extended in the future based on the directions given in this article.

Keywords Matlab Interface · Electro-/Magnetoencephalography (EEG/MEG) · Electrical Impedance Tomography (EIT) · Finite Element Method (FEM) · Hierarchical Bayesian Model (HBM)

Introduction

This article introduces the *Zeffiro*[1] interface (ZI) version 2.2 for electromagnetic brain imaging and investigations. ZI aims to provide an accessible and multi-modal open-source platform for finite element method (FEM) (Braess 2001) based forward and inverse computations in the Matlab (TheMathWorks Inc.) environment. The FEM is widely applied for modeling electromagnetic fields in a bounded domain, such as the brain and the head (de Munck et al. 2012; Monk 2003). It allows one to discretize realistic three-dimensional tissue parameter distributions in an accurate way, including advanced features such as complex internal boundary layers and anisotropic tissues such as the fibrous white matter of the brain (Rullmann et al. 2009). The FEM can be applied to model an electromagnetic source within the brain (Pursiainen et al. 2016b; Miinalainen et al. 2019) and, thereby, to construct a lead field (LF) matrix to localize brain activity in electro-/magnetoencephalography (EEG/MEG) (Hämäläinen et al. 1993; Niedermeyer and da Silva 2004).

The same quasi-static set of Maxwell's equations that predicts the electric potential field of a neural source can be applied also to model the effect of current injections, where either direct or alternating currents applied through electrodes act as the source of the electromagnetic field. Such an approach is used, for example, in the electrical impedance tomography (EIT) (Cheney et al. 1999) in which

[1] *Zeffiro* is Italian for a *gentle breeze* referring to the ease of use. The source code of ZI can be accessed at: https://github.com/sampsapursiainen/zeffiro_interface.

✉ A. Rezaei
atena.rezaei@tuni.fi

S. Pursiainen
sampsa.pursiainen@tuni.fi

[1] Information Technology, Faculty of Information Technology and Communication Sciences, Tampere University, P.O. Box 692, 33014 Tampere, Finland

[2] Mathematics and Statistics, Faculty of Information Technology and Communication Sciences, Tampere University, P.O. Box 692, 33014 Tampere, Finland

the goal is to map the conductivity distribution or its perturbations within a given domain. EIT constitutes a nonlinear inverse problem which can be linearized with respect to a given background conductivity distribution to obtain a LF matrix, i.e., a linearized forward model. The FEM is a powerful tool in EIT (Vauhkonen 1997), since it does not set any major restrictions for the conductivity distribution. In contrast, the boundary element method (BEM) (He et al. 1987), which is the predominating method in EEG/MEG, sets the conductivity to be a compartment-wise constant parameter, limiting its practical usage in EIT.

Until recently, the FEM has been considered as computationally heavy for discretizing the complex geometry of the brain. To tackle this issue, ZI uses graphics processing unit (GPU) acceleration. It includes forward solvers for EEG/MEG and linearized EIT as well as a set of inverse solvers based on the hierarchical Bayesian model (HBM) which was introduced for EEG/MEG in Calvetti et al. (2009). The ZI platform and function library has been designed to be easily expandable and to allow implementing virtually any FEM based forward model which can be formulated as a product between a LF matrix and a candidate solution vector.

In this paper, we briefly review the mathematics behind ZI, describe the principal operations and usage, and introduce some central points for the developer perspective. We report the results obtained in EEG and EIT inversion tests performed with real and syntetic data, respectively, and demonstrate numerically how the inversion parameters affect the EEG inversion outcome in HBM.

Methodology

The electric potential field u in the head model Ω is assumed to satisfy the elliptic partial differential equation (PDE) of the form $\nabla \cdot (\sigma \nabla u) = \nabla \cdot \mathbf{J}^p$, where σ is the conductivity distribution of the head and $\mathbf{J}^p$ is the primary current density of the neural activity. This equation follows from the current preservation condition $\nabla \cdot \mathbf{J}^t = 0$ for the total current density $\mathbf{J}^t = \mathbf{J}^p - \sigma \nabla u$, that is, the sum of $\mathbf{J}^p$ and the volume current density $-\sigma \nabla u$. The electromagnetic field within Ω can be evoked either by $\mathbf{J}^p$ acting as the source, which is the case in EEG/MEG, or by an external source, e.g., a current pattern injected through contact electrodes in EIT. The dependence between the measurements $\mathbf{y}$ and the unknown of the inverse problem $\mathbf{x}$ in question, e.g., a source localization problem, is here assumed be of the following linear form

$$\mathbf{L}\mathbf{x} = \mathbf{y} + \mathbf{n}, \tag{1}$$

where $\mathbf{L}$ is the LF matrix and $\mathbf{n}$ is the noise vector. The LF matrices for EEG and linearized EIT inverse problem can be formed as shown in Appendix A.1.

Primary Current Model

ZI utilizes the H(div) source model (Pursiainen et al. 2016b) in which both linear and quadratic basis functions constitute the primary current density $\mathbf{J}^p$. In Miinalainen et al. (2019); Pursiainen et al. (2016b), this model was shown to surpass the accuracy of the classical direct source modeling approaches based on the partial integration and St. Venant's principle and to be especially advantageous for thin cortices as well as for inverting data.

A Cartesian set of source orientations can be obtained from a mesh-based set using the Position Based Optimization (PBO) method (Bauer et al. 2015) with an adaptive (Miinalainen and Pursiainen 2017) 10-source stencil in which 4 face and 6 edge functions are applied for each element containing a source (Pursiainen et al. 2016b). Alternatively, the Whitney model (Bauer et al. 2015), i.e., the 4-source stencil (4 face functions), can be used. Moreover, a set of Whitney functions can be applied without interpolation. That is, the LF matrix can be formed directly using the mesh-based set of basis functions as suggested in Miinalainen and Pursiainen (2017). In each active tissue compartment, the sources can either be normally constrained or unconstrained with respect to the surface of the compartment (Creutzfeldt et al. 1962; Hari et al. 2018). The source positions are randomly (uniformly) distributed in each case.

Conductivity Distribution

The current FE meshing strategy employed in ZI treats the conductivity as an isotropic piecewise (element-wise) constant distribution, i.e., a single scalar value is associated with each element in the FE mesh. However, when evaluating an LF matrix, ZI allows the conductivity distribution σ to be anisotropic, i.e., tensor-valued: the ℓ-th row of the form $(\sigma_{11}, \sigma_{22}, \sigma_{33}, \sigma_{12}, \sigma_{13}, \sigma_{23})$ within a multi-row array is associated with the symmetric conductivity tensor σ_{ij}, $i = 1, 2, 3$, $j = 1, 2, 3$ ($\sigma_{ij} = \sigma_{ji}$) in the ℓ-th element.

HBM

The inverse tools of ZI are based on the HBM (Calvetti et al. 2009; O'Hagan and Forster 2004) which enables finding a reconstrution for the unknown $\mathbf{x}$ as either the posterior maximizer, i.e., *maximum a posteriori* (MAP) or

the conditional mean (CM) of the *posterior* probability density. In HBM, the posterior probability for $\mathbf{x}$ is defined via choosing the standard deviation of a Gaussian likelihood density, the hypermodel, i.e., the gamma (G) or inverse gamma (IG) hyperprior determining the actual prior, and the shape and scale parameter β and θ_0 for the hyperprior. For a given measurement vector $\mathbf{y}$, the Bayes formula (O'Hagan and Forster 2004) for the posterior is of the form

$$p(\mathbf{x} \mid \mathbf{y}) = \frac{p(\mathbf{x})\, p(\mathbf{y} \mid \mathbf{x})}{p(\mathbf{y})} \propto p(\mathbf{x})\, p(\mathbf{y} \mid \mathbf{x}), \tag{2}$$

where $p(\mathbf{x})$ is the prior density and $p(\mathbf{y} \mid \mathbf{x})$ the likelihood function (Schmidt et al. 1999). Here, the noise term $\mathbf{n}$, which together with the forward model (1) implies the likelihood $p(\mathbf{y} \mid \mathbf{x})$, is assumed to be a Gaussian zero-mean random vector with independent entries.

In HBM, the prior can be expressed in the following hierarchical form $p(\mathbf{x}, \mathbf{h}) \propto p(\boldsymbol{\theta})\, p(\mathbf{x} \mid \boldsymbol{\theta})$, where $\boldsymbol{\theta}$ is the primary hyperparameter of the model. The conditional part $p(\mathbf{x} \mid \boldsymbol{\theta})$ of the prior is a zero-mean Gaussian density, whose diagonal covariance matrix is predicted by the hyperprior $p(\boldsymbol{\theta})$. The hyperprior is assumed to have a long-tailed density, implying that $\mathbf{x}$ is likely to be a sparse vector corresponding to a well-localized (focal) volumetric distribution. In ZI, it is either G or IG density (Calvetti et al. 2009), which are controlled by the shape and scale parameter β and θ_0. The G and IG hyperprior can be coupled into a single model in a straightforward way, since the reciprocal θ^{-1} of a G-distributed random variable θ with respect to β and θ_0 is IG-distributed w.r.t. β and θ_0^{-1}.

A description of the IAS algorithm applied in ZI can be found in Appendix B. ZI's CM estimation technique is based on the Gibbs sampler algorithm (Spitzer 1971; Murphy 2012) according to (Calvetti et al. 2009).

Hardware Requirements

ZI is principally designed to be used with a workstation or a high-end desktop computer with tens of gigabytes of RAM, a multi-core CPU and one or more GPUs. When generating the FE mesh and the LF matrix ZI is likely to allocate several gigabytes of RAM. A one-millimeter FE mesh resolution might lead to 64 GB of motherboard RAM and 2–4 GB of GPU RAM allocation during the forward computations. The resulting FE mesh will consist of 3-4 M nodes and 20-30 M elements, and the eventual project size, when stored on a hard disk, will be 0.5–1 GB.

GPU Function

ZI utilizes a GPU to accelerate the FE mesh generation process, forward and inverse computations, source interpolation and decompositions, as well as to speed up 3D visualizations. This is vital in order to achieve a convenient, around one hour computing time for a one-millimeter FE mesh resolution which has been shown to be essential in order to obtain physiologically accurate inverse estimates (Rullmann et al. 2009). A GPU is a parallel processing unit which has somewhat limited RAM compared to the motherboard. It can handle computation intensive operations very effectively, while memory intensive operations should be avoided. The operations related to forward and inverse computations can be accelerated due to the fast processing of matrix-vector products in a GPU. The other GPU operations are mainly based on the acceleration of `find` and `sort` routines, evaluating those as blocks rather than individual entries.

Forward Simulation

In the Matlab environment, the most essential speed-up gain is related to the sparse FE matrix-vector products which need to be evaluated iteratively in the forward simulation phase. The GPU-parallelization of the forward simulation is especially important, because Matlab currently handles the sparse matrix products in a single processor thread. To evaluate the lead field matrix as described in Appendix A.4, ZI uses the preconditioned conjugate gradient (PCG) (Golub and van Loan 1989) method with a lumped diagonal preconditioner (LDP) in which each diagonal entry is obtained as the row sum of the absolute entry values. LDP is an advantageous preconditioner regarding the limited GPU memory. While LDP is not optimal with respect to minimizing the iteration steps needed for convergence, it enables establishing a fast forward solver due to the high parallel processing performance provided by a GPU.

IAS Iteration

In the IAS iteration (Appendix B), the most time consuming step is the third one, Eq. 7, in which the size of the matrix to be inverted is determined by the length of the data vector. If a high number of time steps will need to be processed, the fastest processing is obtained by evaluating the matrix-vector product of Eq. 7 in a GPU.

Interface Structure and Function

When started, ZI creates a single data structure (struct) `zef` in Matlab's base workspace. All the parameters and variables, such as the lead field matrix, measurement data and reconstruction, can be accessed via the `zef` structure. The basic workflow consists of three phases illustrated in Fig. 1. In this section, we briefly review the workflow and introduce the most important fields of `zef` for each phase.

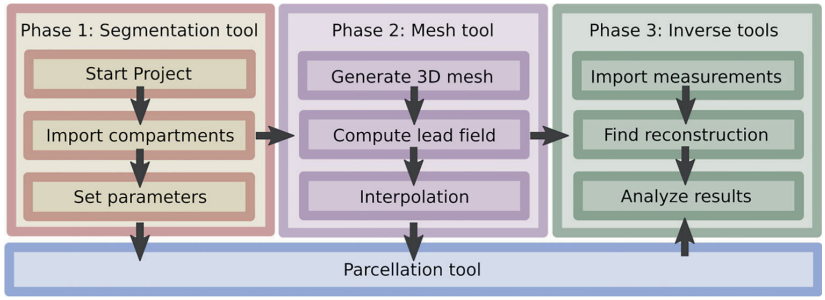

Fig. 1 The basic three-phase workflow in ZI. In phase 1, the head model is first defined using the *segmentation tool*, after which, in phase 2, the three-dimensional FE mesh and the LF matrix are generated with the *mesh tool*. Finally, in phase 3, the *inverse tools* can be applied to reconstruct and analyze parameter distributions, e.g., the primary current density of the brain activity. The *parcellation tool* can be applied in each of the phases 1–3 to assist decomposing the brain into a finite set of ROIs

Segmentation Tool

In the first phase, a surface segmentation describing different tissue structures and properties within Ω is defined using the *segmentation tool* (Fig. 2). A triangular surface mesh for each tissue type is imported in ZI as an ASCII file. In the current version, a single head model can contain up to 27 different tissue compartments. Moreover, several surface meshes (sub-meshes) can be merged together into a single compartment, e.g., the left and right hemisphere of the cerebral cortex. A multi-compartment segmentation can be defined in a single initialization (.INI) file which allows importing a complete head segmentation at once. The nodes and points of each surface mesh can be stored either in two separate .DAT files or in a single .ASC file exported from the FreeSurfer[2] Software Suite (Fischl 2012).

The default set of compartments includes white matter, grey matter, cerebrospinal fluid (CSF), skull, and scalp, whose default conductivity values are 0.14, 0.33, 0.0064, and 0.43 S/m, respectively, according to Dannhauer et al. (2011); Vorwerk et al. (2014). Each compartment can be defined as active or inactive. The set of active compartments contains the DOFs of $\mathbf{x}$. In EEG/MEG, the activity can be either constrained or unconstrained. In the former case, it is restricted into the direction of the surface normal, and in the latter case, it can have any orientation.

Mesh Tool

In the second phase of the workflow, a uniform tetrahedral mesh is generated based on the surface segmentation. The meshing parameters can be defined in the *mesh tool*. The meshing process proceeds from the innermost (detail) compartment to the outermost one. It allows the tissue boundaries to intersect each other which is necessary with a real segmentation obtained from magnetic resonance imaging (MRI) data. Each compartment can be given a priority which is referred to if a tetrahedron has nodes in two or more compartments. The priority parameter allows fine-tuning the width of the thin tissue layers, e.g., the skull: the lower the value the higher the priority. The FE mesh can be also smoothed using the Bi-Laplacian smoothing flow (Ohtake et al. 2001; Pursiainen 2012). After generating the mesh, the LF matrix can be computed for a selected imaging modality and a given number of the degrees of freedom (DOFs). Finally, an interpolation process connecting the DOFs and the FE mesh nodes needs to be performed, to enable inversion of measurement data.

Together with the *figure tool*, the mesh tool allows one to visualize both the surface segmentation and the volumetric FE mesh, or any surface or volumetric distribution (reconstruction) defined on those. The visibility of a compartment can be selected in the Segmentation tool. The *options tool* includes additional options which control, e.g., the colormap, scale, vector component, and the index of the sub-mesh for the visualized distribution, e.g., that of the left or right hemisphere (see Section "Segmentation Tool"). An example of a multi-layer surface segmentation and the resulting volumetric mesh created with ZI are shown in Fig. 3. For further code development, the most important fields of `zef` are the following:

1. `zef.nodes` and `zef.tetra` store the nodes and tetrahedra of the FE mesh, respectively;
2. `zef.L` is the lead field matrix;
3. `zef.source_positions` stores the source positions corresponding to the columns of `zef.L` in the respective order. This array contains the DOF positions also if they do not represent neural sources, which is the case in EIT.

[2] https://surfer.nmr.mgh.harvard.ed

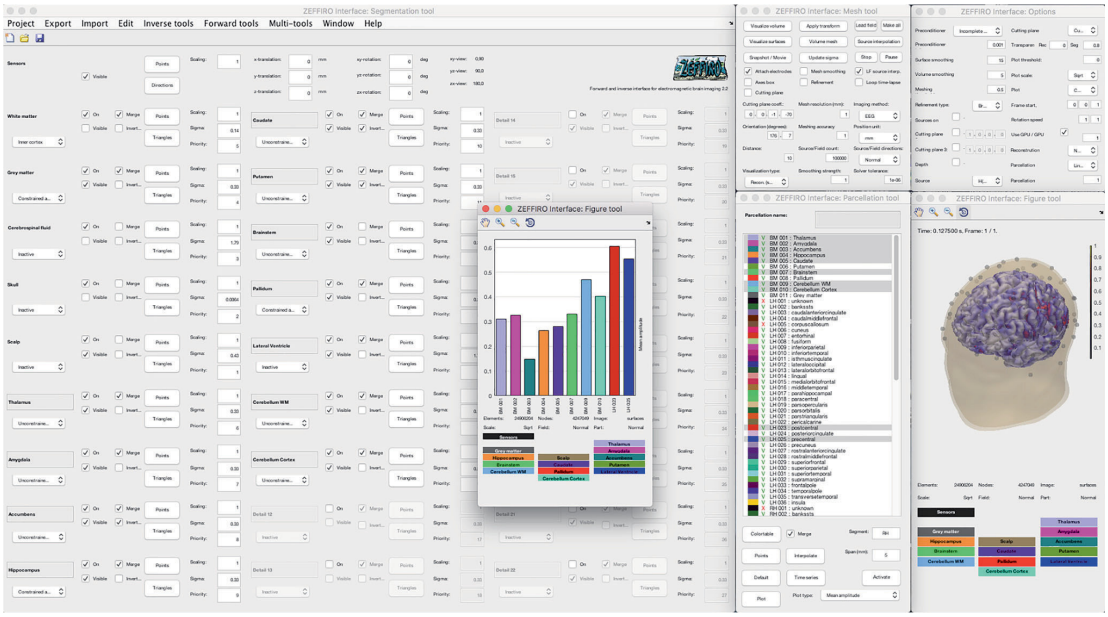

Fig. 2 A screenshot of ZI with figure, mesh, parcellation, and option tool opened

4. `zef.source_directions` contains the source orientations. If Cartesian orientations are used, this field is empty, and the source orientation for the columns of `zef.L` is given by the following regular pattern: position 1, xyz; position 2, xyz; position 3, xyz, etc.;

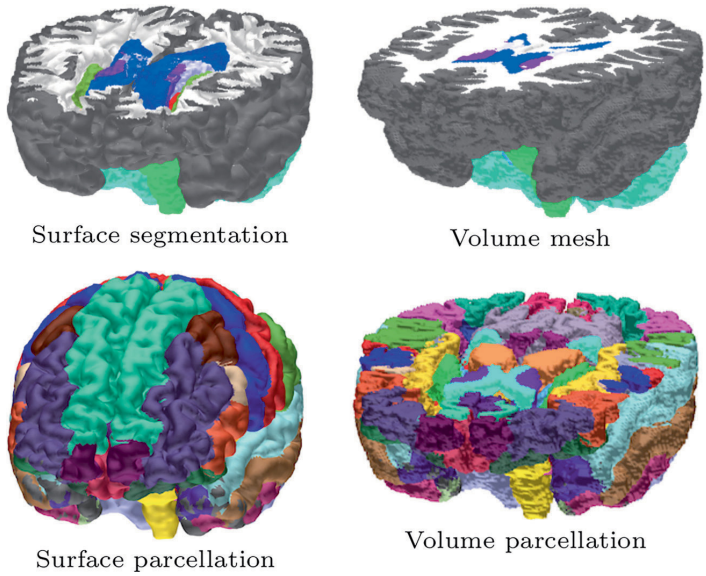

Fig. 3 **Top row:** Surface and volume visualizations of the head model in ZI. **Bottom row:** FreeSurfer-based cortical parcellation with 36 Desikan-Killiany labels

5. `zef.source_interpolation_ind` stores the indices that connect the finite element mesh with the DOFs;
6. `zef.h_axes1` stores the axes handle of the figure tool.

Inverse Tools

In the third phase, the measurement data are imported and, after that, a reconstruction for $\mathbf{x}$ can be obtained using one of the *inverse tools*. A MAP estimate can be obtained via the IAS method using one of the following tools:

1. *IAS MAP estimation* which finds a MAP estimate for the whole domain;
2. *IAS MAP estimation ROI* which focuses on a ROI;
3. *IAS MAP multiresolution* which explores multiple different resolutions.

A CM estimate can be obtained for a ROI using the *Hierarchical Bayesian sampler* tool. For external inverse procedure development, the most important fields are the following:

1. `zef.measurements` is the set of measurements to be inverted; this field can be a matrix or a cell array with the number of rows and columns equal to that of `zef.L` and the time steps in the dataset, respectively;
2. `zef.reconstruction` is the reconstruction of $\mathbf{x}$ corresponding to the set of source positions and orientations.

Parcellation Tool

The *parcellation tool* (Fig. 2) allows importing a parcellation created with the FreeSurfer Software Suite. A single parcellation consists of a file containing a colortable (.MAT) and another one including the points/labels (.ASC). After importing, an interpolation process will need to be performed to connect the points with the DOFs. The parcellation can be used as *a priori* information in the reconstruction or visualization stage. After obtaining a reconstruction, one can evaluate a time series of the activity for each region present in the parcellation. The time series can represent, e.g., the maximal or median activity within a region. The purpose of the time series is to enable the analysis of different statistical properties and connectivity of the activity over a time interval. In the current version, e.g., the amplitude, standard deviation, correlation, covariance, and dynamic time warping (DTW) (Sakoe and Chiba 1978) measure can be evaluated. The most important fields w.r.t. the parcellation tool are the following:

1. `zef.parcellation_colortable` and `zef.parcellation_points` store the colortable and points of the parcellation;
2. `zef.parcellation_interp_ind` contains the indices connecting the parccellated brain regions and the DOFs;
3. `zef.parcellation_time_series` stores the time series obtained for the brain regions after reconstructing the brain activity.

Plugin Utility

ZI can be extended via the *plugin utility*. The list of plugins is defined in the `zeffiro_plugins.ini` file which is located in ZI's root folder. A menu item will be created for each listed plugin. The Hierarchical Bayesian sampler tool (Spitzer 1971; Murphy 2012) is included in the code package as an example plugin (HBSampler).

Numerical Experiments

In the numerical experiments, we demonstrate the practical performance of ZI and the IAS MAP estimation technique via numerical experiments in which EEG and EIT inversion is tested with real and synthetic data, respectively. We also analyze the effect of hyperprior and scale parameter on the source localization in EEG using simulated measurements.

EEG Inversion Test

To enable comparability of the results to an existing solver, in this case that of the Brainstorm[3] software (Tadel et al. 2011), EEG source localization accuracy was examined by inverting Brainstorm's *EEG and epilepsy* tutorial dataset[4] which was used with the consent of Prof. A. Schulze-Bonhage, Epilepsy Centre, University Hospital Freiburg, Germany. The dataset was obtained for a patient who had suffered from focal epilepsy with focal sensory, dyscognitive and secondarily generalized seizures since the age of eight years. It consists of 58 epileptiform discharges (spikes) which were recorded at 256 Hz frequency and detected using Brainstorm by the epileptologists in Freiburg. An invasive EEG study concentrating on the same subject can be found in Dümpelmann et al. (2012).

Following the tutorial, the measurement data to be inverted, depicted in Fig. 4, were obtained for 29 electrodes applying an epoching time interval between -5 and 5 s w.r.t. the time point of the inverted data. All the non-EEG channels have been removed from the measured data. The brain activity was reconstructed via two steps of the IAS MAP estimation algorithm with low-cut and high-cut frequency of 0.5 Hz and 80 Hz, assuming that the likelihood standard deviation is 3 % of the maximum entry in the data,

[3] https://neuroimage.usc.edu/brainstorm/Introduction
[4] https://neuroimage.usc.edu/brainstorm/Tutorials/Epilepsy

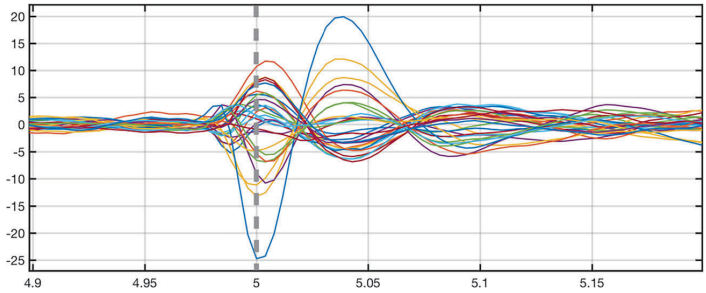

Fig. 4 A butterfly plot of EEG inversion test (Section "EEG Inversion Test") data which were obtained by averaging 58 epileptiform discharges between -5 and 5 s. The vertical axis shows the measured voltage in microvolts, and the horizontal axis the measurement time in seconds. The reconstruction was found for the zero time point 0 s which is indicated by the vertical dashed line

and selecting the shape and scale parameters as $\beta = 1.5$ and $\theta_0 = 1\text{E-}12$. The head model linked to the dataset consists of the surface meshes of the scalp, skull, CSF, grey matter, and white matter. ZI's default conductivity values were used. The LF matrix was generated for 100000 sources using 1 mm mesh resolution. The reconstructions were obtained with ZI's *IAS MAP estimation* inverse tool.

EIT Inversion Test

EIT inversion was examined numerically using the population head model[5] which includes a scalp, skull, CSF, ventricle, grey matter, and white matter compartment (Lee et al. 2016). The default conductivity values were applied, associating the condutivity of the ventricles with that of the CSF. A total of 72 ring electrodes with an assumed 1 kOhm impedance and an outer and inner diameter of 10 and 7.5 mm, respectively, were modeled through the complete electrode model (CEM) described in Appendix A.1.

The head model was discretized using 1 mm mesh resolution. The FE mesh is shown in Fig. 6. A LF matrix was evaluated for a total number of 5000 DOFs using the approach presented in Appendix A.1 and the original piecewise constant conductivity as the background distribution, i.e., the point of the linearization. The DOFs were distributed in the CSF, white matter and grey matter compartment.

The synthetic data were generated by perturbing the conductivity inside the brain within a spherical 30 mm diameter sub-domain representing an intracerebral hemorrhage (Broderick et al. 1993). Following, e.g., Li et al. (2017); Tang et al. (2010), the magnitude of the perturbation was set to be +0.73 S/m and the signal-to-noise ratio was assumed to be 60 dB. The measurement errors consisted of additive Gaussian zero-mean white noise.

[5] https://itis.swiss/virtual-population/regional-human-models/phm-repository/

The likelihood standard deviation was set to be 12 % conciding approximately with the level following from the noise model. The IG hyperprior was employed selecting the shape and scale parameters as $\beta = 1.5$ and $\theta_0 = 0.001$. To reconstruct the deep-lying anomaly, the total set of DOFs was decomposed into randomized 300 subsets which were formed w.r.t. an equal number of randomly (uniformly) distributed center points via the nearest point interpolation technique. The MAP estimate was found by performing two steps of IAS iteration for altogether 100 such randomized decompositions. A serial approach was adopted: the estimate obtained for one decomposition was set as the initial guess for the next one. The final reconstruction was produced as the mean of the resulting 100 MAP estimates.

The motivation to use averaging was to reduce the effect of decomposition-related artifacts which we assumed to be identically distributed for each separate decomposition and, thus, converge towards an expectation of an asymptotical Gaussian distribution based on the law of random numbers and the central limit theorem (O'Hagan and Forster 2004). The averaged reconstruction was obtained using the *IAS MAP multiresolution* inverse tool which allows averaging the reconstruction over one or more resolution levels and multiple randomized decompositions. The resolution is determined by the number of subsets within a single decomposition which is here 300 in each.

Hypermodel and Parameter Selection

The HBM approach requires selecting the hypermodel together with an appropriate value for the shape and scale parameter β and θ. To investigate the effect of the parameter selection on the IAS MAP estimation process, we compared the localization of a simultaneously active pair of synthetic deep and superficial 10 nAm source in the case of EEG. The reconstruction was found as the center of mass of the primary current distribution within two 30 mm ROIs

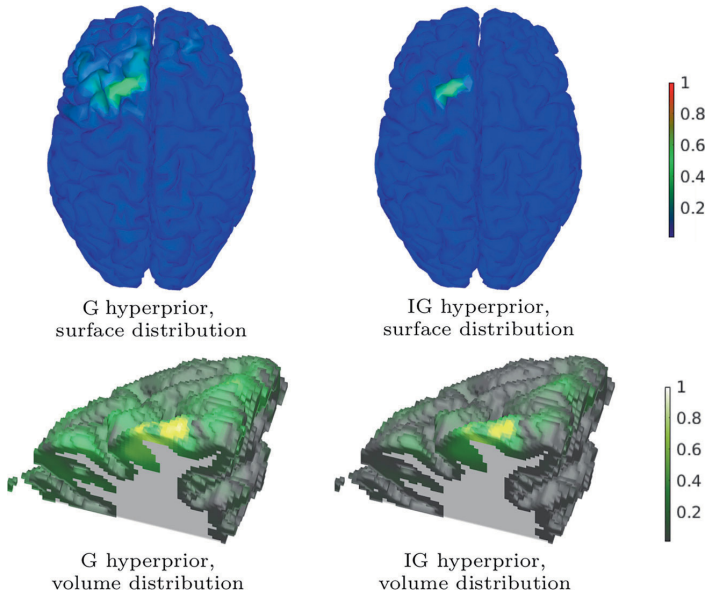

Fig. 5 A surface and volume visualization of reconstructed brain activity (amplitude) obtained in the EEG inversion test (Section "EEG Inversion Test"). The left and right images correspond to G and IG hyperprior, respectively. **Top row:** An axial projection of the reconstructions interpolated on the surface of the grey matter compartment. **Bottom row:** The volumetric reconstructions cut by a coronal plane at the location of the maximal activity. The reconstructions have been normalized to one

centered at the actual source locations. The accuracy was measured by evaluating the position (mm) and orientation (degree) difference with respect to the exact sources. As the computation domain we used a six-compartment (white matter, grey matter, CSF, compact skull, spongious skull, scalp) head model corresponding to a 49-year old male subject with ZI's default conductivity values. For the spongious part of the skull 0.028 S/m was selected (Vorwerk et al. 2014). The EEG LF matrix was formed for a cap of 72 electrodes. The effects of choosing the hyperprior h and scale parameter θ_0 were examined for the following four pars: **(i)** $h = \mathrm{G}, \theta_0 = 1\mathrm{E}-5$, **(ii)** $h = \mathrm{IG}, \theta_0 = 1\mathrm{E}-5$, **(iii)** $h = \mathrm{G}, \theta_0 = 1\mathrm{E}-9$, and **(iv)** $h = \mathrm{IG}, \theta_0 = 1\mathrm{E}-9$, respectively. The shape parameter β was set to be $\beta = 1.5$ in each case. Gaussian white noise with 2 % relative standard deviation was added in the data. Each reconstruction was evaluated for 50 different realizations of the noise vector. The inverse tool applied in the experiment was ZI's *IAS MAP estimation ROI*.

Results

ZI's forward simulation performance was evaluated w.r.t. the computing time for the head model described in Section "Hypermodel and Parameter Selection". The mesh generation, LF matrix evaluation and interpolation processes took 21, 39 and 3.5 minutes, respectively, using NVIDIA[6] Quadro P6000 GPU. GPU acceleration was also found to be necessary to obtain a reasonable computing time as it sped up these routines by more than a factor of ten.

EEG Inversion Test

The results of the EEG inversion test can be found in Fig. 5 which displays the reconstructed brain activity for the surface of the cortex and a volume cut corresponding to the location of the maximal activity. The reconstruction obtained with the IG hyperprior was observed to be more focal than the one corresponding to G. The surface visualizations obtained for the G and IG hyperprior confirm similar active area as illustrated in Brainstorm's *EEG and epilepsy* tutorial, especially, compared to the outcome of the Brainstorm's maximum of entropy on the mean (MEM) framework solution. The volume cuts show the depth of the reconstructed activity.

EIT Inversion Test

In the EIT inversion test, the averaged reconstruction found for the synthetic hemorrhage matched well with its exact location, which is shown in Fig. 6. A visual comparison

[6] https://en.wikipedia.org/wiki/List_of_Nvidia_graphics_processing_units

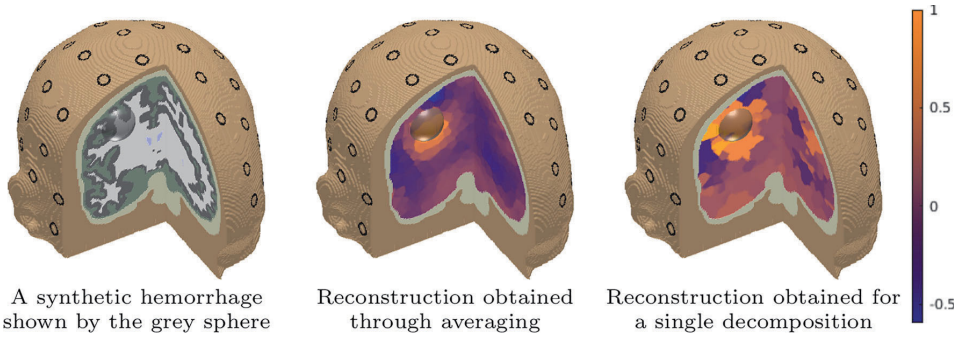

Fig. 6 **Left:** An illustration of the synthetic hemorrhage (grey sphere) which was applied to generate the data of the EIT inversion tests. The diameter of the sphere was 30 mm and its conductivity was set to be 0.73 S/m higher compared to its surroundings. The unperturbed background conductivity distribution was assumed to be constant in each tissue compartment including white matter (white), grey matter (grey), CSF (green and blue), skull (khaki), and scalp (brown). The CEM electrodes (Appendix A.1) are shown as surface patches (black rings): **Center:** An averaged reconstruction of the synthetic hemorrhage found using the *IAS MAP multiresolution* inverse tool. The final distribution was produced as an average of altogether 100 different MAP estimates corresponding to different randomized decompositions of 300 DOFs as explained in Section "EIT Inversion Test". **Right:** A reconstruction (an unaveraged MAP estimate) found for a single decomposition of 300 DOFs. The reconsructions have been normalized to one

between the averaged and unaveraged and reconstruction (Fig. 6) suggests that the averaging process was beneficial w.r.t. the localization accuracy. The resolution (level of detail) of the averaged reconstruction seems to be refined compared to that of the unaveraged one. Moreover, using a comparatively low number of DOFs (here 300) in each randomized decomposition was found to be necessary for detecting the hemorrhage.

Hypermodel and Parameter Selection

Figure 7 illustrates the source localization results obtained in the hypermodel and parameter selection test. G was observed to perform comparably well for the superficial ROI and IG for the deep one. This is reflected by the cases (**i**) and (**iv**) in which the utmost position accuracy was obtained in these ROIs, respectively. Moreover, for G, the larger

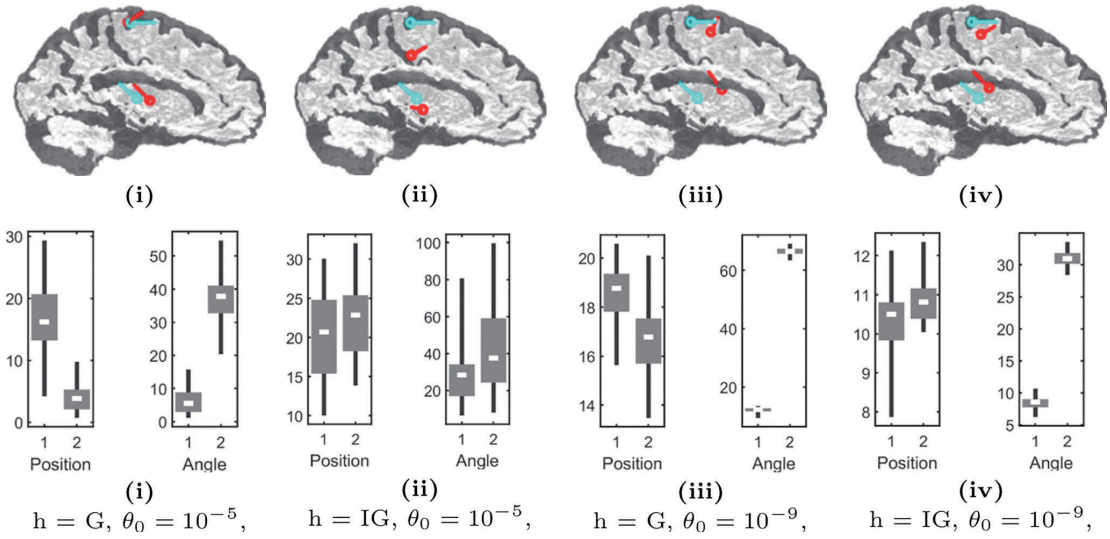

Fig. 7 **Top row:** Examples of the center of mass (red pin) found for the deep and superficial source (1 and 2, respectively) in the cases (**i**)–(**iv**) with synthetic EEG data and the noise level of 2 %. The exact position of each source is also depicted (cyan pin). **Bottom row:** Box-plots showing the distributions (**i**)–(**iv**) of the position (millimeter) and angle error (degree) found for sources 1 and 2 and 50 different realizations of the noise vector

scale parameter value seemed preferable to the smaller one, while, for IG, the situation was the opposite. Regardless of the hyperprior, selecting a smaller scale parameter seemed beneficial for localizing the deep source until a certain level, where noise effects started to affect the reconstruction.

Discussion

This article introduced *Zeffiro* interface (ZI) version 2.2, a GPU accelerated Matlab tool for multi-modal FEM-based modeling of electromagnetic fields in brain imaging and investigations (Braess 2001; de Munck et al. 1988; Monk 2003). It was shown that, when aided by a state-of-the-art GPU, ZI allows one to invert a given set of EEG data for a physiologically accurate (Rullmann et al. 2009) one-millimeter volumetric multi-compartment head model within a reasonable one hour's time. GPU acceleration is needed, specifically, in the forward simulation phase, that is, in the generation of the FE mesh and the LF matrix as well as in the interpolation process connecting the DOFs of the unknown with the nodes of the FE mesh. Since Matlab does not currently parallelize the sparse matrix operations in a CPU, the performance difference between CPU and GPU computations, both applicable in ZI, is particularly pronounced.

As the mutual performance of GPU- and CPU-based codes is strongly system-specific and depends on various factors in addition to the processors themselves, ZI was not directly compared to the alternative tools. These include, for instance, Duneuro[7] (Nüßing et al. 2019) and SimBio[8] (Fingberg et al. 2003) which are open source FEM libraries for EEG/MEG with similar functions as Zeffiro but utilizing C++ language. Brainstorm[9] (Tadel et al. 2011) and Fieldtrip[10] (Oostenveld et al. 2011) are alternative packages for the Matlab platform. The core forward modeling approach of Brainstorm is the BEM (He et al. 1987). Fieldtrip does not have an advanced forward and inverse modeling functions. None of these are currently capable of advanced FEM or GPU computations. The MNE-Python[11] toolbox (Gramfort et al. 2013) is the leading option for Python. It allows utilizing a GPU, but is, nevertheless, limited to a BEM-based forward simulation.

The present results suggest that ZI enables robust inversion of multi-modal data. Firstly, the reconstructions obtained for Brainstrom's *EEG and epilepsy* tutorial dataset show that ZI's forward and inversion methods can be applied to detect brain activity. Secondly, based on the numerical results obtained in the EIT inversion test, it seems that ZI can also be extended for non-linear problems and inversion of scalar-valued fields. The IAS MAP estimation technique was found to be applicable for EIT via averaging MAP estimates obtained for a randomized set of low-resolution domain decompositions. This technique might be usable also for other imaging modalities, for example, to localize deep brain activity. Furthermore, the present EIT solver might be adapted for other applications involving current injections, such as transcranial electric stimulation (Herrmann et al. 2013) in which the brain activity is evoked through external stimuli.

Based on the hyperprior and scale parameter selection experiment, IG seems to be an advantageous choice for the subcortical areas, whereas G seems preferable for the cerebral cortex. The scale parameter applied in the former case should be generally lower than in the latter one. This baseline is in parallel with the previous findings (Calvetti et al. 2009) and might be optimized later on. We also emphasize that the parameter selection is generally a complicated issue which is not covered completely in this study. For example, the effect of the shape parameter, which partially overlaps with that of the scale parameter, is omitted here.

Compared to the BEM, the FEM has at least two major advantages when applied in EEG/MEG. Firstly, while a BEM solver slows down if the surface mesh resolution or the number of surfaces grows, the computational performance of the FEM is virtually independent of these factors. ZI's current design takes this aspect into account, as altogether 27 tissue compartments, each one composed of sub-entities if needed, can be included in a single head model. The uniform mesh generator is well-suited for multi-compartment meshing, since unlike many widely used software, e.g., TetGen[12] (Si 2015) and Netgen[13] (Schöberl 1997), it allows the tissue boundaries to intersect each other without collapsing. This is essential in practice, since the segmentation routines utilizing MRI data do not always render the surfaces smoothly. Moreover, ZI performs appropriately with a high surface resolution, thereby, allowing one to directly use the detailed surfaces exported from the FreeSurfer[14] Software Suite (Fischl 2012).

The second major benefit of the FEM is that the conductivity distribution can be anisotropic (Güllmar et al. 2010; Rullmann et al. 2009). ZI's forward simulation routines are currently capable of handling anisotropicity. The current meshing routine, however, generates an isotropic conductivity distribution. Generating or importing an anisotropic distribution, e.g., from diffusion-weighted MRI data, constitutes a potential topic for the future work.

[7] http://duneuro.org

[8] http://simbio.de

[9] https://neuroimage.usc.edu/brainstorm/Introduction

[10] http://www.fieldtriptoolbox.org

[11] https://martinos.org/mne/stable/index.html

[12] http://wias-berlin.de/software/tetgen/

[13] https://ngsolve.org/

[14] https://surfer.nmr.mgh.harvard.ed

Another potential direction is to develop the inversion methodology: one might apply the HBM for sub-cortical areas (Seeber et al. 2019), with non-diagonal prior covariance structures and/or with sampling-based posterior exploration techniques, e.g., the Gibbs sampler (Spitzer 1971; Murphy 2012). From the practical viewpoint, there is also an obvious need to develop tools for various purposes including epochs, the covariance of the measurements, and connectivity, e.g., phase-locking (Lachaux et al. 1999). Clinical studies would be needed to validate ZI for different applications and measurement situations. Providing command line executable scripts for performing the main operations without the graphical user interface, e.g., in a computing cluster, is also a potential option.

Information Sharing Statement The results of the paper have been produced using the openly available Zeffiro interface (ZI) code package which has been implemented for the MATLAB (The MathWorks Inc.) environment. EEG source localization accuracy has been analyzed with the epilepsy tutorial dataset of the Brainstorm software with the consent of Prof. A. Schulze Bonhage, Epilepsy Center, University Hospital Freiburg, Germany. The EIT results have been computed with the population head model. The parcellation of the brain (36 Desikan-Killiany labels) has been obtained with the FreeSurfer software suite and visualized with ZI.

Acknowledgments QH, AR, and SP contributed equally to this study. This study was supported by the Academy of Finland Centre of Excellence in Inverse Modelling and Imaging 2018–2025. We are grateful for DAAD's (Deutscher Akademischer Austausch Dienst) bilateral travel funding support between Mathematics and Statistics, Tampere University and Institute for Biomagnetism and Biosignal Analysis, University of Münster (Project: Advancing Finite Element Computations for Reconstructing and Manipulating the Human Somatosensory Cortex, Academy of Finland decision number 317165).

Appendix A: Finite Elements in Multimodal Lead Field Evaluation

To model electromagnetic fields, ZI applies the finite element method which allows obtaining lead field matrices for multiple different applications and data modalities. This appendix shows mathematically, how the lead field matrices of the EEG and linearized EIT problem are obtained in ZI, when the complete electrode model (CEM) is applied.

Complete Electrode Model in Lead Field Evaluation

The governing PDE can be equipped with the following (lumped) CEM boundary conditions (Cheng et al. 1989). **(I)**: $\sigma\nabla u\cdot\mathbf{n}|_{\partial\Omega\setminus\cup_\ell e_\ell}=0$, **(II)**: $\int_{e_\ell}\sigma\nabla u\cdot\mathbf{n}\,dS=I_\ell$, and **(III)**: $(u+Z_\ell\mathcal{A}_\ell\sigma\nabla u\cdot\mathbf{n})|_{e_\ell}=U_\ell$ for $\ell=1,2,\ldots,L$, where $\mathbf{n}$ denotes the surface normal. According to the first condition **(I)**, the normal current $\sigma\nabla u\cdot\mathbf{n}$ on $\partial\Omega$ can flow out of or into the domain only through electrodes e_ℓ, $\ell=1,2,\ldots,L$. The second one **(II)** sets the net current flowing through each electrode is I_ℓ, and the third one **(III)** corresponds to the potential jump on the skin-electrode contact boundary. The voltage of the ℓ-th electrode is denoted by U_ℓ. Z_ℓ is the average contact impedance or resistance and $\mathcal{A}_\ell$ is the contact area of the ℓ-th electrode. An additional condition is the the equation $\sum_{\ell=1}^{L}I_\ell=0$ which guarantees that the subject is grounded appropriately, so that there is no current flowing out of the head through the neck. Integrating the governing PDE for the potential field, i.e., $\nabla\cdot(\sigma\nabla u)=\nabla\cdot\mathbf{J}^p$, by parts yields the for weak form (Pursiainen et al. 2016a):

$$-\int_\Omega(\nabla\cdot\mathbf{J}^p)v\,dV=\int_\Omega\sigma\nabla u\cdot\nabla v\,dV+\sum_{\ell=1}^{L}\frac{1}{Z_\ell\mathcal{A}_\ell}\int_{e_\ell}u\,v\,dS-\sum_{\ell=1}^{L}\frac{1}{Z_\ell\mathcal{A}_\ell^2}\int_{e_\ell}u\,dS\int_{e_\ell}v\,dS-\sum_{\ell=1}^{L}Z_\ell I_\ell. \tag{3}$$

If the divergence of $\mathbf{J}^p$ is square integrable, i.e., if $\mathbf{J}^p\in\{\mathbf{w}\,|\,\nabla\cdot\mathbf{w}\in L^2(\Omega)\}$, the weak form has a unique solution $u\in H^1(\Omega)=\{w\in L^2(\Omega):\partial w/\partial x_i\in L^2(\Omega),\ i=1,2,3\}$ satisfying (3) for all $v\in H^1(\Omega)$. The weak form (3) can be discretized in a straightforward way via the classical Ritz-Galerkin technique (Braess 2001) which yields the system

$$\begin{pmatrix}\mathbf{A}&-\mathbf{B}\\-\mathbf{B}^T&\mathbf{C}\end{pmatrix}\begin{pmatrix}\mathbf{z}\\\mathbf{v}\end{pmatrix}=\begin{pmatrix}-\mathbf{G}\mathbf{x}\\\mathbf{I}\end{pmatrix}. \tag{4}$$

Matrix $\mathbf{A}$ is of the form $a_{i,j}=\int_\Omega\sigma\nabla\psi_i\cdot\nabla\psi_j\,dV+\sum_{\ell=1}^{L}\frac{1}{Z_\ell\mathcal{A}_\ell}\int_{e_\ell}\psi_i\psi_j\,dS$, where ψ_i, $i=1,2,\ldots,n$ are linear (nodal) FE basis functions. To ensure the invertibility of $\mathbf{A}$, it is additionally defined that the identities $a_{i',i'}=1$ and $a_{i',j}=0$ $(j\neq i')$ are satisfied for the index i' corresponding to a basis function ψ_i' which is maximized on the boundary $\partial\Omega\setminus\cup_\ell e_\ell$ not covered by the electrodes. The entries of $\mathbf{B}$, $\mathbf{C}$ and $\mathbf{G}$ are given by $b_{i,\ell}=\frac{1}{Z_\ell}\int_{e_\ell}\psi_i\,dS$, $c_{\ell,\ell}=\frac{1}{Z_\ell}\int_{e_\ell}dS$, $c_{i,\ell}=0$ $(i\neq\ell)$, and $g_{i,j}=\int_\Omega\psi_i(\nabla\cdot\vec{w}_j)dV$, where $\vec{w}_j$, $j=1,2,\ldots,m$ are basis functions belonging to the $H(\mathrm{div})$ space. The current vector $\mathbf{I}=(I_1,I_2,\ldots,I_L)$ is nonzero, if the electrodes are actively injecting currents. The zero-mean electrode voltage vector $\mathbf{y}=(U_1,U_2,\ldots,U_L)$ predicted by Eq. 4 can be obtained via $\mathbf{y}=\mathbf{R}\mathbf{v}$ in which the matrix $\mathbf{R}$ defined by $r_{j,j}=1-1/L$ for $j=1,2,\ldots,L$, and $r_{i,j}=-1/L$ $(i\neq j)$.

EEG Lead Field

In EEG, the electrode currents included in $\mathbf{I}$ are zero, as the electrodes only measure the voltage on the skin. Thus, vector $\mathbf{v}$ can be explicitly solved from Eq. 4 which leads to the expression $\mathbf{y} = \mathbf{R}(\mathbf{B}^T\mathbf{A}^{-1}\mathbf{B} - \mathbf{C})^{-1}\mathbf{B}^T\mathbf{A}^{-1}\mathbf{G}\mathbf{x}$, and, further, to the following EEG LF matrix:

$$\mathbf{L} = \mathbf{R}(\mathbf{B}^T\mathbf{A}^{-1}\mathbf{B} - \mathbf{C})^{-1}\mathbf{B}^T\mathbf{A}^{-1}\mathbf{G}. \tag{5}$$

The lead field of the MEG problem can be derived in an analogous way using the Biot-Savart formula for the magnetic field as shown in Pursiainen (2012).

Linearized EIT Lead Field

In EIT, the primary current density can be assumed to be zero, as the magnitude of the injected currents is far superior to the brain activity. The unknown of the EIT inverse problem is the conductivity distribution σ. The voltage measurements $\mathbf{y} = \mathbf{R}\mathbf{v}$ generated by the current injections $\mathbf{I}$ are used as the data. The forward model that follows is given by $\mathbf{y} = \mathbf{R}\mathbf{M}^{-1}\mathbf{I}$, where $\mathbf{M} = (\mathbf{C} - \mathbf{B}^T\mathbf{A}^{-1}\mathbf{B})$. The conductivity distribution is assumed to be piecewise (element-wise) constant, i.e., of the form $\sigma = \sum_{m=1}^{M} s_m \chi_m$, where χ_m is the indicator function of the element m in the FE mesh. Denoting by $\sigma^{(bg)}$ a background conductivity distribution, i.e., the point of linearization, the unknown of the inverse problem is the difference vector $\mathbf{x} = (s_1 - s_1^{(bg)}, s_2 - s_2^{(bg)}, \ldots, s_M - s_M^{(bg)})$. The LF for linearized EIT can be derived by differentiating both sides of the equation $\mathbf{M}\mathbf{v} = \mathbf{I}$ as follows: $\mathbf{0} = (-\mathbf{B}^T\frac{\partial}{\partial s_m}\mathbf{A}^{-1}\mathbf{B})\mathbf{v} + \mathbf{M}\frac{\partial}{\partial s_m}\mathbf{v}$. Moreover, a straightforward differentiation of the equation $\mathbf{A}\mathbf{A}^{-1} = \mathbf{I}$ shows that $\frac{\partial}{\partial s_m}(\mathbf{A}\mathbf{A}^{-1}) = \frac{\partial \mathbf{A}}{\partial s_m}\mathbf{A}^{-1} + \mathbf{A}\frac{\partial \mathbf{A}^{-1}}{\partial s_m} = \mathbf{0}$, and, further, that $\frac{\partial \mathbf{A}^{-1}}{\partial s_m} = -\mathbf{A}^{-1}\frac{\partial \mathbf{A}}{\partial s_m}\mathbf{A}^{-1}$. Taking into account that $\frac{\partial \mathbf{y}}{\partial s_m} = \mathbf{R}\frac{\partial \mathbf{v}}{\partial s_m}$, the linearized lead field can be written as $\frac{\partial \mathbf{y}}{\partial s_m} = -\mathbf{R}\mathbf{M}^{-1}\mathbf{B}^T(\mathbf{A}^{-1}\frac{\partial \mathbf{A}}{\partial s_m}\mathbf{A}^{-1}\mathbf{B})\mathbf{v}$. Thus, the differential is of the form

$$\frac{\partial \mathbf{y}}{\partial s_m} = -\mathbf{R}\mathbf{M}^{-1}\mathbf{B}^T(\mathbf{A}^{-1}\frac{\partial \mathbf{A}}{\partial s_m}\mathbf{A}^{-1}\mathbf{B})\mathbf{M}^{-1}\mathbf{I}. \tag{6}$$

The linearized forward model of EIT is given by $\mathbf{y} \approx \mathbf{L}\mathbf{x} + \mathbf{y}^{(bg)}$, where $\mathbf{y}^{(bg)}$ is a simulated data vector corresponding to the background conductivity distribution $\sigma^{(bg)}$ and the entries of the lead field matrix $\mathbf{L}$ are of the form $l_{k,m} = \partial y_k / \partial s_m|_{\sigma^{(bg)}}$.

Transfer Matrix

Both EEG and EIT lead field matrix can be formed by first evaluating the so-called transfer matrix $\mathbf{T} = \mathbf{A}^{-1}\mathbf{B}$. Obtaining a single column $\mathbf{t}$ of $\mathbf{T}$ necessitates solving a linear system of the form $\mathbf{A}\mathbf{t} = \mathbf{b}$, where $\mathbf{b}$ is a single column of the matrix $\mathbf{B}$ which has as many columns as there are electrodes in the measurement system.

Appendix B: IAS MAP Inversion

The iterative alternating sequential (IAS) inversion approach (Calvetti and Somersalo 2007; Calvetti et al. 2009, 2018) to find a *maximum a posteriori* estimate for the posterior density is given by:

1. Choose parameters β and θ_0. Set $k = 1$ and $\boldsymbol{\theta}^{(0)} = (\theta_0, \theta_0, \ldots, \theta_0)$.
2. Find $\mathbf{x}^{(k)} = \arg\max_x \, p(\mathbf{x} \mid \mathbf{y}, \boldsymbol{\theta}^{(k-1)})$.
3. Find $\boldsymbol{\theta}^{(k)} = \arg\max_{\boldsymbol{\theta}} \, p(\boldsymbol{\theta} \mid \mathbf{y}, \mathbf{x}^{(k)})$.
4. If k is less than the total number of iterations chosen by the user, then go to 2. and set $k = k + 1$, else set $\mathbf{x}_{MAP} = \mathbf{x}^{(k)}$.

IAS finds a conditional maximum of the posterior alternatingly with respect to the unknown vector $\mathbf{x}$ and the hyperparameter $\boldsymbol{\theta}$. The algorithm can be, further, written as

1. Set $k = 0$ and $\boldsymbol{\theta}^{(0)} = (\theta_0, \theta_0, \ldots, \theta_0)$.
2. Set $\mathbf{L}^{(k)} = \mathbf{L}\mathbf{D}_{\boldsymbol{\theta}^{(k)}}^{1/2}$ with $\mathbf{D}_{\boldsymbol{\theta}^{(k)}}^{1/2} = \operatorname{diag}\left(\sqrt{|\boldsymbol{\theta}_1^{(k)}|}, \sqrt{|\boldsymbol{\theta}_2^{(k)}|}, \ldots, \sqrt{|\boldsymbol{\theta}_n^{(k)}|}\right)$.
3. Evaluate

$$\mathbf{x}^{(k+1)} = \mathbf{D}_{\boldsymbol{\theta}^{(k)}}^{1/2}\mathbf{L}^{(k)^T}(\mathbf{L}^{(k)}\mathbf{L}^{(k)^T} + \nu^2\mathbf{I})^{-1}y, \tag{7}$$

   where ν denotes the standard deviation of the likelihood.
4. Update the hyperparameter based on the hypermodel.
   - If the hypermodel is G, set $\theta_i = \frac{1}{2}\theta_0\left(\eta + \sqrt{\eta^2 + 2x_i^{(k)^2}/\theta_0}\right)$ with $\eta = \beta - 3/2$, $i = 1, 2, \ldots, n$.
   - Else, if the hypermodel is IG, set $\theta_i^{(k+1)} = (\theta_0 + \frac{x_i^{(k)^2}}{2})/\kappa$ with $\kappa = \beta + 3/2$, $i = 1, 2, \ldots, n$.
5. Set $k = k + 1$ and go back to 2., if k is less than the total number of iterations defined by the user.

References

Bauer, M., Pursiainen, S., Vorwerk, J., Köstler, H., Wolters, C.H. (2015). Comparison study for Whitney (Raviart-Thomas) type source models in finite element method based EEG forward modeling. *IEEE Transactions on Biomedical Engineering*, *62*(11), 2648–56.

Braess, D. (2001). *Finite elements*. Cambridge: Cambridge University Press.

Broderick, J.P., Brott, T.G., Duldner, J.E., Tomsick, T., Huster, G. (1993). Volume of intracerebral hemorrhage. A powerful and easy-to-use predictor of 30-day mortality. *Stroke*, *24*(7), 987–993.

Calvetti, D., & Somersalo, E. (2007). A gaussian hypermodel to recover blocky objects. *Inverse Problems*, *23*(2), 733.

Calvetti, D., Hakula, H., Pursiainen, S., Somersalo, E. (2009). Conditionally Gaussian hypermodels for cerebral source localization. *SIAM JImaging Sci*, *2*(3), 879–909.

Calvetti, D., Pitolli, F., Somersalo, E., Vantaggi, B. (2018). Bayes meets Krylov: statistically inspired preconditioners for CGLS. *SIAM Review*, *60*(2), 429–461.

Cheney, M., Isaacson, D., Newell, J.C. (1999). Electrical impedance tomography. *SIAM Review*, *41*(1), 85–101.

Cheng, K.S., Isaacson, D., Newell, J., Gisser, D.G. (1989). Electrode models for electric current computed tomography. *IEEE Transactions on Biomedical Engineering*, *36*(9), 918–924.

Creutzfeldt, O.D., Fromm, G.H., Kapp, H. (1962). Influence of transcortical dc currents on cortical neuronal activity. *Experimental Neurology*, *5*(6), 436–452.

Dannhauer, M., Lanfer, B., Wolters, C.H., Knösche, T.R. (2011). Modeling of the human skull in EEG source analysis. *Human Brain Mapping*, *32*, 1383–1399. https://doi.org/10.1002/hbm.21114.

Dümpelmann, M., Ball, T., Schulze-Bonhage, A. (2012). Sloreta allows reliable distributed source reconstruction based on subdural strip and grid recordings. *Human Brain Mapping*, *33*(5), 1172–1188.

Fingberg, J., Berti, G., Hartmann, H., Basermann, A., Wolters, C.H., Anwander, A., McCarthy, A., Woods, S. (2003). Bio-numerical simualtions with SimBio. *NEC Research and Development*, *44*(1), 140–145.

Fischl, B. (2012). FreeSurfer. *NeuroImage*, *62*(2), 774–781.

Golub, G., & van Loan, C. (1989). *Matrix computations*. Baltimore: The John Hopkins University Press.

Gramfort, A., Luessi, M., Larson, E., Engemann, D.A., Strohmeier, D., Brodbeck, C., Goj, R., Jas, M., Brooks, T., Parkkonen, L., et al. (2013). MEG And EEG data analysis with MNE-python. *Frontiers in Neuroscience*, *7*, 267.

Güllmar, D., Haueisen, J., Reichenbach, J. (2010). Influence of anisotropic electrical conductivity in white matter tissue on the EEG/MEG, forward and inverse solution. A high-resolution whole head simulation study. NeuroImage https://doi.org/10.1016/j.neuroimage.2010.02.014.

Hämäläinen, M., Hari, R., Ilmoniemi, R.J., Knuutila, J., Lounasmaa, O.V. (1993). Magnetoencephalography — theory, instrumentation, and applications to invasive studies of the working human brain. *Reviews of Modern Physics*, *65*, 413–498.

Hari, R., Baillet, S., Barnes, G., Burgess, R., Forss, N., Gross, J., Hämäläinen, M., Jensen, O., Kakigi, R., Mauguière, F., et al. (2018). IFCN-endorsed practical guidelines for clinical magnetoencephalography (MEG). Clinical Neurophysiology.

He, B., Musha, T., Okamoto, Y., Homma, S., Nakajima, Y., Sato, T. (1987). Electric dipole tracing in the brain by means of the boundary element method and its accuracy. IEEE Transactions on Biomedical Engineering (6), 406–414.

Herrmann, C.S., Rach, S., Neuling, T., Strüber, D. (2013). Transcranial alternating current stimulation: a review of the underlying mechanisms and modulation of cognitive processes. *Frontiers in Human Neuroscience*, *7*, 279.

Lachaux, J.P., Rodriguez, E., Martinerie, J., Varela, F.J. (1999). Measuring phase synchrony in brain signals. *Human Brain Mapping*, *8*(4), 194–208.

Lee, E., Duffy, W., Hadimani, R., Waris, M., Siddiqui, W., Islam, F., Rajamani, M., Nathan, R., Jiles, D. (2016). Investigational effect of brain-scalp distance on the efficacy of transcranial magnetic stimulation treatment in depression. *IEEE Transactions on Magnetics*, *52*(7), 1–4.

Li, G., Sun, J., Ma, K., Yan, Q., Zheng, X., Qin, M., Jin, G., Ning, X., Zhuang, W., Feng, H., et al. (2017). Construction of a cerebral hemorrhage test system operated in real-time. *Scientific Reports*, *7*, 42,842.

Miinalainen, T., & Pursiainen, S. (2017). A case study of focal Bayesian EEG inversion for whitney element source spaces: mesh-based vs.Cartesian orientations. In *EMBEC & NBC 2017* (pp. 1065–1068). Berlin: Springer.

Miinalainen, T., Rezaei, A., Us, D., Nüßing, A., Engwer, C., Wolters, C.H., Pursiainen, S. (2019). A realistic, accurate and fast source modeling approach for the EEG forward problem. *NeuroImage*, *184*, 56–67.

Monk, P. (2003). *Finite element methods for Maxwell's equations*. Oxford: Clarendon Press.

de Munck, J., van Dijk, B., Spekreijse, H. (1988). Mathematical dipoles are adequate to describe realistic generators of human brain activity 35(11), 960–966.

de Munck, J., Wolters, C.H., Clerc, M. (2012). EEG & MEG forward modeling. In Brette, R., & Destexhe, A. (Eds.) *Handbook of neural activity measurement*. New York: Cambridge University Press. https://doi.org/10.1017/CBO9780511979958.006.

Murphy, K.P. (2012). *Machine learning: a probabilistic perspective. Adaptive Computation and Machine Learning*. Cambridge: MIT Press.

Niedermeyer, E., & da Silva, F.L. (2004). *Electroencephalography: basic principles, clinical applications and related fields*, 5th edn. Philadelphia: Lippincott Williams & Wilkins.

Nüßing, A., Piastra, M.C., Schrader, S., Miinalainen, T., Brinck, H., Wolters, C.H., Engwer, C. (2019). Duneuro-a software toolbox for forward modeling in neuroscience. arXiv:190102874.

O'Hagan, A., & Forster, J.J. (2004). *Kendall's advanced theory of statistics, volume 2B: Bayesian inference* Vol. 2. London: Arnold.

Ohtake, Y., Belyaev, A., Bogaevski, I. (2001). Mesh regularization and adaptive smoothing. *Computer-Aided Design*, *33*, 789–800.

Oostenveld, R., Fries, P., Maris, E., Schoffelen, J.M. (2011). FieldTrip: open source software for advanced analysis of MEG, EEG, and invasive electrophysiological data. Comput Intell Neurosci. https://doi.org/10.1155/2011/156869.

Pursiainen, S. (2012). Raviart–thomas-type sources adapted to applied EEG and MEG: implementation and results. *Inverse Problems*, *28*(6), 065,013.

Pursiainen, S., Lew, S., Wolters, C.H. (2016a). Forward and inverse effects of the complete electrode model in neonatal EEG. Journal of Neurophysiology. https://doi.org/10.1152/jn.00427.2016.

Pursiainen, S., Vorwerk, J., Wolters, C. (2016b). Electroencephalography (EEG) forward modeling via H(div) finite element sources with focal interpolation. *Physics in Medicine and Biology*, *61*(24), 8502–8520. https://doi.org/10.1088/0031-9155/61/24/8502.

Rullmann, M., Anwander, A., Dannhauer, M., Warfield, S.K., Duffy, F.H., Wolters, C.H. (2009). EEG source analysis of epileptiform activity using a 1 mm anisotropic hexahedra finite element head model. *NeuroImage*, *44*(2), 399–410.

Sakoe, H., & Chiba, S. (1978). Dynamic programming algorithm optimization for spoken word recognition. IEEE Transactions on Acoustics, Speech, and Signal Processing ASSP-26, 43–49.

Schmidt, D.M., George, J.S., Wood, C.C. (1999). Bayesian inference applied to the electromagnetic inverse problem. *Human Brain Mapping*, *7*(3), 195–212.

Schöberl, J. (1997). Netgen an advancing front 2D/3D-mesh generator based on abstract rules. *Computing and Visualization in Science*, *1*(1), 41–52.

Seeber, M., Cantonas, L.M., Hoevels, M., Sesia, T., Visser-Vandewalle, V., Michel, C.M. (2019). Subcortical electrophysiological activity is detectable with high-density EEG source imaging. *Nature Communications*, *10*(1), 753.

Si, H. (2015). Tetgen, a delaunay-based quality tetrahedral mesh generator. *ACM Transactions on Mathematical Software (TOMS)*, *41*(2), 11.

Spitzer, F. (1971). Markov random fields and Gibbs ensembles. *The American Mathematical Monthly*, *78*(2), 142–154.

Tadel, F., Baillet, S., Mosher, J.C., Pantazis, D., Leahy, R.M. (2011). Brainstorm: a user-friendly application for MEG/EEG analysis. *Computational Intelligence and Neuroscience*, *2011*, 8.

Tang, T., Oh, S., Sadleir, R. (2010). A robust current pattern for the detection of intraventricular hemorrhage in neonates using electrical impedance tomography. *Annals of Biomedical Engineering*, *38*(8), 2733–2747.

Vauhkonen, M. (1997). *Electrical impedance tomography and prior information*. Kuopio, dissertation: University of Kuopio.

Vorwerk, J., Cho, J.H., Rampp, S., Hamer, H., Knösche, T.R., Wolters, C.H. (2014). A guideline for head volume conductor modeling in EEG and MEG. *NeuroImage*, *100*, 590–607.

PUBLICATION III

Randomized Multiresolution Scanning in Focal and Fast E/MEG Sensing of Brain Activity with a Variable Depth

A. Rezaei, A. Koulouri, and S. Pursiainen

Journal of Brain Topography 33(2), 161–175
DOI: 10.1007/s10548-020-00755-8

Brain Topography (2020) 33:161–175
https://doi.org/10.1007/s10548-020-00755-8

ORIGINAL PAPER

Randomized Multiresolution Scanning in Focal and Fast E/MEG Sensing of Brain Activity with a Variable Depth

A. Rezaei[1] · A. Koulouri[1] · S. Pursiainen[1]

Received: 28 May 2019 / Accepted: 4 February 2020 / Published online: 19 February 2020

Abstract
We focus on electro-/magnetoencephalography imaging of the neural activity and, in particular, finding a robust estimate for the primary current distribution via the hierarchical Bayesian model (HBM). Our aim is to develop a reasonably fast *maximum a posteriori* (MAP) estimation technique which would be applicable for both superficial and deep areas without specific *a priori* knowledge of the number or location of the activity. To enable source distinguishability for any depth, we introduce a randomized multiresolution scanning (RAMUS) approach in which the MAP estimate of the brain activity is varied during the reconstruction process. RAMUS aims to provide a robust and accurate imaging outcome for the whole brain, while maintaining the computational cost on an appropriate level. The inverse gamma (IG) distribution is applied as the primary hyperprior in order to achieve an optimal performance for the deep part of the brain. In this proof-of-the-concept study, we consider the detection of simultaneous thalamic and somatosensory activity via numerically simulated data modeling the 14-20 ms post-stimulus somatosensory evoked potential and field response to electrical wrist stimulation. Both a spherical and realistic model are utilized to analyze the source reconstruction discrepancies. In the numerically examined case, RAMUS was observed to enhance the visibility of deep components and also marginalizing the random effects of the discretization and optimization without a remarkable computation cost. A robust and accurate MAP estimate for the primary current density was obtained in both superficial and deep parts of the brain.

Keywords Brain imaging · Depth reconstruction · EEG and MEG data · Hierarchical Bayesian model · Randomized multiresolution scanning

Introduction

This study concentrates on electro-/magnetoencephalography (E/MEG) imaging of the brain activity (He et al. 2018). The present focus is on the hierarchical Bayesian model (HBM) (Calvetti et al. 2009; Lucka et al. 2012) which allows one to find a focal and robust reconstruction by exploring a posterior probability distribution following from a conditionally Gaussian prior model. Our aim is, in particular, to develop a fast *maximum a posteriori* (MAP) estimation technique which would be applicable for both superficial and deep areas without additional *a priori* knowledge of the brain activity, such as physiological depth weighting (Calvetti et al. 2015, 2018; Homa et al. 2013). While high-density measurements (Seeber et al. 2019) and advanced signal processing strategies (Pizzo et al. 2019) have recently been shown to be essential in distinguishing deep activity, this study focuses on the importance to reduce the random effects of the numerical discretization and optimization errors on the reconstruction process.

We introduce a randomized multiresolution scanning (RAMUS) method in which the MAP estimate of the brain activity is refined gradually in the reconstruction procedure. RAMUS aims at reducing the random effects of the numerical discretization on the final estimate. It processes the well and ill-conditioned parts of the source space separately which has been suggested for ill-posed problems, e.g., in (Pursiainen 2008; Liu et al. 1995; Piana and Bertero 1997a). A multiresolution decomposition provides an approximative split between detectable and undetectable parts for different

Handling Editor: Christoph M. Michel.

✉ A. Rezaei
atena.rezaei@tuni.fi

[1] Faculty of Information Technology and Communication Sciences, Tampere University, P.O. Box 692, 33101 Tampere, Finland

source depths, as the maximal source localization accuracy varies strongly with respect to the depth (Tarkiainen et al. 2003; Cuffin et al. 2001a, b; Grover 2016; Wang et al. 2009) with only the low resolution fluctuations being visible in the deep part of the brain (Pascual-Marqui et al. 1999; Pascual-Marqui 1999). At each resolution level, a MAP estimate is evaluated via the iterative alternating sequential (IAS) algorithm and the inverse gamma (IG) hyperprior which has been found to be advantageous for detecting deep activity (Calvetti et al. 2009).

The previous results suggest that HBM can find a focal solution deep in the head via the Markov chain Monte Carlo (MCMC) sampling techniques, especially, if the activity can be constrained into a region of interest (ROI) (Calvetti et al. 2009; Lucka et al. 2012). However, processing large data sets involving temporal measurement sequences with an advanced MCMC approach without *a priori* knowledge of a ROI might be computationally too expensive for the practical use. Therefore, finding a robust and fast approach to distinguish activity reliably is crucial regarding the practical applications. In this proof-of-the-concept study, we consider the detection of simultaneous somatosensory and thalamic activity with numerically simulated data. This setup models the detection of the somatosensory evoked potentials and fields (SEP/F) in response to the electrical stimulation of the median nerve, particularly, thalamic (deep) P14/N14 and somatosensory (superficial) P20/N20 component peaked at 14 and 20 ms post-stimulus, respectively (Buchner et al. 1988, 1995, 1994a, b; Haueisen et al. 2007; Attal and Schwartz 2013; Fuchs et al. 1998).

In the numerical experiments, both a spherical and realistic model has been used to analyze the source reconstruction discrepancies with RAMUS. The results suggest that a randomized set of decompositions (Mallat 1989; Clark et al. 1995) is essential to marginalize out the possible modeling errors due to projecting the source space into different resolution levels which, again, is necessary in order to achieve the depth-invariance of the final MAP estimate.

Methodology

Observation Model

For the EEG source modelling, we employ the finite element method and the current preserving H(div) approach (Pursiainen 2012a; Pursiainen et al. 2016; Miinalainen et al. 2019) in which the primary current distribution of the neural activity is assumed to have a square-integrable divergence $\mathbf{J}^P \in H(\mathrm{div}) = \{\mathbf{w} | \nabla \cdot \mathbf{w} \in L^2(\Omega)\}$ in the source space denoted by $\mathcal{S}$. The observation model is

$$\mathbf{y} = \mathbf{L}\mathbf{x} + \mathbf{n}, \tag{1}$$

where $\mathbf{y} \in \mathbb{R}^m$ is the measurement vector, $\mathbf{L} \in \mathbb{R}^{m \times 3K}$ is the lead field matrix, $\mathbf{x} \in \mathbb{R}^{3K}$ is the unknown primary current distribution with K denoting the total number of the source positions, and $\mathbf{n} \in \mathbb{R}^m$ is the measurement noise vector which is modelled as Gaussian random variable with zero mean and covariance matrix of the form $\sigma^2\mathbf{I} \in \mathbb{R}^{m \times m}$. In this numerical study, the diagonal covariance is used for simplicity as it allows fixing the noise level with a single parameter, i.e., the standard deviation σ. We refer to $\mathbb{R}^{3K}$ as the source space $\mathcal{S}$ for the inverse problem of finding $\mathbf{x}$ given the data $\mathbf{y}$. The number of sources is three times the number of their positions, as each position is assumed to have three sources oriented along the Cartesian coordinate axes.

Hierarchical Bayesian Model

In the HBM framework, the prior of $\mathbf{x}$ is not fixed but random. It is determined by the realization of the so-called hyperparameter $\boldsymbol{\theta}$. The hyperparameter follows an *a priori* assumed distribution, i.e., the hyperprior. Consequently, the prior is a joint density given by $p(\mathbf{x}, \boldsymbol{\theta}) \propto p(\boldsymbol{\theta})\, p(\mathbf{x} \mid \boldsymbol{\theta})$ of $\mathbf{x}$ and $\boldsymbol{\theta}$. The conditional part of the prior $p(\mathbf{x} \mid \boldsymbol{\theta})$ corresponds to a zero mean Gaussian density with a diagonal covariance matrix predicted by the hyperprior $p(\boldsymbol{\theta})$. The hyperparameter $\boldsymbol{\theta}$ is of the same dimension as $\mathbf{x}$ with each entry defining the variance of its respective entry in $\mathbf{x}$. The density of the hyperprior is long-tailed, implying that $\mathbf{x}$ is likely to be a sparse vector with only few nonzeros, which is advantageous for finding a focal reconstruction of the brain activity. As a hyperprior, one can use, e.g., the gamma (G) or inverse gamma $\mathrm{IG}(\boldsymbol{\theta} \mid \beta, \theta_0)$ density (Calvetti et al. 2009), whose shape and scale are controlled by the parameters β and θ_0, respectively. IG is a conjugate prior for a Gaussian distribution with an unknown variance (here the conditional prior), meaning that the corresponding posterior (here the actual prior) is also Gaussian. Again, G is a conjugate prior with respect to the reciprocal of the variance (O'Hagan and Forster 2004).

The *posterior* probability density of $\mathbf{x}$, following from the classical Bayes formula (O'Hagan and Forster 2004), is of the form

$$p(\mathbf{x}, \boldsymbol{\theta} \mid \mathbf{y}) = \frac{p(\mathbf{x}, \boldsymbol{\theta})\, p(\mathbf{y} \mid \mathbf{x})}{p(\mathbf{y})} \propto p(\mathbf{x}, \boldsymbol{\theta})\, p(\mathbf{y} \mid \mathbf{x}), \tag{2}$$

i.e., it is proportional to the product between the prior density $p(\mathbf{x}, \boldsymbol{\theta})$, and the likelihood function $p(\mathbf{y} \mid \mathbf{x}) \propto \exp(-(2\sigma^2)^{-1} \|\mathbf{L}\mathbf{x} - \mathbf{y}\|^2)$ given by the measurement noise model (Schmidt et al. 1999).

We consider finding the inverse estimate via the *iterative alternating sequential* (IAS) MAP estimation method

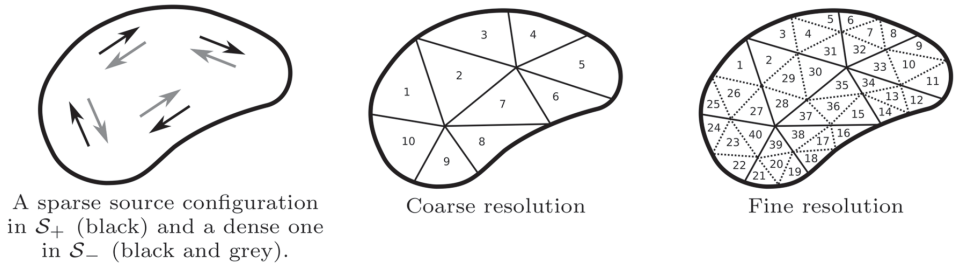

Fig. 1 *1st from the left* In E/MEG, a coarse enough source configuration can be distinguished, i.e., it belongs to $\mathcal{S}_\varepsilon^+$, while a dense one has modes that cancel each other and might be indetectable, i.e., in $\mathcal{S}_\varepsilon^-$ (Fig. 1). *2nd and 3rd from the left:* An example of subdividing the grey matter compartment to subdomains in the case of a coarse (center) and fine (right) resolution. Here, the sparsity factor s, i.e., the ratio between number of subdomains for two consequtive resolution levels, would be four. An example of mapping a subdomain from a coarse to fine resolution is given by $\{2\} \rightarrow \{2, 28, 29, 30\}$

(Appendix 5) using primarily the IG density as the hyperprior. IG has been suggested for depth localization in Calvetti et al. (2009), where the IG and G based IAS MAP estimate have been shown to correspond to the minimum support and minimum current estimate (MSE and MCE) (Nagarajan et al. 2006), respectively, while the first step of the iteration concides with the classical minimum norm estimate (MNE) (Hämäläinen et al. 1993). A recent comparison between IAS and other brain activity reconstruction techniques can be found in (Calvetti et al. 2018).

The numerical exploration of the posterior density $p(\mathbf{x}, \boldsymbol{\theta} \mid \mathbf{y})$ is subject to the numerical discretization, i.e., the numerical definition of the source space $\mathcal{S}$ for $\mathbf{x}$ and the resulting lead field matrix. We aim to reduce the effect of the discretization via the following two strategies motivating the introduction of the RAMUS approach:

(1) The reduction of the source space is essential to improve the ability of a solver to recover focal sources both in deep and superficial locations. Furthermore, since a sparse source space results here in source reconstruction of low spatial resolution, a source space refinement during the reconstruction process of this study is crucial.
(2) A randomized set of decompositions enables averaging out (marginalizing) the effect of the discretization error.

The theoretical justification of (1) and (2) are given in the following sections "Coarse-to-Fine Optimization" and "Randomized Scanning", respectively.

Coarse-to-Fine Optimization

The EEG source imaging problem is severely ill-posed (Grech et al. 2008) and it is well-known that most of the solvers suffer from depth bias effects (Pascual-Marqui 1999; Koulouri et al. 2017; Awan et al. 2018). A way to reduce the ill-conditioning in the computations is by introducing coarser (sparse) source space, i.e., regularization by discretization (Hansen 2010; Kirsch 2011), or by approximating the source distribution as a linear combination of spatial basis functions (redundant dictionaries) as proposed in Haufe et al. (2008). With a dimensionality reduction, the linear system to be solved is often over-determined and stable estimates can be obtained. However, this comes at a cost of poor resolution reconstructions due to large discretization errors. The idea of employing a multiresolution approach (Mallat 1989), where a progressive refinement in the source space is performed in order to obtain more accurate estimates, has been proposed for the E/MEG problem for example in Gavit et al. (2001); Malioutov et al. (2005).

The source space $\mathcal{S}$ can be decomposed via the direct sum of $\mathcal{S}_\varepsilon^+ = \{\mathbf{0}\} \cup \{\mathbf{x} \,:\, \|\mathbf{Lx}\| \geq \varepsilon\}$ and $\mathcal{S}_\varepsilon^- = \{\mathbf{x} \,:\, \|\mathbf{Lx}\| < \varepsilon\}$, i.e. $\mathcal{S} = \mathcal{S}_\varepsilon^+ \oplus \mathcal{S}_\varepsilon^-$, where ε is determined by the noise level. $\mathcal{S}_\varepsilon^+$ and $\mathcal{S}_\varepsilon^-$ represent the sets of the detectable and undetectable source distributions, respectively. If possible, it is advantageous to decompose $\mathcal{S}$ into $\mathcal{S}_\varepsilon^+$ and $\mathcal{S}_\varepsilon^-$ as, thereby, one can avoid source localization errors related to the indetectable distributions $\mathcal{S}_\varepsilon^-$ (Pursiainen 2008; Piana and Bertero 1997b; Liu et al. 1995). In E/MEG, a coarse enough source configuration can be distinguished, i.e., it belongs to $\mathcal{S}_\varepsilon^+$, while a dense one has modes that cancel each other and might be indetectable, i.e., in $\mathcal{S}_\varepsilon^-$ (Fig. 1). The coarsity is specifically

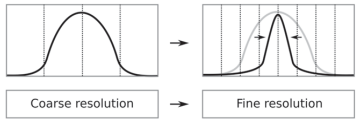

Fig. 2 Once an approximation for a non-zero source has been found at a coarse resolution level (left) the its support will shrink at the finer levels (right)

important considering deep activity for which the magnitude of the lead field is comparably low and, therefore, any deep source configuration is likely to belong to $\mathcal{S}_\varepsilon^-$. For a given lead field matrix $\mathbf{L}$, the maximum possible number of detectable sources and, thereby, the maximal dimension of $\mathcal{S}_\varepsilon^+$ is determined by the maximum number of nonzero singular values which coincides with the smaller dimension of $\mathbf{L}$, that is, the number of the data entries m.

In the coarse-to-fine reconstruction strategy, the aim is to first limit the source space $\mathcal{S}$ to a subspace $\mathcal{S}_\varepsilon^+$ by restricting its resolution, to gradually increase its resolution, and to eventually obtain an approximation for the whole space $\mathcal{S}$. A nested set of restricted subspaces with different resolutions referred here to as a multiresolution decomposition is obtained recursively by selecting a uniformly random set of source positions from a given source space and associating those with the original set of positions through nearest interpolation. The coarsest resolution level is associated with the index $\ell = 1$. When moving from the ℓ-th resolution level to the $(\ell + 1)$-th one, the number of source positions is assumed to grow by a constant sparsity factor $s > 1$. An example for a dual resolution decomposition and a mapping of the subdomains between them can be found in Fig. 1.

In the IAS MAP estimation process, once the activity has been found at a coarse reconstruction level, the support of the candidate solution will shrink along with the increasing resolution (Fig. 2). That is, the size of the details found is subject to the resolution level. Therefore, the final estimate is found as a combination of the estimates obtained for the different levels. In order to distinguish the weakly detectable activity, especially, the deep components, the number of the dimensions in the initial set should be of the same size with m, following from the maximal dimensionality of $\mathcal{S}_\varepsilon^+$.

Randomized Scanning

Since a sparse source space is likely to induce a bias to the consequent estimates, we propose to use a random set of (initial) sparse source spaces that aims to reduce the propagation of random discretization and optimization errors. The relationship between the global posterior optimizer $\mathbf{x}^*$ and $\mathbf{x}_k$ for the original source space $\mathcal{S}$ and its restriction $\mathcal{S}_k$, respectively, can be modeled via the equation

$$\mathbf{x}_k = \mathbf{x}^* + \mathbf{d}_k + \mathbf{v}_k, \tag{3}$$

where $\mathbf{d}_k$ and $\mathbf{v}_k$ represent a discretization and optimization error, respectively. Of these, $\mathbf{v}_k$ depends of the quality of the MAP optimization method and vanishes in the ideal case, while $\mathbf{d}_k$ is fixed. If the degrees of freedom in $\mathcal{S}_1, \mathcal{S}_2, \ldots, \mathcal{S}_D$ have an independent and identical random distribution, the respective discretization errors $\mathbf{d}_1, \mathbf{d}_2, \ldots, \mathbf{d}_D$ can be modeled as independently and identically distributed random variables and, by the law of large numbers and the central limit theorem, the discretization error term $\frac{1}{D}\sum_{k=1}^{D} \mathbf{d}_k$ of the mean

$$\frac{1}{D}\sum_{k=1}^{D} \mathbf{x}_k = \mathbf{x}^* + \frac{1}{D}\sum_{k=1}^{D} \mathbf{d}_k + \frac{1}{D}\sum_{k=1}^{D} \mathbf{v}_k \tag{4}$$

is an asymptotically Gaussian variable with expectation $\tilde{\mathbf{d}}$ and the rate of convergence $\frac{1}{D}\sum_{k=1}^{D} \to \tilde{\mathbf{d}}$ is of the order $O(D^{-1/2})$ with respect to the number of source spaces (Liu 2001). Consequently, the random effects of the discretization errors can be marginalized via estimating $\mathbf{x}^*$ in multiple randomly (independently and identically) generated source spaces. The expectation $\tilde{\mathbf{d}}$ can be regarded as the remaining systematic discretization error which is specific to the set $\mathcal{S}_1, \mathcal{S}_2, \ldots, \mathcal{S}_D$, i.e., the resolution level, and is related, for example, to the relationship between the maximal achievable level of detail and the structure of the actual unknown brain activity.

Since the outcome of the optimization process for each given source space is *a priori* sensitive to the discretization errors, the estimate for $\mathbf{x}_k$ is found using the one for $\mathbf{x}_{k-1}$ as the initial guess. This approach is motivated by the present gradually progressing coarse-to-fine subdivision due to which the subsequent optimizers will be nearly similar. We consider it necessary in order to maintain each estimate in the vicinity of the global optimum and, thereby, the norm of the optimization error $\mathbf{v}_k$ as small as possible. Namely, using a fixed initial guess might mean that, instead the global optimizer, a local one is found for some of the source spaces as depicted in Fig. 3. The global optimum might correspond to a situation in which both a superficial and deep source are detected, while the deep activity might be undetected at a local one.

Technically, updating the initial guess makes the estimate for $\mathbf{x}_k$ dependent on the previous one obtained for $\mathbf{x}_{k-1}$, i.e., the sequence of the estimates is a time-homogeneous Markov chain. We regard the present approach as a surrogate transition rule (Liu 2001) estimating the outcome of an ideal optimization method which would find the global optimum precisely with $\mathbf{v}_k = 0$, thereby, resulting in the identity

$$\frac{1}{D}\sum_{k=1}^{D} \mathbf{x}_k = \mathbf{x}^* + \frac{1}{D}\sum_{k=1}^{D} \mathbf{d}_k \to \mathbf{x}^* + \tilde{\mathbf{d}}, \tag{5}$$

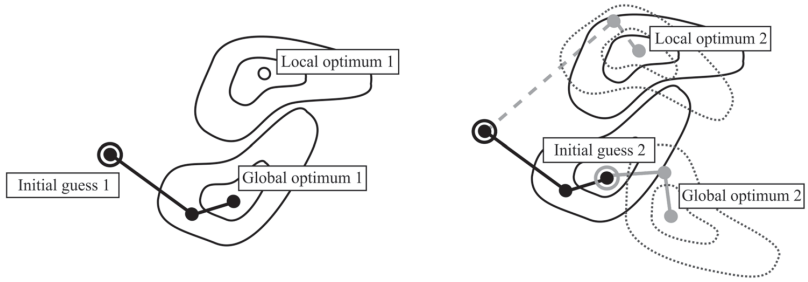

Fig. 3 An estimate for the global posterior optimizer $\mathbf{x}_k$ obtained for the source space $\mathcal{S}_k$ is found using the estimate for $\mathbf{x}_{k-1}$ as the initial guess (" Randomized Scanning" section). We consider this approach necessary in order to maintain the estimates as close to the global optimum as possible. Namely, using a fixed initial guess might mean that the global optimizer is not found for some of the source spaces. Left: The global posterior optimizer is found for the posterior of space 1 (solid contours). Right: For space 2 (dashed contours), it is found (solid grey path), if the final estimate obtained in the case one 1 is used as the initial guess for 2 (grey circled point), while a local optimizer is obtained (dashed grey path) with the original initial guess 1 (black circled point) resulting in an optimization error. The global optimum might, in practice, correspond to a situation in which both a superficial and deep source are detected, while the deep activity might be undetected at the local one

which will hold approximately, if the surrogate rule is accurate enough.

RAMUS

We propose the following algorithm for RAMUS to reduce the random discretization and optimization effects when finding a reconstruction for the unknown parameter $\mathbf{x}$ with the IAS MAP estimation method.

1. Choose the desired number of the resolution levels L and the sparsity factor (the ratio of source counts) s between each level. The number of the sources at a given resolution level will be $K_\ell = Ks^{(\ell-L)}$, where $\ell = 1, 2, \ldots, L$ is the index of the resolution level, the larger the value of the index ℓ the finer the resolution.
2. For each resolution level $\ell = 1, 2, \ldots, L$, create a random uniformly distributed set of center points $\mathbf{p}_1, \mathbf{p}_2, \ldots, \mathbf{p}_{K_\ell}$. Find source point subsets B_1, B_2, …, B_{K_ℓ} applying the nearest interpolation scheme with respect to the center points. That is, each subset B_j consists of those source positions of the total source space $\mathcal{S}$, whose nearest neighbor with respect to $\mathbf{p}_1, \mathbf{p}_2, \ldots, \mathbf{p}_{K_\ell}$ is $\mathbf{p}_j$. The average number of source positions associated with B_j is approximately given by the sparsity factor s. The resolution of this subdivision grows along the number of the center points. The unknown parameter is assumed to be constant in each subset, and the actual source count is assumed to stay unchanged regardless of the resolution.
3. Repeat the first two steps to generate a desired number D of independent multiresolution decompositions $\mathfrak{S}_1$, $\mathfrak{S}_2$, …, $\mathfrak{S}_D$.
4. Start the reconstruction process with the decomposition $\mathfrak{S}_1$ and a suitably chosen initial guess $\mathbf{x}^{(0)}$.
5. For decomposition $\mathfrak{S}_k$, find a reconstruction $\mathbf{x}^{(\ell)}$ with the IAS MAP technique with the initial guess $\mathbf{x}^{(\ell-1)}$ for the resolution levels $\ell = 1, 2, \ldots, L$.
6. After going through all the decompositions, obtain the final estimate for the decomposition (basis) k as the normalized mean

$$\overline{\mathbf{x}}^{(k)} = \sum_{\ell=1}^{L} \mathbf{x}^{(\ell)} \Big/ \sum_{\ell=1}^{L} s^{(L-\ell)}, \tag{6}$$

   where the denominator follows from the need to balance out the effect of the multiplied source count following from the interpolation of a coarse level estimate to a denser resolution level.
7. If $k < D$, move to the next decomposition, i.e., update $k \to k+1$, and repeat the previous step with the initial guess $\overline{\mathbf{x}}^{(k-1)}$ for the resolution level $\ell = 1$.
8. Obtain the final reconstruction as the mean:

$$\overline{\overline{\mathbf{x}}}^{(k)} = \frac{1}{D} \sum_{k=1}^{D} \overline{\mathbf{x}}^{(k)}. \tag{7}$$

Technically, this process is equivalent to first evaluating the mean (7) for each resolution level and then the normalized mean (6) over the different resolutions, showing that an approximation of the form (3) is, in fact, obtained for each set of independent and identically generated source spaces. Since the final reconstruction is obtained as a mean over all the reconstruction levels, also the potential systematic discretization errors will be averaged with an equal weighting. This approach is used, as different resolution levels localize

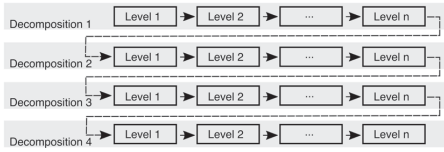

Fig. 4 A schematic visualization of the data flow during the reconstruction process for the multiresolution decompositions $1, 2, \ldots, D$ each one with resolution levels $1, 2, \ldots, L$. The final estimate (6) obtained for the decomposition k is used as the level-one initial guess for the decomposition $k + 1$. This sequential strategy for selecting the initial guess aims to minimize the effect of the optimization errors as suggested in Fig. 3. Note that with a good enough initial guess the global optimum is always found, meaning that the differences between the optimization results can be associated with the discretization errors which are modeled here as independently and identically distributed random variables

different details ("Coarse-to-Fine Optimization" section). Consequently, the details found for the most levels are likely to gain the highest intensity in the final reconstruction. A schematic illustration of the resulting data flow has been included in Fig. 4.

Numerical Implementation with Zeffiro Interface

The forward and inverse solvers applied in this study were implemented in the Matlab (The MathWorks Inc.) as a part of the *Zeffiro Interface* (ZI) code package which is openly available in GitHub[1]. ZI is a tool enabling finite element (FE) based forward and inverse computations in electromagnetic brain applications. The forward approach of ZI together with the basic version of the IAS source reconstruction approach have been validated numerically in (Miinalainen et al. 2019; Pursiainen 2012b). ZI generates a uniform tetrahedral finite element (FE) mesh. Each source distribution is obtained by picking the first K entries of the randomly (uniformly) permuted set of the tetrahedron centers for the brain compartment. Due to the uniform mesh structure, this strategy leads to an evenly distributed set of source points. $\mathbf{x}$.

ZI allows performing the source reconstruction routines using either a CPU or a GPU (graphics processing unit) type processor. Today, effective GPUs are available in power PCs an workstations but most laptops are still limited to CPU processing. Therefore, to compare the performance difference between GPU and CPU platforms, the computing time for forming a random set of multiresolution decompositions and inverting a given measurement data vector were evaluated for NVIDIA Quadro P6000 workstation GPU and Intel i7 5650U laptop CPU.

[1] https://github.com/sampsapursiainen/zeffiro_interface

Table 1 The conductivities (S/m) of the different compartments for PHM and Ary model (Ary et al. 1981)

Model	WM	GM	CSF	Skull	Skin
Ary		0.33		0.0042	0.33
Deep	0.14	0.33	1.79	0.0064	0.43

Justification of the values used for the realistic model can be found in Dannhauer et al. (2011)

Numerical Experiments

In the numerical experiments, we used the realistic population head model[2] (PHM) (Lee et al. 2016), consisting of five layers (white matter, grey matter, cerebrospinal fluid (CSF), skull, and skin) and the three-layer Ary model in which concentric 87, 92 and 100 mm spheres present grey matter, skull and scalp layer. The cerebellum and vetricle layers included in the PHM were modeled as part of the grey matter and CSF, respectively. The conductivity of each layer can be found in Table 1. The PHM and Ary model were discretized with a uniform point lattice with the resolution 0.85 and 1 mm, leading to 24M and 30M tetrahedral elements and 4M and 5M nodes, respectively. In both cases, a single lead field matrix was generated for 10000 randomly distributed synthetic source positions. The lead field matrix entries were evaluated in SI units, i.e., Ohm/m and $1/m^2$ for EEG and MEG, respectively. Each point contained three sources oriented along x-, y- and z-directions. Since the grey matter compartment of PHM does not include the thalamus, the source space was extended to cover both the white and grey matter compartment. Note that the lead field matrix and the corresponding source space have to be generated only once after which the space can be decomposed in multiple ways, e.g., different resolutions, as is the case in the proposed RAMUS process.

Simulated Measurements

For the Ary model, a total of 102 sensor points were distributed over the upper hemisphere. Using those, both electrode and radial magnetometer measurements of the electromagnetic field were simulated as shown in Fig. 5. The magnetometer locations were obtained by scaling the radial component of the source locations by a factor of 1.2. The electrodes were modeled using the complete electrode model (Pursiainen et al. 2012). The inner and outer radius of the ring were 5 and 10 mm, respectively. The average contact resistance of each electrode was assumed to be 1 kOhm. In

[2] https://itis.swiss/virtual-population/regional-human-models/phm-repository/

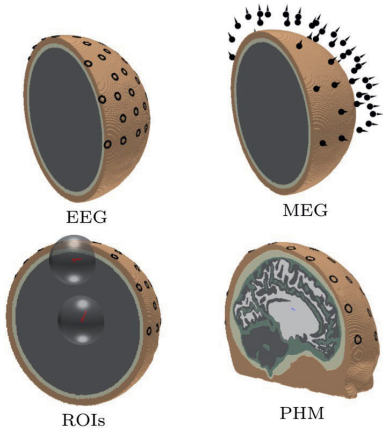

Fig. 5 The volumetric FE mesh for the realistic five-layer PHM and three-layer Ary model. Top row: The left image shows the domain with 102 EEG ring electrodes on it and the right one visualizes the positioning of the 102 radial magnetometers which has been obtained by scaling the electrode locations by the factor of 1.2. Bottom row: The source locations with the ROIs for the Ary model (left) and a cut-view of the PHM (right) with 1cm diameter ring electrodes which were modeled using the complete electrode model (Pursiainen et al. 2012)

Table 2 The source locations and orientations utilized in the numerical experiments

Type	Corresp.	x (mm)	y (mm)	z (mm)	Angle (°)
Superf.	P20/N20	− 5	0	77	11
Deep	P14/N14	7	0	5	68

the case of PHM, an EEG cap with 72 ring electrodes (10 mm outer and 5 mm inner diameter, 1 kOhm resistance) was attached on the head model.

Two current dipoles were placed in shallow and deep parts of the grey matter. The source locations can be found in Table 2. Physiologically these could be interpreted as the somatosensory (superficial) P20/N20 and thalamic (deep) P14/N14 component, i.e., the 20 and 14 ms post-stimulus peaks. Activity for both locations occurs at the same time in the SEP/F response to the median nerve stimulus (Buchner et al. 1988, 1994a, 1995). When active simultaneously, the deep source was assumed to be slightly stronger in magnitude compared to the superficial one to enable the visibility of the deep part. This situation occurs momentarily in the median nerve stimulation, since the thalamic source obtains its maximum before the somatosensory activity increases in magnitude.

As the measurement error term, we used zero mean Gaussian white noise with standard deviation of 3% respect to maximal signal amplitude. To investigate the noise-robustness of the source reconstruction, 5% noise was used in a single test. For the generality of the results, the maximum data entry of each dataset was normalized to one. The accuracy of the source recovery was analyzed in two 60 mm diameter spherical ROIs centered at the source locations (Fig. 5).

IAS MAP Iteration

The previous experience shows that, in order to distinguish deep activity (Calvetti et al. 2009), the hyperparameter values for the hyperprior have to be set as small as possible without risking the numerical stability of the reconstruction process. In the present study, the scale parameter θ_0 was chosen to be 1E-10 and the shape parameter β was given the smallest possible value 1.5. These values were found to work generally well and they are supported also by the earlier studies (Calvetti et al. 2009). Ten iteration steps were performed to obtain a MAP estimate for a single resolution level. A single step was utilized in a single test.

Validation Tests

We analyzed the performance of the RAMUS reconstruction approach both visually and numerically in the tests (A)–(I) using the Ary model. The spherical domain was used in order to optimize the clarity of the results. In addition to these reconstructions, one test (J) was performed using PHM, i.e., the realistic model. The specifications for (A)–(J) can be found in Table 3.

The accuracy obtained in the cases (A)–(I) was analyzed by comparing the average position (center of mass), orientation and magnitude of the reconstructed distribution within the ROI to that of the actual dipole source. These average estimates were obtained with respect to the final reconstructed distribution of 10000 sources in each case (A)–(I) and for both single and multiple resolution reconstructions. In addition, the relative magnitude (between 0 and 1) of the distribution was calculated for each ROI. The source was classified as detected, if the relative maximum exceeded the value 0.1, and otherwise undetected. This threshold criterion was chosen as it represents roughly the limit of a visually detectable source. In (A)–(I), we varied the number of multiresolution decompositions, sparsity factor, hyperprior, the source magnitudes, and the measurement modality (EEG or E/MEG). When combining the lead field matrices for E/MEG, the MEG lead field matrix and data was scaled so that the Frobenius norm, i.e., the 2-norm of all the entries, was equal to that of the EEG lead field matrix.

The case (I), was studied using three alternative approaches in addition to the basic multiresolution scheme. In the first one of these, the noise level was increased to 5%.

Table 3 The specifications of the reconstructions computed in the numerical experiments

ID	Geom.	Data	s[a]	Dec.[b]	Hyperprior	Amplitude	
						Deep	Superf.
(A)	Ball	EEG	8	100	IG	10	5
(B)	Ball	EEG	8	100	IG	10	0
(C)	Ball	EEG	8	100	IG	0	5
(D)	Ball	EEG	8	100	IG	10	7
(E)	Ball	EEG	5	100	IG	10	7
(F)	Ball	EEG	8	20	IG	10	7
(G)	Ball	EEG	8	100	G	10	5
(H)	Ball	E/MEG	8	100	IG	10	5
(I)	Ball	E/MEG	8	100	IG	10	7
(J)	PHM	EEG	8	100	IG	10	7

[a]Scaling factor

[b]Number of decompositions

The second one involved only the coarse resolution level with otherwise unchanged parameters. In the last one, only single IAS MAP iteration was performed on each reconstruction level, meaning that the estimate obtained coincided with MNE (Calvetti et al. 2009).

A total of 100–400 source positions at the coarse level, i.e., a number roughly comparable to that of the data entries ("Coarse-to-Fine Optimization" section), was found to work appropriately in the detection of the deep activity. When the sparsity factor between $s = 8$ and $s = 5$, the source position count was within this interval at the coarsest level of a three-level multiresolution decomposition for the initial set of 10000 source positions. At the coarsest level, each source position was associated to about s^2 (s^{L-1} with $L = 3$), i.e., between 64 and 25 finest-level source positions, respectively. The number D of multiresolution decompositions was chosen to be comparable to this number, slightly below or above that, in order to guarantee sufficient averaging over all the possible random basis choices.

Results

The results obtained in the numerical experiments have been included in Tables 4, 5 and Figs. 6, 7, 8, 9, 10 and 11. In each case, the deep and superficial component have been analyzed separately. Histograms for the cases (A)–(I) illustrate the accuracy of the reconstructed source with respect to the source position (mm), orientation (deg), amplitude, and the relative maximum of the current density within the ROI (Figs. 6, 7, 8 and 9) with respect to the global maximum.

Table 4 The computing time (in seconds) for 100 random three-level multiresolution decompositions and of a corresponding RAMUS (randomized multiresolution scan) estimate obtained with a NVIDIA Quadro P6000 workstation GPU and Intel i7 5650U laptop CPU

Processor	Dec.	EEG	E/MEG
Quadro P6000	36	14	28
i7 5650U	176	55	116

Table 5 The percentage of the reconstructions fulfilling the source detection criterion (the local maximum in the ROI >0.1 of the global maximum). This threshold criterion was chosen as it represents roughly the limit of a visually detectable source. In case (B), where only the deep source is present there are 4% false positive detections for the superficial one. This is due to the relatively large deviation of the deep source due to which it is moved partially in the superficial ROI in the corresponding estimates

Type	$\mathbf{n}$[a]	ℓ[b]	ROI	(A)	(B)	(C)	(D)	(E)	(F)	(G)	(H)	(I)
MAP	3	1–3	Deep	100	100	0	98	100	86	0	100	92
			Sup.	100	4	100	100	100	100	100	100	100
	5		Deep								100	90
			Sup.								100	100
MNE	3	1–3	Deep									0
			Sup.									100
MAP	3	1	Deep									96
			Sup.									100

[a]Noise level (%)

[b]The resolution levels (ℓ) in the reconstruction process

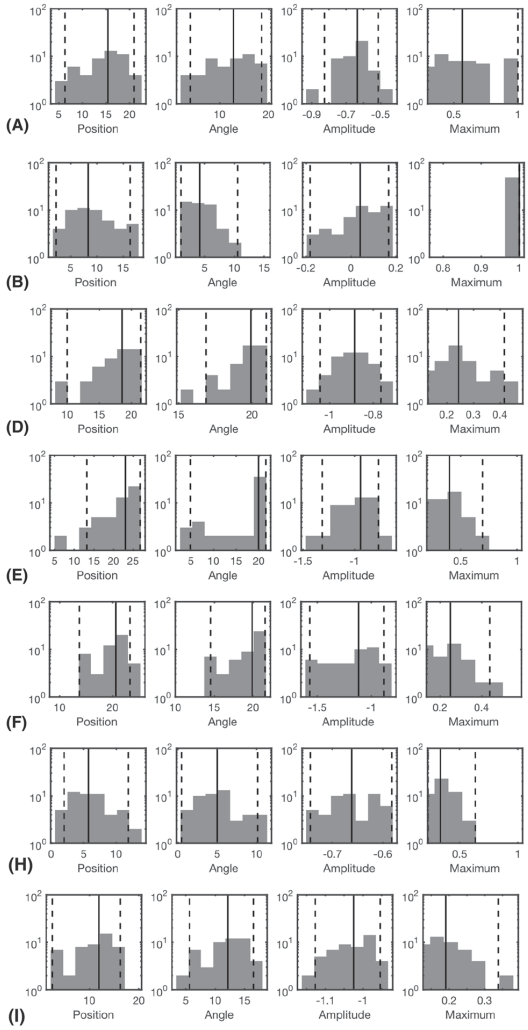

Fig. 6 The results of the deep source localization for the numerical experiments (**A**–**I**) conducted in the spherical domain (Table 3). The distributions of the position (mm), angle (°) and relative logarithmic (log10) amplitude difference to the exact dipole source, computed in the ROI, have been analyzed as histograms. The sample size is 50. Each reconstruction in the sample has been obtained by reconstructing the activity in the whole brain for an independent random realization of the noise vector and associating the total integrated activity in each ROI to the corresponding (deep or superficial) dipole source. Additionally, the histogram of the relative maximum in the ROI is given. The solid vertical line shows the median for each distribution, and the dashed lines mark the 90% confidence interval. In general, the results show that the IG hyperprior is necessary for detecting the deep source. The accuracy and reliability of the results increase along with the number of multiresolution decompositions. Furthermore, using E/MEG instead of EEG increased the accuracy of the deep source localization, while EEG was advantageous with respect to the amplitude of the deep source. The results are not visualized for the cases in which the localization criterion (relative maximum > 0.05) was satisfied by less than 5% of the reconstructions

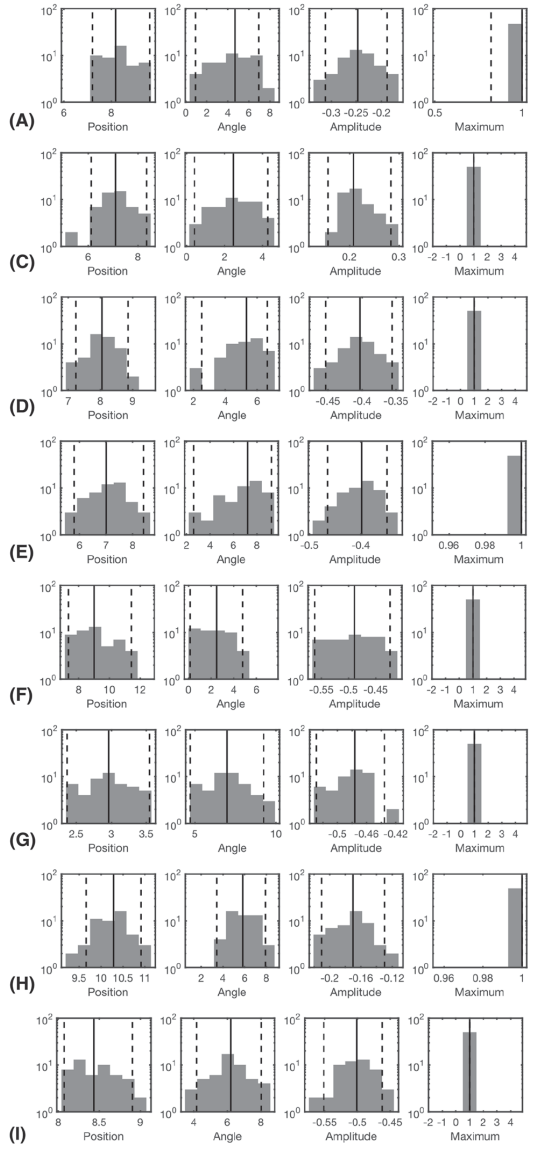

Fig. 7 The results of the superficial source localization for the numerical experiments (**A**–**I**) conducted in the spherical domain (Table 3). In contrast to the case of the deep source, the superficial one is detected accurately in each case where its amplitude differs from zero. The most accurate results were obtained, when the deep source was absent. E/MEG yielded superior result compared to EEG

The last one of these is utilized as a measure for the distinguishability of the source within the ROI. Examples of the reconstructions in the cases (A)–(I) are illustrated in Fig. 10, and the distributions obtained for (J), i.e., the realistic PHM,

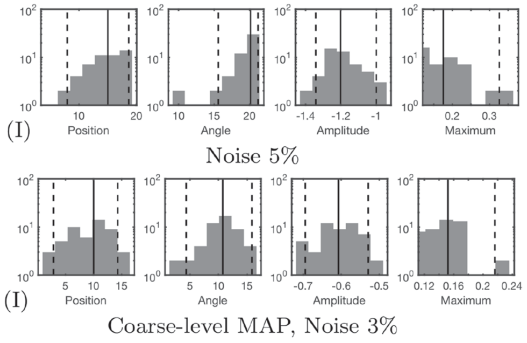

Fig. 8 The additional deep source localization results obtained in the case (I) for the deep source

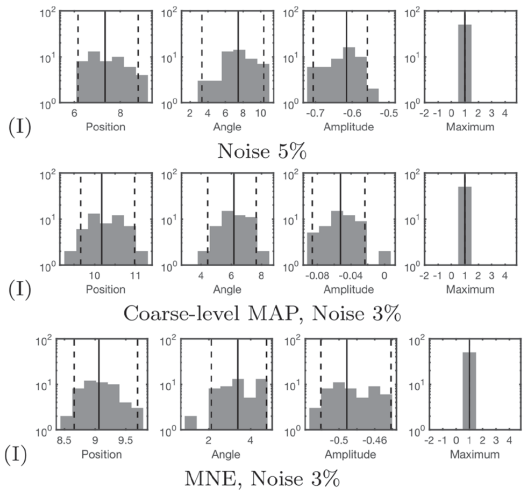

Fig. 9 The additional superficial source localization results obtained in the case (I) for the superficial source

are shown in Fig. 11. The additional cases evaluated for (I), are presented in Fig. 8 and 9.

The histograms in Figs. 6, 7, 8 and 9 illustrate the numerical accuracy of the RAMUS reconstruction approach. Case (A) suggests that the activity in both superficial and deep areas can be reconstructed in EEG, when applying IG as hyperprior. In (A), the superficial source is found with the median positioning accuracy of 8 mm, angle difference of 4.5° and logarithmic (log10) relative amplitude error of − 0.25, i.e., the amplitude of the reconstructed source is 56% compared to that of the actual one. For the deep source these errors are 15 mm, 12 deg, -0.65 (22% amplitude), respectively. Furthermore, as shown by the relative maximum, the superficial source always maximizes the (global) reconstruction, and the relative maximum within the deep ROI is around 50% of the global one in median.

Based on (B) and (C), it is obvious that the reconstruction accuracy is better, if only one of the two sources is active. Furthermore, increasing the intensity of the superficial source decreases the reconstruction accuracy for deep one which is shown by the case of (D) for which the median position, orientation amplitude, and relative maximum for the deep source are 18 mm, 17°, − 0.85 and 0.25, respectively. That is, the accuracy is lower than in (A). In (E), a sparsity factor of 5 was used instead of 8, meaning that the resolution difference between the subsequent levels was less steep, resulting in a weaker distinguishability of the deep source. The same observation was made in the case (F) in which 20 randomized decompositions instead of 100 were used. The deep activity was absent in (G), where we used the G hyperprior instead of IG, confirming the necessity of IG as the hyperprior. In (H) and (I), the use of the E/MEG lead field was observed to improve the deep localization accuracy around 7 mm and orientation accuracy about 8° with respect to the corresponding cases (A) and (D) of EEG data, while the superficial localization accuracy was practically unchanged for (H) and deviated less than 2 mm and 1 deg for (I). The results for E/MEG were visually more focal than the ones obtained with EEG (Fig. 10).

In the three additional tests performed with the parameter setting (I), the increased 5% noise level led to 5 mm and 3 deg lower positioning and orientation accuracy for the deep source, and a smaller 1 mm and 1 deg deviation for the superficial one. In the case of the coarse-level MAP iteration with 3% noise, 2 mm and 1 deg position and orientation improvement was observed for the deep source. For the superficial one, there was a 2 mm deviation in the position, while the orientation accuracy remained unchanged. The coarse-level estimate was visually less focal compared to the ones obtained with multiple resolution levels. MNE detected only the superficial source for which 1 mm position deflection and 3 deg orientation improvement were obtained compared to the basic case (I).

In (J), simultaneous localization of the simulated radial thalamic and tangential somatosensory component was found to be feasible with the realistic PHM model (Fig. 11). Similar to the spherical case, the deep activity had a lower amplitude than the superficial one. In the somatosensory area, with the physiological normal constraint, i.e., the assumption that the primary current is oriented along the inward surface normal, the activity was localized in the posterior wall of the central sulcus similar to the synthetic P20/N20 component used in generating the data.

The results concerning the computing times have been included in Table 4. Those show that a superior performance was obtained with GPU processing which provided

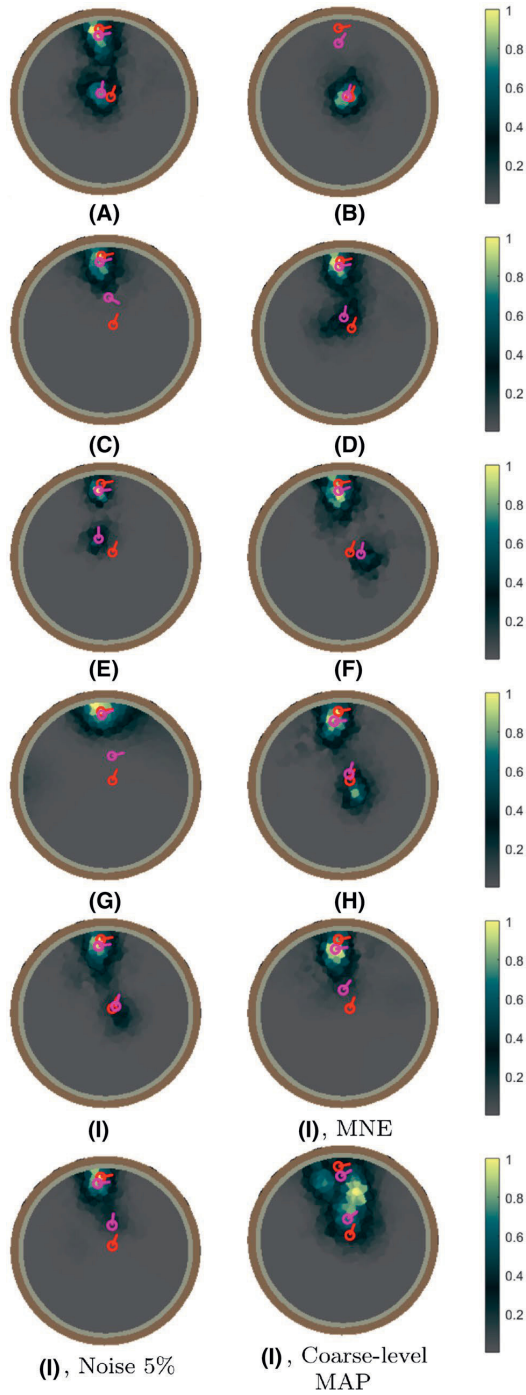

Fig. 10 Examples of the reconstructions obtained in the numerical experiments (**A**–**I**) in the spherical domain (Table 3). In each image, the actual source and the center of mass of the reconstruction w.r.t. a ROI centered at the actual source position, are marked by the red and purple arrow, respectively. The case (**I**), was studied using the following three alternative approaches in addition to the basic multiresolution scheme. MNE: only single IAS MAP iteration was performed on each reconstruction level, meaning that the estimate obtained coincided with MNE. Noise 5%: the noise level was increased to 5%. Coarse-level MAP: only the coarse resolution level was applied in the MAP estimation process with otherwise unchanged parameters

the randomized set of decompositions and a reconstruction in 1/5 to 1/4 of the time required by the laptop CPU.

Discussion

The present numerical results suggest that via the proposed randomized multiresolution scanning (RAMUS) technique one can obtain a robust and accurate MAP estimate for the primary current density in both superficial and deep parts of the brain. RAMUS was observed to enhance the visibility of deep components and also marginalizing the effect of the discretization without a remarkable computation cost. The noise-robustness of RAMUS was shown for 3% and 5% noise levels. As expected, the effect of the noise was observed to be the most obvious with respect to the deep source.

Utilizing a multiresolution approach was found to be crucial *per se* for the reconstruction quality, since maximal achievable accuracy for the deep components is significantly lower than for the superficial one. Detecting the deep source necessitated the presence of a coarse resolution level in the MAP estimation process, i.e., a sparsity factor s larger than one. The superior results were obtained with $s = 8$. Decreasing the value of s, i.e., increasing the source count, quickly diminished the detectability of the deep component which can be observed based on the results obtained for $s = 5$. The distinguishability of the deep source in the final estimate was determined by the number of the source positions at the coarsest level which, in this study, was observed to be around 100–400 roughly matching the sparsity factors between $s = 8$ and $s = 5$. Investigating this interval was motivated by the fact that the maximal number of the detectable sources in the numerical system is determined by the number of the data entries ("Coarse-to-Fine Optimization" section) which is 102 for EEG and 204 for E/MEG, i.e., roughly of the same magnitude. In practice, the optimal size of the coarse system should also take the physiological modeling aspects into account and might be, therefore, also considerably larger than the present choice. For example, if the neural activity is limited to *a priori* known ROIs a larger number might be well-motivated. A comparison between the

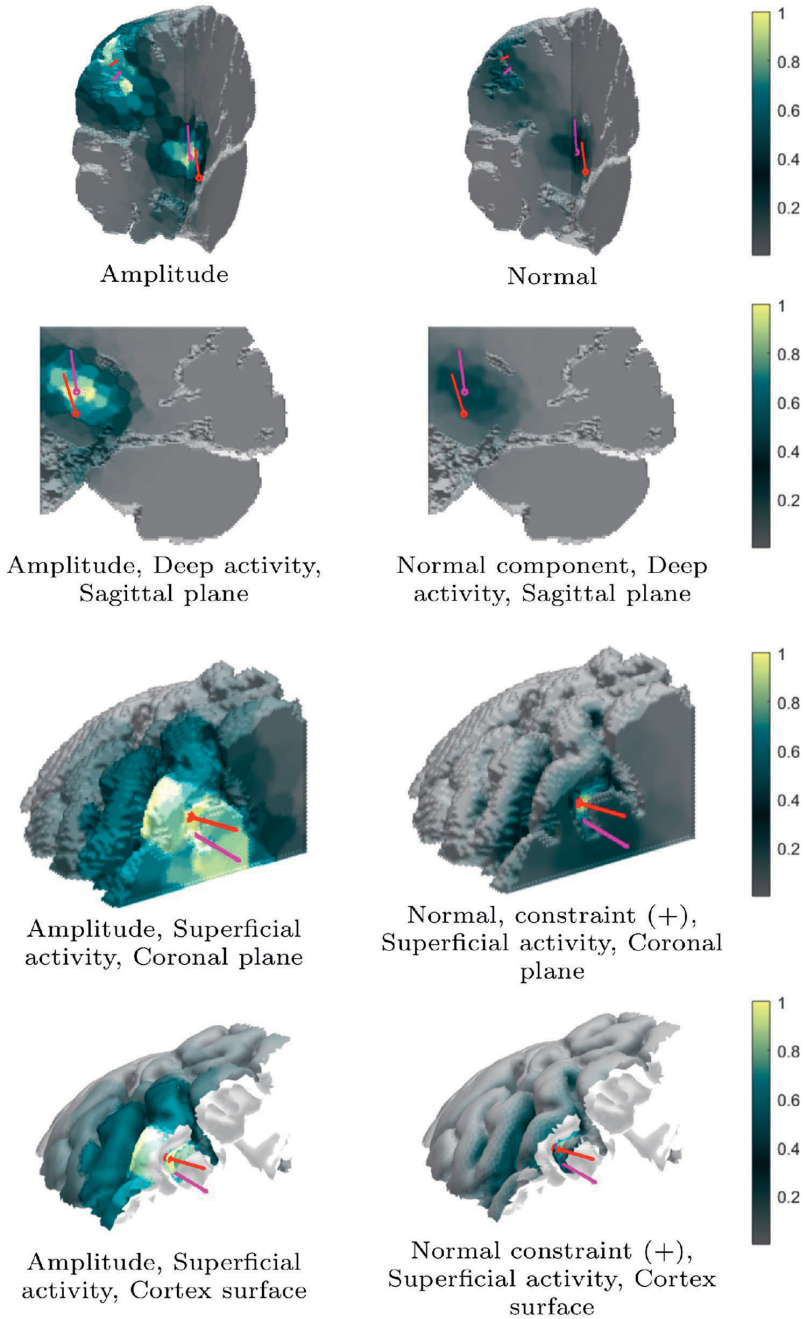

Fig. 11 The reconstruction (I) of the primary current density for the numerically modeled deep (thalamic P14/N14) and superficial (somatosensory P20/N20) activity obtained using the population head model (PHM). On each row, the left column shows the amplitude and the right one the normal component in the direction of the surface normal. On 3rd and 4th row, the normal activity has been constrained into the outward direction. In each image, the actual source and the center of mass of the reconstruction w.r.t. a ROI centered at the actual source position, are marked by the red and purple arrow, respectively

single (coarse-level) and multiple resolution results showed that the refinement of the resolution during the reconstruction process improves the focality of the reconstruction and its accuracy in the superficial areas. Nevertheless, the coarse-level reconstruction was marginally superior in the deep part, emphasizing that here the finer resolution levels slightly affected the coarser level outcome, which is here presumably optimal for the weakly distinguishable deep

activity. Thus, it is important to adjust the decomposition parameters appropriately. The marginalization of the discretization errors via random scanning was perceived to be vital in order to optimize the robustness of the reconstruction which was observed to grow along the number of the multiresolution decompositions utilized.

When coupled with the iterative alternating sequential (IAS) algorithm, RAMUS constitutes essentially a repetitive MAP optimization process for HBM (O'Hagan and Forster 2004; Calvetti et al. 2009). Marginalizing the result over a given number of random multiresolution decompositions can be associated with computing an equal number of MAP estimates. Since the computational cost of the IAS algorithm is largely determined by the product between the lead field matrix and a candidate solution which is parallelized effectively in both CPU and GPU processors. Here, the latter option was found to achieve the fastest performance with the total computation time for a single reconstruction being 14 seconds which would be feasible in processing a larger dataset. Overall, the computational effort of evaluating the MAP via the RAMUS technique can be regarded as moderate compared to a full MCMC sampling based conditional mean (CM) estimate for the posterior density which has been evaluated in (Calvetti et al. 2009) within a ROI. Namely, achieving a full convergence of MCMC would require thousands of iterations (Liu 2001) and the effort of one iteration step is comparable to a single step of IAS. Thus, MCMC would be a slower option. Even though an optimization method, RAMUS can be also interpreted as a surrogate for CM, as it, on one hand, increases the robustness of the source reconstruction via sampling, but, on the other hand, does not provide as extensive information about the posterior density itself as an actual Bayesian sampler does.

The results obtained suggest that the IG hyperprior (O'Hagan and Forster 2004) is necessary in conjunction with IAS, when it is coupled with RAMUS, as the deep activity was not detected with G. Since here the cases of the G hyperprior and single-step MAP can be associated with the 1-norm regularized MCE and MNE (Uutela et al. 1999; Hämäläinen et al. 1993) ("Hierarchical Bayesian Model" section), respectively, it also seems that RAMUS would not enable correcting a depth bias related to either of these estimates. Previously, in (Calvetti et al. 2009), IG was found to perform well for the deep part, when a region of interest was used. Based on the present results, RAMUS provides the means to utilize the advantage of the IG within the whole brain and with a high imaging resolution, while maintaining the computational cost on an appropriate level.

We emphasize that the present conditionally Gaussian prior, in its current formulation, is depth, resolution and decomposition invariant. That is, additional physiological or operator based weighting or prior conditioning (Homa et al. 2013; Calvetti et al. 2015, 2018) is not necessary in order to balance the depth performance of the MAP estimate. Our interpretation for this is that RAMUS can correct the depth localization inaccuracies that are otherwise found with MAP estimates, as it, via the multiresolution approach, decomposes the source space into a set of a visible and invisible fluctuations, explores both sets, and also helps to marginalize the random numerical discretization and optimization errors out of the final estimate. Central here are the visibility of the deep activity at low resolution levels (Pascual-Marqui 1999), the concept of the sensitivity decomposition (Liu et al. 1995) and forming such through projections and multiresolution decompositions which have been investigated in the context of other inverse problems, e.g., in (Piana and Bertero 1997a; Pursiainen 2008).

In addition to the investigated properties, the choice for the scale parameter was also observed to be important in order to guarantee proper function of RAMUS. In each MAP estimation process, the present value 1E−10 was found to work well in detecting activity for both the spherical and realistic head model. The workable range for the scale parameter was observed to be from 1E−10 to 1E−08 similar to the previous findings (Calvetti et al. 2009). Outside this interval the deep activity was not found appropriately or the orientation accuracy of the estimates was lost. In the latter case, the estimate was locked into the direction of a Cartesian coordinate axis, meaning that, due to overly strong focality condition, only single component in the estimate differed from zero in the end of the iteration. Locking was also observed for MAP optimization sequences considerably longer than 10 iteration steps. With a sufficiently large scale parameter there was no locking, but the reconstructions obtained were also less focal.

The results of this article concern only the present numerical framework in which a deep and superficial source were detected simultaneously. Future work will include testing and analyzing the performance of the RAMUS approach with real experimental SEP/F data with the goal to distinguish cortical and sub-cortical activity, e.g., the P14/N14 (deep) and P20/N20 (superficial) components occuring in the stimulation of the median nerve. A comparison with other inverse methods capable of deep localization, such as LORETA and Beamforming (Pascual-Marqui et al. 2002, 1999; Jonmohamadi et al. 2014), will also be important. Further method development topics will include a deeper investigation on the inverse effects of the hyperprior and decomposition parameters as well as finding alternative strategies to update the initial guess for the IAS MAP estimation technique. In the latter case, for instance, an averaged initial guess obtained with respect to several multiresolution decompositions might provide a potential alternative for the current approach which relies on a single decomposition. To make the random scanning computationally more efficient a solver based on parallel scanning processes might be

developed. We also emphasize that RAMUS with its current formulation, the proposed algorithm can be applied to reduce discretization errors not only with the present IAS MAP method but potentially for a variety of source reconstruction techniques.

Acknowledgements AR and SP were supported by the Academy of Finland Centre of Excellence in Inverse Modelling and Imaging 2018–2025 and the Vilho, Yrjö and Kalle Väisälä Foundation of Finnish Academy of Science and Letters. AK was supported by the Academy of Finland Postdoctoral Researcher Grant Number 316542.

Appendix

A IAS MAP Estimation

The IAS algorithm finds a MAP estimate for the posterior $p(\mathbf{x}, \boldsymbol{\theta} \mid \mathbf{y})$ as follows:

1. Set $k = 0$ and $\boldsymbol{\theta}^{(0)} = (\theta_0, \theta_0, \ldots, \theta_0)$.
2. Set $\mathbf{L}^{(k)} = \mathbf{L}\mathbf{D}_{\boldsymbol{\theta}^{(k)}}^{1/2}$ with

$$\mathbf{D}_{\boldsymbol{\theta}^{(k)}}^{1/2} = \mathrm{diag}(\sqrt{|\boldsymbol{\theta}_1^{(k)}|}, \sqrt{|\boldsymbol{\theta}_2^{(k)}|}, \ldots, \sqrt{|\boldsymbol{\theta}_n^{(k)}|}). \tag{8}$$

3. Evaluate

$$\mathbf{x}^{(k+1)} = \mathbf{D}_{\boldsymbol{\theta}^{(k)}}^{1/2}\mathbf{L}^{(k)^T}(\mathbf{L}^{(k)}\mathbf{L}^{(k)^T} + \sigma^2\mathbf{I})^{-1}\mathbf{y}, \tag{9}$$

   where σ denotes the standard deviation of the likelihood.
4. Update the hyperparameter based on the hypermodel.
   - If the hypermodel is G, set

$$\theta_i = \frac{1}{2}\theta_0\left(\eta + \sqrt{\eta^2 + 2x_i^{(k)^2}/\theta_0}\right) \tag{10}$$

     with $\eta = \beta - 3/2, i = 1, 2, \ldots, n$.
   - Else, if the hypermodel is IG, set

$$\theta_i^{(k+1)} = (\theta_0 + \frac{x_i^{(k)^2}}{2})/\kappa \tag{11}$$

     with $\kappa = \beta + 3/2, i = 1, 2, \ldots, n$.
5. Set $k = k + 1$ and go back to 2., if k is less than the total number of iterations defined by the user.

References

Ary JP, Klein SA, Fender DH (1981) Location of sources of evoked scalp potentials: corrections for skull and scalp thicknesses. IEEE Trans Biomed Eng 6:447–452

Attal Y, Schwartz D (2013) Assessment of subcortical source localization using deep brain activity imaging model with minimum norm operators: a MEG study. PLoS ONE 8(3):e59,856

Awan FG, Saleem O, Kiran A (2018) Recent trends and advances in solving the inverse problem for EEG source localization. Inverse Probl Sci Eng 27(11):1521–1536. https://doi.org/10.1080/17415977.2018.1490279

Buchner H, Ferbert A, Hacke W (1988) Serial recording of median nerve stimulated subcortical somatosensory evoked potentials (SEPs) in developing brain death. Clin Neurophysiol 69(1):14–23

Buchner H, Adams L, Knepper A, Rüger R, Laborde G, Gilsbach JM, Ludwig I, Reul J, Scherg M (1994a) Preoperative localization of the central sulcus by dipole source analysis of early somatosensory evoked potentials and three-dimensional magnetic resonance imaging. J Neurosurg 80(5):849–856

Buchner H, Fuchs M, Wischmann HA, Dössel O, Ludwig I, Knepper A, Berg P (1994b) Source analysis of median nerve and finger stimulated somatosensory evoked potentials: multichannel simultaneous recording of electric and magnetic fields combined with 3d-mr tomography. Brain Topogr 6(4):299–310

Buchner H, Adams L, Müller A, Ludwig I, Knepper A, Thron A, Niemann K, Scherg M (1995) Somatotopy of human hand somatosensory cortex revealed by dipole source analysis of early somatosensory evoked potentials and 3d-nmr tomography. Electroencephalogr Clin Neurophysiol 96(2):121–134

Calvetti D, Hakula H, Pursiainen S, Somersalo E (2009) Conditionally Gaussian hypermodels for cerebral source localization. SIAM J Imaging Sci 2(3):879–909

Calvetti D, Pascarella A, Pitolli F, Somersalo E, Vantaggi B (2015) A hierarchical Krylov–Bayes iterative inverse solver for MEG with physiological preconditioning. Inverse Probl 31(12):125005

Calvetti D, Pascarella A, Pitolli F, Somersalo E, Vantaggi B (2018) Brain activity mapping from meg data via a hierarchical bayesian algorithm with automatic depth weighting. Brain Topogr 32(3):363–393

Clark I, Biscay R, Echeverría M, Virués T (1995) Multiresolution decomposition of non-stationary EEG signals: a preliminary study. Comput Biol Med 25(4):373–382

Cuffin BN, Schomer DL, Ives JR, Blume H (2001a) Experimental tests of EEG source localization accuracy in realistically shaped head models. Clin Neurophysiol 112(12):2288–2292

Cuffin BN, Schomer DL, Ives JR, Blume H (2001b) Experimental tests of EEG source localization accuracy in spherical head models. Clin Neurophysiol 112(1):46–51

Dannhauer M, Lanfer B, Wolters CH, Knösche TR (2011) Modeling of the human skull in EEG source analysis. Hum Brain Mapp 32:1383–1399. https://doi.org/10.1002/hbm.21114

Fuchs M, Wagner M, Wischmann HA, Köhler T, Theißen A, Drenckhahn R, Buchner H (1998) Improving source reconstructions by combining bioelectric and biomagnetic data. Clin Neurophysiol 107(2):93–111

Gavit L, Baillet S, Mangin JF, Pescatore J, Garnero L (2001) A multiresolution framework to MEG/EEG source imaging. IEEE Trans Biomed Eng 48(10):1080–1087

Grech R, Cassar T, Muscat J, Camilleri KP, Fabri SG, Zervakis M, Xanthopoulos P, Sakkalis V, Vanrumste B (2008) Review on solving the inverse problem in EEG source analysis. J NeuroEng Rehabil 5(1):25. https://doi.org/10.1186/1743-0003-5-25

Grover P (2016) Fundamental limits on source-localization accuracy of eeg-based neural sensing. In: Information Theory (ISIT), 2016 IEEE International Symposium on, IEEE, pp 1794–1798

Hämäläinen M, Hari R, Ilmoniemi RJ, Knuutila J, Lounasmaa OV (1993) Magnetoencephalography: theory, instrumentation, and applications to invasive studies of the working human brain. Rev Mod Phys 65:413–498

Hansen P (2010) Discrete inverse problems: insight and algorithms. Society for Industrial and Applied Mathematics, Fundamentals of Algorithms. https://books.google.fi/books?id=r-uK2bzAUrUC

Haueisen J, Leistritz L, Süsse T, Curio G, Witte H (2007) Identifying mutual information transfer in the brain with differential-algebraic modeling: evidence for fast oscillatory coupling between cortical somatosensory areas 3b and 1. NeuroImage 37(1):130–136

Haufe S, Nikulin VV, Ziehe A, Müller KR, Nolte G (2008) Estimating vector fields using sparse basis field expansions. In: Proceedings of the 21st International Conference on Neural Information Processing Systems, Curran Associates Inc., USA, NIPS'08, pp 617–624, http://dl.acm.org/citation.cfm?id=2981780.2981857

He B, Sohrabpour A, Brown E, Liu Z (2018) Electrophysiological source imaging: a noninvasive window to brain dynamics. Annu Rev Biomed Eng 20:171–196

Homa L, Calvetti D, Hoover A, Somersalo E (2013) Bayesian preconditioned CGLS for source separation in MEG time series. SIAM J Sci Comput 35(3):B778–B798

Jonmohamadi Y, Poudel G, Innes C, Weiss D, Krueger R, Jones R (2014) Comparison of beamformers for EEG source signal reconstruction. Biomed Signal Process Control 14:175–188

Kirsch A (2011) Regularization by discretization. Springer, New York, pp 63–119. https://doi.org/10.1007/978-1-4419-8474-6_3

Koulouri A, Rimpiläinen V, Brookes M, Kaipio JP (2017) Prior variances and depth un-biased estimators in EEG focal source imaging. In: EMBEC & NBC 2017, Springer, Singapore, pp 33–36. https://doi.org/10.1007/978-981-10-5122-7_9

Lee E, Duffy W, Hadimani R, Waris M, Siddiqui W, Islam F, Rajamani M, Nathan R, Jiles D (2016) Investigational effect of brain-scalp distance on the efficacy of transcranial magnetic stimulation treatment in depression. IEEE Trans Magn 52(7):1–4

Liu J (2001) Monte Carlo strategies in scientific computing. Springer series in statistics. Springer, Berlin

Liu J, Guenier B, Benard C (1995) A sensitivity decomposition for the regularized solution of inverse heat conduction problems by wavelets. Inverse Probl 11(6):1177

Lucka F, Pursiainen S, Burger M, Wolters CH (2012) Hierarchical bayesian inference for the EEG inverse problem using realistic FE head models: depth localization and source separation for focal primary currents. NeuroImage 61(4):1364–1382. https://doi.org/10.1016/j.neuroimage.2012.04.017

Malioutov D, Cetin M, Willsky A (2005) A sparse signal reconstruction perspective for source localization with sensor arrays. IEEE Trans Signal Process 53(8):3010–3022. https://doi.org/10.1109/tsp.2005.850882

Mallat SG (1989) A theory for multiresolution signal decomposition: the wavelet representation. IEEE Trans Pattern Anal Mach Intell 7:674–693

Miinalainen T, Rezaei A, Us D, Nüßing A, Engwer C, Wolters CH, Pursiainen S (2019) A realistic, accurate and fast source modeling approach for the EEG forward problem. NeuroImage 184:56–67

Nagarajan SS, Portniaguine O, Hwang D, Johnson C, Sekihara K (2006) Controlled support MEG imaging. NeuroImage 33(3):878–885

O'Hagan A, Forster JJ (2004) Kendall's advanced theory of statistics, volume 2B: Bayesian inference, vol 2. Arnold

Pascual-Marqui RD (1999) Review of methods for solving the EEG inverse problem. Int J Bioelectromagn 1(1):75–86

Pascual-Marqui RD, Lehmann D, Koenig T, Kochi K, Merlo MC, Hell D, Koukkou M (1999) Low resolution brain electromagnetic tomography (loreta) functional imaging in acute, neuroleptic-naive, first-episode, productive schizophrenia. Psychiatry Res 90(3):169–179

Pascual-Marqui RD, Esslen M, Kochi K, Lehmann D et al (2002) Functional imaging with low-resolution brain electromagnetic tomography (loreta): a review. Methods Find Exp Clin Pharmacol 24(Suppl C):91–95

Piana M, Bertero M (1997a) Projected landweber method and preconditioning. Inverse Probl 13(2):441

Piana M, Bertero M (1997b) Projected Landweber method and preconditioning. Inverse Probl 13(2):441–463

Pizzo F, Roehri N, Villalon SM, Trébuchon A, Chen S, Lagarde S, Carron R, Gavaret M, Giusiano B, McGonigal A et al (2019) Deep brain activities can be detected with magnetoencephalography. Nat Communications 10(1):971

Pursiainen S (2008) Coarse-to-fine reconstruction in linear inverse problems with application to limited-angle computerized tomography. J Inv Ill Posed Probl 16(9):873–886

Pursiainen S (2012a) Raviart–Thomas -type sources adapted to applied EEG and MEG: implementation and results. Inverse Probl 28(6):065,013

Pursiainen S (2012b) Raviart–Thomas-type sources adapted to applied EEG and MEG: implementation and results. Inverse Probl 28(6):065,013

Pursiainen S, Lucka F, Wolters CH (2012) Complete electrode model in EEG: relationship and differences to the point electrode model. Phys Med Biol 57(4):999–1017

Pursiainen S, Vorwerk J, Wolters C (2016) Electroencephalography (EEG) forward modeling via H(div) finite element sources with focal interpolation. Phys Med Biol 61(24):8502–8520. https://doi.org/10.1088/0031-9155/61/24/8502

Schmidt DM, George JS, Wood CC (1999) Bayesian inference applied to the electromagnetic inverse problem. Hum Brain Mapp 7(3):195–212

Seeber M, Cantonas LM, Hoevels M, Sesia T, Visser-Vandewalle V, Michel CM (2019) Subcortical electrophysiological activity is detectable with high-density EEG source imaging. Nat Commun 10(1):753

Tarkiainen A, Liljeström M, Seppä M, Salmelin R (2003) The 3d topography of MEG source localization accuracy: effects of conductor model and noise. Clin Neurophysiol 114(10):1977–1992

Uutela K, Hämäläinen M, Somersalo E (1999) Visualization of magnetoencephalographic data using minimum current estimates. NeuroImage 10:173–180

Wang G, Yang L, Worrell G, He B (2009) The relationship between conductivity uncertainties and eeg source localization accuracy. In: Engineering in Medicine and Biology Society, 2009. EMBC 2009. Annual International Conference of the IEEE, IEEE, pp 4799–4802

PUBLICATION IV

Parametrizing the Conditionally Gaussian Prior Model for Source Localization with Reference to the P20/N20 Component of Median Nerve SEP/SEF

A. Rezaei, M. Antonakakis, MC. Piastra, C. H. Wolters and S. Pursiainen

Journal of Brain Sciences 10(12), 1–22
DOI: 10.3390/brainsci10120934

brain sciences

MDPI

Article

Parametrizing the Conditionally Gaussian Prior Model for Source Localization with Reference to the P20/N20 Component of Median Nerve SEP/SEF

Atena Rezaei [1,*], Marios Antonakakis [2], MariaCarla Piastra [2,3], Carsten H. Wolters [2,4] and and Sampsa Pursiainen [1]

1 Computing Sciences, Faculty of Information Technology and Communication Sciences, Tampere University, Hervanta Campus, P.O. Box 1001, 33014 Tampere, Finland; sampsa.pursiainen@tuni.fi
2 Institute of Biomagnetism and Biosignalanalysis, University of Münster, Malmedyweg 15, D-48149 Münster, Germany; marios.antonakakis@uni-muenster.de (M.A.); mariacarla.piastra@donders.ru.nl (M.P.); carsten.wolters@uni-muenster.de (C.H.W.)
3 Cognitive Neuroscience, Donders Institute for Brain, Cognition and Behaviour, Radboud University Nijmegen Medical Centre, Kapittelweg 29, 6525 EN Nijmegen, The Netherlands
4 Otto Creutzfeldt Center for Cognitive and Behavioral Neuroscience, University of Münster, 48149 Münster, Germany
* Correspondence: atena.rezaei@tuni.fi

Received: 2 October 2020; Accepted: 25 November 2020; Published: 3 December 2020

Abstract: In this article, we focused on developing the conditionally Gaussian hierarchical Bayesian model (CG-HBM), which forms a superclass of several inversion methods for source localization of brain activity using somatosensory evoked potential (SEP) and field (SEF) measurements. The goal of this proof-of-concept study was to improve the applicability of the CG-HBM as a superclass by proposing a robust approach for the parametrization of focal source scenarios. We aimed at a parametrization that is invariant with respect to altering the noise level and the source space size. The posterior difference between the gamma and inverse gamma hyperprior was minimized by optimizing the shape parameter, while a suitable range for the scale parameter can be obtained via the prior-over-measurement signal-to-noise ratio, which we introduce as a new concept in this study. In the source localization experiments, the primary generator of the P20/N20 component was detected in the Brodmann area 3b using the CG-HBM approach and a parameter range derived from the existing knowledge of the Tikhonov-regularized minimum norm estimate, i.e., the classical Gaussian prior model. Moreover, it seems that the detection of deep thalamic activity simultaneously with the P20/N20 component with the gamma hyperprior can be enhanced while using a close-to-optimal shape parameter value.

Keywords: electroencephalography (EEG); magnetoencephalography (MEG); somatosensory evoked potentials; somatosensory evoked fields; P20/N20 component; hierarchical bayesian model; parametrization; deep activity

1. Introduction

This article concerns computational source localization methods for the activity of the brain in electro- and magnetoencephalography (EEG and MEG) [1–3]. Reconstructing the primary current density of the neurons as a three-dimensional (3D) distribution restricted to the grey matter is an ill-posed inverse problem, in which the prior model and reconstruction technique applied have a major effect on the final result [3]. Consequently, *a priori* information, such as an anatomically and

physiologically accurate head model, is needed. When the inverse problem is formulated via Bayesian statistics, the *a priori* knowledge can be rigorously modelled as a statistical prior distribution [4–8].

EEG and, particularly, MEG, are famously known to be more sensitive to the superficial parts than to the deeper lying areas, e.g., the thalamus [9,10]. In this study, we focused on developing the conditionally Gaussian hierarchical Bayesian model (CG-HBM) [11], which, based on numerical simulations [4–8], has been suggested as a potential approach to reconstructing networks of focal sources with variable depth. In CG-HBM, the prior has a hierarchical structure; the variance of a Gaussian conditional prior is steered by a heavy-tailed hyperprior. This allows the primary current density to have a considerably greater focal amplitude when compared to the background fluctuations than what is otherwise possible with a Gaussian prior. CG-HBM forms a superclass for different inversion methods as well as a potential platform for the development of new source localization methods [12]. In clinical applications, focal reconstructions are needed, e.g., in epileptic focus localization and in the analysis of epileptic networks during seizures for adults and paediatrics [13–15].

The aim and novelty of this proof-of-concept study is to improve the applicability of the CG-HBM for localizing sources with variable depth by proposing a simple and robust parametrization approach that has been designed to remain invariant with respect to alterations in the noise level [10,16–18] and the size of the source space [5,19,20], with both these factors being essential with respect to the localization outcome. An important goal is to obtain an appropriate localization performance with different hypermodels and reconstruction techniques. Namely, one of the major challenges in using CG-HBM is that the mutual differences between these models and techniques can be significant, if the model parameters are not optimally set [6,7]. We referred to both simulated and experimental somatosensory evoked potential (SEP) and field (SEF) datasets, and then selected the parameter values with the aim of detecting the activity corresponding to the P20/N20 component, i.e., the 20 ms post-stimulus response, occurring in the median nerve (wrist) stimulation [21–24]. The Brodmann area 3b activity in the hand-knob of the primary somatosensory cortex was reconstructed with a high-density forward model. This stable and transient activity generally has an excellent signal-to-noise ratio (SNR), especially in MEG, but also in EEG [22,25] and it is, therefore, well-suited for finding a high-density reconstruction. Additionally, a sparse model [19] was applied in order to detect the deep thalamic activity that is associated with the P20/N20 response.

We compared the gamma (G) and inverse gamma (IG) hyperprior in detecting the activity in these regions. The previous numerical simulation studies [7,12] suggest that G and IG can lead to two characteristically different reconstructions, if the shape and scale parameter, i.e., β and the θ_0 determining the hyperprior are not ideally set. In particular, the shape parameter value $\beta = 1.5$ results in a suppressed deep activity with G hyperprior, as shown in [12]. We minimized the posterior difference between G and IG by optimizing β, while an initial range for θ_0 was obtained based on the prior-over-measurement signal-to-noise ratio (PM-SNR), i.e., the relative weight of the prior compared to the measurement noise. Here, we introduce PM-SNR as a new concept to allow for balancing the θ_0-value with respect to the source space size and the estimated level of the measurement and modeling errors. The initial value for PM-SNR can be related to the existing knowledge of the Tikhonov-regularized minimum norm estimate (MNE) [26,27] following from the classical Gaussian prior model [28].

In our experiments, the iterative alternating sequential (IAS) and Markov chain Monte Carlo (MCMC) sampling techniques presented in [7,29,30] were applied in order to reconstruct the activity. We used a finite element method (FEM) that is based on the forward modeling approach [31,32], which allows for creating an accurate volumetric discretization of a multi-compartment head segmentation regarding its conductivity distribution and strongly folded tissue structures [33–37]. The source localization experiments were performed while using the *Zeffiro* interface (the source code is available online at https://github.com/sampsapursiainen/zeffiro_interface) (ZI) software pipeline [38], which couples the FEM forward model with CG-HBM.

The results that were obtained for the known synthetic source suggest that, through *maximum a posteriori* (MAP) estimation, one can reconstruct a simulated P20/N20 component without *a priori* limiting the region of the activity. It was observed that MCMC sampling allowed for the posterior to be adopted to the structure and resolution of the underlying numerical model and geometry, thus avoiding numerical bias, e.g., overly focal results. We compared our CG-HBM reconstructions to Tikhonov-regularized MNE [1] and the minimum current estimate (MCE) [39], which can be interpreted as special cases of the IAS method in combination with the G hyperprior and with $\beta = 1.5$. Based on our findings for three subjects, we suggest that, by choosing an optimization-based shape parameter value $\beta = 3$ and a PM-SNR of 0–30 dB, with the exact value being determined by the modeling accuracy assumed, the cortical generator of the P20/N20 component can be localized in the Brodmann area 3b with both simulated and measured data. Moreover, it seems that the detection of the correlated sub-cortical thalamic activity, simultaneously with the cortical one, could be enhanced using the close-to-optimal shape parameter value, when the G hyperprior was used.

2. Methods

This section briefly reviews the mathematical CG-HBM approach and its implementation in this study. The primary current density is denoted by $\mathbf{x}$, which is the discretized approximation of the primary current density $|\vec{J}^p|$ in the brain, i.e., the unknown of the inverse problem, and the measurement data vector is represented by $\mathbf{y}$. In both EEG and MEG, the dependence of $\mathbf{y}$ on $\mathbf{x}$, i.e., the forward model can be formulated via the lead field matrix equation of the form $\mathbf{y} = \mathbf{L}\mathbf{x} + \mathbf{n}$, where $\mathbf{n}$ is a noise vector and $\mathbf{L}$ is the so-called lead field matrix [1]. Here, $\mathbf{L}$ is obtained via the FEM discretization of the classical field equations following from the quasi-static approximation of the Maxwell equations, as described in [31,40,41]. For the generality of the presentation, we assume that $\mathbf{L}$ is obtained using SI-units, while $\mathbf{y}$ and $\mathbf{n}$ are normalized with respect to the amplitude A (here, the ℓ^2-norm) of the measured or simulated signal.

2.1. Conditionally Gaussian Hierarchical Bayesian Model

For a single given dataset $\mathbf{y}$, the classical Bayes formula for subjective conditional probabilities can be written as

$$p(\mathbf{x} \mid \mathbf{y}) = \frac{p(\mathbf{x})\, p(\mathbf{y} \mid \mathbf{x})}{p(\mathbf{y})} \propto p(\mathbf{x})\, p(\mathbf{y} \mid \mathbf{x}). \tag{1}$$

That is, the *posterior* probability density $p(\mathbf{x} \mid \mathbf{y})$ of the unknown discretized primary current density $\mathbf{x}$ in the brain is proportional to the product between the prior density $p(\mathbf{x})$, i.e., the *a priori* knowledge of $\mathbf{x}$, and the likelihood function $p(\mathbf{y} \mid \mathbf{x})$ that follows from the measurement noise model [42].

The measurement error is assumed here to be a Gaussian zero mean random vector $\mathbf{n} = \mathbf{y} - \mathbf{L}\mathbf{x}$ with independent entries. Consequently, the likelihood is of the form $p(\mathbf{y} \mid \mathbf{x}) \propto \exp(-(2\sigma^2)^{-1}\|\mathbf{L}\mathbf{x} - \mathbf{y}\|^2)$, where σ is the standard deviation of the noise. In the hierarchical Bayesian approach, one assumes the prior to be a joint density $p(\mathbf{x}, \boldsymbol{\theta}) \propto p(\boldsymbol{\theta})\, p(\mathbf{x} \mid \boldsymbol{\theta})$ of $\mathbf{x}$ and a hyperparameter $\boldsymbol{\theta}$. That is, the posterior is of the form

$$p(\mathbf{x}, \boldsymbol{\theta} \mid \mathbf{y}) \propto p(\boldsymbol{\theta})\, p(\mathbf{x} \mid \boldsymbol{\theta})\, p(\mathbf{y} \mid \mathbf{x}). \tag{2}$$

In CG-HBM [7,11,43], the conditional part $p(\mathbf{x} \mid \boldsymbol{\theta})$ is also a zero mean Gaussian density. Its diagonal covariance matrix is predicted by a heavy-tailed hyperprior $p(\boldsymbol{\theta})$, which means that the variance vector, i.e., the set of diagonal entries, is likely to contain outliers. Thus, it is implicitly assumed that $\mathbf{x}$ is a sparse vector with a small subset of entries, which are noticeably large in absolute value when compared to the other entries [6]. The number and intensity of these outliers are controlled by the hyperprior [43]. The resulting impulse-like prior model for the unknown is particularly useful in obtaining a focal reconstruction for the brain activity. The parameters determining the hyperprior

allow for the level of the focality to be tuned, i.e., the rough relative portion of the x-entries that are likely to *a priori* differ from zero.

2.1.1. Posterior Exploration

Given the posterior, the actual reconstruction can be found via several different approaches. The most common ones can be divided into optimization and sampling techniques. The former include the MAP algorithms, which are aimed at finding the maximizer of the posterior density, i.e., $x_{MAP} = \text{argmax}\, p_{\text{post}}(x, \boldsymbol{\theta} \mid y)$. MAP estimation usually provides a faster, but less robust, way to obtain a reconstruction than the sampling techniques, e.g., MCMC methods, which approximate the conditional mean $x_{CM} = E(\mathbf{x}, \boldsymbol{\theta} \mid \mathbf{y}) = \int (\mathbf{x}, \boldsymbol{\theta}) p_{\text{post}}(\mathbf{x}, \boldsymbol{\theta} \mid \mathbf{y})\, \mathrm{d}\mathbf{x}\, \mathrm{d}\boldsymbol{\theta}$ [28]. MCMC methods generate samples from the posterior distribution by constructing a Markov chain that has the target posterior distribution as its equilibrium distribution. A more detailed descriptions for the IAS MAP estimation method and the MCMC sampler that was employed for conditional mean (CM) estimation can be found in [7].

2.1.2. Gamma and Inverse Gamma Hyperprior

As the hyperprior, we use both the gamma $\mathrm{G}(\boldsymbol{\theta} \mid \beta, \theta_0)$ and inverse gamma $\mathrm{IG}(\boldsymbol{\theta} \mid \beta, \theta_0)$ distributions, whose densities are supported on the set of non-negative real numbers with a structure that is determined by the scale and shape parameter θ_0 and β, respectively. In the present approach, the scale parameter $\theta_0 > 0$ essentially sets the expected variance of the conditionally Gaussian prior. It can be interpreted as the capability of the prior to detect brain activity growing along with the value of θ_0. The shape parameter steers the rate of the decay for the tail part. Finding a suitable value for θ_0 and β is essential in avoiding an over- or under- sensitive prior, which might involve depth-bias or emphasized noise-effects. Based on our earlier experience, this is especially important with regard to G hyperprior, which might suppress deep activity, when $\beta = 1.5$ [12]. In order to make both the G and IG hyperpriors perform similarly given θ_0, we select β to be uniformly $\beta = 3$, which can be interpreted as a close-to-optimal choice for minimizing the differences between the outcomes of G and IG (Appendix A).

2.1.3. Total Scale

The source-wise scale parameter θ_0 can be adapted to a given forward model by introducing a total scale $\theta_0^{(\text{tot})}$, which gives the scale per distribution, while θ_0 represents the scale per source. This follows from the additivity of the Gaussian prior variance, i.e., that the nearby sources s_1 and s_2 with variances θ_1 and θ_2 have the total variance $\theta_1 + \theta_2$, if interpreted as a single source $s = s_1 + s_2$. Thus, the relationship between the total and source-wise scale parameter can be written as

$$\theta_0 = \frac{\theta_0^{(\text{tot})} \sigma^2 A^2}{N} \quad \text{or} \quad \theta_0^{(\text{tot})} = \frac{\theta_0 N}{\sigma^2 A^2} \tag{3}$$

Namely, to have an invariant weight with respect to the likelihood, the scale $\theta_0^{(\text{tot})}$ of the conditionally Gaussian prior must be directly proportional to the source position count N of the forward model and inversely proportional to the relative noise variance σ^2 and the squared amplitude A^2. Because we assume $\theta_0^{(\text{tot})}$ to be an application-specific constant, we introduce here, as a new concept, the following prior-over-measurement signal-to-noise ratio

$$\text{PM-SNR} = \mathrm{dB}(\sqrt{\theta_0^{(\text{tot})}}) = \mathrm{dB}(\sqrt{N}) + \mathrm{dB}(\delta) + \mathrm{dB}(A) - \mathrm{dB}(\delta^{(\text{ref})}) \quad \text{with} \quad \delta = \frac{\sqrt{\theta_0}}{\sigma A}, \quad \delta^{(\text{ref})} = \frac{|\vec{J}^p|}{A}, \tag{4}$$

and $\mathrm{dB}(x) = 20 \log_{10} x$. Here, $\delta^{(\text{ref})}$ is a reference level which is obtained as the ratio between the *a priori* estimated norm of the primary current density $|\vec{J}^p|$ and the signal amplitude A. The term

$\mathrm{dB}(A)$ is included in (4), as we present θ_0 and $\theta_0^{(\mathrm{tot})}$ with respect to normalized amplitude $A = 1$. PM-SNR measures the relative weight of the prior as compared to the noise level and it is balanced by the system size. At the reference level, when PM-SNR is 0 dB or $\delta\sqrt{N} = \delta^{(\mathrm{ref})}$, $\sqrt{\theta_0}$ matches the *a priori* noise-induced fluctuation of the candidate solution normalized by $A\sqrt{N}$, which is, $\sqrt{\theta_0} = \sigma|\vec{J}^p|/(A\sqrt{N})$. In order to generalize these expressions for the case of a non-diagonal noise covariance, one can interpret the relative noise variance σ^2 as the largest eigenvalue, i.e., the ℓ^2-norm, of the noise covariance matrix. The PM-SNR of the scale parameter values (Table 1) that were applied in this study refer to the present EEG amplitude $A = 10^{-6}$ V that was obtained as the ℓ^2-norm of the measured P20/N20 component, relative noise standard deviation of $\sigma = 0.03$, and the typical 10 nAm dipolar source strength in the brain [1,44,45], i.e., $|\vec{J}^p| = 10^{-8}$ Am.

Because δ also represents the relative weight of a non-conditional Gaussian prior, it can be associated with the Tikhonov regularization parameter of MNE [7,26,28]. In the Brainstorm software, the default level of the relative prior weight is set to a constant value $dB(\delta)$= 9 dB, as shown in the tutorial [27]. Taking into account the source count of this tutorial, which is 15,000, this would result in a PM-SNR of 10 dB. However, notice that a constant default level is not invariant under changing the dimension of the source space.

Note that the current definition (4) of PM-SNR has been selected in order to obtain a uniform representation with respect to G and IG hyperprior. Alternatively, PM-SNR can be defined with respect to the mean of the hyperprior that is given by the total scale, i.e., $\theta_0^{(\mathrm{tot})}\beta$ and $\theta_0^{(\mathrm{tot})}/(\beta - 1)$ for G and IG, resulting in a correction of $+\mathrm{dB}(\sqrt{\beta}) = +5$ dB and $-\mathrm{dB}(\sqrt{\beta - 1}) = -3$ dB, when $\beta = 3$, respectively.

2.1.4. Latent Noise Effects

We assume that the relative (total) noise standard deviation is of the form $\sigma = s\overline{\sigma}$, where $\overline{\sigma}$ is the standard deviation of the *a priori* known noise and $s \geq 1$ is a correcting term due to latent noise effects, such as forward modeling inaccuracies due to the quasi-static approximation, inter-individual head tissue conductivity differences, and/or segmentation errors, see e.g., [46]. Denoting $\overline{\delta} = \sqrt{\theta_0}/(\overline{\sigma}A)$, it follows that the PM-SNR is of the form

$$\text{PM-SNR} = \overline{\text{PM-SNR}} + \mathrm{dB}(s), \tag{5}$$

where $\mathrm{dB}(s)$ is the total contribution of the latent noise effects. Thus, PM-SNR will be greater than $\overline{\text{PM-SNR}}$ for models including latent noise, i.e., when $s > 1$: the greater the latent noise, the greater weight of the prior. When $\overline{\text{PM-SNR}}$ is 0 dB, PM-SNR is given by $\mathrm{dB}(s)$ and the explicit formula for the scaling parameter is $\sqrt{\theta_0} = s\sigma|\vec{J}^p|/(A\sqrt{N})$, where σ corresponds to the known noise level and s to the *a priori* assumption of the latent noise strength.

The shape parameter choice defines the spread of the hyperprior that can be related to the uncertainty of $\delta^{(\mathrm{ref})}$ following from, e.g., the potentially varying source depth that affects the amplitude of the measurement: the smaller the shape parameter value, the greater the spread. With the current value $\beta = 3$, the interdecile range (Appendix B) of the hyperprior $p(\theta)$ obtains values from $0.4E(\theta)$ to $1.8E(\theta)$ with $E(\theta)$ denoting the hyperprior mean. Thus, $\sqrt{\theta}$, i.e., the expected source strength given θ, varies $\mathrm{dB}(\sqrt{1.8/0.4}) = 7$ dB over the interdecile range. This matches our approximation for the variation of $\delta^{(\mathrm{ref})}$ that was obtained as the interquartile range of the lead field based simulated ℓ^2-norm signal amplitude over the source space.

2.2. Numerical Model

2.2.1. Head Segmentation

The FE implementation approach that was presented in [47] was applied, including the formula for the EEG and MEG lead field matrix. A tetrahedral finite element mesh was generated by subdividing each voxel in a surface-based regular hexahedral segmentation into six tetrahedra. The FE meshes were generated while using a six-layer surface segmentation based on T1-weighted and T2-weighted

MRI sequences recorded with a 3T MRI scanner. The surfaces (level-sets) of skin, compact bone (skull), spongious bone (skull), cerebrospinal fluid (CSF), grey matter, and white matter were included in the model. An FE mesh was generated for both 1 and 2 mm resolution (voxel size). The first of these included 3.8 M nodes and 22 M tetrahedra and the second one 0.47 M nodes and 2.7 M tetrahedra.

2.2.2. Source Space

In order to generate the source space of **x**, we used the FEM-based quadratic H(div) approach presented in [31], employing the Position Based Optimization (PBO) interpolation with the 10-source (eight-point) stencil. That is, a given dipolar current source was estimated via the four linear face and six quadratic edge-based vector basis functions that are associated with the barycenter of the tetrahedron containing the source position. The sources were placed in the interior part of the grey matter compartment in the elements with a full set (four) of neighbors belonging to the same compartment. The rest of the compartment forming the boundary layer of the grey matter contained no sources, since the modeling accuracy is known to be reduced for the boundary layer [40].

A total of 10^5 points were distributed randomly in the grey matter for each FE mesh in order to obtain a uniform (mesh-independent) source density for reconstructing the somatosensory 3b activity. This initial source count was selected to allow the present source localization accuracy, in principle, to surpass the *a priori* known maximum limit of EEG and MEG, which is about 9 mm and 2–4 mm, respectively [22,48–51]. A uniform point spread was obtained through a straightforward random permutation due to the uniform mesh structure.

The points that were placed on the boundary layer in the initial stage were filtered out of the eventual distribution, which consisted of 7.6×10^4 and 6.1×10^4 positions for the 1 and 2 mm FE meshes, respectively. The slightly lower source count for the 2 mm case was caused by the thicker boundary layer that arose from the larger element size. Each position comprised three sources that were oriented along the three Cartesian coordinate axes. Hence, the total number of sources was 2.28×10^5 and 1.83×10^5 for the 1 and 2 mm FE meshes, respectively. The source localization experiments were primarily conducted with the 1 mm resolution, while the 2 mm accuracy was utilized in order to examine the forward modeling effects on the source localization. In addition to the dense source space, a sparse one was created to enhance the detectability [19] of the thalamic component simultaneously with the Brodmann area 3b activity [21,52,53]. In the sparse distribution, the number of source positions was 1/100 as compared to that of the dense one and so the 1 mm mesh was used in the forward simulation. The Cartesian set of sources was used in inverting the data. After the inversion process, the distribution obtained was projected in the cortical areas while using the normal constraint (Figure 1) of the cortex. In other words, the vector field component parallel to the surface normal constituted the final reconstruction. In the sub-cortical areas, the normal projection was not applied, as the sub-cortical neurons are not generally oriented along the surface normal of the neuronal tissue.

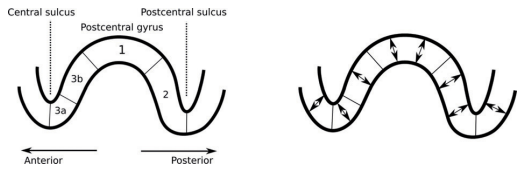

Figure 1. Left: a schematic illustration depicting the sagittal cut of the primary somatosensory cortex. The P20/N20 component of the somatosensory activity occurs in the Brodmann area 3b, which is located in the posterior wall of the central sulcus [24]. **Right:** the orientation of the primary currents (somatosensory evoked potential (SEP)/somatosensory evoked field (SEF) components) in the cerebral cortex is normal with respect to the surface due to the normal alignment of the pyramidal cells [10].

2.3. Measured Data

The source localization experiments were conducted while using a dataset that was obtained for three healthy and right-handed adult male subjects (I), (II), and (III), who were 49, 32, and 27 years old, respectively. The right median nerve was stimulated with the subject lying in a supine position in a magnetically shielded room. Simultaneous SEP/SEF measurements were performed while using 80 AgCl sintered ring electrodes (EASYCAP GmbH, Herrsching, Germany), including 74 EEG channels with an additional six channels for detecting eye movements together with an MEG setup (OMEGA2005, VSM MedTech Ltd). Four out of a total of 275 magnetometers and two out of 74 EEG sensors were reported as defective channels. Therefore, the measurements from 72 electrodes and 271 magnetometers (Figure 2) were used in the eventual dataset. A total of 1200 stimuli were obtained during a 10 min. measurement session. The electric pulse duration was 0.5 ms. In order to determine the magnitude, the stimulus strength was increased until a clear movement of the thumb was visible. Each measurement had a 300 ms total duration, which was subdivided into a 100 ms pre-stimulus and 200 ms post-stimulus sub-interval. The inter-stimulus interval varied between 350 and 450 ms to avoid habituation. The measurements were averaged and pre-processed while using a notch filter for the 50 Hz frequency and its harmonics to remove the power-line noise. The responses measured for the different stimuli were averaged to produce the SEP/SEF dataset (Figure 3) the amplitude of which was normalized to one.

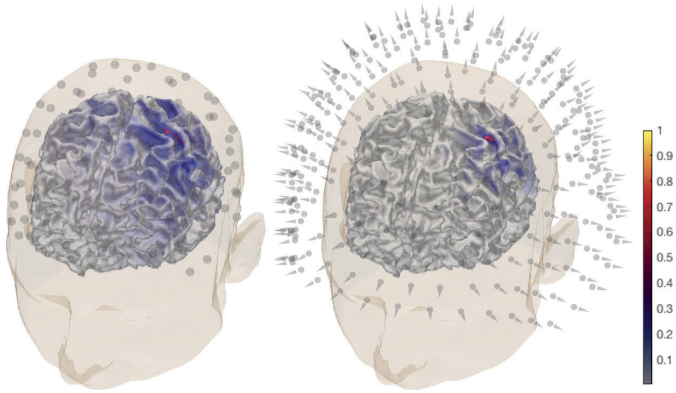

Figure 2. General overview of the P20/N20 component reconstruction for subject (I). The activity is found in the posterior bank of the central sulcus, the Brodmann 3b area for electroencephalography (EEG) (**left**) and magnetoencephalography (MEG) dataset (**right**). A MAP estimate of the global source distribution is visualized on the surface of the white matter. The locations of 72 EEG electrodes and 271 magnetometers are shown in the left and right images, respectively.

The data were filtered while using a bandpass of 20–250 Hz [52]. The data vector **y** for the inversion computation corresponded to the P20/N20 activity peak occurring at the 20 ms post-stimulus time point (Figure 3).

2.4. Synthetic Data

In order to enable a comparison between the measured and synthetic data, a normally-oriented synthetic dipolar source was placed in the hand-knob of the 3b area in the posterior wall of the central sulcus (Figure 4). Its position in the MNI (Montreal Neurological Institute) coordinate system was $x = -38$ mm, $y = -28$ mm, $z = 56$ mm with ± 2 mm accuracy. The data for the source were simulated while using the present FEM-based forward model and additive zero mean Gaussian noise with 3% standard deviation with respect to the maximal signal amplitude. The same noise model was also applied in order to obtain the likelihood function for the measured data.

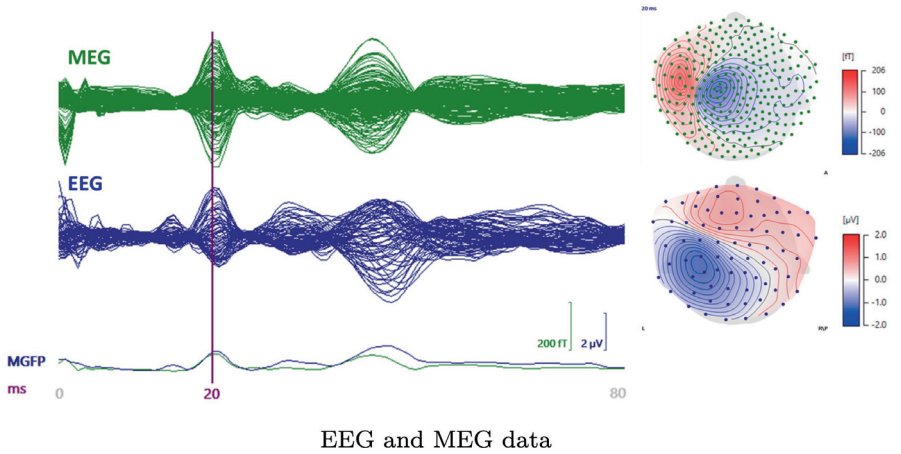

Figure 3. A butterfly plot of the somatosensory evoked field (SEF) (upper left) and potential (SEP) (lower left) from 0 to 80 ms post-stimulus with the 20 ms time point being indicated by the vertical line. The P20/N20 peak topographies for SEF (upper, right) and SEP (lower right) are also visualized.

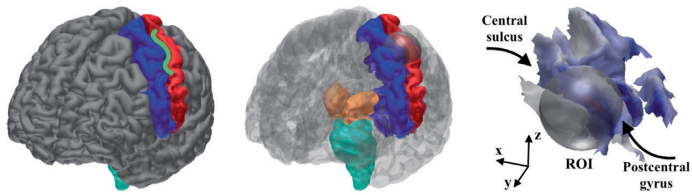

Figure 4. (**Left**) the hand knob (green Ω shape) is a part of the Brodmann area 3b in the central sulcus (between the pre-central (blue) and post-central (red) areas) [10]. (**Center**) regions of interest (ROIs) for the CM computations; the spherical region of interest (ROI) for detecting the 3b activity in the hand-knob together with the ROI for the thalamic activity detection, including the post-central area (red), thalamus (orange), and brainstem (cyan). (**Right**) the 24 mm diameter spherical ROI (grey) approximately covers the hand-knob of the left hemisphere. A global MAP estimate for the synthetic EEG data is visualized on the cortex.

2.5. Source Localization Estimates

The source localization tests were performed using the dense and sparse source distributions (Table 1) that are described in Section 2.2.2. The first of these was applied to be as accurate as possible in detecting the cortical source of the P20/N20 component in the 3b area using both measured and synthethic data. The reason for using the sparse distribution was to enhance the detectability of the thalamic activity [19], which occurs simultaneously with the cortical peak [52,53].

The MAP estimate was found via three IAS iteration steps. For CM, a sample of 10,000 points was created with the MCMC sampler. Of these, 1000 points in the beginning of the sequence were neglected as a burn-in phase. When examining the 3b area, the MCMC-based CM evaluation was due to the high dimensionality of the source space, performed by limiting the activity within a relatively small spherical ROI that was defined based on the MAP estimates (Figure 2). The placement of the ROI (Figure 4) was selected according to the literature on the hand-knob within the Brodmann area 3b [10]. The difference vector pointing from the synthetic source position to the center point of the ROI was $\Delta x = 4$ mm, $\Delta y = -1$ mm, $\Delta z = 2$ mm. Rather than being regarded as a complete reconstruction approach, the spherical ROI is primarily regarded here as a tool for analyzing the peak of the posterior

in the vicinity of the area where the activity is maximized. When reconstructing the thalamic source via MCMC sampling, the ROI covered the somatosensory area together with the sub-cortical thalamus and brainstem structures (Figure 4). In order to investigate the effects of the measurement noise, the P20/N20 response was reconstructed with G hyperprior by averaging the EEG data for 300 and 100 epochs. When compared to the principal case of 1200 epochs, this can be estimated to lead to +6 dB and +10 dB increments of the relative measurement noise level σ, based on the central limit theorem, i.e., $\mathrm{dB}(\sqrt{1200/300}) \approx +6$ dB and $\mathrm{dB}(\sqrt{1200/100}) \approx +10$ dB. In the case of elevated noise, the scale parameter was adjusted according to (4), while assuming that PM-SNR is unaffected by any change in σ. Moreover, MNE and MCE were investigated as alternative reconstruction approaches for EEG. These were obtained as the first and third step iterates of the IAS algorithm while using the G hyperprior with $\beta = 1.5$, i.e., the value that yields the match between IAS, MNE, and MCE [7].

Table 1. The values of the prior-over-measurement signal-to-noise ratio (PM-SNR) for different reconstructions specified by the type of data (Measured/Synthetic), measurement modality (EEG/MEG), estimate (MAP/CM), and the hyperprior (G/IG). The source-wise θ_0-value that was used for the dense and sparse source distribution corresponds to the total scale. PM-SNR can be associated with the *a priori* assumption on the latent noise strength, i.e., $\mathrm{dB}(s)$ (Section 2.1.4). When PM-SNR is 0 dB, the weight of the prior matches the *a priori* known noise level of 3%.

Data	Modality	Estimate	Hyp.	PM-SNR (dB)	Sparse θ_0	Dense θ_0
Meas.	EEG	MAP	G	20	10^{-10}	10^{-12}
			IG	30	10^{-9}	10^{-11}
		CM	G	20	10^{-10}	10^{-12}
			IG	20	10^{-10}	10^{-12}
	MEG	MAP	G	20	10^{-10}	10^{-12}
			IG	30	10^{-9}	10^{-11}
		CM	G	20	10^{-10}	10^{-12}
			IG	20	10^{-10}	10^{-12}
Synth.	EEG	MAP	G	20	10^{-10}	10^{-12}
			IG	30	10^{-9}	10^{-11}
		CM	G	0	10^{-12}	10^{-14}
			IG	0	10^{-12}	10^{-14}
	MEG	MAP	G	30	10^{-9}	10^{-11}
			IG	30	10^{-9}	10^{-11}
		CM	G	0	10^{-12}	10^{-14}
			IG	0	10^{-12}	10^{-14}

Implementation in Zeffiro Interface

The present forward and inverse methods have been implemented in the *Zeffiro* interface (ZI) [38] toolbox, which uses the Matlab (The MathWorks Inc., Natrick, MA 01760, USA) platform. ZI aims to provide a user-friendly tool for advanced forward and inverse computations, e.g., accurate lead field matrix construction, source localization, and time-lapse data analysis. ZI's on-line code repository (see Introduction) includes the methods that were used in the present study. To speed up the processing, ZI utilizes a Graphics Processing Unit (GPU) in the following processes: (1) segmenting the FE grid, (2) creating the lead field, (3) source space interpolation for visualizing the reconstructions, and (4) inverting the data. The following computation times were obtained for a 1 mm resolution six-compartment test mesh with 36 M elements, 6 M nodes, and 0.5 M sources while using a Lenovo P910 ThinkStation (Lenovo, Hong Kong, China) that was equipped with 2 × Intel Xeon E5-2697A v4 CPUs (Intel, Santa Clara, CA 95054, USA)(RAM 256 GB) and 2 ×NVIDIA Quadro P6000 GPUs (NVIDIA,Santa Clara, CA 95051, USA)(RAM 24 GB): (1) FE mesh generation = 1329 s, (2) EEG lead

field for 128 electrodes = 2362 s, (3) MEG lead field for 154 magnetometers = 4826 s, and (4) Source space interpolation = 212 s.

3. Results

This section describes the results that were obtained with the data of subjects (I)–(III). An in-depth source localization analysis was conducted in the case of (I). Additionally, the parameters that were suggested by this analysis were tested with (II) and (III) in order to learn about the inter-subject variability of the results. The results of the source localization analysis have been included in Figures 5–10 and Table 2 shows the results of the additional tests.

Table 2. Subject (I). The spread of the current distribution reconstructed in the Brodmann area 3b together with the position and orientation difference between the synthetic and reconstructed source. The position and orientation of the reconstruction was obtained from its center of mass in the spherical ROI. The MAP estimates were obtained without restricting the source space. In the case of CM, the reconstruction process was limited to ROI.

FE Mesh	Data	Model	Data	MAP /CM	Space	Hyper.	Spread (mm^2)	Orientation Δ (deg)	Position Δ (mm)
1 mm	Meas.	HBM	EEG	MAP	Global	G	44.7	9.7	3.4
					Global	IG	43.9	9.5	3.4
				CM	ROI	G	71.8	13.3	3.8
					ROI	IG	37.7	14.4	3.8
			MEG	MAP	Global	G	32.0	10.8	3.4
					Global	IG	32.2	10.8	3.4
				CM	ROI	G	48.8	11.7	3.7
					ROI	IG	42.0	12.5	3.8
	Synth.		EEG	MAP	Global	G	42.0	5.8	3.5
					Global	IG	40.3	5.7	3.5
				CM	ROI	G	64.8	11.5	3.7
					ROI	IG	69.9	12.1	3.7
			MEG	MAP	Global	G	22.0	12.8	3.5
					Global	IG	13.7	14.3	3.5
				CM	ROI	G	52.5	12.8	3.7
					ROI	IG	52.6	12.6	3.7
		+6 dB	EEG	MAP	Global	G	43.2	10.3	3.4
				CM	ROI	G	68.9	14.8	3.7
		+10 dB		MAP	Global	G	26.8	11.1	3.4
				CM	ROI	G	40.2	17.2	3.7
		Regul.	EEG	MNE	Global	G	38.1	9.2	3.4
				MCE	Global	G	12	8.8	3.6
2 mm	Meas.		EEG	MAP	Global	G	34.8	9.7	3.4
					Global	IG	30.9	9.7	3.4
				CM	ROI	G	43.4	10.8	3.5
					ROI	IG	67.7	7.0	3.4
			MEG	MAP	Global	G	87.9	11.5	3.5
					Global	IG	87.9	11.5	3.5
				CM	ROI	G	99.4	15.8	3.5
					ROI	IG	115.9	15.6	3.5
	Synth.		EEG	MAP	Global	G	64.2	6.7	3.3
					Global	IG	64.2	6.7	3.3
				CM	ROI	G	39.1	13.7	3.5
					ROI	IG	8.3	14.2	3.3
			MEG	MAP	Global	G	60.2	10.2	3.5
					Global	IG	51.0	10.0	3.5
				CM	ROI	G	109.0	16.1	3.5
					ROI	IG	110.2	16.1	3.5

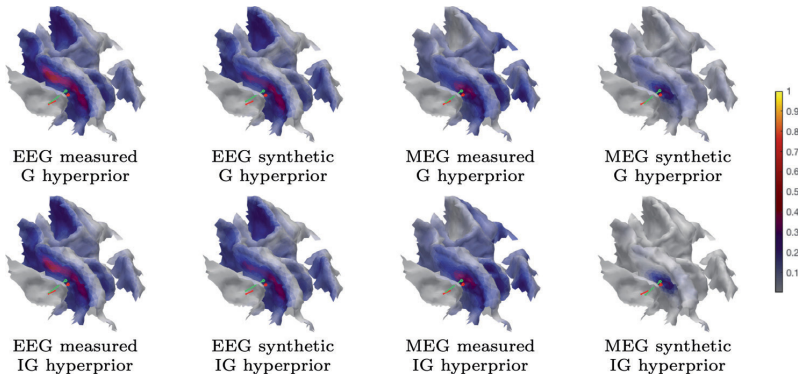

Figure 5. Subject (**I**). The MAP estimation results obtained with the iterative alternating sequential (IAS) iteration corresponding to the measured and synthetic data and the 1 mm FE mesh. The placement and orientation of the synthetic source is shown by the red pin and the mass center of the reconstruction by the green one. The MAP estimates shown have been obtained using a global source space.

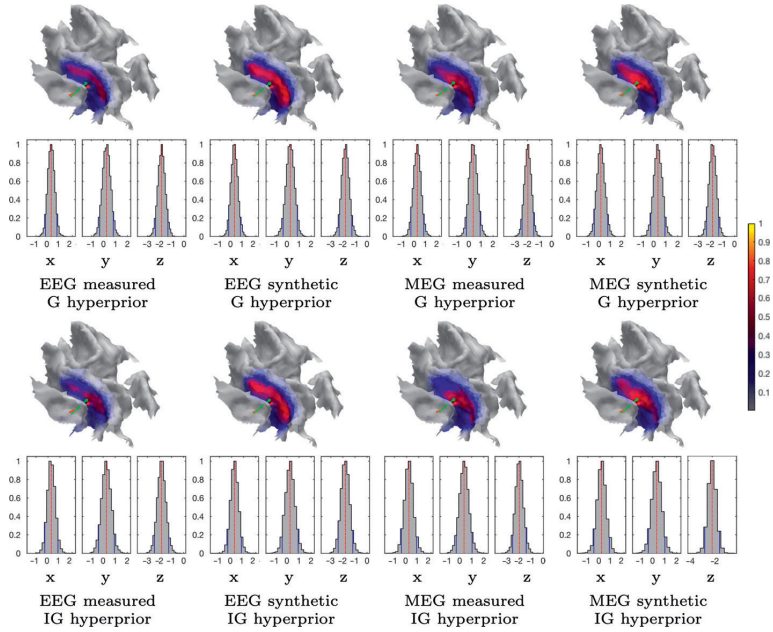

Figure 6. Subject (I). The CM estimation results that were obtained with the sampler corresponding to the measured and synthetic data and the 1 mm FE mesh. The marginal density (histograms) of the (volumetric) posterior mass centre is illustrated for each case and the Cartesian coordinate component, including the median (red dashed line) and the 90% credibility interval, is conditional on the subjectively selected parameters (solid blue line). The placement and orientation of the synthetic source is shown by the red pin and mass center of the reconstruction by the green one. The CM estimates shown have been obtained by limiting the source space within ROI

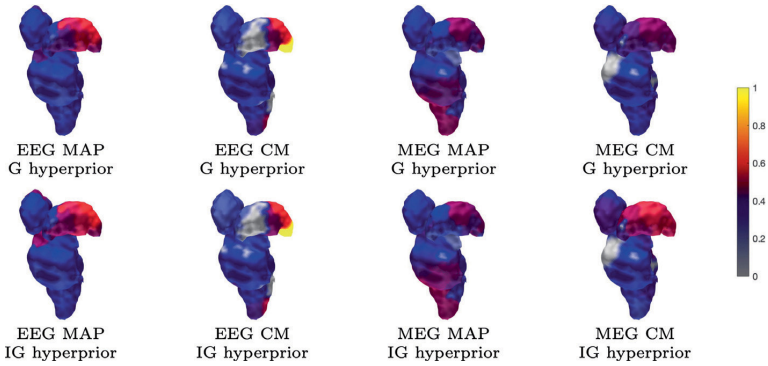

Figure 7. Subject (I). The thalamic activity found with 1200 epochs and 1 mm FE mesh resolution. The ventral posterolateral part of the left thalamus (contralateral to the stimulation side) can be observed as having been activated in most reconstructions. The source space is global for the MAP estimates and limited to ROI in the case of CM.

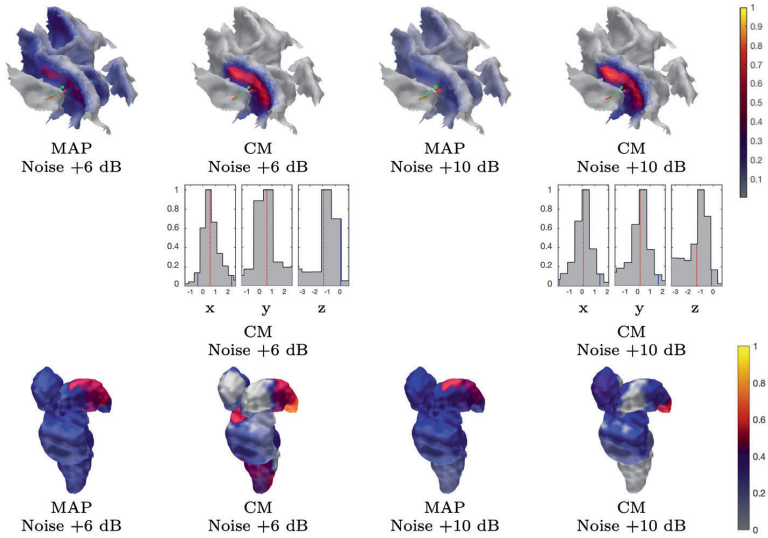

Figure 8. Subject (I). The results obtained with an EEG and G hypermodel while using 300 and 100 epochs, i.e., approximately +6 dB and +10 dB noise level, respectively. The source space is global for the MAP estimates and limited to ROI in the case of CM.

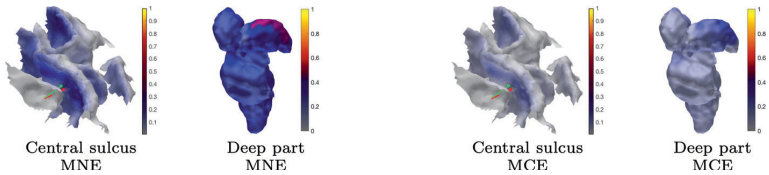

Figure 9. Subject (I). Minimum norm estimation (MNE) and minimum current estimation (MCE) results for the P20/N20 component network for surface activity (central sulcus) and deep activity (thalamus). The source space is global for both MNE and MCE.

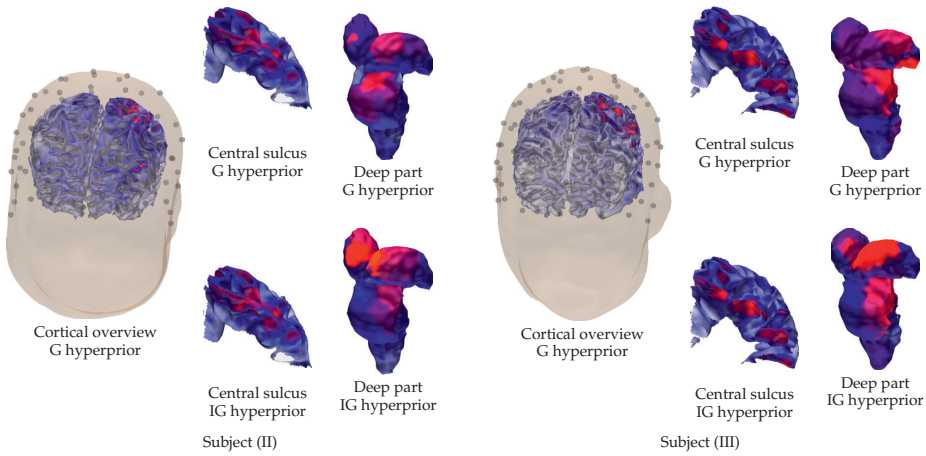

Figure 10. Visualization of the cortical and sub-cortical activity reconstructed for subjects (II) on the left and (III) on the right using the EEG data corresponding to the P20/N20 component. In addition to the cortical overview, showing the reconstruction that was obtained with G hyperprior, excerpts of the cortical activity around the central sulcus and the sub-cortical (deep) activity are shown for G and IG hyperprior.

3.1. Subject (I)

The proposed parametrization approach was found to perform appropriately in detecting the peak of the P20/N20 component in the area 3b of the left hemisphere. In addition to the activity of the 3b area, the overlaid thalamic component was found to be detectable in the experiments that were performed with the sparse source density. In each source localization test, the scale parameter value was selected based on PM-SNR, whose case-specific value was within the range 0–30 dB depending on the assumption of the latent noise level (Section 2.1.4): the greater the latent noise, the larger the PM-SNR, i.e., the stronger the prior. PM-SNR was chosen to be 20 dB and 0 dB for the measured and synthetic data, respectively, when assuming that the latent modeling errors that are related to the measured data are emphasized by a +20 dB difference in PM-SNR as compared to the simulated case. The PM-SNR value for the MAP estimation process was set to be larger than for the CM evaluation, allowing +10 dB for the latent errors due to the *a priori* lower accuracy of the MAP as compared to CM [28], if the gradient-based IAS algorithm did not otherwise find the peak of the posterior. An important criterion in selecting PM-SNR was the shape of the posterior density, whose peak in the 3b area was assumed to be a few millimeters diameter w.r.t. the mass center of $\mathbf{x}$, i.e., comparable to the mutual distance of the lead field source space density. This was done in order to avoid the failure of the sampling process due to an excessively peaked posterior structure.

3.1.1. Brodmann Area 3b

Table 2 includes a numeric measure for the spread (focality) of the reconstructed and normally restricted activity (in the 3b area), defined as the area of the set, in which its intensity exceeds 80% of the maximum value. The position and orientation differences between the synthetic source and mass center of the reconstructed activity are also given. In the case of the measured data, the synthetic source is regarded as a numerical reference point and it should not be confused with the actual activity (ground truth). Figures 5, 6, 8, and 9 visualize the reconstructed activity on the white matter surface (i.e. on the inner surface of the grey matter) in the vicinity of the ROI. Each distribution shows the activity in the direction of the outward-pointing surface normal.

3.1.2. MAP Estimation

The MAP estimates obtained for the 3b area are shown in Figures 5, 8, and 9. The CG-HBM estimates obtained using 1200 epochs generally localize the activity in the sulcal wall with the difference in position and orientation being less than 0.4 mm and 10.4 degrees. In the 1 mm case, they were a maximum 3.8 mm and 14.4 degrees, respectively. MEG provided slightly more focal reconstructions than EEG, and the IG hyperprior led to more focal outcomes than G for three out of the four reconstructions. The 1 mm FE mesh resolution yielded a greater similarity between the MAP estimates obtained with both the measured and synthetic data than the 2 mm mesh did, as shown by Table 2. In the 2 mm case, the reconstructions were less intense and more spread out than those that were obtained with the 1 mm mesh. The estimates obtained with 300 and 100 epochs (Figure 8), i.e., with +6 dB and +10 dB noise levels, show that the distinguishability of the 3b activity decreases as the noise increases as; the activity is clearly visible in the +6 dB case, but barely detectable with +10 dB noise. The estimates that were obtained with MNE and MCE (Figure 9) show a clear difference in the 3b area, suggesting that the stronger tendency of the MCE to find a focal estimate results in a clearer source distinction than with MNE, while the peak of both estimates is less intense than with the CG-HBM estimates.

3.1.3. CM Estimation

Figures 6 and 8 illustrate the CM estimates that were obtained for the spherical ROI together with the corresponding marginal densities (histograms) for the volumetric mass center of the posterior. Overall, CM had a higher maximum intensity in a mutual comparison to MAP for both real and synthetic data. This is particularly clear for the estimates with the elevated measurement noise (Figure 8). However, the location of the maximum was virtually the same. The marginal densities obtained show that, in the case of 1200 epochs, the maximum length of the 90% credibility interval for the marginal posterior's mass center, conditional to the subjectively selected parameters, was in the range 0.9–1.4 and 1.2–2.3 mm, respectively, for the 1 and 2 mm FE mesh resolutions, thus matching the targeted range. The mutual differences in the median, for each coordinate direction, were less than 0.2 and 1.1 mm, respectively. As with the MAP, the spread of the CM that was obtained with the 2 mm FE mesh resolution varied more between the different reconstructions than in the case of the 1 mm mesh, while the maximal intensity of the CM was observed to vary less than that of the MAP. The marginal densities are clearly more spread out in the case of the elevated noise (Figure 8), i.e., with 300 and 100 epochs.

3.1.4. Thalamic Component

The results for reconstructing the thalamic activity in the case of the sparse source space can be found in Figures 7–9. Overall, when compared to the estimates obtained for the 3b area, the thalamic activity is less well-localized in its *a priori* expected location, which we expect to be primarily the ventral posterolateral nucleus [21] of the left thalamus contralateral to the stimulation side. This can be observed in the form of a greater variation between the estimates that were obtained for the thalamic component when compared to the 3b source localization. Some of these estimates were spread over the brainstem as well as the thalamic area [52,54]. Based on Figure 7, EEG has a greater tendency to find the deep activity than MEG. The CM estimate that is obtained with IG hyperprior is similar for both EEG and MEG, which suggests that the posterior exploration technique (here, MAP or CM) had a significant effect on detecting deep fluctuations. The reconstruction quality seems to be diminished when the noise level is elevated, as was the case for the 3b area (Figure 8). Nevertheless, the thalamic component was distinguishable with each noise level. Regarding the MNE and MCE estimates, MNE localized the deep activity, while MCE led to a strongly suppressed reconstruction (Figure 9).

3.2. Subject (II) and (III)

The results that were obtained for subjects (II) and (III) are visualized in Figure 10 in the case of the P20/N20 component and the EEG data. The results obtained show that the parameters used for subject (I) result in a largely appropriate reconstruction around the cortical (Brodmann 3b) and thalamic areas. The results are somewhat less focal than in the case of subject (I), which is obviously due to the measurement or head model creation process, while the activity is found with a uniform parameter choice for (I)–(III).

4. Discussion

In this proof-of-concept study, we proposed an approach for parametrizing the conditionally Gaussian hierarchical Bayesian model (CG-HBM) [7,8] and applied it to invert the P20/N20 response of the median nerve somatosensory evoked potentials and fields (SEP and SEF). We introduced an approach for parameter selection and analyzed its performance in source localization tests. The activity that corresponds to the P20/N20 response was detected in the Brodmann area 3b and the thalamus [21,22,52,53,55] while using both a dense and sparse source space [19], respectively. The source localization experiments were performed while using the Zeffiro interface (ZI) software tool [38].

In our approach, the shape and scale parameter determining the hyperprior and, thereby, also the conditionally Gaussian prior of the CG-HBM, were chosen based on optimization and *a priori* knowledge of the prior-over-measurement signal-to-noise ratio (PM-SNR), respectively. The shape parameter value $\beta = 3$ was found to be close-to-optimal in minimizing the posterior differences between the gamma (G) and inverse gamma (IG) hyperprior (Appendix A). PM-SNR is a model specific constant which determines the scale parameter θ_0 given the dimension and noise level of the forward model. The noise can consist of both a known and latent component. In this study, PM-SNR varied between 0 dB and 30 dB, depending on the assumption of the latent errors; the greater the errors, the higher the PM-SNR, i.e., the stronger the prior. As potential factors causing latent noise, we recognized (1) the forward modeling inaccuracies that are related to the measured data, e.g., the potential deviations of the conductivity distribution [46], which are absent for the simulated data, and also (2) the performance differences between the IAS and CM posterior estimation method. The value range applied in this study is in agreement with the Brainstorm software's default MNE regularization value [27], which we estimated to match a PM-SNR of 10 dB with respect to EEG data.

The range that is proposed here is also supported by our recent studies [38] and [12]. In the first of these, IAS was shown to reconstruct a cortical epileptic (gyral) activity in EEG with both the G and IG hyperpriors, when the PM-SNR was set to 20 dB (following from $\theta_0 = 10^{-12}$, $\sigma = 0.03$, $N = 100{,}000$). In the other study, a scale parameter range from 10^{-10} to 10^{-8} was found to be applicable for IAS MAP estimation of numerically simulated deep activity with the IG hyperprior and a sparse source space (N from 100 to 400), converting to PM-SNR of 30 dB and 20 dB for $\theta_0 = 10^{-8}, N = 100$ and $\theta_0 = 10^{-10}, N = 400$, respectively.

The results obtained suggest that PM-SNR might also be applicable with elevated measurement noise levels, i.e., fewer averaged epochs, as both the 3b and thalamic activity components were found to be detectable in the cases of +6 dB and +10 dB noise. This result cannot be generalized, because the distinguishability of the responses is not obvious with fewer than the recommended minimum number of averaged epochs, which is 1000–4000 for SEPs [16–18] regarding the investigated 20 ms latency. Nevertheless, a lower number of averaged trials can be relevant in other EEG and MEG applications. For example, in [38], the reconstructions obtained with CG-HBM correspond to 58 averaged epileptiform discharges.

Comparing the performance of IAS obtained with the proposed settings and with those corresponding to MNE and MCE suggests that the present parametrization of CG-HBM can be related to, and also explain the performance of, classical regularization approaches. MNE was shown to find the thalamic activity with the selected PM-SNR, while it led to a visually less focal estimate in

the 3b area than CG-HBM. In the case of $\beta = 1.5$, MCE was observed to result in a suppressed deep activity, which suggested that the choice $\beta = 3$ is advantageous with respect to MAP estimation with the G hyperprior. In particular, it seems that, with $\beta = 3$, both the G and IG hyperpriors can find the deep source, supporting our approach of selecting β, so that it minimizes the difference between the hyperpriors. This difference is obvious, when $\beta = 1.5$, which is, when the posterior maximizer of the prior variance θ will be zero for G and $\theta_0/3$ for IG (see Equation (A1)), suggesting that any weakly distinguishable (close-to-zero) fluctuations, especially the deep ones, will be suppressed by G.

The estimates that were obtained for the deep part varied more than those for the 3b area. This was expected, since the accuracy of both EEG and MEG is known to be limited with regard to far-field activity. Indeed, it has only recently been proposed that the localization of the deep sources is feasible based on non-invasive measurements [56,57]. In order to obtain an appropriate reconstruction for the thalamus, we applied a sparse source space, as it has recently been suggested that this can improve the detectability of the deep components [19]. Based on the results, it is obvious that the method applied in the posterior exploration has a major effect on the deep part of the reconstruction. As indicated by the numerical results of [7], the CM provided a more focal estimate for the thalamic activity than MAP in the case of MEG, which, in turn, is generally regarded as having less advantageous modality for depth-localization than EEG [10].

While the activity of the thalamus is generally known to overlap with that of the 3b area [21,22,53], there is less exact knowledge about the deep response network compared to that of the cortical one, and its activity varies subject-wise. For example, in [53], the activity that corrresponds to the P20/N20 peak was exclusively limited to the 3b area in ten subjects, while the thalamus was only found to be additionally activated in two subjects. In contrast, the somatosensory 3b component, i.e., the first cortical contribution in the median nerve SEP/SEF, is known to be well-localized in the posterior wall of the sulcus, while the gyral components will be visible a few milliseconds after 20 ms [21,52,58]. In order to obtain the best possible source localization outcome for both the superficial and deep areas, CG-HBM can be adapted to utilize multiple source space densities in finding a single reconstruction. An example of such a method is the recently proposed randomized multiresolution scanning (RAMUS) algorithm [12], which finds a reconstruction without imposing any restrictions regarding active brain areas or the source depth. The present restrictions (ROIs) have been introduced, as, here, our focus is on CG-HBM as a superclass of methods, rather than on the individual reconstruction techniques originating from it. That is why, here, we have restricted the number of moving parameters, other than the ones describing the statistical model.

Based on the present results, especially the position difference with respect to the mass center, it seems that a source localization accuracy of around 4 mm could be achieved in the 3b area. This coincides with the maximal spatial accuracy found for the MEG, i.e., 2–4 mm for the superficial areas [48,49], and even surpasses that of EEG, whose accuracy for superior locations was estimated to be, on average, approximately 9 mm [22,50,51]. A significant factor affecting the accuracy of EEG is the uncertainty related to the conductivity distribution [46,59]. However, while taking the total estimated 32–116 mm^2 areal spread of the estimates obtained for the 3b area into account, the accuracy found here does not exceed the suggested maximal accuracy limits. The spread of the estimates arises from the current numerical framework as the maximal achievable focality without a potential numerical bias. The relationship between the estimates found and the actual physiological spread of the source is not evaluated here and it would necessitate further work.

CG-HBM might be advantageous as a statistical model for obtaining robust sampling-based inverse estimates, as suggested by the present results. When the parameters are chosen appropriately, the sampler-based approach seems to provide a robust technique for estimating the marginal posterior and the CM, giving information about the posterior distribution, shape and structure. Here, it allowed us to adapt it according to the underlying numerical model and geometry, whereas the IAS MAP estimation technique alone did not completely reveal the posterior shape, thereby increasing the risk of obtaining, e.g., overly focal estimates. It also seems that estimating the CM via a sampling

approach and defining a ROI for the sampler is beneficial with respect to the distinguishability of the activity obtained. Because the IAS MAP estimation technique can be associated with many classical regularization methods, including MNE and MCE [7], sampling-based CG-HBM can also be seen as a potential way to enhance the outcome that was obtained with these classical methods.

The present forward simulation approach was found to perform adequately with both 1 and 2 mm resolution. Agreeing with the existing knowledge of physiologically accurate volumetric head modeling and forward simulation [32,60], the FE mesh resolution of 1 mm was observed to be advantageous for obtaining a satisfactorily consistent reconstruction quality. The present GPU-based approach to the forward simulation was found to be essential in order to achieve a suitably short computation time for the 1 mm mesh generation and lead field matrix evaluation processes with our ZI implementation. The approach of finding the reconstruction while using Cartesian source orientations was found to be suitable in the present modeling context, since it allows slight orientation changes during the source localization process, thereby resulting in a smooth posterior distribution. However, ZI also allows the normal orientations for cortical areas (Section 1) to be applied directly, as the differences between the directly normal and present normally-projected reconstructions seem minor.

More work will need to be done in order to optimize the outcome of CG-HBM for a given subject and dataset, as the present results mainly provide a proof-of-concept for a potentially applicable parametrization together with rough estimates for the parameter ranges. Therefore, an important objective of any future work will be to apply the present hyperprior parametrization technique for more datasets, e.g., including temporal correlations and combined E/MEG data, (see [12] for preliminary numerical simulation results, and subjects), in order to learn more about the practical localization capability of the CG-HBM. Potential directions for the development of mathematical method include, e.g., incorporating physiological knowledge to the hyperprior [61,62] and/or the source space that can be adapted to the properties of the active neural tissue: e.g., many brain structures have the primary current density of approximately 1 nAm/mm^2 when active [63]. The development of source localization techniques for the multiple resolution levels [12], e.g., a full MCMC sampler implementation, provides a further potential application for the current parametrization approach. Finally, while our present focus is on CG-HBM and the corresponding reconstruction methods, i.e., IAS, MCMC sampling, MCE, and MNE, further research would be necessary in order to relate the performance of CG-HBM with that of the most promising alternative methods that do not belong to the CG-HBM superclass, such as the beamformer techniques [64–66].

Author Contributions: Methodology, S.P.; software, S.P.; validation, A.R.; formal analysis, A.R.; investigation, A.R.; writing—original draft preparation, A.R., S.P.; writing—review and editing, A.R., S.P., M.A., M.P., C.H.W.; visualization, A.R.; supervision, S.P., C.H.W.; project administration, S.P.; funding acquisition, S.P., C.H.W. All authors have read and agreed to the published version of the manuscript.

Funding: AR and SP were supported by the Academy of Finland Centre of Excellence in Inverse Modelling and Imaging 2018–2025. AR, SP, CHW and MA were supported by DAAD projects 57523877 and 57405052 (AoF decision numbers 317165 and 326668). AR was also supported by the Vilho, Yrjö and Kalle Väisälä Foundation. MA, MCP and CHW were supported by the Deutsche Forschungsgemeinschaft (DFG), project WO1425/7-1 and the Priority Program 1665 of the DFG (WO1425/5-2) and by EU project ChildBrain (Marie Curie Innovative Training Networks, grant agreement 641652). AR, SP, and CHW are funded by the ERA PerMed project "Personalised diagnosis and treatment for refractory focal paediatric and adult epilepsy" (ERA decision ERAPERMED2020-227).

Conflicts of Interest: The authors declare no conflict of interest.

Appendix A. Shape Parameter Optimization

In HBM, the i-th entry $\mathbf{x}$, is assumed to have an independent zero mean Gaussian distribution with variance θ_i determined by the G or the IG hyperprior. Given a shape and scale parameter $\beta \geq 3/2$ and $\theta_0 > 0$, the G and IG are maximized at the points $\theta^{(\mathrm{G})}_{i,\max} = (\beta - 1)\theta_0$ and $\theta^{(\mathrm{IG})}_{i,\max} = \theta_0/(\beta + 1)$ and the mean is at $\theta^{(\mathrm{G})}_{i,\mathrm{mean}} = \beta\theta_0$ and $\theta^{(\mathrm{IG})}_{i,\mathrm{mean}} = \theta_0/(\beta - 1)$, respectively. Assuming that $\theta \ll \beta \ll 1/\theta_0$, the magnitude of these follows essentially from that of θ_0. That is, the scale parameter sets the initial informativeness

of the prior or the initial sensitivity of the hypermodel to localized brain activity. Generally, the smaller the value, the less informative is the prior, whose effect is slighter than the likelihood.

Given the i-th entry x_i, the maximizer of the joint prior $p(\boldsymbol{\theta}, \mathbf{x})$ and of the conditional posterior $p(\boldsymbol{\theta} \mid \mathbf{x})$ w.r.t. $\boldsymbol{\theta}$, independent of the measurements $\mathbf{y}$ [7], is of the form

$$\tilde{\theta}^{(\mathrm{G})}_{i,\max} = \frac{1}{2}\theta_0(\beta - \frac{3}{2}) + \frac{1}{2}\theta_0\sqrt{(\beta - \frac{3}{2})^2 + \frac{2x_i^2}{\theta_0}} \quad \text{and} \quad \tilde{\theta}^{(\mathrm{IG})}_{i,\max} = \frac{1}{\beta + \frac{3}{2}}(\theta_0 + \frac{x_i^2}{2}). \tag{A1}$$

In order to obtain comparable results with G and IG hyperprior and, thereby, to avoid any depth-localization bias of the G hyperprior [7,12], we optimize β so that the corresponding conditional posterior distributions are locally equally sensitive to the increment of x_i^2. That is, we optimize the shape parameter so that $\tilde{\theta}^{(\mathrm{G})}_{i,\max} \approx c\,\tilde{\theta}^{(\mathrm{IG})}_{i,\max}$ locally with some constant c corresponding to a given x_i^2. We require that, following from the form $\tilde{\theta}^{(\mathrm{IG})}_{i,\max}(s,\beta) = \nu + \nu s$, $\nu = \theta_0/(\beta + 3/2)$, $s = x_i^2/(2\theta_0)$, there is a match between the zeroth and first-order coefficient of the first-order Taylor polynomial $F(s,\beta) \approx F(s_0,\beta) + \frac{\partial F(s_0,\beta)}{\partial s}(s - s_0)$ with $F(s,\beta) = \tilde{\theta}^{(\mathrm{G})}_{i,\max}(s,\beta)$, resulting in the equation

$$F(s_0,\beta) - \frac{\partial F(s_0,\beta)}{\partial s}(s_0 + 1) = 0 \tag{A2}$$

with respect to β. Furthermore, we set the point of linearization proportional to the mean of the IG hyperprior, i.e., $s_0 = \alpha/[2(\beta - 1)]$ or $x_i^2 = \alpha\,\theta^{(\mathrm{IG})}_{i,\mathrm{mean}}$. That is, x_i^2 is assumed to be proportional to the expected variance of the conditional Gaussian prior. We make this choice, since a zero-mean Gaussian density is invariant with respect to a scale proportional to its variance.

(Figure A1) illustrates the results obtained by solving the Equation (A2) numerically with respect to β for each integer α from $\alpha = 1$ to $\alpha = 1000$. For $\alpha = 100$, the solution and the corresponding scaling constant satisfy $\beta \approx 3$ and $c \approx 1$, meaning that $\theta^{(\mathrm{IG})}_{i,\mathrm{mean}} \approx \theta^{(\mathrm{G})}_{i,\mathrm{mean}}$ at the point of linearization. For this match, we interpret $\beta = 3$ as a close-to-optimal shape parameter value to minimize the differences between the G and IG hyperprior. As can be observed from (Figure A1), an IG hyperprior generally leads to a heavier-tailed conditional posterior distribution than G at the point of linearization, meaning that, in principle, it allows a higher probability for outliers such as focal activity spots.

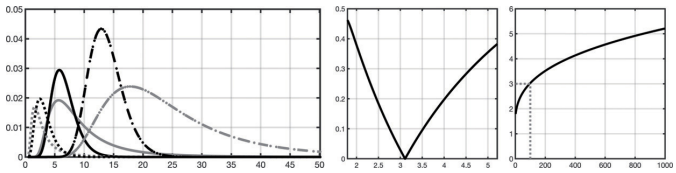

Figure A1. (**Left**) The i-th component of the conditional posterior $p(\theta_i \mid x_i)$ optimized with respect to the shape parameter β so that $\tilde{\theta}^{(\mathrm{G})}_{i,\max} \approx c\,\tilde{\theta}^{(\mathrm{IG})}_{i,\max}$ close to the point of linearization $x_i^2 = \alpha\theta_0/(\beta - 1)$ with some constant c (Appendix A). The gray curves correspond to IG and the black ones to G hyperprior. The solid, dashed and dash-dotted curves have been obtained with $\alpha = 100$, $\alpha = 10$ and $\alpha = 1000$, respectively. In each case the scale parameter is $\theta_0 = 1$. The maximizers match approximately, i.e., $c \approx 1$, when $\alpha = 100$ (solid) and the optimizer is $\beta \approx 3$. (**Center**) The relative scale deviation $|c - 1|/c$ w.r.t. $c = 1$ as a function of the optimizer β, vanishing when $\beta \approx 3$. (**Right**) The optimizer β as the function of α.

Appendix B. Effect of the Shape Parameter

The effect of the shape parameter on the hyperprior is visualized in Figure A2. The weight of the tail is the greater the smaller the shape parameter which is shown by the interdecile range (the interval between 10 and 90% quantile).

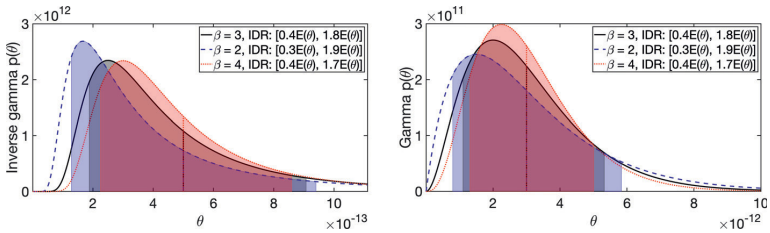

Figure A2. The effect of the shape parameter on the IG (**left**) and G (**right**) hyperprior. The black (solid), shows the hyperprior density $p(\theta)$ for $\beta = 3$ and $\theta_0 = 1 \times 10^{-12}$ (see Table 1). The blue (dashed) and red (dotted) curves correspond to the same expectation $E(\theta)$ with $\beta = 2$ and $\beta = 4$, respectively. The greater the weight of the tail is, the smaller the shape parameter is. This is shown by the colored interdecile range (IDR), i.e., the interval between 10 and 90% quantile, which is presented here with respect to $E(\theta)$. The colors correspond to those of the curves.

References

1. Hämäläinen, M.; Hari, R.; Ilmoniemi, R.J.; Knuutila, J.; Lounasmaa, O.V. Magnetoencephalography— Theory, instrumentation, and applications to invasive studies of the working human brain. *Rev. Mod. Phys.* **1993**, *65*, 413–498.
2. Niedermeyer, E.; da Silva, F.L. *Electroencephalography: Basic Principles, Clinical Applications, and Related Fields*, 5th ed.; Lippincott Williams & Wilkins: Philadelphia, PA, USA, 2004.
3. Brette, R.; Destexhe, A. *Handbook of Neural Activity Measurement*; Cambridge University Press: New York, NY, USA, 2012.
4. Wipf, D.; Nagarajan, S. A unified Bayesian framework for MEG/EEG source imaging. *NeuroImage* **2009**, *44*, 947–966. [CrossRef] [PubMed]
5. Friston, K.; Harrison, L.; Daunizeau, J.; kiebel, S.; Phillips, C.; Trujillo-Barreto, N.; Henson, R.; Flandin, G.; Mattout, J. Multiple sparse priors for the M/EEG inverse problem. *NeuroImage* **2008**, *39*, 1104–1120. [CrossRef] [PubMed]
6. Sato, M.; Yoshioka, T.; Kajihara, S.; Toyama, K.; Goda, N.; Doya, K.; Kawato, M. Hierarchical bayesian estimation for MEG inverse problem. *NeuroImage* **2004**, *23*, 806–826. [CrossRef] [PubMed]
7. Calvetti, D.; Hakula, H.; Pursiainen, S.; Somersalo, E. Conditionally Gaussian hypermodels for cerebral source localization. *SIAM J. Imaging Sci.* **2009**, *2*, 879–909. [CrossRef]
8. Lucka, F.; Pursiainen, S.; Burger, M.; Wolters, C.H. Hierarchical bayesian inference for the EEG inverse problem using realistic FE head models: Depth localization and source separation for focal primary currents. *NeuroImage* **2012**, *61*, 1364–1382. [CrossRef] [PubMed]
9. Ahlfors, S.P.; Han, J.; Belliveau, J.W.; Hämäläinen, M.S. Sensitivity of MEG and EEG to source orientation. *Brain Topogr.* **2010**, *23*, 227–232. [CrossRef]
10. Hari, R.; Baillet, S.; Barnes, G.; Burgess, R.; Forss, N.; Gross, J.; Hämäläinen, M.; Jensen, O.; Kakigi, R.; Mauguière, F.; et al. IFCN-endorsed practical guidelines for clinical magnetoencephalography (MEG). *Clin. Neurophysiol.* **2018**, *129*, 1720–1747. [CrossRef]
11. O'Hagan, A.; Forster, J.J. *Kendall's Advanced Theory of Statistics*; Volume 2B: Bayesian Inference; Arnold: London, UK, 2004; Volume 2.
12. Rezaei, A.; Koulouri, A.; Pursiainen, S. Randomized multiresolution scanning in focal and fast E/MEG sensing of brain activity with a variable depth. *Brain Topogr.* **2020**, *33*, 161–175. [CrossRef]
13. Rampp, S.; Stefan, H.; Wu, X.; Kaltenhäuser, M.; Maess, B.; Schmitt, F.C.; Wolters, C.H.; Hamer, H.; Kasper, B.S.; Schwab, S.; et al. Magnetoencephalography for epileptic focus localization in a series of 1000 cases. *Brain* **2019**, *142*, 3059–3071. [CrossRef]
14. Foley, E.; Cerquiglini, A.; Cavanna, A.; Nakubulwa, M.A.; Furlong, P.L.; Witton, C.; Seri, S. Magnetoencephalography in the study of epilepsy and consciousness. *Epilepsy Behav.* **2014**, *30*, 38–42. [CrossRef] [PubMed]

15. Foley, E.; Cross, J.H.; Thai, N.J.; Walsh, A.R.; Bill, P.; Furlong, P.; Wood, A.G.; Cerquiglini, A.; Seri, S. MEG assessment of expressive language in children evaluated for epilepsy surgery. *Brain Topogr.* **2019**, *32*, 492–503. [CrossRef] [PubMed]
16. American Clinical Neurophysiology Society and others, Guideline 9A: Guidelines on evoked potentials. *J. Clin. Neurophysiol. Off. Publ. Am. Electroencephalogr. Soc.* **2006**, *23*, 125.
17. Cruccu, G.; Aminoff, M.J.; Curio, G.; Guerit, J.M.; Kakigi, R.R.; Mauguiere, F.; Rossini, P.M.; Treede, R.D.; Garcia-Larrea, L. Recommendations for the clinical use of somatosensory-evoked potentials. *Clin. Neurophysiol.* **2008**, *119*, 1705–1719. [CrossRef]
18. Desmedt, J.E.; Guy, C. Somatosensory evoked potentials to finger stimulation in healthy octogenarians and in young adults: Wave forms, scalp topography and transit times of pariental and frontal components. *Electroencephalogr. Clin. Neurophysiol.* **1980**, *50*, 404–425. [CrossRef]
19. Krishnaswamy, P.; Obregon-Henao, G.; Ahveninen, J.; Khan, S.; Babadi, B.; Iglesias, J.E.; Hämäläinen, M.S.; Purdon, P.L. Sparsity enables estimation of both subcortical and cortical activity from MEG and EEG. *Proc. Natl. Acad. Sci. USA* **2017**, *114*, E10465–E10474. [CrossRef]
20. Samuelsson, J.G.; khan, S.; Sundaram, P.; Peled, N.; Hämäläinen, M.S. Cortical Signal Suppression (CSS) for detection of subcortical activity using MEG and EEG. *Brain Topogr.* **2019**, *32*, 215–228. [CrossRef]
21. Haueisen, J.; Leistritz, L.; Süsse, T.; Curio, G.; Witte, H. Identifying mutual information transfer in the brain with differential-algebraic modeling: Evidence for fast oscillatory coupling between cortical somatosensory areas 3b and 1. *NeuroImage* **2007**, *37*, 130–136. [CrossRef]
22. Buchner, H.; Fuchs, M.; Wischmann, H.A.; Dössel, O.; Ludwig, I. ; Knepper, A.; Berg, P. Source analysis of median nerve and finger stimulated somatosensory evoked potentials: Multichannel simultaneous recording of electric and magnetic fields combined with 3D-MR tomography. *Brain Topogr.* **1994**, *6*, 299–310. [CrossRef]
23. Hari, R.; Puce, A. *MEG-EEG Primer*; Oxford University Press: Oxford, UK, 2017.
24. Allison, T.; Wood, C.C.; McCarthy, G.; Spencer, D.D. Cortical somatosensory evoked potentials. ii. effects of excision of somatosensory or motor cortex in humans and monkeys. *J. Neurophysiol.* **1991**, *66*, 64–82. [CrossRef]
25. Fuchs, M.; Wagner, M.; Wischmann, Ha.; Köhler, T.; Theißen, A.; Drenckhahn, R.; Buchner, H. Improving source reconstructions by combining bioelectric and biomagnetic data. *Clin. Neurophysiol.* **1998**, *107*, 93–111. [CrossRef]
26. Baillet, S.; Mosher, J.C.; Leahy, R.M. Electromagnetic brain mapping. *IEEE Signal Process. Mag.* **2001**, *18*, 14–30. [CrossRef]
27. Tutorial 22: Source Estimation. 2020. Available online: https://neuroimage.usc.edu/brainstorm/Tutorials/SourceEstimation (accessed on 2 February 2020).
28. Kaipio, J.P.; Somersalo, E. *Statistical and Computational Methods for Inverse Problems*; Springer: Berlin, Germany, 2004.
29. Nummenmaa, A.; Auranen, T.; Hämäläinen, M.S.; Jääskeläinen, I.P.; Lampinen, J.; Sams, M.; Vehtari, A. Hierarchical Bayesian estimates of distributed MEG sources: Theoretical aspects and comparison of variational and MCMC methods. *NeuroImage* **2007**, *35*, 669–685. [CrossRef] [PubMed]
30. Sommariva, S.; Sorrentino, A. Sequential Monte Carlo samplers for semi-linear inverse problems and application to magnetoencephalography. *Inverse Probl.* **2014**, *30*, 114020. [CrossRef]
31. Pursiainen, S.; Vorwerk, J.; Wolters, C.H. Electroencephalography (EEG) forward modeling via H(div) finite element sources with focal interpolation. *Phys. Med. Biol.* **2016**, *61*, 8502–8520. [CrossRef]
32. De Munck, J.C.; Wolters, C.H.; Clerc, M. EEG & MEG forward modeling. In *Handbook of Neural Activity Measurement*; Brette, R., Destexhe, A., Eds; Cambridge University Press: New York, NY, USA, 2012.
33. Braess, D. *Finite Elements*; Cambridge University Press: Cambridge, UK, 2001.
34. Haueisen, J.; Tuch, D.S.; Ramon, C.; Schimpf, P.H.; Wedeen, V.J.; George, J.S.; Belliveau, J.W. The influence of brain tissue anisotropy on human EEG and MEG. *NeuroImage* **2002**, *15*, 159–166. [CrossRef]
35. Ramon, C.; Schimpf, P.; Haueisen, J. Influence of head models on EEG simulations and inverse source localizations. *Biomed. Eng. Online* **2006**, *5*, 1–13. [CrossRef]
36. Beltrachini, L. Sensitivity of the projected subtraction approach to mesh degeneracies and its impact on the forward problem in EEG. *IEEE Trans. Biomed. Eng.* **2018**, *66*, 273–282. [CrossRef]
37. Vorwerk, J.; Cho, J.H.; Rampp, S.; Hamer, H.; Knösche, T.R.; Wolters, C.H. A guideline for head volume conductor modeling in EEG and MEG. *NeuroImage* **2014**, *100*, 590–607. [CrossRef]

38. He, Q.; Rezaei, A.; Pursiainen, S. Zeffiro user interface for electromagnetic brain imaging: A GPU accelerated fem tool for forward and inverse computations in Matlab. *Neuroinformatics* **2019**, *18*, 237–250. [CrossRef]
39. Uutela, K.; Hämäläinen, M.; Somersalo, E. Visualization of magnetoencephalographic data using minimum current estimates. *NeuroImage* **1999**, *10*, 173–180. [CrossRef] [PubMed]
40. Miinalainen, T.; Rezaei, A.; Us, D.; Nüßing, A.; Engwer, C. .; Wolters, C.H.; Pursiainen, S. A realistic, accurate and fast source modeling approach for the EEG forward problem. *NeuroImage* **2019**, *184*, 56–67. [CrossRef] [PubMed]
41. Pursiainen, S. Raviart–Thomas-type sources adapted to applied EEG and MEG: Implementation and results. *Inverse Probl.* **2012**, *28*, 065013. [CrossRef]
42. Schmidt, D.M.; George, J.S.; Wood, C.C. Bayesian inference applied to the electromagnetic inverse problem. *Hum. Brain Mapp.* **1999**, *7*, 195–212. [CrossRef]
43. Calvetti, D.; Somersalo, E. A Gaussian hypermodel to recover blocky objects. *Inverse Probl.* **2007**, *23*, 733. [CrossRef]
44. Ahlfors, S.P.; Hämäläinen, M.; Sharon, D.; Ishitobi, M.; Vaina, L.M.; Stufflebeam, S.M. Mapping the signal-to-noise-ratios of cortical sources in magnetoencephalography and electroencephalography. *Hum. Brain Mapp.* **2009**, *30*, 1077–1086.
45. Wolters, C.H.; Lew, S.; Macleod, R.S.; Hämäläinen, M. Combined EEG/MEG source analysis using calibrated finite element head models *Biomed. Tech. Eng. Rostock. Ger. Walter Gruyter* **2010**, *55*, 64–68.
46. Antonakakis, M.; Schrader, S.; Wollbrink, A.; Oostenveld, R.; Rampp, S.; Haueisen, J.; Wolters, C.H. The effect of stimulation type, head modeling, and combined EEG and meg on the source reconstruction of the somatosensory P20/N20 component. *Hum. Brain Mapp.* **2019**, *40*, 5011–5028. [CrossRef]
47. Pursiainen, S.; Lucka, F.; Wolters, C.H. Complete electrode model in EEG: Relationship and differences to the point electrode model. *Phys. Med. Biol.* **2012**, *57*, 999. [CrossRef]
48. Tarkiainen, A.; Liljeström, M.; Seppä, M.; Salmelin, R. The 3D topography of MEG source localization accuracy: Effects of conductor model and noise. *Clin. Neurophysiol.* **2003**, *114*, 1977–1992. [CrossRef]
49. Cohen, D.; Cuffin, B.N. EEG versus MEG localization accuracy: Theory and experiment. *Brain Topogr.* **1991**, *4*, 95–103. [CrossRef] [PubMed]
50. Cuffin, B.N.; Schomer, D.L.; Ives, J.R.; Blume, H. Experimental tests of EEG source localization accuracy in realistically shaped head models. *Clin. Neurophysiol.* **2001**, *112*, 2288–2292. [CrossRef]
51. Cuffin, B.N.; Schomer, D.L.; Ives, J.R.; Blume, H. Experimental tests of EEG source localization accuracy in spherical head models. *Clin. Neurophysiol.* **2001**, *112*, 46–51. [CrossRef]
52. Buchner, H.; Adams, L.; Müller, A.; Ludwig, I.; Knepper, A.; Thron, A.; Niemann, K.; Scherg, M. Somatotopy of human hand somatosensory cortex revealed by dipole source analysis of early somatosensory evoked potentials and 3D-NMR tomography. *Electroencephalogr. Clin. Neurophysiol. Potentials Sect.* **1995**, *96*, 121–134. [CrossRef]
53. Götz, T.; Huonker, R.; Witte, O.W.; Haueisen, J. Thalamocortical impulse propagation and information transfer in EEG and MEG. *J. Clin. Neurophysiol.* **2014**, *31*, 253–260. [CrossRef] [PubMed]
54. Buchner, H.; Adams, L.; Knepper, A.; Rüger, R.; Laborde, G.; Gilsbach, J.M.; Ludwig, I.; Reul, J.; Scherg, M. Preoperative localization of the central sulcus by dipole source analysis of early somatosensory evoked potentials and three-dimensional magnetic resonance imaging. *J. Neurosurg.* **1994**, *80*, 849–856. [CrossRef]
55. Buchner, H.; Knoll, G.; Fuchs, M.; Rienäcker, A.; Beckmann, R.; Wagner, M.; Silny, J.; Pesch, J. Invers localization of electric dipole current sources in finite element models of the human head. *Electroencephalogr. Clin. Neurophysiol.* **1997**, *102*, 267–278. [CrossRef]
56. Seeber, M.; Cantonas, L.M.; Hoevels, M.; Sesia, T.; Visser-Vandewalle, V.; Michel, C.M. Subcortical electrophysiological activity is detectable with high-density EEG source imaging. *Nat. Commun.* **2019**, *10*, 753. [CrossRef]
57. Pizzo, F.; Roehri, N.; Villalon, S.M.; Trébuchon, A.; Chen, S.; Lagarde, S.; Carron, R.; Gavaret, M.; Giusiano, B.; McGonigal, A.; et al. Deep brain activities can be detected with magnetoencephalography. *Nat. Commun.* **2019**, *10*, 971. [CrossRef]
58. Papadelis, C.; Eickhoff, S.B.; Zilles, K.; Ioannides, A.A. BA3b and BA1 activate in a serial fashion after median nerve stimulation: Direct evidence from combining source analysis of evoked fields and cytoarchitectonic probabilistic maps. *Neuroimage* **2011**, *54*, 60–73. [CrossRef]

59. Wang, G.; Yang, L.; Worrell, G.; He, B. The relationship between conductivity uncertainties and EEG source localization accuracy. In Proceedings of the 2009 Annual International Conference of the IEEE Engineering in Medicine and Biology Society, Minneapolis, MN, USA, 3–6 September 2009; pp. 4799–4802.
60. Vorwerk, J.; Aydin, Ü.; Wolters, C.H.; Butson, C.R. Influence of head tissue conductivity uncertainties on EEG dipole reconstruction. *Front. Neurosci.* **2019**, *13*, 531. [CrossRef] [PubMed]
61. Calvetti, D.; Pascarella, A.; Pitolli, F.; Somersalo, E.; Vantaggi, B. A hierarchical Krylov–Bayes iterative inverse solver for MEG with physiological preconditioning. *Inverse Probl.* **2015**, *31*, 125005. [CrossRef]
62. Calvetti, D.; Pascarella, A.; Pitolli, F.; Somersalo, E.; Vantaggi, B. Brain activity mapping from MEG data via a hierarchical Bayesian algorithm with automatic depth weighting. *Brain Topogr.* **2018**, *32*, 363–393. [CrossRef] [PubMed]
63. Murakami, S.; Okada, Y. Invariance in current dipole moment density across brain structures and species: Physiological constraint for neuroimaging. *Neuroimage* **2015**, *111*, 49–58. [CrossRef] [PubMed]
64. Steinsträter, O.; Sillekens, S.; Junghoefer, M.; Burger, M.; Wolters, C.H. Sensitivity of beamformer source analysis to deficiencies in forward modeling. *Hum. Brain Mapp.* **2010**, *31*, 1907–1927. [CrossRef] [PubMed]
65. Sekihara, K.; Sahani, M.; Nagarajan, S.S. Localization bias and spatial resolution of adaptive and non-adaptive spatial filters for MEG source reconstruction. *Neuroimage* **2005**, *25*, 1056–1067. [CrossRef]
66. Neugebauer, F.; Möddel, G.; Rampp, S.; Burger, M.; Wolters, C.H. The effect of head model simplification on beamformer source localization. *Front. Neurosci.* **2007**, *11*, 625. [CrossRef]

Sample Availability: The Neurophysiological data (for one subject) is available on the Zenodo portal: https://doi.org/10.5281/zenodo.3888381. The ZI software utilized in this study is openly accessible in GitHub: https://github.com/sampsapursiainen/zeffiro_interface.

PUBLICATION V

Reconstructing Subcortical and Cortical Somatosensory Activity via the RAMUS Inverse Source Analysis Technique using Median Nerve SEP Data

A. Rezaei, J. Lahtinen, F. Neugebauer, M. Antonakakis, MC. Piastra, A. Koulouri, C. H. Wolters and S. Pursiainen

Submitted to NeuroImage Journal